ABSOLUTE DISTANCE CONTOURING AND A PHASE UNWRAPPING ALGORITHM FOR PHASE MAPS WITH DISCONTINUITIES

XINJUN XIE

A thesis submitted in partial fulfillment of the requirements of

Liverpool John Moores University for the Degree of Doctor of Philosophy

JUNE 1997

To my wife, Yi, son, Yu,
and family

Acknowledgements

The author would like to thank his supervisor, Professor M. J. Lalor, for his constant guidance, stimulation and encouragement provided throughout the period of this work, and in the preparation of this thesis.

Professor D. R Burton, his second academic supervisor, for his invaluable advice and encouragement throughout this study.

Dr. M. M. Shaw, his academic supervisor, for his helpful guidance and advice on this research work.

Dr. J. T. Atkinson, my former supervisor, for all his help and encouragement during the first two years of this program.

Professor C. A. Hobson, Dr. D. M. Harvey, Dr. J. D. Pearson, Mr. F. Lilley and Professor R. Morgan, for their academic and personal support.

The members of the Coherent and Electro-Optics Research group, School of Electrical Engineering, Electronics and Physics, and School of Engineering and Technology Management, for technical support and help on many occasions.

Last, but by no means least, the author wishes to acknowledge the support of his wife, Yi Yin and son, Yu, during the writing of this thesis.

Abstract

Absolute Distance Contouring and a Phase Unwrapping Algorithm for Phase Maps with Discontinuities

Xinjun Xie Doctor of Philosophy

This thesis describes a new technique, absolute distance contouring, and a phase unwrapping algorithm for phase maps with discontinuities.

Absolute distance contouring, which is based on the shadow moiré method, using the rotation of a grating, is a technique which can be used for the measurement of absolute distance from the grating to the object and the determination of an object's height. By the selection of suitable rotation angles, images are captured at different positions of the grating to obtain the required data. The technique is divided into three different methods, according to the number of images required for each measurement and the rotation angles. These are known as: the absolute distance contouring method, the four-image method, and the three-image method.

Using these methods, the three-dimensional shape of the object can be obtained directly and it is not necessary to determine the absolute moiré fringe order nor to judge the hills and valleys of the object's surface. Some of the problems of the previous shadow moiré methods can be solved and some inconvenience can be overcome by the proposed methods. The techniques have been verified by experimental work which was carried out on a specially designed system. The results show that the methods are fast and the accuracy is better than 10μm. The maximum measurable range is related to the geometry of the optical system and the rotation angles.

The phase unwrapping algorithm is a technique to obtain the correct phase distribution for a phase map with discontinuities. A crossed grating , which has two sets of lines in two different directions, is projected onto the surface to be measured. The modulated grating image, which is equal to the superposition of two separate modulated images, is captured and Fourier transformed. The two images are separated in the Fourier domain. After filtering and frequency shifting, they are inverse transformed to obtain two phase maps with different precisions. Phase unwrapping at each pixel is carried out independently and the correct phase values can be obtained in the presence of discontinuities caused by a surface with steps or noise. This fast algorithm has been verified experimentally by measuring the shapes of objects with height steps, and it only requires a single image for each measurement.

The methods of absolute distance contouring and the new phase unwrapping algorithm are new techniques for the measurement of three-dimensional object profile, which will find application in many areas.

June 1997

Contents

Abbreviations and Symbols.....vi

Chapter 1. Introduction

1.1 Introduction.....2

1.2 Shadow Moiré Contouring.....2

1.2.1 Determination of Fringe Order, Hills, and Valleys.....5

1.2.2 Automatic Data Processing.....7

1.2.3 Phase Shifting.....7

1.2.4 Applications of Shadow Moiré.....8

1.3 Projection Moire.....9

1.3.1 Phase Shifting.....11

1.3.2 Fourier Transform.....13

1.3.3 Phase Unwrapping.....15

1.4 Absolute Distance Contouring.....17

1.5 Proposed Phase Unwrapping Algorithm.....19

Chapter 2. Theory of Absolute Distance Contouring

2.1 Introduction.....21

2.2 Variation of a Grating's Period.....21

2.3 Theoretical Analysis.....26

2.3.1 Sinusoidal Wave Intensity Grating.....26

2.3.2 Square Wave Intensity Grating.....28

2.4 Signal Analysis.....31
2.4.1 The Features of the Signal 31
2.4.2 Sensitivity.....35
2.5 Relationship Between the Absolute Distance and the Parameters.....35
2.6 Proposed Method for Signal Processing.....37
2.7 Error Analysis.....39
2.8 Summary.....41

Chapter 3. Theory of Four-Image Absolute Distance Contouring

3.1 Introduction.....43
3.2 Four-Image Absolute Distance Contouring.....43
3.3 Relationship of the Parameters.....46
3.4 Error Analysis.....50
3.5 Summary.....53

Chapter 4. Theory of Three-Image Absolute Distance Contouring

4.1 Introduction.....55
4.2 Three-Image Absolute Distance Contouring.....55
4.3 Relationship of the Parameters and Rotation Angles.....58
4.4 Error Analysis.....62

4.5 Summary.....66

Chapter 5. Experiments and Results of Absolute Distance Contouring

5.1 Introduction.....68

5.2 Experimental System.....68

5.3 Experimental Procedure and Signal Processing.....70

5.3.1 Absolute Distance Contouring.....70

5.3.2 Four-Image Absolute Distance Contouring.....72

5.3.3 Three-Image Absolute Distance Contouring.....75

5.4 Experiments and Results of Absolute Distance Contouring.....75

5.4.1 Experiments of Absolute Distance Contouring.....75

5.4.2 Experimental Results.....77

5.4.3 Discussions.....82

5.5 Experiments and Results of the Four - Image Contouring Method.....87

5.6 Experiments and Results of the Three - Image Contouring Method.....90

5.7 Summary.....92

Chapter 6. Comparison between the Three Absolute Distance Contouring Methods

6.1 Introduction.....95

6.2 Comparison Between the Three Absolute Distance Contouring Methods.....95
6.2.1 Relationship Between the Absolute Distance and the Parameters of the System.....95
6.2.2 Rotation angles.....96
6.2.3 Measurable Ranges.....96
6.2.4 Factors Which Affect Measurement Accuracy.....98
6.3 Summary.....100

Chapter 7. Phase Unwrapping in the Presence of Discontinuities

7.1 Introduction.....103
7.2 Principle of the Fourier Transform and Phase Unwrapping.....103
7.2.1 Fourier Transform.....103
7.2.2 Phase Unwrapping.....105
7.3 Phase Unwrapping in the Presence of Discontinuities.....07
7.3.1 Phase Jumps Less Than 2π.....110
7.3.2 Phase Jumps Greater Than 2π.....111
7.4 Use of a Crossed Grating.....112
7.5 Simulation of the Crossed Grating System.....114
7.6 Summary.....122

Chapter 8. Experiments and Results of Phase Unwrapping

8.1 Introduction.....124

8.2 Experimental Arrangement.....124

8.3 Signal Processing Procedure.....126

8.4 Experimental Results.....127

8.4.1 The Phase Jump for Different Grating Periods.....128

8.4.2 Measurement of 3-D Object Containing a Height Step Using a Crossed Grating.....132

8.4.3 Discussion.....137

8.5 Summary.....138

Chapter 9. Conclusions and Recommendations for Further Work

9.1 Introduction.....140

9.2 Conclusions.....141

9.3 Recommendations for Further Work.....144

References.....147

Appendix

Publications.....160

Full Papers.....163

Abbreviations and Symbols

a	Background Intensity
A	Sinusoidal Value of θ_1
A	$2\pi y/P_0$
A	Length
A	Frequency Spectra of a
A'	Sinusoidal Value of θ'_1
A_0	DC Component of the Signal
$A_{1\text{-}4}$	Terms of Moiré Pattern
b	Amplitude of Cosine Function
B	Sinusoidal Value of θ_2
B	$2\pi\sin\omega t(y\text{-}z\tan\alpha)/P_0$
B'	Sinusoidal Value of θ'_2
c	Coefficient
c^*	Coefficient
C	Sinusoidal Value of θ_3
C	Positive Frequency Spectra
C^*	Negative Frequency Spectra
C'	Sinusoidal Value of θ'_3
cos	Cosine
$\cos^{-1}$	Inverse Cosine
CCD	Charge Coupled Device
d	Distance Between Camera and Projector
D	Sinusoidal Value of θ_4
f	Frequency
f_0	Carrier Frequency
f_1	Carrier Frequency
FFT	Fast Fourier Transform
h	Object Height
H	$0.5(M'_1\text{-}M'_2)/(M'_3\text{-}M'_4)$

H'	$0.5(M''_1-M''_2)/(M''_2-M''_3)$
i	$\sqrt{-1}$
I	Frequency Spectra
I	Intensity on Object Surface
I_0	Intensity of Light Source
Im	Imaginary Part
INT	Operator to Obtain the Integer Value
k	$2\pi/P$
k	Integer Number
k	Constant
k_0	Coefficient
k_1	Constant
L	Distance Between Camera and Reference Plane
m	Integer Number
M	Moiré Pattern
M'	Contour Term
M_{max}	Maximum Value of M
M_{min}	Minimum Value of M
M'_{1-4}	Contour Terms of Four-Image Method
M''	Contour Term
M''_{1-3}	Contour Terms of Three-Image Method
n	Integer Number
n	Fringe number
N	Number of Steps
O	Intensity on the Object's Surface
P	Period of Grating
P_0	Original Period of Grating
PSI	Phase Shifting Interferometry
q	Integer Number
R	Reflectivity of the Object
Re	Real Part

sin	Sine
S	Measured Area
t	Time
T	Transmission Function
T	Sampling Time
VFG	Variable-Scan Frame Grabber
x	Position at X Axis
y	Position at Y Axis
y_s	Distance Between the Camera and the Light Source
z	Distance from the Grating to the Object
z_0	Distance from the Grating to the Camera or the Light Source
z_{max}	Maximum Measurable Range of Four-Image Method
z'_{max}	Maximum Measurable Range of Three-Image Method
α	Angle of Incidence
θ	Rotation Angle
θ'	Angle
θ_{1-4}	Angle Values of Four-Image Method
θ'_{1-3}	Angle Values of Three-Image Method
θ_n	Maximum Rotation Angle
ω	Angular Velocity
μm	Micrometer
φ	Phase Value
φ_0	Phase Value
φ_1	Phase Value
Φ	Phase
Φ	$2\pi z y_s/(P_0(z+z_0))$
Φ'	$2\pi z y_s/(P_0(z+z_0))$
Φ_r	Phase at Reference Plane
Φ_0	Phase Produced by Object
Φ_{max}	Maximum Value of Φ
Φ'_{max}	Maximum Value of Φ'

∞	Infinity
^{o}	Degree
Δh	Contour Depth
ΔP_0	Error of P_0
Δy_s	Error of y_s
Δz	Error of z
Δz_0	Error of z_0
$\Delta \theta_n$	Error of θ_n
$\Delta \theta_{1\text{-}4}$	Errors of $\theta_{1\text{-}4}$
$\Delta \theta'_{1\text{-}3}$	Errors of $\theta'_{1\text{-}3}$
$\Delta \varphi$	Phase Difference
$\Delta \varphi_1$	Phase Difference
$\Delta \Phi$	Error of Φ
$\Delta \Phi'$	Error of Φ'

Chapter 1

Introduction

1.1 Introduction

The measurement of absolute distance and three-dimensional profiles are very important in many application areas including metrology, automated manufacturing, component quality control, medical diagnosis, and robotics. Among the various types of techniques, optical methods are very popular [Sciammarella 1979; Strand 1985; Atkinson and Lalor 1986], because of their non-contact nature. Optical methods which include moiré, speckle [Butters and Leendertz 1971; Ennos 1975; Nakadate 1983 and 1985], and holography [Butters 1970; Sommargren 1977; Nakadate 1981; Sciammarella 1982; Hariharan 1983], for the measurement of distance and three-dimensional object profile, are widely studied. Moiré techniques are particularly suitable for mapping the absolute shape of a given surface or the difference between that surface and a master surface or accidental shape changes [Sciammarella 1982; Post 1982 and 1991; Reid 1984; Kafri and Glatt 1989; Walker 1994]. These methods are characterized by their simplicity and the fact that only readily available and unsophisticated equipment is required.

In this chapter, shadow moiré contouring techniques, including the determination of the fringe order, hills, and valleys, automatic data processing, phase shifting, and their applications, are reviewed in section 1.2. Projection moiré techniques including phase shifting, Fourier transform, and phase unwrapping are reviewed in section 1.3. A proposed new technique, absolute distance contouring, which is used to improve the previous shadow moiré methods, is described in section 1.4. Section 1.5 is a newly proposed phase unwrapping algorithm for use on phase maps with discontinuities.

1.2 Shadow Moiré Contouring

The moiré phenomenon, noted over 100 years ago by Lord Rayleigh [Rayleigh 1874], is associated with the visible fringe system caused by superposing two similar grid structures. The word moiré derives from the French name for a silk fabric imported from ancient china, in which the threads form patterns that give to the fabric its peculiar

appearance. The fringes, called moiré fringes, are clearly seen when grids are nearly parallel and their frequency space, (or their multiples), are about the same. Although the phenomenon was further treated by some authors, interest in the field seemed to diminish until the end of the Second World War, despite the many advantages the effect offers in metrology [Durelli and Parks 1970].

The moiré technique can be divided into shadow moiré and projection moiré, which are widely studied and used in different application areas. Since the techniques differ in their applications, it is customary to make a distinction between shadow moiré and projection moiré. In the former method, the projection of a grating onto the object is obtained very simply by placing the grating as close as possible to the object's surface and by casting its shadow onto this surface by means of collimated or diverging light beams, the moiré pattern being observed through the grating itself. In the latter method, use is made of a projection lens to image a master grating onto the object's surface [Pirodda 1982], and viewed through a reference grating. Apart from the above feature, which is, of course, of considerable practical importance, the two methods can be considered theoretically similar and studied in a unified approach.

In this section, the shadow moiré technique, or shadow moiré contouring, will be explained in more detail. One great characteristic of the shadow moiré contouring technique is its extreme simplicity. In order to perform an elementary experiment, one only requires a point or line source and a grating placed in front of the object. Such an experiment could have been conceived and performed in Galileo's time, at least in cases where a coarse grating is needed. It is perhaps surprising that the principle and implementation of so humble a method only emerged at the same time as more complex techniques such as holographic and speckle interferometry.

The shadow moiré method was used in the first scientific application of moiré. Work in this area goes back to 1925 [Mulot 1925]. The method was later reintroduced by a number of authors [Weller and Shephard 1948; Kaezer and Kroupa 1952; Theocaris 1964]. All of these authors were concerned with the formation of moiré patterns by the projection of the shadow of a grating onto an object's surface with collimated or

diverging light beams and observing the grating and its shadow so that the viewing point was effectively at infinity.

Later, a group of authors generalized the conditions of the observation and illumination [Pirodda 1969; Meadow 1970; Takasaki 1970]. In their systems, they utilised gratings which were illuminated and observed from points at an infinite distance. In these arrangements, the fringes do not have a simple interpretation, the fringe order is a function of the distance from the object surface to the reference plane and a one-dimensional description is sufficient to provide the answer to the problem. The fringes give lines of equal deflection in a direction normal to the plane of the grating. If the observation and illumination sources are at finite distances, the above interpretation is no longer valid. The analysis of the fringe formation in the above cases has followed two approaches that the literature calls the communication theory [Meadow 1970], and the ray-tracing method [Chiang 1969 and 1975; Takasaki 1970]. The communication theory approach is an application of the treatment introduced by Sciammarella [Sciammarella 1965], to the shadow moiré method, whereas the ray-tracing method is a generalization of the geometrical optics approach to moiré fringes. A unification of both theories has been attempted by Heiniger and Tschudi [Heiniger and Tschudi 1979], and the results include the possibility of introducing layers of different diffraction indices between the surface and the grating. The optical law of moiré fringes [Sciammarella 1965], is utilised by Roger [Roger 1979], to provide an alternative derivation of some of the equations obtained by previous authors. The results show that the optical law of moiré patterns and the ray-tracing method lead to identical results in terms of the interpretation applied to the fringes.

One limitation of the shadow moiré method results from the shadow cast by the features of the object surface. This limitation could be overcome by utilizing two-point light sources [Meadow 1970; Takasaki 1970]. In this case, the observation point must be half way between the two illumination points to obtain optimum fringe contrast. An alternative method to the two-source technique is to project two gratings onto the object. In this case, the fringes are visible on the surface of the object, thus making observation easier. However, the contrast of the fringes is poor and this is an

inconvenience [Hovanesian and Hung 1971; Bryngdahl 1976; Yoshino and Takasaki 1976; Lim 1989].

In order to obtain good quality moiré patterns and high accuracy measurements using the shadow moiré method, many authors have attempted to use different techniques. An averaging process can be used to remove the grating lines during photographic recording of moiré topograms by moving the grating [Allen and Meadow 1971]. Using this method, four exposures are made on the film with the grid in four different positions, each position separated by a distance of a quarter of the grating's period. The resulting picture will have no unwanted terms or non-contour patterns. Another way of achieving the same result is to average a number of video frames recorded during the translation of the grating at a specified speed [Dirckx 1990]. A fringe-scanning method using a general function instead of an arctangent function, is used for shadow moiré. The general function is analysed by the numerical analysis to obtain high resolution and accuracy [Arai 1995].

Since the grating is very important in shadow moiré techniques, the possibility of using a different grating in shadow moiré has been studied by different authors. Kafri and Livant proposed the tunable grating, which is formed by placing one grating upon another with a varying angle between them, to obtain optimal resolution and to help distinguish between hills and valleys [Kafri and Livant 1979]. A curved grating can be used to improve the accuracy of the measurement [Marasco 1975; Wegdam 1992]. Krumm and Shafer developed a model of a sampled-grating moiré system and compared it with a crossed-grating system [Krumm and Shafer 1991]. A three-way grating and three-dimensional grating for moiré method are studied by Patorski and Kujawinska [Patoski and Kujawinska 1985], and Ibrahim [Ibrahim 1982], respectively.

1.2.1 Determination of Fringe Order, Hills, and Valleys

When the observation and projection points are at finite distances, the displacements, (or the distance from the grating to the object's surface), are functions of the fringe order. Consequently, the fringe order must be known. There have been several methods that

determine the absolute order of shadow moiré fringes. Takasaki proposed a method - which adds a vertical line to the grating to obtain the absolute order of a moiré fringe [Takasaki 1973]. However, the absolute order of a fringe can be obtained only after measuring the photograph and performing some calculations. The application of two-frequency gratings in front of the object rather than the usual single frequency grating was suggested by Ibrahim [Ibrahim and Takasaki 1985]. Three interesting techniques have been proposed to solve the problem of the determination of the absolute order of a moiré fringe. Respectively, these use a photometric model to connect the image brightness values with the surface orientation of the object [Ding and Pekelsky 1987 and Pekelsky 1987], periodic color structures generated by superimposing two moiré patterns with different colors [Yuk 1994], and a moving-light-source method with the Fast Fourier Transform [Lim 1989].

Another problem of shadow moiré contouring is that the observation of shadow moiré contours does not allow a direct determination of whether a contour showing concentric fringes is a hill or a valley. This judgment can only be made if one knows the object's shape. This type of determination cannot be applied to an unknown object or in automatic processing. There are several solutions including the stereo pair method, where a stereo picture pair is taken of an object on which the contour pattern is localized, and a two light source method where a second source is placed a very short distance from the camera, to produce a coarse moiré fringe pattern. This is added to a fine contour pattern produced by the other light source. If the coarse fringe pattern is broadened to cover the depth of interest, the hill will be bright or dark centered [Takasaki 1973 and 1979]. In the double-exposure and color-difference method, after the first exposure, the object is translated normal to the grating by a certain distance and a color filter is placed in front of the camera lens prior to the second exposure. The order of the color sequence in each contour line definitely determines the slope direction [Livant 1980]. The misalignment method, the mismatch method and the grid-shifting procedure were also introduced to solve the same problem [Murakami 1978].

1.2.2 Automatic Data Processing

The shadow moiré technique has many important applications in different areas. For example, it can be used to establish the shape of an object after manufacture, or to compare an object to a reference specimen. However, a successful application requires some form of automation of the data processing.

When an initial reference grating is introduced by electronic means [Ideawa 1977], the moiré fringes can be displayed alone by electronically removing the carrier and reference gratings. Image-processing techniques are introduced to generate color contours to separate the hills and valleys and to obtain absolute fringe orders. Automatic data processing was introduced by Perrin and Thomas [Perrin and Thomas 1979], where an optoelectronic technique is used to measure the moiré fringe phase and sign. The method is based on the two reference beam method of holographic interferometry proposed by the same authors. This method leads to the phase measurement by heterodyning.

Digital image processing was introduced to the moiré technique by Yatagai [Yatagai 1982] and Gasvik [Gasvik 1983], amongst others, which made real-time measurements of object contour possible. Cline proposed that the computer-aided technique uses a digitized 2-D fringe image that is analyzed to calculate contours between the fringes [Cline 1982 and 1984]. The method of analyzing the moiré contour pattern in terms of the phase rather than the intensity of the fringes was studied by Reid [Reid 1986]. Recently, different image processing methods for the moiré pattern analysis are also studied by other authors [Ning and Peng 1988; Jin and Tang 1989; Ivnitsky and Voloshin 1990; Liao and Voloshin 1993].

1.2.3 Phase Shifting

In the case of projection moiré, the phase-shifting method can be easily applied because two gratings are arranged with a separation and one of the gratings can be moved to produce a mutual phase difference between them. However, for the shadow moiré

technique, where only one grating is used, the mutual phase difference between the reference grating and the deformed grating image cannot be produced by a moving grating. Allen and Meadow used this fact to develop their grating translation technique to obtain moiré pictures with high contrast fringes [Allen and Meadow 1971]. In Dirckx's method, the phase shift between different moiré topograms is obtained by a slight variation of the object-to-grating distance[Dirckx and Decraemer 1988, 1989 and 1990]. As the phase of the grating does not influence the location of the moiré fringes on the object, the projected grating lines can be averaged out during the exposure by moving the grating in its own plane [Takasaki 1982]. At the same time, the convexity and concavity of the surface are automatically determined. Yoshizawa studied phase-shifting of the shadow moiré method by moving both the grating and light source to achieve the required phase shift [Yoshizawa 1993]. A complete analysis of the shadow moiré phase-shifting method, showing the influence of different parameters, was presented by Mauvoisin [Mauvoisin 1994].

1.2.4 Applications of Shadow Moiré

The shadow moiré method, in its all different varieties, is an extremely valuable tool, not only in the area of experimental mechanics, but also as a means of measuring and controlling shapes. Since the first scientific application in 1925, the shadow moiré technique has found applications in many different areas. It has been used in the aeronautical industry [Dykes 1970], the study of the impact of thin plates by blunt projectiles [Beynet 1971; Andrews 1982], surface inspection [Redner 1990], metrology [Reid 1984; Gasvik 1987], vibration studies [Hung 1977; Kafri 1985], and machine vision [Gasvik and Hovde 1989]. In the area of medicine, shadow moiré has been applied to obstetrics, orthopedics and biostereometrics, obtaining surface contour information on patients receiving radiotherapy [Takasaki 1974 and 1979; Chu 1981; Pirodda 1982; Ivnitsky 1990]. Other applications of shadow moiré techniques in different areas have also been reported [Redner 1985; Walker 1994].

For the various shadow moiré methods mentioned above, even though they have been used in many different applications, there are still limitations and problems in practical

uses [Cline 1984; Graham 1990; Wykes 1995; Yasuhiko 1995]. There are difficulties that occur in complex shapes where the surfaces are not single valued and reconstruction is not unique. The surface to be measured cannot be too steeply sloped because the density of fringes cannot exceed the resolution of the video system. Actual surfaces may not be uniform in reflectivity and will not yield clean fringe patterns. Techniques such as painting the surface matt white may be needed for shiny metallic surfaces. The determination of the absolute fringe order and the ability to distinguish between the hills and valleys of the object's surface can be made by some of the previous methods, but it is not convenient. Only the object's relative height rather than the absolute distance between the grating and the object's surface can be measured. So it is necessary to improve the shadow moiré technique.

1.3 Projection Moiré

Projection moiré topography is a well known and popular method for non-contact profilometric measurement of diffuse objects and intensively studied by many researchers [Idesawa 1977; Srinivasan 1984; Chang 1991]. Using this technique, the optical fringes which are projected onto an object can be grating lines [Halioua 1983; Reid 1984; Srinivasan 1985; Gasvik 1986], or interference fringes generated by a conventional interferometer [Chang 1991; Gruber 1992; Peng 1995]. Once a straight line grating with sinusoidal or square wave intensity distribution is projected onto an object, the surface height distribution is translated into a phase distribution of the deformed grating or interference fringes, and thus the techniques of phase measuring can be used for the quantitative analysis of the surface topography. The basic experiments for the projection grating method and the method of projected fringes are shown in figure 1.1.

In figure 1.1(a), a source projects a plane equispaced master grating onto the object whilst an image of the object is formed in the plane of a reference grating, which is assumed to be the image of the projection of the grating. Interference between the grating image and the reference grating causes a number of moiré fringes to appear

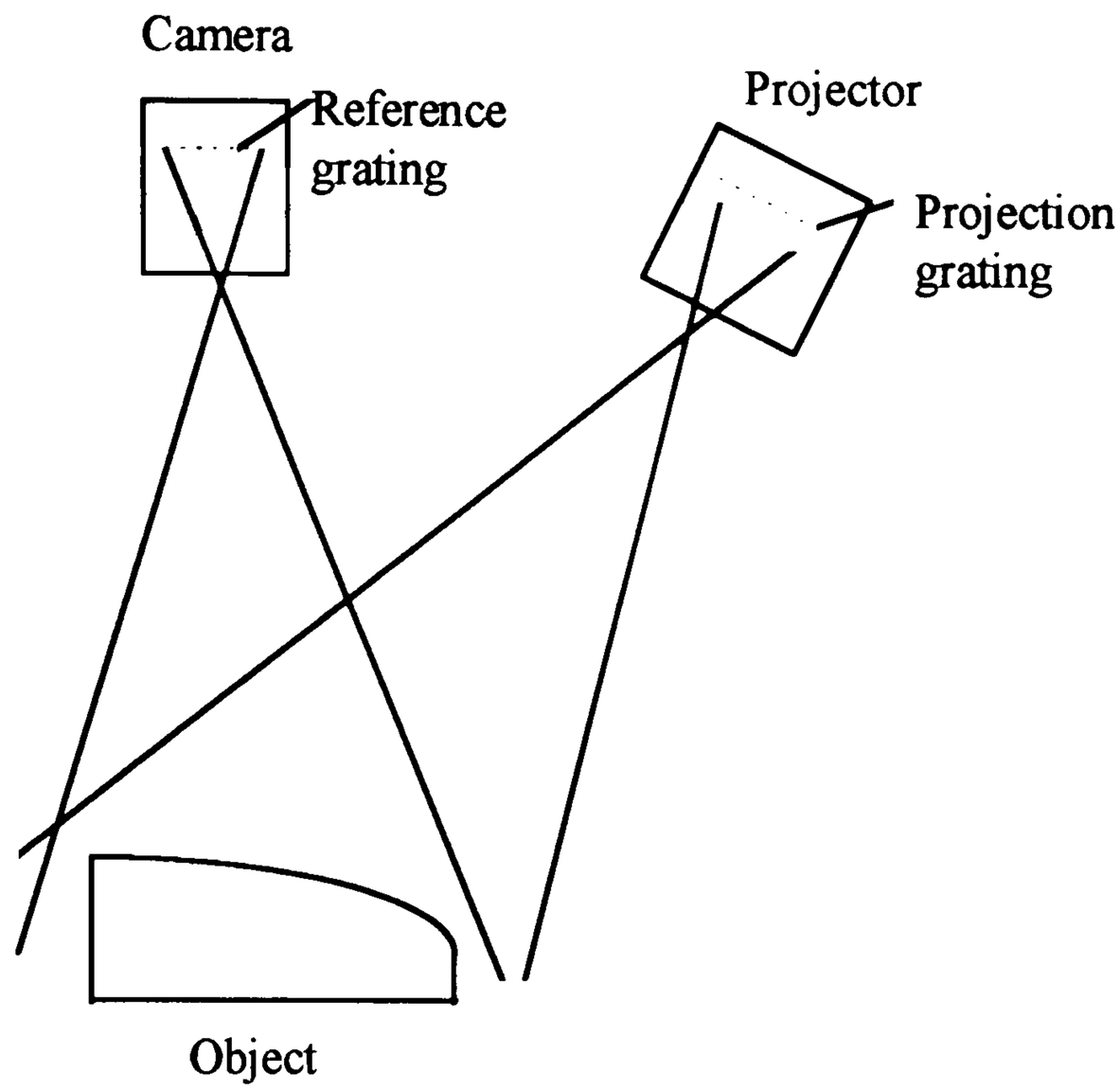

(a) system with projection and reference gratings

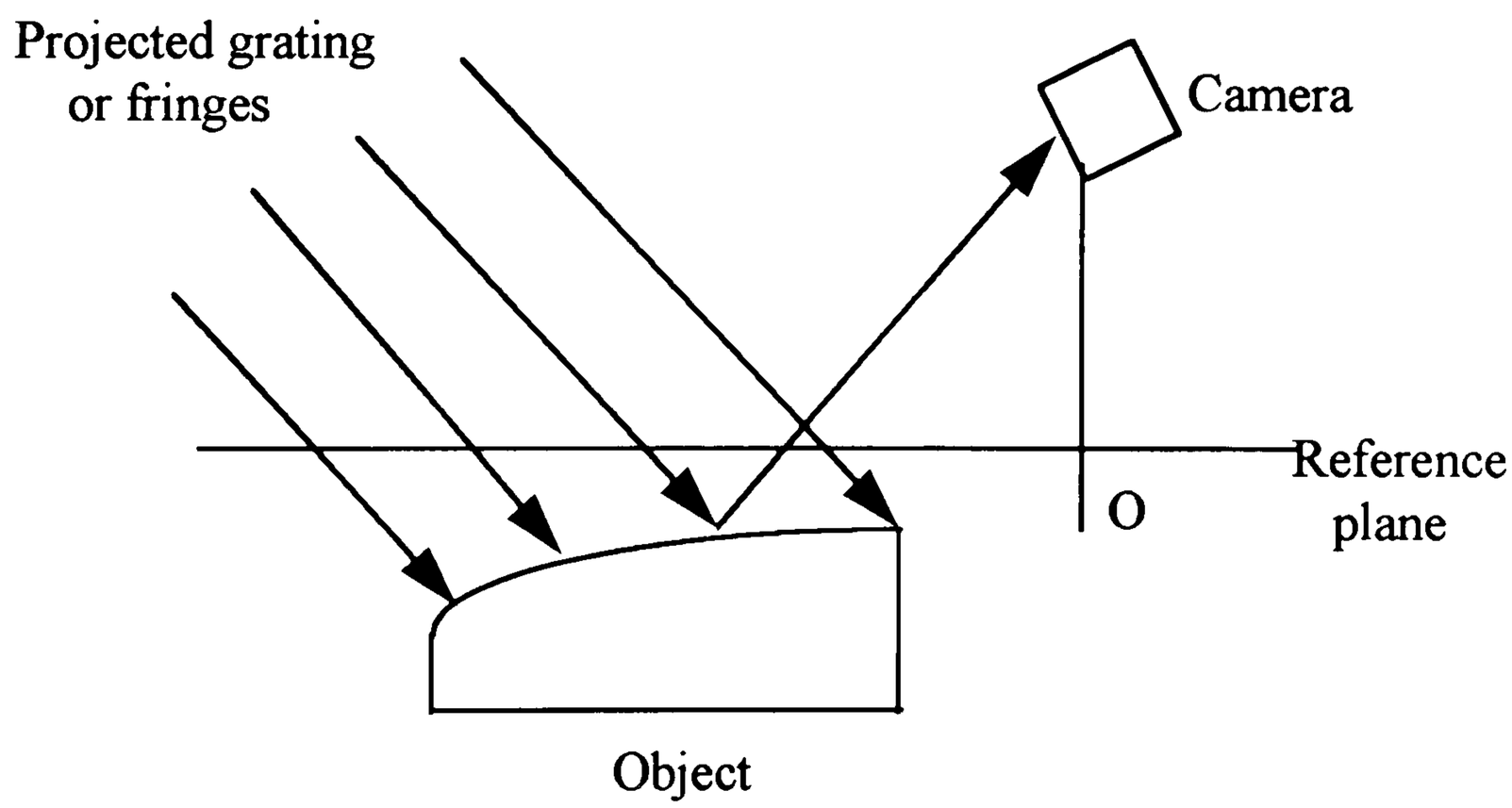

(b) projection system with a single grating or interference fringes

Figure 1.1 Schematic Diagrams of Projection Moiré Topography

superimposed upon the surface of the object. Such fringes can be readily interpreted in terms of the shadow moiré principles [Pirodda 1982]. Figure 1.1(b) is a schematic diagram of a projection system in which one grating or set of interference fringes is projected and the image of the projection of the grating or interference fringes is observed directly rather than through the reference grating. The projection grating may be of a sinusoidal or square wave intensity distribution [Su 1992].

The deformed grating image or the observed fringe pattern contains information about the object's height distribution which is in the form of a phase distribution. It is necessary to calculate the phase distribution of the fringe pattern to obtain the object's height distribution. Several methods can be used in order to achieve this. In particular, the phase shifting method and the Fourier transform technique will be discussed in the following sections.

1.3.1 Phase Shifting

To obtain the object's height distribution, one must obtain the phase distribution of the deformed grating pattern. There are several methods used for this purpose, including phase shifting, the Fourier transform method, and spatial phase detection [Toyooka 1986]. Different methods require a different number of images. Phase shifting and the Fourier transform technique are two of the most popular methods. Both are based on an almost identical analysis, the main difference being that the phase shifting algorithms perform computations in the spatial domain, while the computations for the Fourier transform method are performed in the frequency domain. In this section, the phase shifting methods are examined, which require more than two images to extract the phase information.

Phase shifting interferometry, (PSI), which is now used widely in many application areas is a general automatic phase measurement technique. The basic idea of PSI is to introduce three or four discrete phase steps into the interferogram, measuring the light intensity distribution across the pupil for each phase shift, thus measuring the phase of the interferogram. It has been used in optical metrology, holographic interferometry,

speckle interferometry, and in both shadow moiré and projection moiré methods [Chang 1985; Creath 1985; Dirckx 1988; Mauvoisn 1994; Perry 1993].

Moiré patterns contain inherent noise due to the original gratings, which is especially noticeable when coarse gratings are used. Topographical fringes, in addition, are often plagued by spurious moiré in the regions of large slopes. It has been shown that, in a shadow moiré arrangement, these artifacts can be eliminated by a grating translation technique [Takasaki 1970; Allen 1971]. In the case of the projection grating being observed through the reference grating, (figure 1.1(a)), simultaneous translation of the reference and projection gratings at a certain speed can generate high definition contour fringes without any of the noise problems associated with standard moiré [Halioua 1983].

If there are two gratings in the projection system, phase shifting is accomplished by moving the projection grating a certain distance between each image. The first image is obtained with the grating in its original position. If the projection grating's period is P_p, the grating is moved through a distance P_p/k. The phase of the projection grating is thus moved through an angle of $2\pi/k$, where k is an integer number and $k>2$. This process is repeated until the projection grating has moved through (k-1) equal steps and a total of k images have been captured, so that k intensity levels have been stored at each pixel location [Reid 1984].

If there is only one grating in the projection system, the deformed image is observed directly by the camera and phase shifting is realized by moving the projection grating N steps, with one image being captured at each position. The number of images required could be three, four, five, or more [Srinivasan 1985; Poon 1993]. The five-image algorithm, which is most popular in commercial interferometers, is an extension of the four-image algorithm, in the sense that the first image is replaced by the average of the first and fifth image, corresponding to phase shifts of 0 and 2π. It has been shown to be less sensitive to miscalibration [Hariharan 1987]. A similar extension of the N-image algorithm, retaining both the insensitivity to phase-shift miscalibration and the possibility

of using many frames to improve the signal-noise ratio is studied by Surrel [Surrel 1993]. A profilometry sensor that combines phase shifting with a Talbot self-image of a sinusoidal grating as the illumination part of the sensor is also proposed [Oreb 1994].

Since precise movement of the grating is required to obtain accurate images at each step in the projection grating methods, the grating could be replaced by interference fringes to improve the accuracy and the sensitivity of the method. When a sinusoidal intensity distribution generated by an interference pattern between two coherent plane wave fronts is projected onto the surface of a three-dimensional diffuse object, the mathematical representation is similar to that of the deformed grating image intensity distribution encountered in the conventional projection grating method. Srinivasan used a laser illuminated shearing polarization interferometer as a means of replacing the projection grating. By rotating the polarizer, the sinusoidal intensity distribution of the interference pattern can be modulated [Srinivasan 1984]. Similar research has also been carried out by the use of interference patterns to solve the problems of the "hills and valleys" interpretation between fringes by using digital image processing techniques [Gasvik 1986; Chang 1991]. Sinusoidal fringes with precise shifts generated by the astigmatic imaging of a binary transmission pattern and an optical fibre based moiré interferometer are studied [Gruber 1992; Valera 1993]. Phase and amplitude information obtained from phase-shifting interferometry may be combined to obtain a complex-valued phasor for every pixel in the image. This provides a simple yet effective concept for filtering, visualization, masking, and unwrapping interferometric phase maps [Strobel 1996].

1.3.2 Fourier Transform

The phase shifting methods discussed in section 1.3.1, all require at least 3 images to generate a phase map. An important aspect of the PSI analysis is that the phase of the wavefront under study is determined independently at each point, without the need to consider data at other points in the image. This means that arbitrary discontinuities in the fringe pattern will be correctly interpreted and the 'sense' of the wavefront will be

automatically and unambiguously resolved. The alternative method is the well-known Fourier transform. The Fourier transform has the advantage of requiring only one interferogram for the analysis. This makes it particularly attractive for dynamic applications, or instances where vibrations make interferometric measurement difficult. However, difficulties arise with this method near edges and in the presence of fringe pattern discontinuities.

The basic Fourier fringe pattern analysis algorithm proposed by Takeda [Takeda 1982], was based on a one-dimensional Fourier transform. This one-dimensional technique adds to the phase information in an interferogram, a phase which is a linear function of the coordinates, for example, by tilting one of the mirrors in the interferometer. This heterodyning process separates, in the frequency space, the positive and negative frequency components of the sinusoidal intensity from each other and from some of the spurious intensity contributions. By filtering to retain only the positive frequency components, the underlying phase can be retrieved. This technique was extended by Macy [Macy 1983], to handle 2-D data. This extension, however, is still essentially a 1-D analysis of slices of the data. The technique was refined by employing a two-dimensional Fourier transform [Bone 1986]. This technique gives better separation of the desired information from unwanted components. This is achieved without incurring any penalties in processing time, as the more selective filtering afforded by the 2-D transform removes the need for later smoothing of the phase. Several other refinements to the technique are also introduced. These include an improved method for removal of the heterodyning and a technique for reducing the large phase errors at the boundary associated with the use of a numerical data window. In addition, improved estimates of the band limits are proposed which permit optimization of the interferogram using parameters easily measured from a test interferogram. In the large fringe shift limit, these band limits lead to a rule of thumb which makes it possible to ensure that the information components are isolated in the transform plane.

In the last ten years, the Fourier transform techniques have been widely studied and used for the analysis of interferograms. For example, it has been used for mapping the complex fringe visibility in several types of interferogram by Roddier [Roddier 1987],

for automatic measurement of three-dimensional object shapes in which the technique has a much higher sensitivity than the conventional moiré method and is capable of fully automatic distinction between a depression and an elevation on the object's surface. There is no requirement for assigning fringe orders and interpolating data in the regions between contour fringes [Takeda 1983; Li 1990; Lin 1995]. The application of the Fourier transform method in the analysis of speckle, shadow moiré, and phase shifting interferometry to obtain the three-dimensional profile of diffuse objects, has been reported [Suganuma 1991; Takeda 1994; Lim 1989; Morimoto 1994].

1.3.3 Phase Unwrapping

A major aim in interferometric fringe analysis is to automate the process. The extent to which this can be achieved is a matter of some debate. It has been proposed that expert systems be employed as an aid to automatic methods [Judge 1994]. Automatic methods aim to eliminate the need for expert knowledge in the interpretation of fringe patterns and thereby allow it to be used more widely. Automatic techniques are essential if systems are to be used unsupervised, for example, in quality assurance on the production line. However, a general automated approach to the phase unwrapping problem in fringe analysis has been elusive.

Two generally applicable phase encoding/decoding techniques have been involved which are of great assistance in the resolution of directional ambiguity. These are phase shifting and the Fourier transform techniques [Srinivasan 1985; Reid 1986/7]. Both these techniques yield a phase map which is referred to as a wrapped phase map. The basic technique for analyzing these wrapped phase maps is known as fringe counting or fringe scanning. This involves traversing the scan lines of the digitally processed field to search for the phase roll over points at the fringe edges, where the phase changes abruptly between 2π and zero, or vice versa. Since noise in the wrapped phase map can cause a problem of disrupting the fringe edges, upon which the technique relies, this makes phase unwrapping a potentially difficult exercise.

However, phase unwrapping techniques have recently been developed which are

tolerant of spike noise. Ghiglia describes the discovery of a cellular automaton which can unwrap consistent phase data in n dimensions in a path-independent manner and which can automatically accommodate noise-induced, point like, inconsistencies [Ghiglia 1987]. The technique requires a large number of iterations to converge. Algorithms based on cuts which are also tolerant of such noise and computationally efficient are described by Goldstein [Goldstein 1988], and Huntley [Huntley 1989]. Bone has described a fast flood fill algorithm which improves the speed of the cut algorithms [Bone 1991]. Takeda has recently proposed a phase unwrapping strategy using a neural network, which also employs cut lines [Takeda 1993]. Noise-tolerant algorithms, based on minimizing phase changes between pixels via minimum spanning trees, have been are described [Judge 1992].

Although robust for consistent phase data, these procedures do not cope with fringe fields that contain large scale phase disturbances, such as those which contain noise spikes significantly larger than pixel size, and which may not be detected by a local pixel level inspection. Large scale discontinuities can occur for a variety of reasons. Shadows can cause large discontinuities, as can spaces between objects or their parts. Such spaces are especially problematic when they occur with a spatial frequency of the same order as the fringe spacing, since their size means that they may not be filtered out.

Several approaches have been taken to those types of problem. Judge's minimum spanning tree algorithm incorporates region level processing [Judge 1992]. The dimensions of the pixel tiles employed are related to the size of the discontinuities to be detected; pixel order tiles enable the unwrapping of consistent phase maps containing spike noise, whereas larger tiles allow larger local features of inconsistency to be identified.

Gierloff has proposed a method which also confronts the problem posed by large scale discontinuities [Gierloff 1987]. This method segments the fringe field into areas of apparent consistency and attempts to intelligently relate these areas to each other. Green and Walker have described a phase unwrapping algorithm that eliminates discontinuities based on the expected frequency band limits of a fringe field [Green 1988]. The

interferogram represents a slowly varying function and should not, therefore, contain high frequency components. High frequency components are due to the step changes at roll over points and noise. The algorithm attempts to eliminate the step changes by examining the spectrum of the unwrapped phase.

For phase unwrapping in the presence of discontinuities, an algorithm called multi-channel Fourier fringe analysis, which is used for the problem of automatic phase unwrapping in the presence of surface discontinuities, is proposed by Burton [Burton 1994]. The algorithm requires the presence of more than one fringe pattern on the surface. Bhat proposed a method based on the computation of the phase obtained directly from the wrapped phase maps [Bhat 1994]. By this method, the phase discontinuities are eliminated by converting the wrapped phase map into a continuous fringe pattern and the phase derivative is obtained using a differentiator in the Fourier space. A phase unwrapping algorithm, using two phase images with different precisions, is proposed by Zhao and can produce an approximately correct unwrapped image in the presence of discontinuities [Zhao 1994]. Using this method, two phase images are obtained by the phase shifting technique with different grating periods, so that a total of eight images are required for each measurement. An algorithm based on the identification of discontinuity sources that mark the start or end of a 2π phase discontinuity is studied by Cusack [Cusack 1995]. In this method, branch cuts between sources act as barriers to unwrapping, resulting in a unique phase map that is independent of the unwrapping route. Quiroga proposed a stable-marriage algorithm for processing phase maps with discontinuity sources, which is implemented as a recursive procedure [Quiroga 1995].

1.4 Absolute Distance Contouring

To improve shadow moiré contouring techniques, a new technique called absolute distance contouring, is proposed. It is based on the shadow moiré method and the rotation of a grating, and can be used for the measurement of the absolute distance from the grating to the object and the object's height. Using this technique, the three-

dimensional shape of the object can be obtained directly and it is not necessary to determine the absolute moiré fringe order, nor to judge the hills and valleys of the object's surface. Some of the problems of the previous shadow moiré methods can be solved and some inconvenience can be overcome by the proposed new technique.

In the new shadow moiré system, the period of a grating is varied by rotating it, so that the phase of the moiré pattern is changed as well. By the selection of suitable rotation angles, images are captured at different positions of the grating to obtain the absolute distance from the object to the grating, as well as the object's height. The absolute distance contouring technique is divided into three different methods: absolute distance contouring method, four-image contouring method, and three-image contouring method, according the number of the images required for each measurement and the rotation angles. In the first method, the number of images for each measurement is not fixed and depends on the distance to be measured and the resolution required. Only one maximum rotation angle needs to be chosen and the steps to be rotated by the grating from zero to the selected maximum angle is decided by the image number. For the four-image method, the number of images is four, there are two angles to be chosen and this determines the remaining two angles according to a fixed relationship. In the three-image method, only one angle is to be chosen, the other two being decided by the relevant equations. Each of the methods has its own particular features.

The three different absolute distance contouring methods proposed have been verified by experiment carried out by a specially designed experimental system. The results show that the methods are fast and the accuracy is better than 10μm. The maximum measurable range is related to the parameters of the experimental arrangement and the rotation angles.

The theoretical analysis of the three different absolute distance contouring methods is given in chapters two to four respectively. Chapter five describes the experimental system which was used to verify the theoretical analysis of each of the proposed methods. The experimental results and the features of the three different methods are analyzed and compared in chapter six.

1.5 Proposed Phase Unwrapping Algorithm

Although there have been many different algorithms for phase unwrapping in the presence of discontinuities, caused by an object having holes or steps, none of them seem to deal completely with the problem. The algorithm proposed here is a phase unwrapping algorithm to obtain a correct three-dimensional profile of an object with discrete height steps, by using a crossed grating.

A crossed grating, which has two sets of lines in different directions, is projected onto the object surface to be measured. The deformed crossed grating image which is equal to the sum of the two deformed conventional grating images, is captured and Fourier transformed. The two images are separated in the Fourier domain. After filtering the unwanted frequency components in the frequency space, they are inverse transformed to obtain two phase maps. These two phase maps have different phase distributions because the two sets of grating lines are in different directions so that their equivalent periods are different. If a suitable angle between the two sets of lines is chosen, the two phase images will have different precisions. Phase unwrapping of each pixel is carried out independently and the correct phase values for each pixel can be obtained in the presence of discontinuities. The theoretical analysis of the phase unwrapping algorithm is presented and the algorithm has been verified experimentally. The process only requires a single image and the results show that the algorithm is fast and can be used to measure the objects' surfaces.

In chapter seven, the theoretical analysis of the proposed phase unwrapping algorithm is described, and the simulated results are presented. The experiments used to verify the technique, and the corresponding results are given in chapter eight.

Chapter 2

Theory of Absolute Distance Contouring

2.1 Introduction

Moiré contouring is very well documented and much work has been performed using this technique. However, there are some disadvantages for the previously mentioned shadow moiré techniques. For example, only the relative object height or distance can be measured and some extra information is needed to determine the absolute moiré fringe order and discriminate between the hills and valleys. Some methods have been proposed to provide improvements, but they are still not convenient. In this chapter, the theory of absolute distance contouring is described. It is based on the shadow moiré contouring principle and the rotation of a grating. It can be used to measure the absolute distance from the grating to an object's surface, as well as the object's topography. It starts from a basic mathematical analysis of the method, including an analysis for a variation in the grating's period, including the case where sinusoidal and square wave intensity gratings have been used. This is followed by a signal analysis, the relationships of the parameters of the experimental arrangement, the grating's period, and the angle, which the grating is rotated, with the measured absolute distance from the grating to the object's surface. The proposed method for signal processing gives an idea of how to obtain the absolute distance and the object height from the captured images. The last two sections describe an analysis of the errors of the measurement and the conclusions for this section of the work.

2.2 Variation of a Grating's Period

Figure 2.1 shows the typical shadow moiré contouring arrangement. The shadow of a grating is cast onto the object's surface. It is viewed back through the grating, the moiré pattern observed, being a contour map of the object. It is assumed that the object is viewed normal to the grating, using parallel projection. The contour depth is given by:

$$\Delta h = \frac{P}{\tan \alpha} \tag{2-1}$$

where α is the angle of incidence and P is the period of the grating.

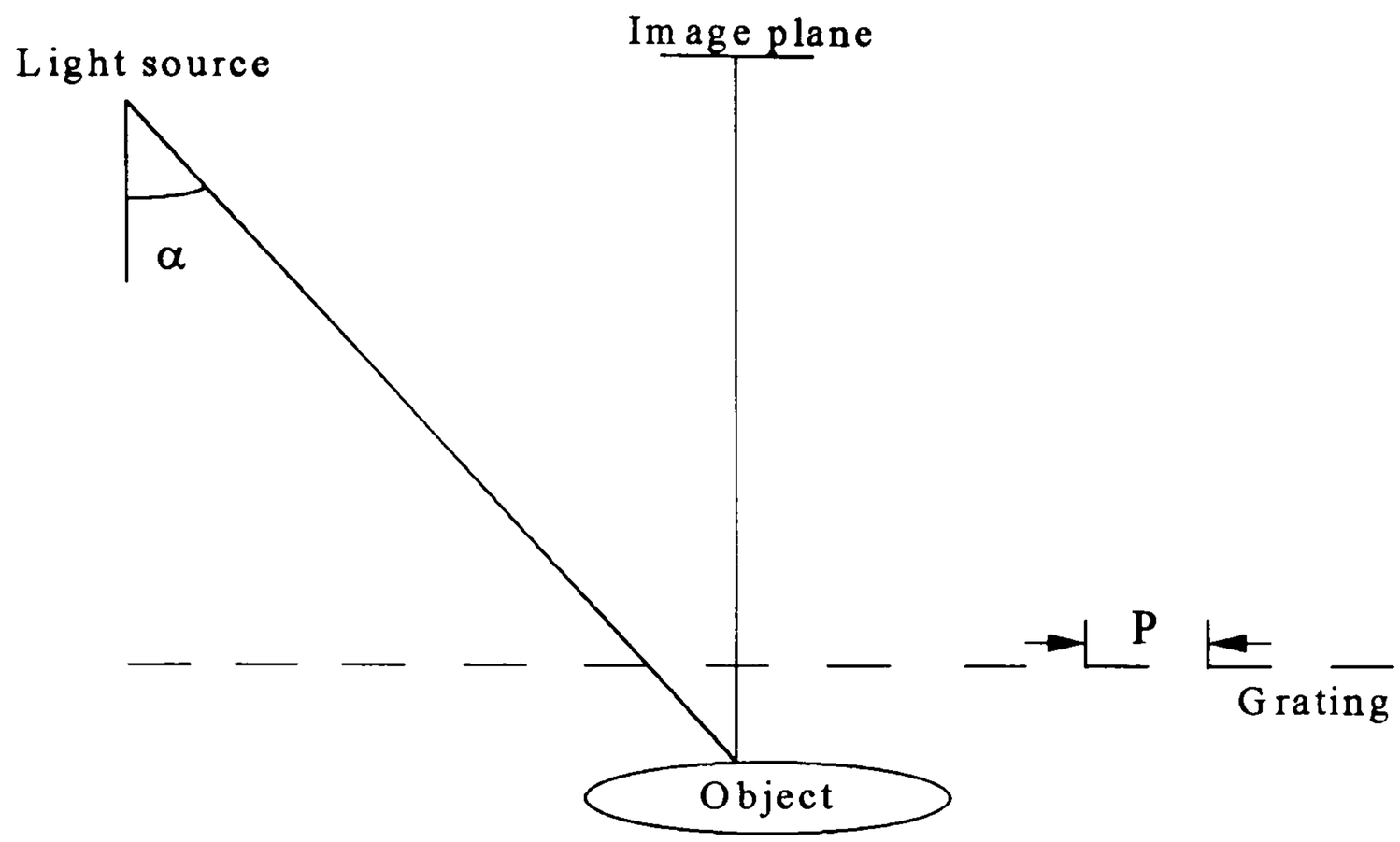

Figure 2.1 Typical Shadow Moiré Contouring Arrangement

In order to vary the contour depth Δh, it is necessary to vary P or α. The most practical of these alternatives is to vary P from infinity to some finite value P_0. P is defined as the period of the grating measured perpendicular to the plane defined by the illumination, observation and object points. Variation of P and therefore Δh is achieved by rotating the grating in its own plane about any axis normal to it. When this is done, moiré fringes are seen to move over the object's surface. Figure 2.2 is a schematic diagram of the proposed absolute distance contouring arrangement. Figure 2.3 shows how P varies with the angle of rotation, θ.

If the grating is rotated at a constant angular velocity, ω, the measured period of the grating changes such that:

$$P = \frac{P_0}{\sin\theta} \qquad \text{where } \theta = \omega t \tag{2-2}$$

Therefore, when $\theta = 0$, $P = \infty$ and when $\theta = \pi/2$, $P = P_0$. Where P_0 is the grating's original period.

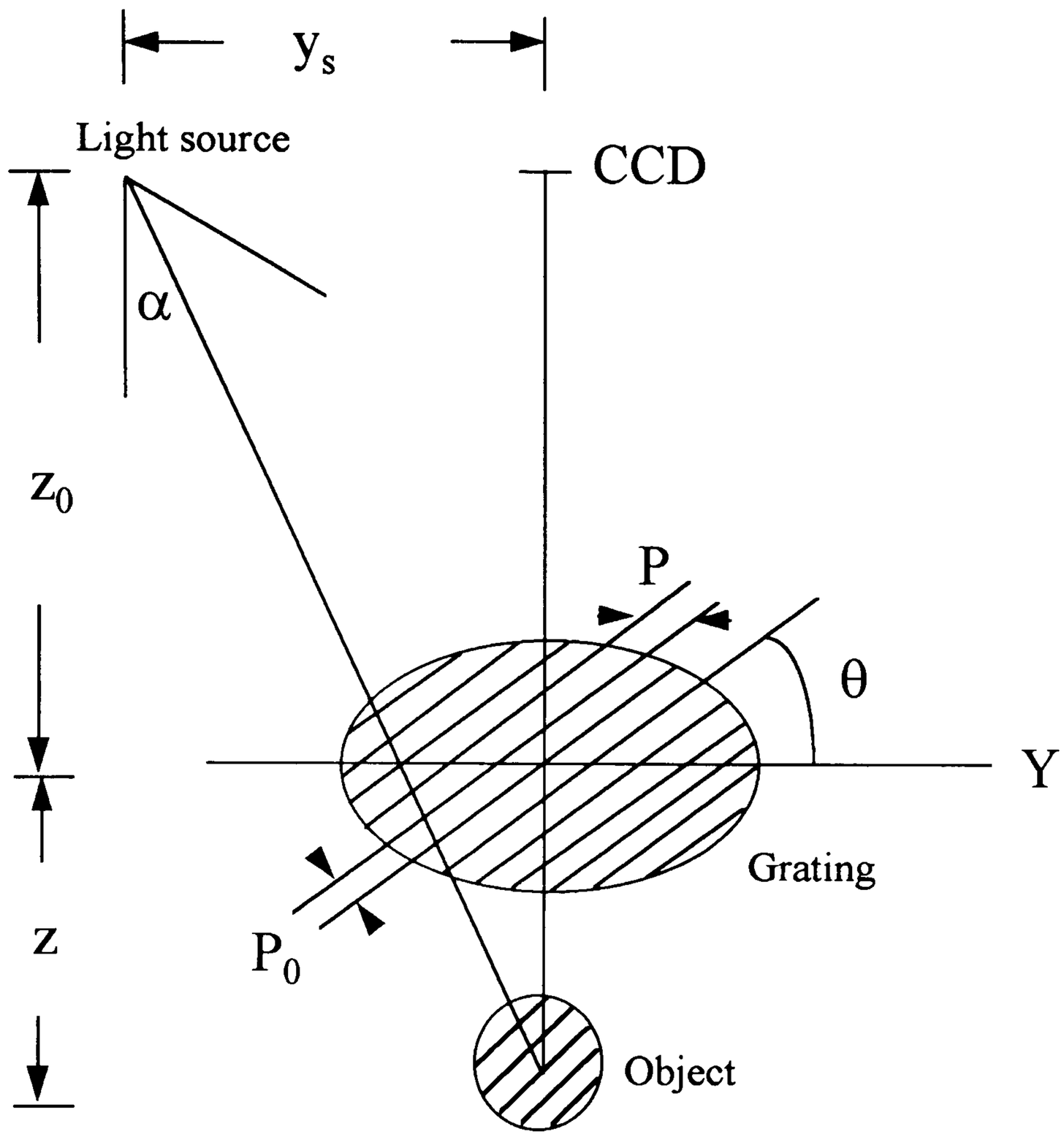

Figure 2.2 Absolute Distance Contouring Arrangement

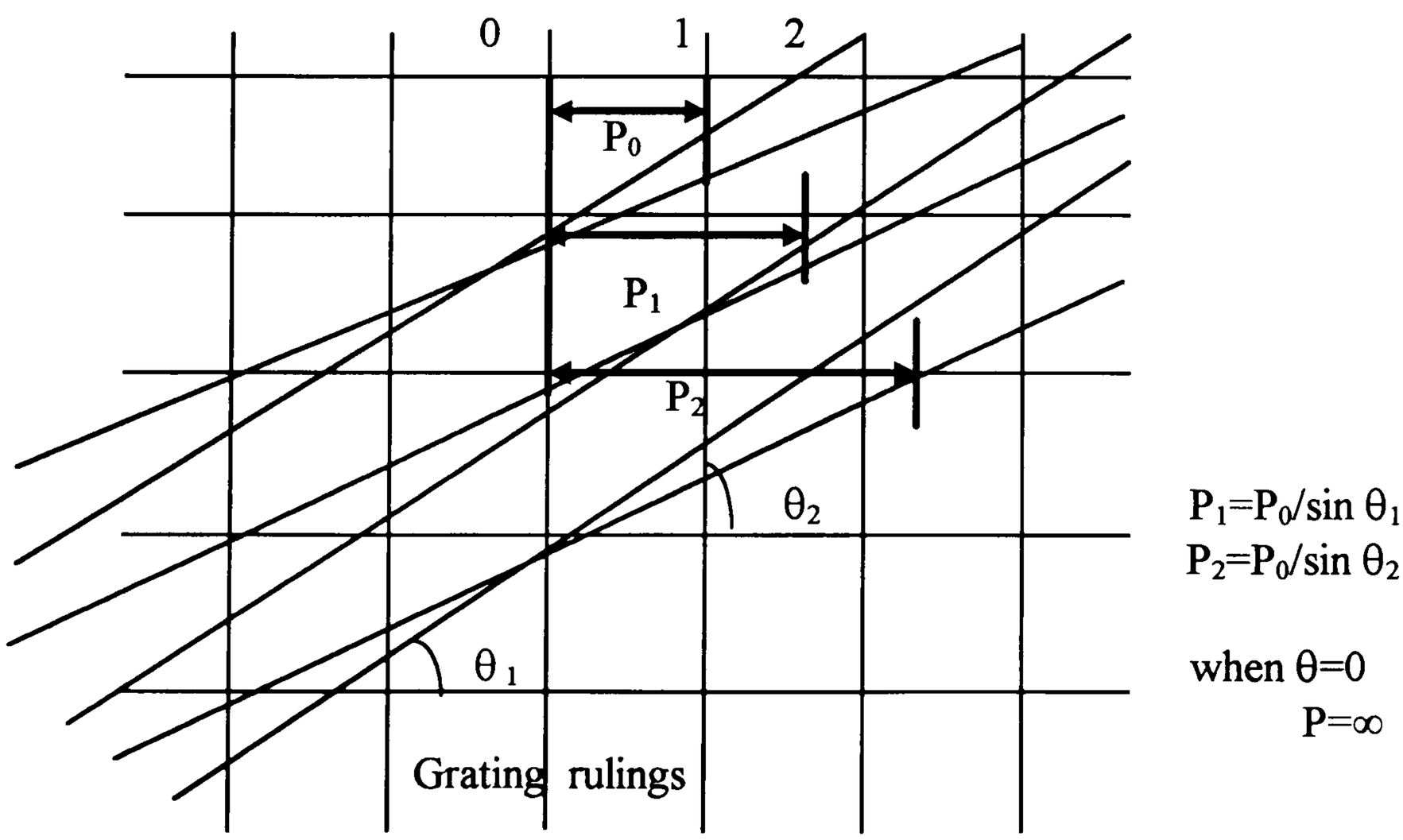

Figure 2.3 Variation of Grating's Period P with θ

Figure 2.4 shows a simple absolute distance contouring arrangement for the basic experiment. The grating is mounted on a bearing, such that it can be rotated about an axis normal to the plane of the rulings. The object is located behind the grating and illuminated by a light source which need not be coherent. The shadow of the grating is cast onto the object's surface through an angle α. Hence the shadow on the object is shifted in the y direction by a distance $z(x,y)\tan\alpha$ relative to the grating. Light from this scene passes through the grating and a lens, forming an image in the region of the CCD camera. The light source and the lens are the same perpendicular distance, z_0, from the grating. Together with the object point at z, they define a plane. The intersection of this plane with the grating defines a line along which the period, P, of the grating is measured. This line also serves as the datum for the rotation of the grating. When the rulings are parallel to it, the angle θ is zero.

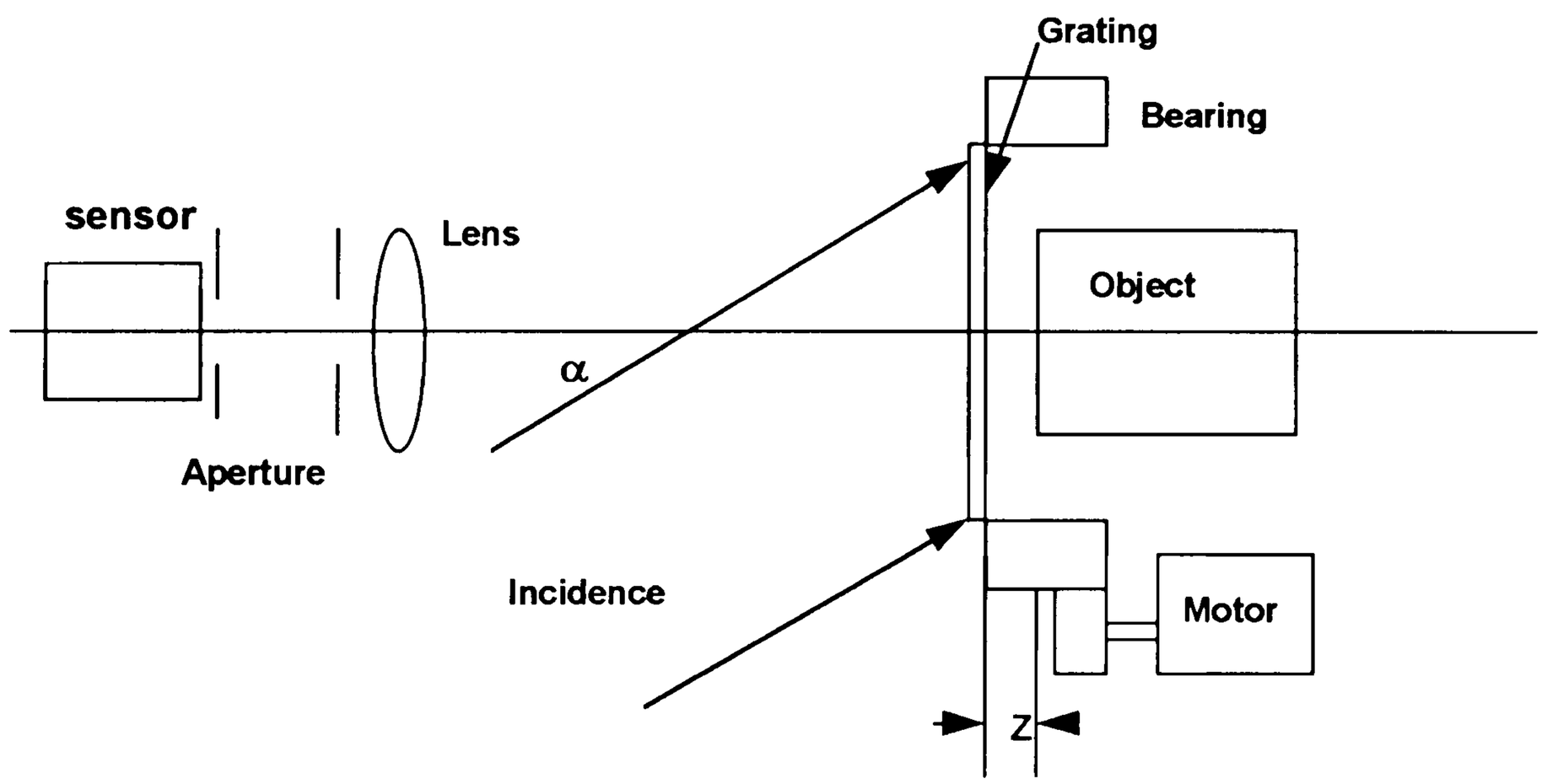

Figure 2.4 A Simple Absolute Distance Contouring Arrangement

The bearing, upon which the grating is mounted, is driven by a motor at a constant velocity, ω. The object and grating are imaged together by suitably stopping down the aperture of the lens. Figure 2.5 shows a view of the bearing, grating and object from the position of the CCD camera. Figure 2.6 shows the expected time varying output from a single pixel of the CCD camera, for one

revolution of the grating. Under certain conditions, the representation shown is found to be true experimentally.

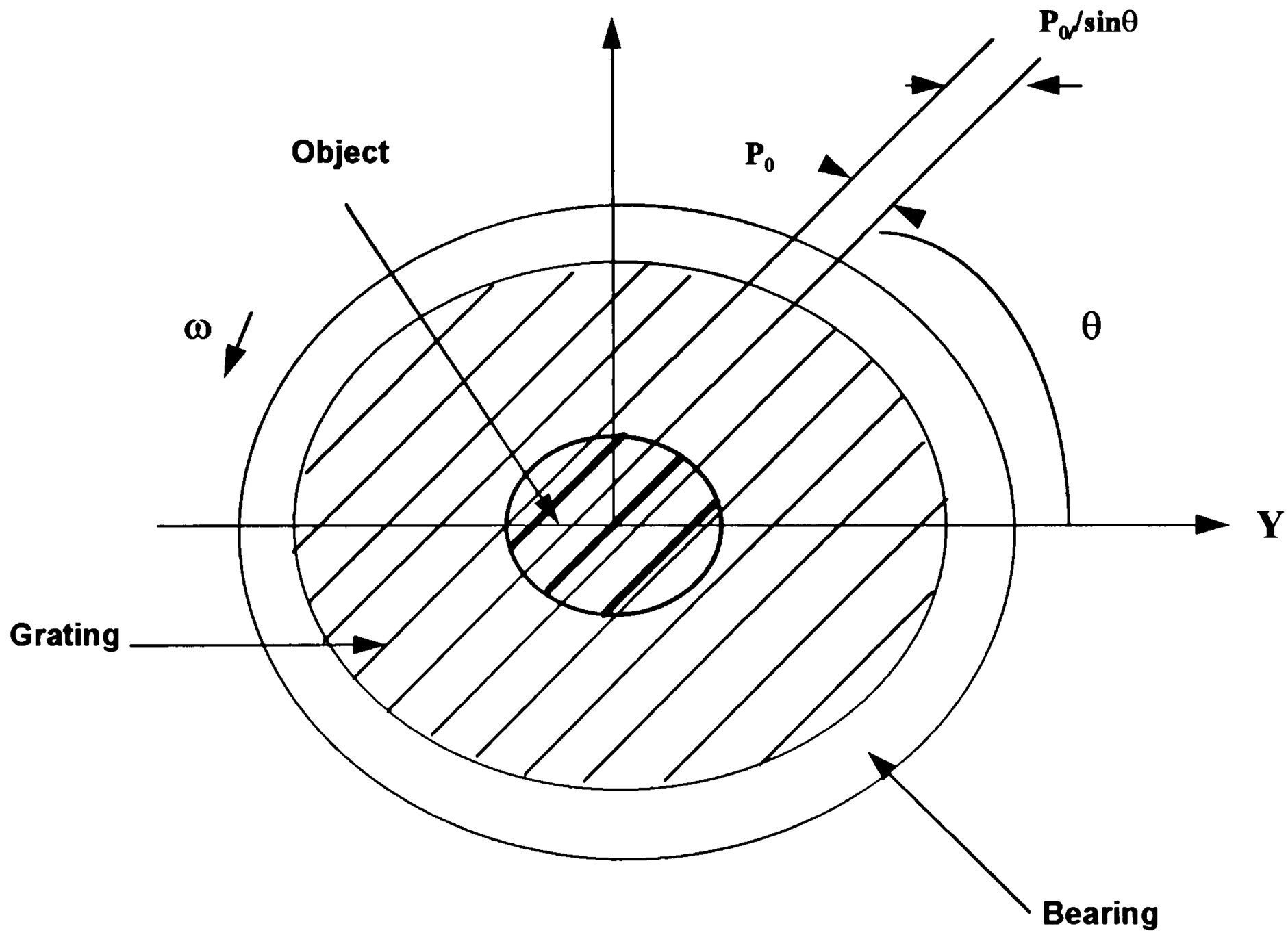

Figure 2.5 View of Bearing, Grating and Object From the CCD Camera

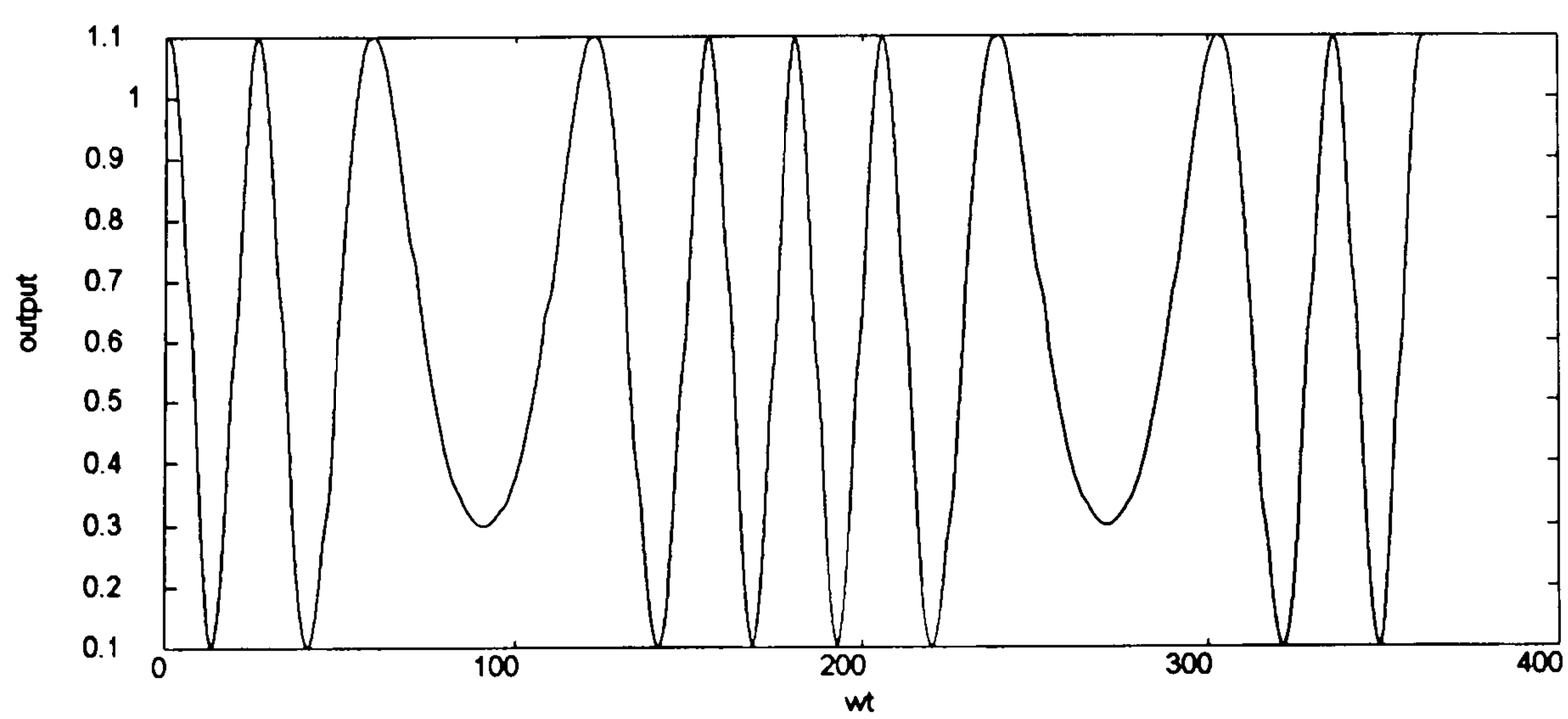

Figure 2.6 The Expected Time Varying Output

2.3 Theoretical Analysis

It is assumed that $T(y)$ is the transmission function of the grating, the grating is illuminated by a light source of intensity, I_0, and at an incidence angle, α, as shown in figure 2.2. The intensity falling on the object's surface, $O(y)$, will be:

$$O(y) = I_0 T(y - z\tan\alpha) \tag{2-3}$$

When the object is viewed through the grating, the moiré pattern $M(y)$ can be written as

$$M(y) = RO(y)T(y) = I_0 RT(y)T(y - z\tan\alpha) \tag{2-4}$$

where R is the reflectivity of the object's surface.

2.3.1 Sinusoidal Wave Intensity Grating

For a sinusoidal wave grating, the transmission function, as shown in figure 2.7, can be written as:

$$T(y) = \frac{1}{2} + \frac{1}{2}\sin\left(\frac{2\pi y}{P}\right) \tag{2-5}$$

where P is the period of the grating.

From equation (2-4), the moiré pattern of the sinusoidal grating is given as:

$$M(y) = I_0 R\left(\frac{1}{2} + \frac{1}{2}\sin\left(\frac{2\pi y}{P}\right)\right)\left(\frac{1}{2} + \frac{1}{2}\sin\left(\frac{2\pi(y - z\tan\alpha)}{P}\right)\right)$$

$$= \frac{I_0 R}{4}\left(1 + \sin\left(\frac{2\pi y}{P}\right) + \sin\left(\frac{2\pi(y - z\tan\alpha)}{P}\right) + \sin\left(\frac{2\pi y}{P}\right)\sin\left(\frac{2\pi(y - z\tan\alpha)}{P}\right)\right) \tag{2-6}$$

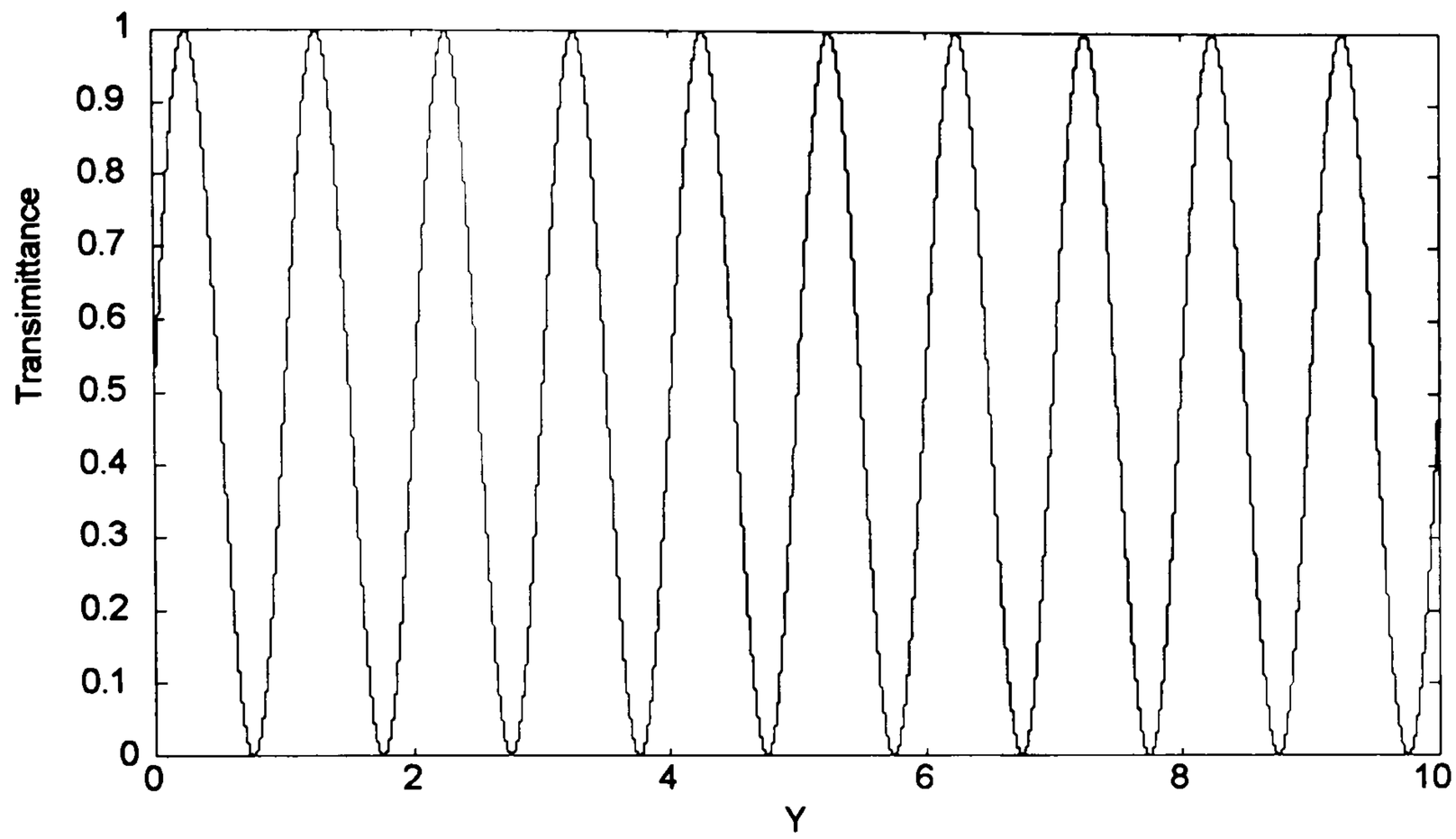

Figure 2.7 Transmittance of a Sinusoidal Wave Intensity Grating

From figure 2.2, it can be shown that:

$$\tan\alpha = \frac{y_s}{z + z_0} \tag{2-7}$$

Therefore, equation (2-6) becomes

$$M(y) = \frac{I_0 R}{4}\left(1 + \sin\left(\frac{2\pi y}{P}\right) + \sin\left(\frac{2\pi\left(y - \frac{z y_s}{z + z_0}\right)}{P}\right) + \sin\left(\frac{2\pi y}{P}\right)\sin\left(\frac{2\pi\left(y - \frac{z y_s}{z + z_0}\right)}{P}\right)\right)$$

$$= \frac{I_0 R}{4}\left(1 + \sin\left(\frac{2\pi y}{P}\right) + \sin\left(\frac{2\pi\left(y - \frac{z y_s}{z + z_0}\right)}{P}\right)\right.$$

$$\left. - \frac{1}{2}\cos\left(\frac{2\pi\left(2y - \frac{z y_s}{z + z_0}\right)}{P}\right) + \frac{1}{2}\cos\left(\frac{2\pi \frac{z y_s}{z + z_0}}{P}\right)\right) \tag{2-8}$$

The last term in equation (2-8), $\frac{I_0 R}{8}\cos\left(\frac{2\pi \frac{zy_s}{z+z_0}}{P}\right)$, depends solely on z and yields the contour line on the object's surface. The above contour term, by using equation (2-2), can be rewritten as:

$$M' = \frac{I_0 R}{8}\cos\left(\frac{2\pi z y_s \sin\omega t}{(z+z_0)P_0}\right) \tag{2-9}$$

This equation represents an extended cosine wave with respect to time. Each peak of the output trace corresponds to an integer fringe number, n. These integer values of n occur at values of θ_n at which the contour depth of the system is the nth fraction of z. This is defined in equation (2-10).

$$\sin\theta_n = \frac{nP_0}{zy_s}(z+z_0) \tag{2-10}$$

The distance, z, from the grating to the object, can be found from equation (2-11).

$$z = \frac{z_0 n P_0}{y_s \sin(\theta_n) - nP_0} \tag{2-11}$$

It is clear that z_0, y_s, and P_0 are known values of the optical arrangement. To calculate z from the CCD camera's output, a suitable value of n is chosen and the value of θ at which n occurs, is measured.

2.3.2 Square Wave Intensity Grating

For a Ronchi, or square wave intensity grating, the transmittance is shown in figure 2.8 and the transmission function can be written as:

$$T(y)=\frac{1}{2}+\frac{2}{\pi}\sum_{n=0}^{\infty}\frac{\sin((2n+1)ky)}{2n+1} \tag{2-12}$$

where $k=\frac{2\pi}{P}$, P is the period of the grating, and n=0, 1, 2, 3, ...

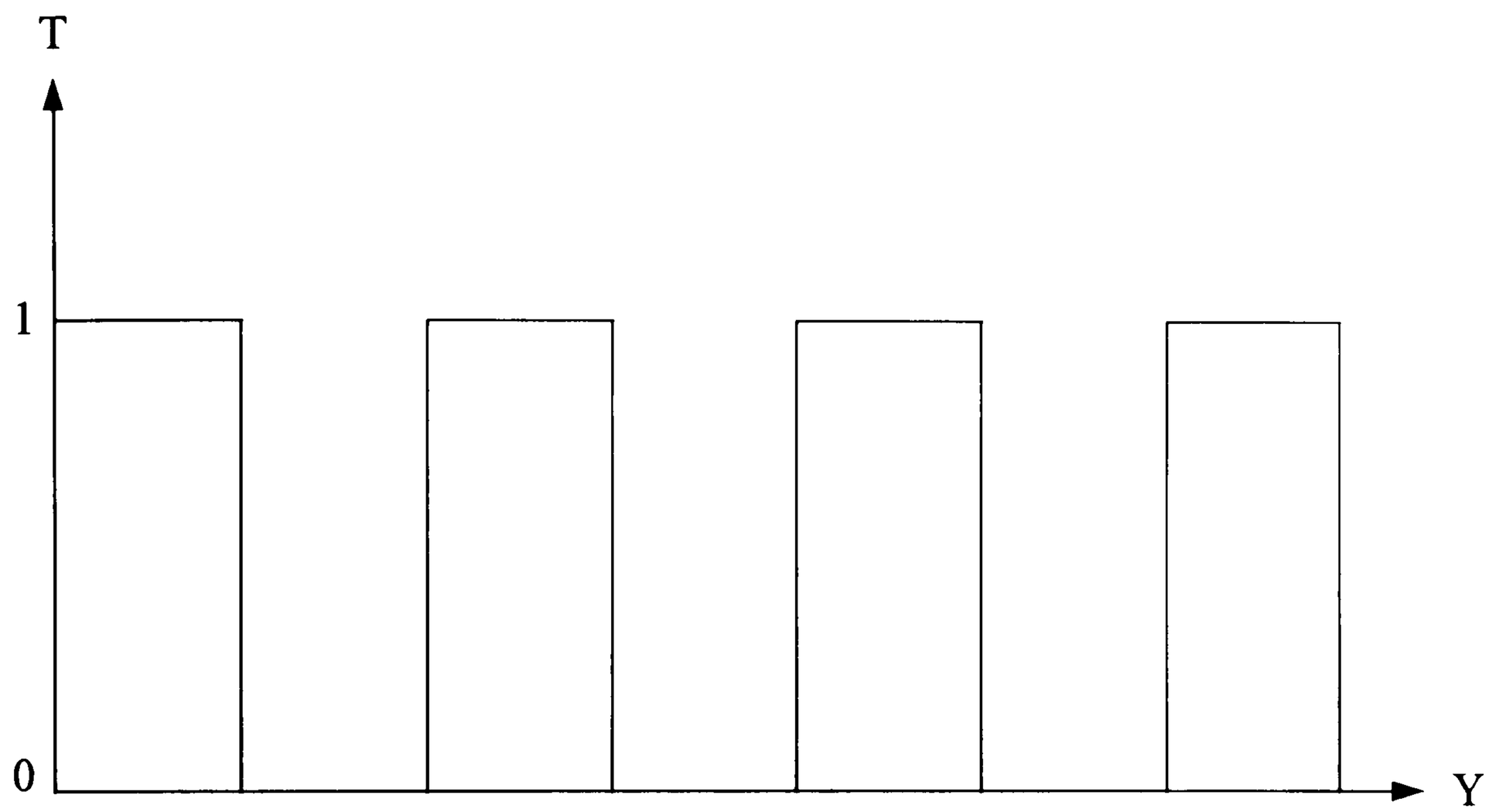

Figure 2.8 Transmittance of a Ronchi Grating

From equation (2-4), the moiré pattern of the Ronchi grating is written as a function of time:

$$M(y,t)=I_0R\left(\frac{1}{2}+\frac{2}{\pi}\sum_{0}^{\infty}\frac{\sin\left((2n+1)y\frac{2\pi}{P_0}\sin\omega t\right)}{(2n+1)}\right)$$

$$*\left(\frac{1}{2}+\frac{2}{\pi}\sum_{0}^{\infty}\frac{\sin\left((2n+1)(y-z\tan\alpha)\frac{2\pi}{P_0}\sin\omega t\right)}{(2n+1)}\right) \tag{2-13}$$

Writing $A=\frac{2\pi y}{P_0}\sin\omega t$ and $B=\frac{2\pi}{P_0}(y-z\tan\alpha)\sin\omega t$, the above equation becomes

$$M(y,t)=I_0R\left(\frac{1}{2}T(y,t)+\frac{1}{2}T(y-z\tan\alpha,t)\right.$$

$$+\frac{1}{4}+\frac{4}{\pi^2}\sum_0^\infty\frac{\sin(2n+1)A\sin(2n+1)B}{(2n+1)^2}$$

$$\left.+\frac{4}{\pi^2}\sum_{L=0}^\infty\frac{\sin(2L+1)A}{(2L+1)}\sum_{n=0}^\infty\frac{\sin(2n+1)B}{(2n+1)}\right) \tag{2-14}$$

where n ≠ L in the last term.

The moiré difference contouring term in equation (2-14) can be written as

$$\frac{4}{\pi^2}\sum_0^\infty\frac{\sin[(2n+1)A]\sin[(2n+1)B]}{(2n+1)^2}=$$

$$\frac{2}{\pi^2}\sum_0^\infty\frac{\cos(2n+1)\Delta}{(2n+1)^2}-\sum_0^\infty\frac{\cos(2n+1)(A+B)}{(2n+1)^2} \tag{2-15}$$

where $\Delta=\frac{2\pi}{P_0}$ z tan α sin ωt.

The right hand side of equation (2-14) also contains the primary grating terms and the moiré sum terms. If the unwanted terms are removed, the contour term can be written as:

$$M'(y,t)=\frac{4I_0R}{\pi^2}\sum_0^\infty\frac{\cos\left((2n+1)\left(\frac{2\pi}{P_0}z\tan\alpha\sin\omega t\right)\right)}{(2n+1)^2} \tag{2-16}$$

Equation (2-16) is a triangular wave with respect to sinωt. The only unknown in equation (2-16) is the absolute distance, z. From equation (2-16), similar to the analysis of the sinusoidal grating, each peak of the trace corresponds to an integer fringe number, n. These integer values of n occur at values of θ_n at which the contour depth Δz of the system is the nth fraction of z. Therefore, similar expressions to equations (2-10) and (2-11) can be obtained.

2.4 Signal Analysis

2.4.1 The Features of the Signal

From the above theoretical analysis, it is seen that for the square wave grating, the moiré pattern expression, equation (2-13) , is complicated although in theory it is possible to "wash out" the unwanted terms. There are several methods of removing the unwanted higher frequency fringes from the output signal, but it is very difficult to realize in a real system. It has been verified by experimental work that the square wave grating with a period of less than 1.0mm, as described in a chapter five, can be treated in the same way as a sinusoidal grating by defocusing the image and using a low pass filter function.

Compared with a square wave grating, the output signal for a sinusoidal grating, (equation (2-8)), is simple. For convenience replacing P, in equation (2-8), by $P_0/\sin\omega t$, results in equation (2-17).

$$M(y,t)=\frac{I_0R}{4}\left(1+\sin\left(\frac{2\pi y\sin\omega t}{P_o}\right)+\sin\left(\frac{2\pi\left(y-\frac{zy_s}{z+z_0}\right)\sin\omega t}{P_0}\right)\right.$$
$$\left.-\frac{1}{2}\cos\left(\frac{2\pi\left(2y-\frac{zy_s}{z+z_0}\right)\sin\omega t}{P_0}\right)+\frac{1}{2}\cos\left(\frac{2\pi\frac{zy_s}{z+z_0}\sin\omega t}{P_0}\right)\right) \qquad (2\text{-}17)$$

The whole signal contains four time-varying terms with different frequencies. For convenience, rewrite equation (2-17) as:

$$M(y,t) = A_0 + A_1 + A_2 + A_3 + A_4 \tag{2-18}$$

where

$$A_0 = \frac{I_0 R}{4}$$

$$A_1 = \frac{I_0 R}{4}\sin\left(\frac{2\pi y \sin\omega t}{P_0}\right)$$

$$A_2 = \frac{I_0 R}{4}\sin\left(\frac{2\pi\left(y - \frac{z y_s}{z + z_0}\right)\sin\omega t}{P_0}\right)$$

$$A_3 = -\frac{I_0 R}{8}\cos\left(\frac{2\pi\left(2y - \frac{z y_s}{z + z_0}\right)\sin\omega t}{P_0}\right)$$

$$A_4 = \frac{I_0 R}{8}\cos\left(\frac{2\pi \frac{z y_s}{z + z_0}\sin\omega t}{P_0}\right)$$

A_1, A_2, A_3, and A_4 have different frequencies with respect to time. Assuming that $z_0 =$ 450mm, y_s =100mm, P_0 = 1mm, z = 3mm, y = 5mm and $\theta = \omega t$ varies from 0° to 90°, $M(y,t)$, A_1, A_2, A_3, and A_4 are shown in figure 2.9.

From figure 2.9 it can be seen that the contour term A_4 has a slower variation with respect to time than the non-contour terms, A_1, A_2 and A_3. This means that the moiré contour frequency is lower than those of all non-contour terms. Therefore, it is possible to eliminate the unwanted non-contour terms from the signal by defocusing the image and using a low-pass filter.

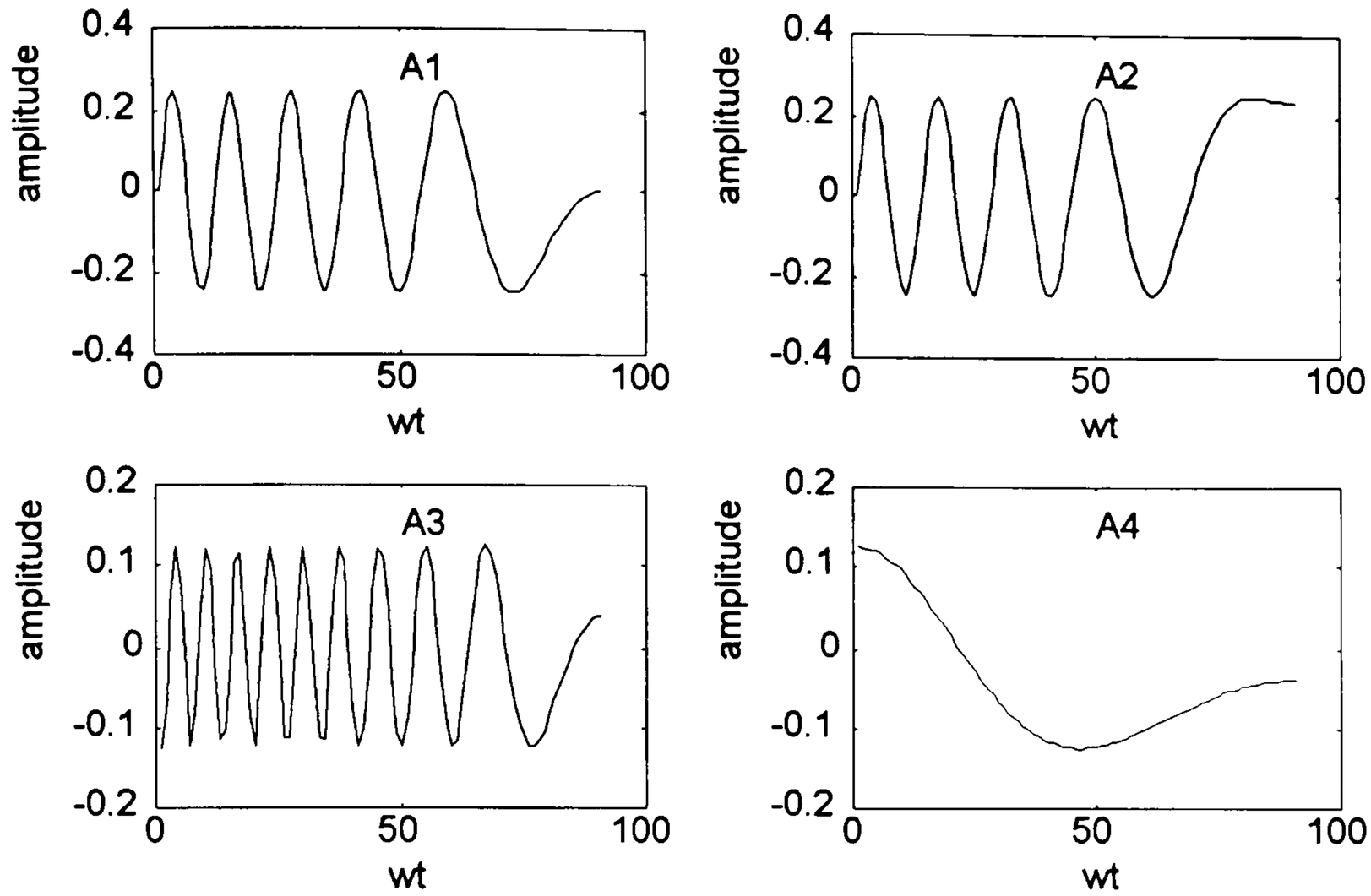

(a)

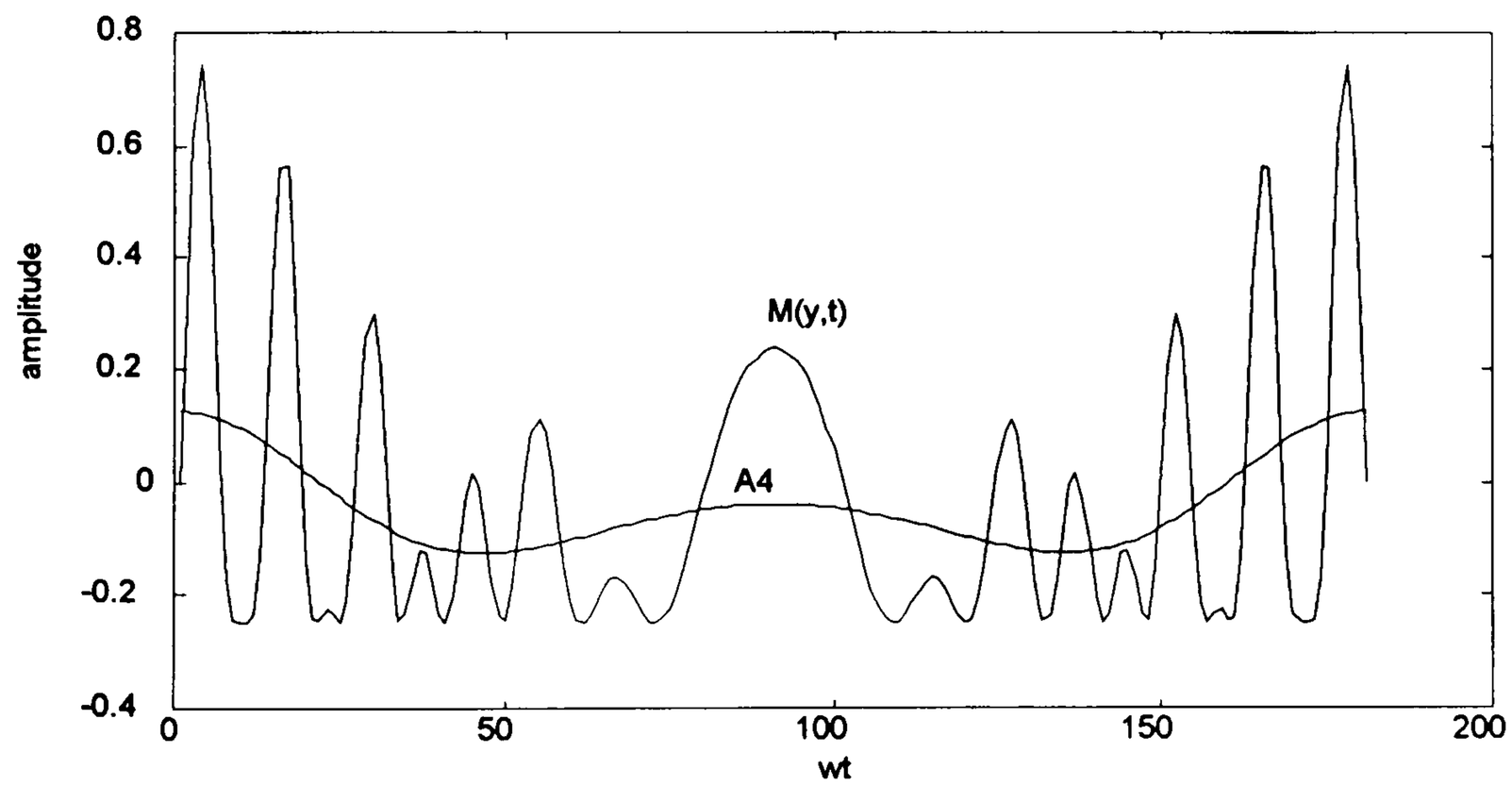

(b)

Figure 2.9 Theoretical Curves of Output Signal From CCD Camera where $z_0 = 450$mm, $y_s = 100$mm, $P_0 = 1$mm, $z = 3$mm and $y = 5$mm

(a) A1, A2, A3 and A4, ωt varying from 0° to 90°.

(b) M(y,t) and A4, ωt varying from 0° to 180°.

From figure 2.2, if $\alpha = \frac{\pi}{4}$, equation (2-10) reduces to:

$$\sin\theta_n = \frac{nP_0}{z} \tag{2-19}$$

and equation (2-9) becomes

$$M' = \frac{I_0 R}{8} \cos\left(\frac{2\pi z}{P_0} \sin\theta\right) \tag{2-20}$$

To find z, it is necessary to assign a value of θ to an easily recognizable and precise value of n. Integer values of n are easy to recognize particularly when θ=π/4. In practice, however, where θ approaches π/2, it becomes more difficult.

It is desirable to work in this region since preliminary calculations show that if any of the signal peaks lie there, it is possible to measure z accurately. Differences in $\frac{z}{P_0}$ as small as 0.001 will give differences of about 3° in θ_n, under optimum conditions. Figure 2.10 shows plots of M' verses θ for $\frac{z}{P_0}$ = 1, 1.001, 1.01 and 1.1. When the output is a maximum, the values of θ are 90°, 87.4°, 81.9° and 65.4° for $\frac{z}{P_0}$ = 1, 1.001, 1.01, 1.1, respectively.

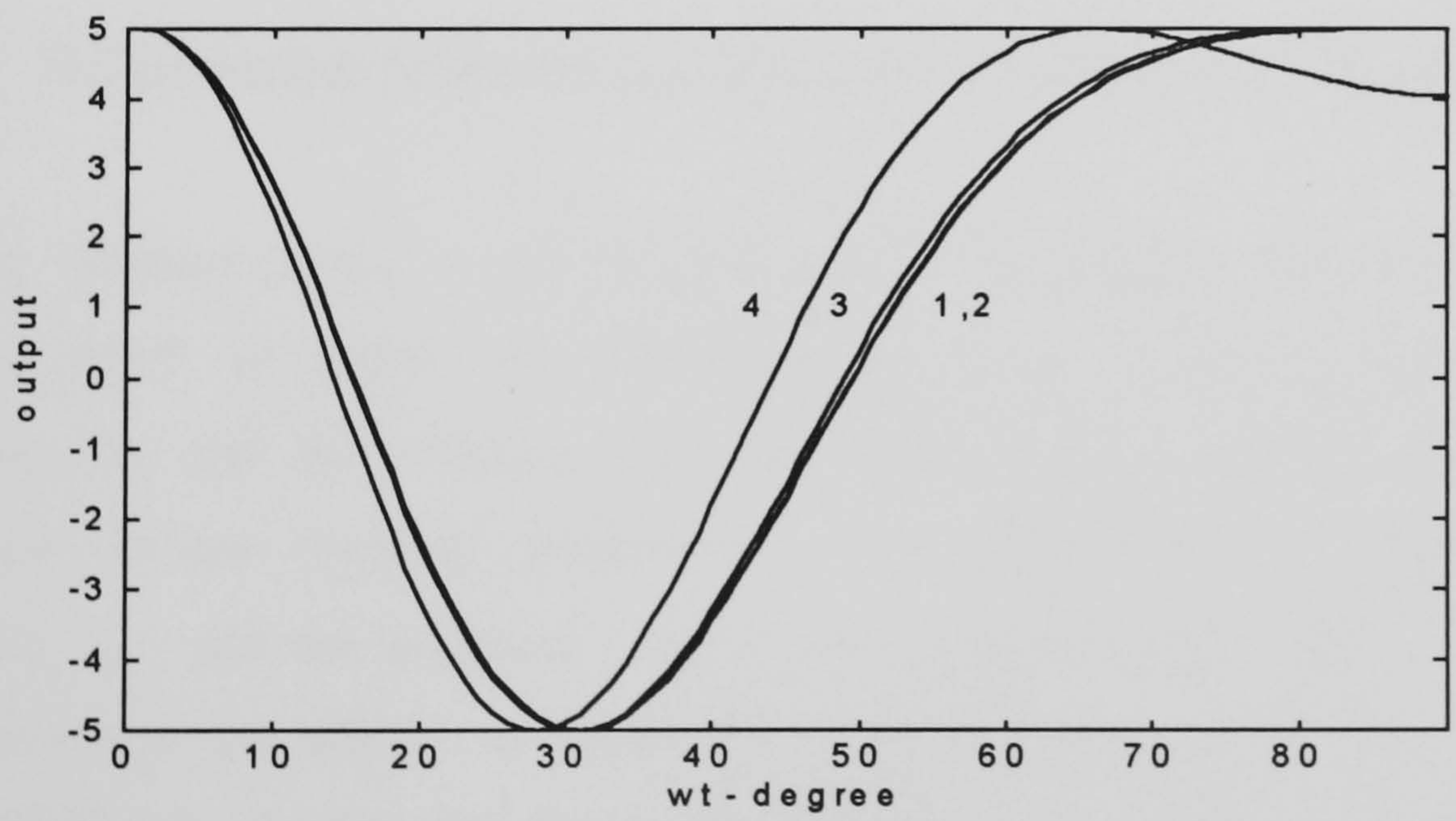

Figure 2.10 Plots of Theoretical Output vs θ for $\frac{z}{P_0}$= 1, 1.001, 1.01, and 1.1 Corresponding to 1, 2, 3, and 4 respectively

2.4.2 Sensitivity

From equation (2-19), consider that the value of z is changed by Δz, from z_1 to z_2, then θ_{n1} and θ_{n2} will change as follows:

$$\sin\theta_{n2} = \sin\theta_{n1}\left(1 - \frac{\Delta z}{z_2}\right) \tag{2-21}$$

and if $\theta_{n1} = 90^{\circ}$

$$\theta_{n2} = \sin^{-1}\left(1 - \frac{\Delta z}{z_2}\right) \tag{2-22}$$

If a grating of period 500μm is used, and z has an initial value of 125μm (so that $\theta_{n=0.25}$ is 90°), then increasing the value of z by 0.1μm would cause $\theta_{n=0.25}$ to change to 87.7°. This means that the technique is very sensitive if n is chosen such that θ_n approaches 90°.

2.5 Relationship between the Absolute Distance and the Parameters

From equation (2-11), it can be seen that z, the absolute distance from the grating to the object is directly proportional to the fringe number, n, the period of the grating, P_0, and the distance from the reference plane, (grating surface), to the camera, z_0, and inversely proportional to the distance from the camera to the light source, y_s, and the sinusoidal value of the rotation angle, $\sin\theta_n$. All of these relationships are shown in figure 2.11. Figure 2.11(a) shows the relationship of the calculated absolute distance, z, for different grating periods of 0.5mm, 1.0mm, and 1.5mm, when the fringe number is varied from 1 to 15. Figure 2.11(b) shows the relationship between z and the distance from the camera to the grating, when z_0 = 350mm, 450mm, and 550mm. Figure 2.11(c) shows the relationship between z and the distance from the camera to the light source, when y_s = 50mm, 100mm, and

200mm. Figure 2.11(d) shows the relationship between z and the different rotation angles, when $\theta = 15^\circ$, 30°, 60°, and 90°. The relationships of the absolute distance, z, and rotation angle, θ, and y_s, are shown in figure 2.12, when θ is continuously varied from a very small value to 90°, and y_s is varied from a very small value to about 200mm.

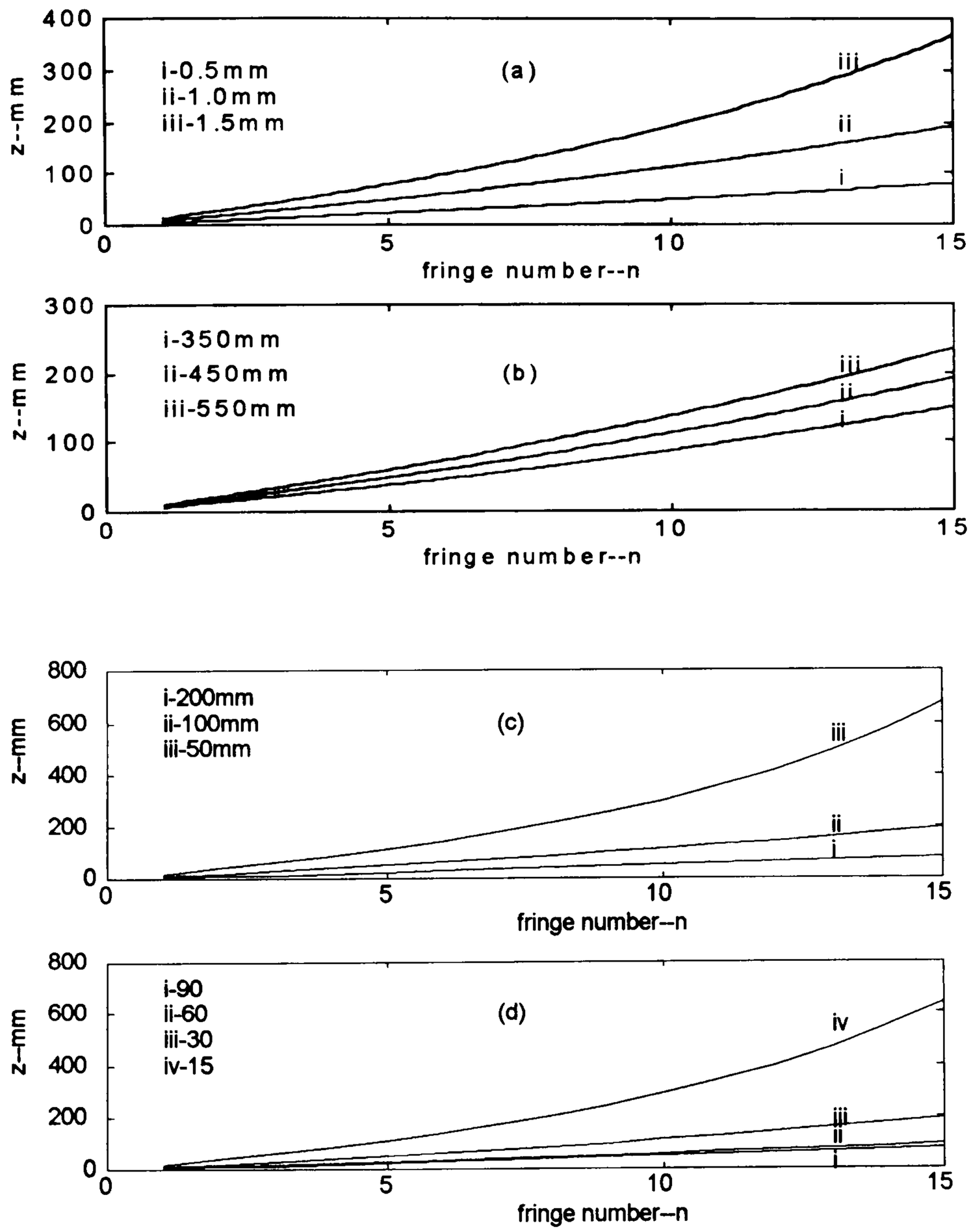

Figure 2.11 Relationship Between z and n for Different P_0, z_0, y_s and θ.

(a) $z_0 = 450$mm, $y_s = 100$mm, $\theta = 30^\circ$, $P_0 = 0.5$mm, 1mm, 1.5mm

(b) $y_s = 100$mm, $P_0 = 1$mm, $\theta = 30^\circ$, $z_0 = 350$mm, 450mm, 550mm

(c) $z_0 = 450$mm, $P_0 = 1$mm, $\theta = 30^\circ$, $y_s = 50$mm, 100mm, 200mm

(d) $z_0 = 450$mm, $P_0 = 1$mm, $y_s = 100$mm, $\theta = 15^\circ$, 30°, 60°, 90°

From figures 2.11 and 2.12, it was found that because of the relationships between z, the period of grating, the rotation angle, and other parameters, this technique can be used to measure the absolute distance with different ranges and accuracies by choosing different gratings, or rotation angles, or other parameters relating to the geometry of the system. The resolution and accuracy will be discussed in detail in chapter five.

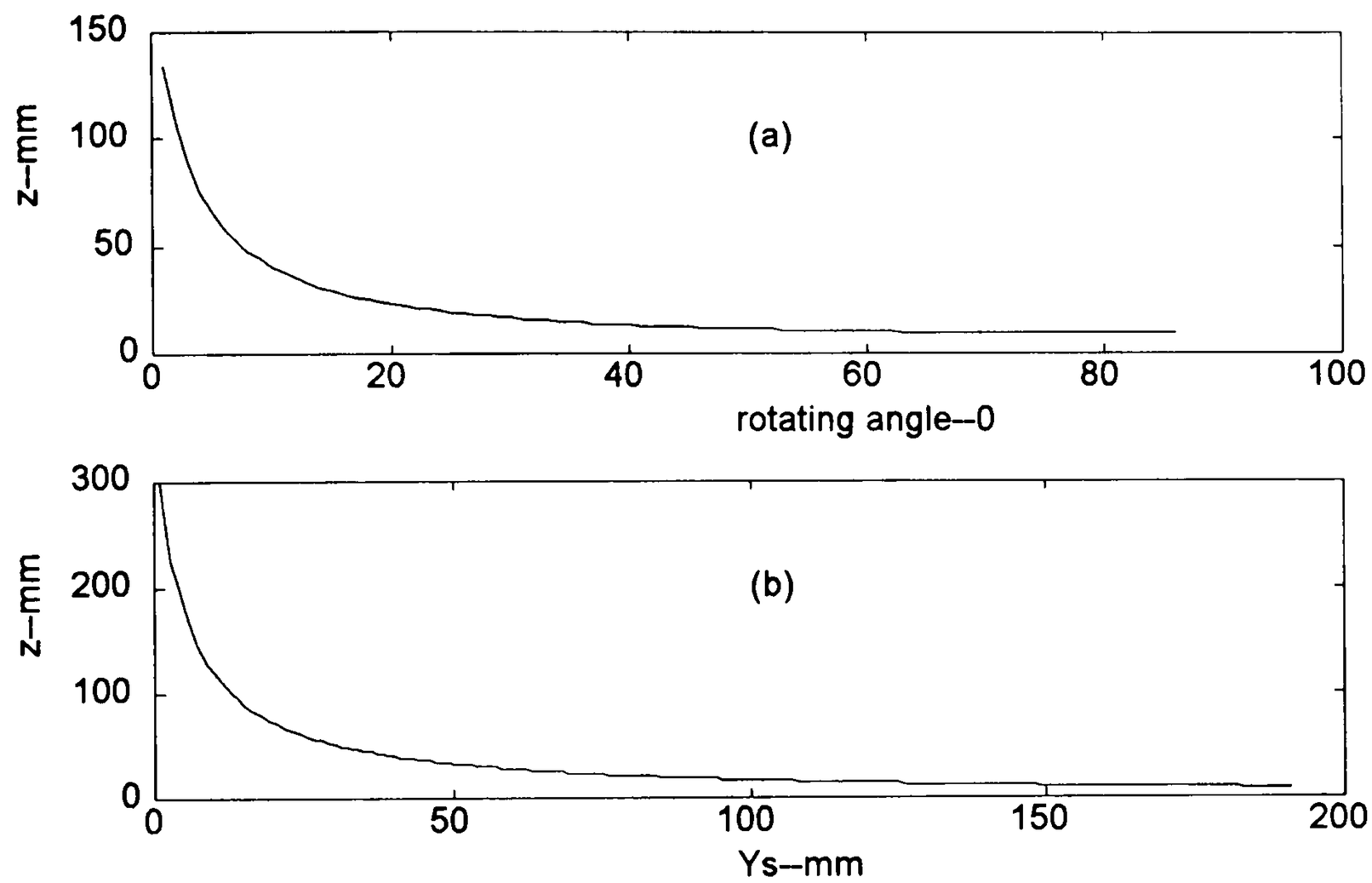

Figure 2.12 z Varies with (a) θ and (b) y_s.

2.6 Proposed Method for Signal Processing

From the analysis in sections 2.3 and 2.4, it was shown that for a given experimental arrangement and grating, if a suitable integer value, n, is chosen, and the number of the peaks measured from the output signal, and the value of θ_n at which that peak value is measured, then the absolute distance, z, could be calculated by equation (2-11). In practice this is not so easy to do.

From equation (2-9) and the typical time varying output shown in figure 2.6, it can be seen that the output signal is a cosine function with a varying frequency

determined by the sinusoidal value of the rotation angle. If the grating is rotated step by step, for a certain value of θ, the phase changes between each position of the grating can be obtained for each sample point. Then the total phase value obtained, when the grating is continuously rotated from zero to θ degrees, is the sum of the individual phase changes. Therefore, the total fringe number, as well as the absolute distance, z, can be calculated by equation (2-11).

The signal processing procedure is to first choose an angle, θ, and to then decide the number of steps, N, through which the grating should be rotated. Therefore, the angle rotated through each step will be:

$$\Delta\theta = \frac{\theta}{N} \tag{2-23}$$

If a single image is captured at each step, a total of N+1 images will be recorded. For each sample point or pixel, there are N+1 data values which represents the intensity variation at each pixel as the grating is rotated. After the background signal is removed and the maximum and minimum values are found from the N+1 data points, the phases at each position for all N+1 steps, at the sample point (i,j), can be calculated by equation (2-24).

$$\varphi_m(i,j) = \cos^{-1}\left(\frac{8M'_m(i,j)}{I_0 R}\right) \tag{2-24}$$

where m=1 to N+1.

The absolute value of the phase varied from position m-1 to m is

$$\Delta\varphi_{m,m-1} = |\varphi_m - \varphi_{m-1}| \tag{2-25}$$

and the total phase variation achieved when the grating is rotated N steps is:

$$\Delta\varphi = \sum_{q=1}^{N} \Delta\varphi_{q+1,q} \tag{2-26}$$

The fringe number for sample point (i,j) is given by

$$n = \frac{\Delta\varphi}{2\pi} \tag{2-27}$$

where n may not necessarily be an integer value.

The absolute distance, z, can be calculated by substituting the values of the fringe number, obtained from equation (2-27), into equation (2-11). The object height can be obtained by subtracting the absolute distance from the maximum absolute distance of the whole measured area. This was verified by experiment as a effective method. The details of the signal processing procedure and the design of the program used for signal processing are described in chapter five.

2.7 Error Analysis

There may be errors in results obtained by the method described in section 2.6. The errors may come from a number of sources such as errors in the parameters of the experimental arrangement, z_0, y_s, grating period, P_0, rotation angle, θ, and the nonlinear response of the camera.

From equation (2-11), if the camera's non-linearity is ignored, then Δz, the error of the measured absolute distance, z, caused by errors, Δz_0, Δy_s, ΔP_0 and $\Delta\theta_n$, can be expressed as follows:

$$\Delta z = \frac{nP_0}{y_s \sin\theta_n - nP_0}\Delta z_0 - \frac{z_0 n P_0 \sin\theta_n}{(y_s \sin\theta_n - nP_0)^2}\Delta y_s + \left(\frac{z_0 n}{y_s \sin\theta_n - nP_0} + \frac{z_0 n^2 P_0}{(y_s \sin\theta_n - nP_0)^2}\right)\Delta P_0$$

$$- \frac{z_0 y_s n P_0 \cos\theta_n}{(y_s \sin\theta_n - nP_0)^2}\Delta\theta_n \tag{2-28}$$

There are different relationships for absolute error, Δz, and the errors of the four parameters. In order to analyse this error, equation (2-28) is rewritten in a relative form as follows:

$$\frac{\Delta z}{z} = \frac{1}{z_0}\Delta z_0 - \frac{\sin\theta_n}{y_s \sin\theta_n - nP_0}\Delta y_s + \left(\frac{1}{P_0} + \frac{n}{y_s \sin\theta_n - nP_0}\right)\Delta P_0 - \frac{y_s \cos\theta_n}{y_s \sin\theta_n - nP_0}\Delta\theta_n \quad (2\text{-}29)$$

From this equation, it can be seen that except for the first term, caused by the error of z_0, all terms are dependent upon the fringe number. To obtain practical values from each term, assume $n = 1.0$, $z_0 = 450$mm, $y_s = 100$mm, $P_0 = 1.0$mm, and $\theta_n = 30°$. Thus, z, calculated from equation (2-11), is 9.1836mm. From this, equation (2-29) becomes

$$\Delta z = 0.0202\Delta z_0 - 0.0937\Delta y_s + 9.3709\Delta P_0 - 16.2311\Delta\theta_n \quad (2\text{-}30)$$

Therefore, a 0.1mm error in the measurements of z_0 and y_s, will result in errors of 2μm and 9.4μm respectively for z. It is necessary to reduce the errors from z_0, y_s, P_0, and θ_n by appropriate calibration, in order to increase the accuracy of the measurement. What is of concern is the error caused by the measurement in the rotation angle. For the above values of z_0, y_s, and P_0, the errors, Δz, caused by a given error $\Delta\theta_n = 0.01°$, for a varying fringe number, n, and for fixed fringe number, $n = 1$, with varying values of θ_n, are shown in Figure 2.13. When the error in the rotation angle is fixed, (0.01° accuracy of rotation angle could be achieved by the stepper motor), the error in z is directly proportional to the fringe number and inversely proportional to the rotation angle. To achieve a minimum error from the rotation angle, for a given z, a small number of fringes or a large rotation angle should be chosen. However, from equation (2-11), when the rotation angle is large, the fringe number will also be large for a given z. Therefore, a suitable rotation angle should be chosen to ensure as high an accuracy as possible.

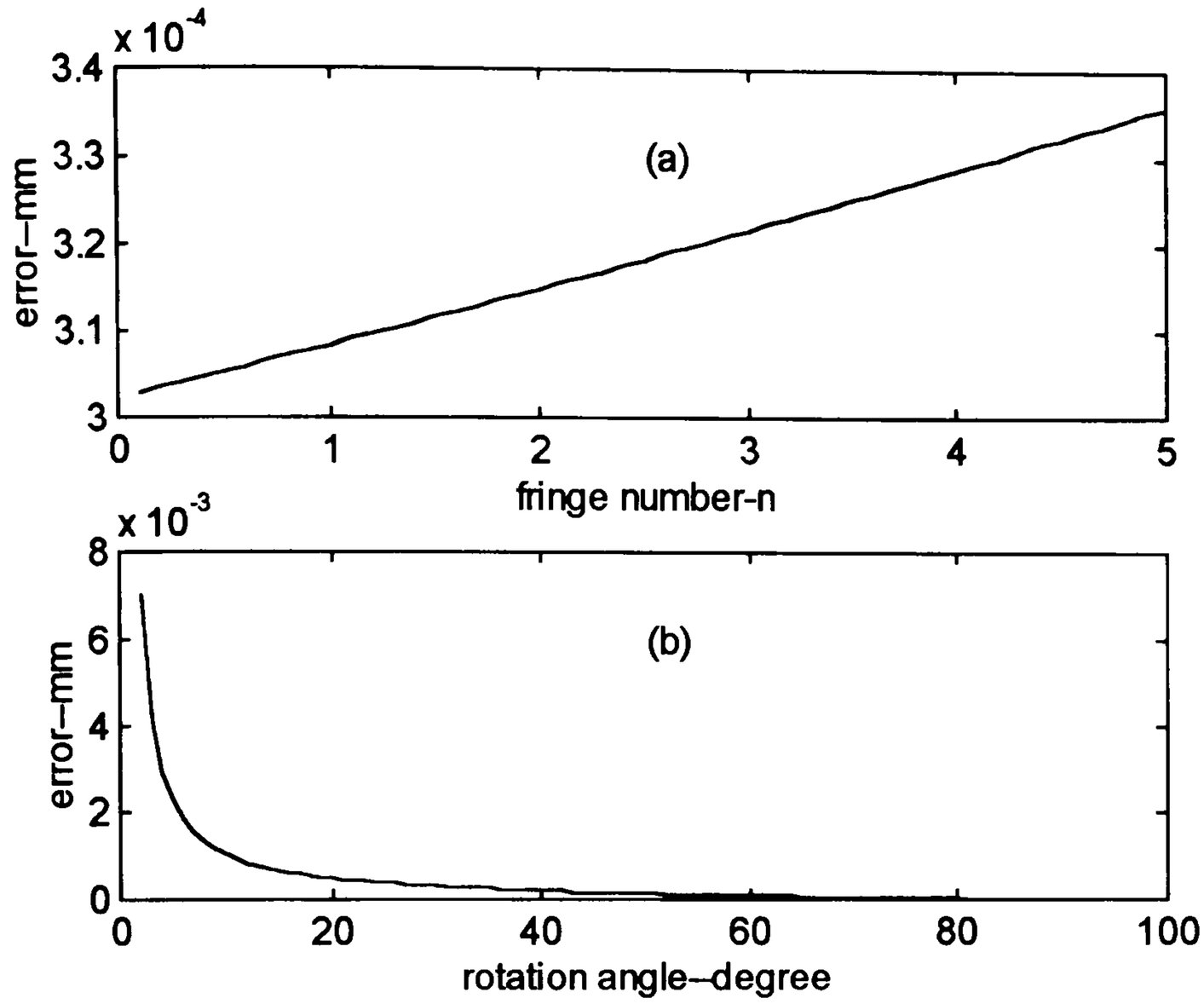

Figure 2.13 The Errors, Δz, Caused by the Rotation Angle Error $\Delta\theta_n$=0.01° (a) for varying fringe number (b) for different rotation angles θ_n when n=1

2.8 Summary

In this chapter, the theoretical analysis of the absolute distance contouring method has been presented. The theoretical analysis has verified that the proposed method can be used for the measurement of absolute distance as well as object height. A method for signal processing is proposed. The formulae for the calculation of the absolute distance and the absolute and relative error have been obtained. If suitable parameters of geometry and rotation angle are chosen, the measurement of the absolute distance or the object height, are relatively accurate.

Chapter 3

Theory of Four-Image Absolute Distance Contouring

3.1 Introduction

The absolute distance and three-dimensional profile measurement method, proposed and analyzed in chapter two, requires many images for each measurement to ensure good resolution and accuracy. This means that more computer memory is needed and that the time required for signal processing is large. It is possible to reduce the number of images so that, like phase stepping in the fringe projection technique, only three or four images are required. A four-image absolute distance contouring method is proposed. It is based on the theoretical analysis given in chapter two. It is different from the technique of phase shifting used in the projection moiré system in that the phase change for each step is not constant, but chosen at certain rotation angles. For each measurement, only four images are required. The maximum measurable range is determined by the geometry of the experimental arrangement, the period of the grating, and the chosen rotation angles. Compared with the method described in chapter two, it is fast and requires fewer computing resources. The mathematical analysis of the method and the relationships between the experimental parameters, grating period, rotation angles, and maximum measurable range, as well as errors caused by the uncertainty in rotation angles, are given in sections 3.2 to 3.4.

3.2 Four-Image Absolute Distance Contouring

From the analysis given in chapter two, it is known that for the sinusoidal grating used in the system shown in figure 2.2, the contour term can be written as:

$$M' = \frac{RI_0}{8}\cos\left(\frac{2\pi}{P_0}\frac{zy_s}{(z+z_0)}\sin\theta\right) \tag{3-1}$$

Therefore, if the grating is rotated to different positions, different moiré patterns and different contour terms will result, which are related to the values of the rotation angles. If an image is captured at each of the grating positions, θ_1, θ_2, θ_3, and θ_4, the four contour terms obtained can be written as follows:

$$M'_1 = \frac{RI_0}{8}\cos\left(\frac{2\pi}{P_0}\frac{zy_s}{(z+z_0)}\sin\theta_1\right) \tag{3-2}$$

$$M'_2 = \frac{RI_0}{8}\cos\left(\frac{2\pi}{P_0}\frac{zy_s}{(z+z_0)}\sin\theta_2\right) \tag{3-3}$$

$$M'_3 = \frac{RI_0}{8}\cos\left(\frac{2\pi}{P_0}\frac{zy_s}{(z+z_0)}\sin\theta_3\right) \tag{3-4}$$

$$M'_4 = \frac{RI_0}{8}\cos\left(\frac{2\pi}{P_0}\frac{zy_s}{(z+z_0)}\sin\theta_4\right) \tag{3-5}$$

For convenience, let $A = \sin\theta_1$, $B = \sin\theta_2$, $C = \sin\theta_3$, $D = \sin\theta_4$ and

$$\Phi = \frac{2\pi}{P_0}\frac{zy_s}{(z+z_0)} \tag{3-6}$$

Then the relationship of the four contour terms can be written as:

$$\frac{M'_1 - M'_2}{M'_3 - M'_4} = \frac{\cos(A\Phi) - \cos(B\Phi)}{\cos(C\Phi) - \cos(D\Phi)} = \frac{\sin\left(\frac{A+B}{2}\Phi\right)\sin\left(\frac{A-B}{2}\Phi\right)}{\sin\left(\frac{C+D}{2}\Phi\right)\sin\left(\frac{C-D}{2}\Phi\right)} \tag{3-7}$$

Assume that the sinusoidal values of the four different angles satisfying the following conditions:

$$A + B = 2(C + D) \tag{3-8}$$

$$A - B = C - D \tag{3-9}$$

Then

$$C = \frac{1}{4}(3A - B) \tag{3-10}$$

$$D = \frac{1}{4}(3B - A) \tag{3-11}$$

Substituting equations (3-10) and (3-11) into equation (3-7), results in equation (3-12).

$$\frac{M'_1 - M'_2}{M'_3 - M'_4} = 2\cos\left(\frac{A+B}{4}\Phi\right) \tag{3-12}$$

Φ can be determined as a function of the intensity of the four captured images as follows:

$$\Phi = \frac{4}{A+B}\cos^{-1}\left(0.5 * \frac{M'_1 - M'_2}{M'_3 - M'_4}\right) = \frac{4}{A+B}\cos^{-1}(H) \tag{3-13}$$

where

$$H = 0.5 * \frac{M'_1 - M'_2}{M'_3 - M'_4} \tag{3-14}$$

After the value of Φ has been obtained, the absolute distance can be calculated from equation (3-6).

$$z = \frac{z_0 P_0 \Phi}{2\pi y_s - P_0 \Phi} = \frac{z_0 P_0 \cos^{-1}(H)}{0.5\pi(A+B)y_s - P_0 \cos^{-1}(H)}$$

$$= \frac{z_0 P_0 \cos^{-1}\left(0.5\frac{M'_1 - M'_2}{M'_3 - M'_4}\right)}{0.5\pi(A+B)y_s - \cos^{-1}\left(0.5\frac{M'_1 - M'_2}{M'_3 - M'_4}\right)} \tag{3-15}$$

If the absolute distance z, compared with z_0, is very small, which is a valid agreement for most situations, the above equation can be simplified to:

$$z = \frac{P_0 z_0}{2\pi y_s}\Phi = \frac{2z_0 P_0}{\pi y_s(A+B)}\cos^{-1}(H)$$

$$= \frac{2z_0 P_0}{\pi y_s(A+B)}\cos^{-1}\left(0.5\frac{M'_1 - M'_2}{M'_3 - M'_4}\right) \tag{3-16}$$

In equation (3-15) or (3-16), P_0, z_0 and y_s are known values of the geometry and grating, the only unknown is the value of Φ. To calculate z, it is required to choose appropriate values of $A(\theta_1)$ and $B(\theta_2)$, then decide the values of $C(\theta_3)$ and $D(\theta_4)$ using equations (3-10) and (3-11). If four images are captured at the given positions, then the absolute distance from the grating to the object, as well as the object's height, can be determined by using equation (3-15).

3.3 Relationship of the Parameters

From equations (3-13) and (3-14), it was found that H and Φ are periodic functions of z, and that the calculated absolute distance by using equation (3-15) is also a periodic function. The theoretical relationships, when $\theta_1 = 90^\circ$, $\theta_2 = 60^\circ$, $z_0 = 450$mm, $y_s = 100$mm, $P_0 = 1.0$mm, and z varies from zero to 30mm, are shown in figures 3.1 (a), (b), and (c), which show the relationship of H, Φ and the calculated absolute distance with the simulated distance, z, respectively. Figure 3.1(d) shows the error between the calculated absolute distance and the simulated distance.

From the above simulation, it can be seen that the calculated absolute distance is incorrect except for the first part, because it is a periodic function. Therefore, only the first part, where z varies from zero to its maximum value, z_{max}, can be used for practical measurements. The maximum value of the calculated absolute distance is determined by the maximum value of Φ in equation (3-13), which is given as:

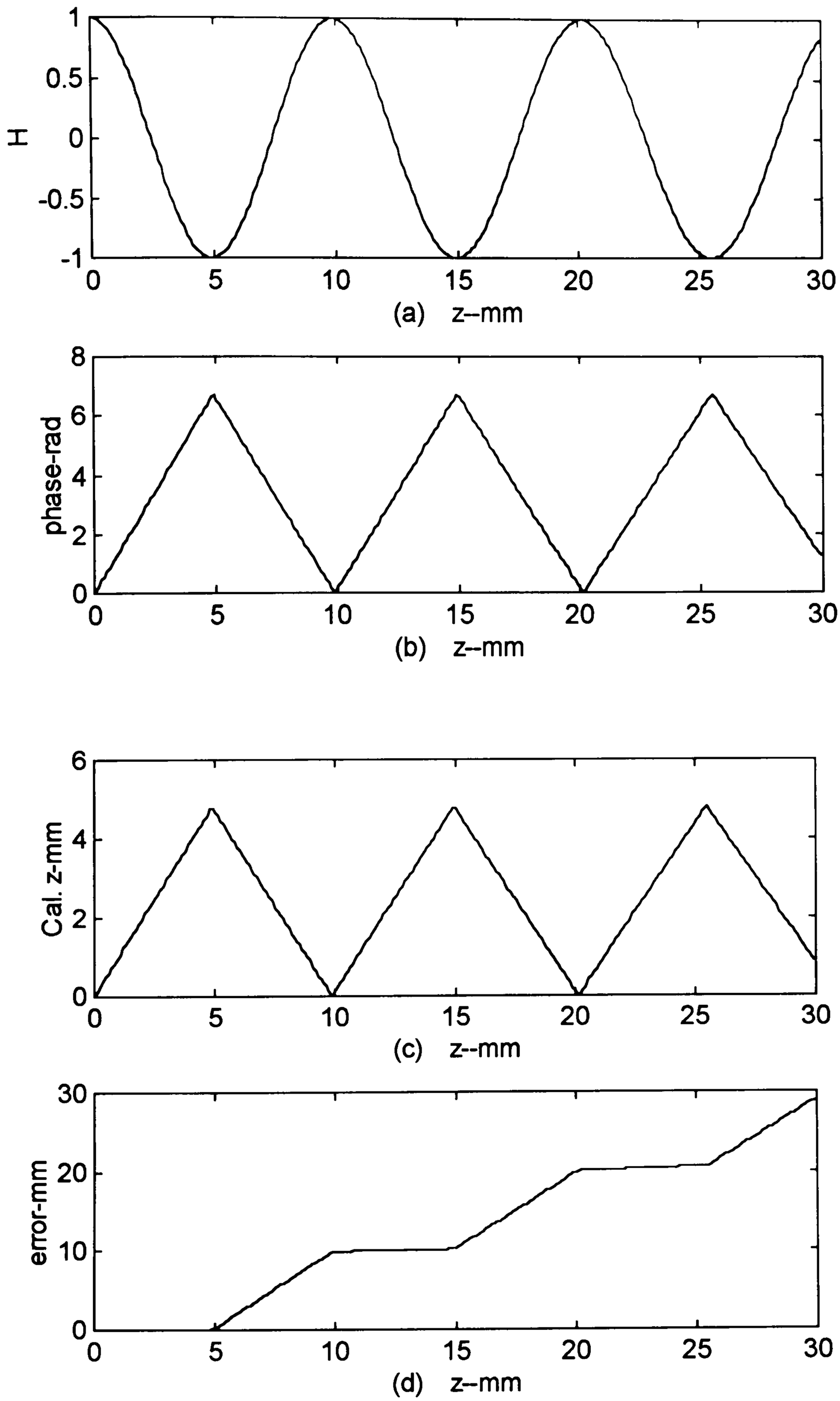

Figure 3.1 The Relationship of H, Φ, Calculated Absolute Distance and the Error Between the Calculated and Simulated z, when θ_1=90°, θ_2=60°, z_0=450mm, y_s=100mm, P_0=1.0mm, and z is Varied From Zero to 30mm.

$$\Phi_{max} = \frac{4\pi}{A+B} \tag{3-17}$$

Therefore, the maximum value of the absolute distance, z_{max}, which is also the maximum measurable range of the method using equation (3-15), would be:

$$z_{max} = \frac{2P_0 z_0}{y_s(A+B) - 2P_0} \tag{3-18}$$

From the above analysis, it can seen that the four-image contouring method cannot be applied directly to the measurement of the absolute distance unless the maximum absolute distance is less than or equal to z_{max}. This is because when $\cos^{-1}(H)$ varies from zero to π, there is a linear relationship between the simulated distance, z, and the calculated distance. Figure 3.2 shows the simulation results of the calculated distance from 0 to z_{max} and the errors in the range, for parameters of z_0=450mm, y_s=100mm,

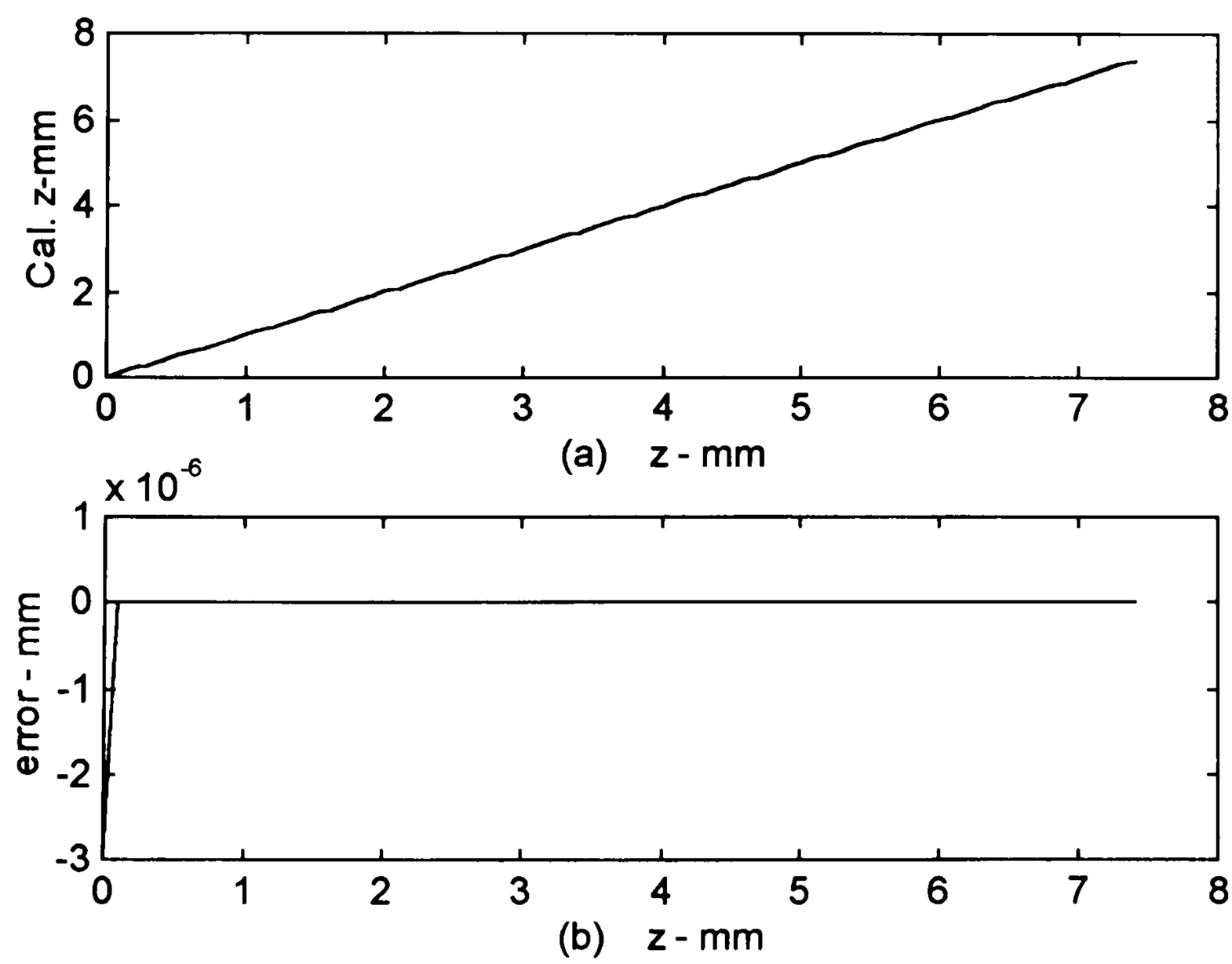

Figure 3.2 The Calculated Absolute Distance from 0 to z_{max} and the Error in the Range when z_0=450mm, y_s=100mm, P_0=1.0mm, θ_1=45° and θ_2=30°

P_0 = 1.0mm, $\theta_1 = 45^0$ and $\theta_2 = 30^o$. It can be seen that the simulated results are accurate since the error is in the order of $10^{-3}\mu m$. Therefore, this method can be used for distance measurement over a certain limited range.

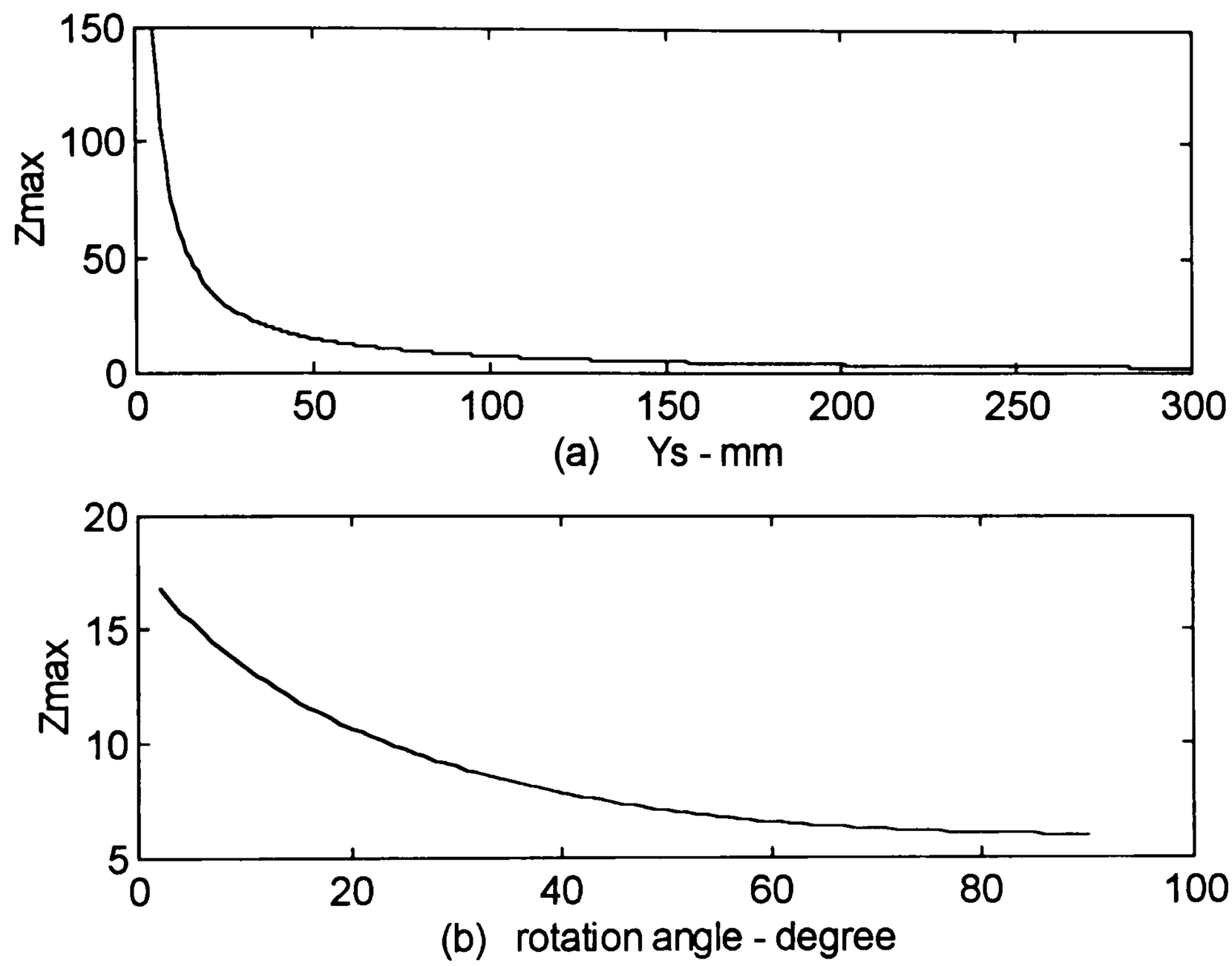

Figure 3.3 The Relationship of the Maximum Measurable Range and Rotation Angle and y_s (a) θ_1=45°, θ_2=30° and y_s from 5mm to 300mm (b) y_s=100mm, θ_2=30° and θ_1 from a small value to 90°

The maximum measurable range, z_{max}, is directly proportional to the grating's period, P_0, and the distance from the grating to the camera, z_0. It is inversely proportional to the distance between the light source and the camera, y_s, and the sum of the sinusoidal values of the rotation angles θ_1 and θ_2. Therefore, it is possible to adjust the measurable range by choosing appropriate values of P_0, z_0, y_s and θ. For a fixed experimental arrangement, it is easier to vary the rotation angles to adjust the maximum measurable range. For example, if P_0 = 1.0mm, z_0 = 450mm, y_s = 100mm, $\theta_1 = 45^o$ and $\theta_2 = 30^o$, then z_{max} is 7.581mm. If the angles are changed to $\theta_1 = 90^o$ and $\theta_2 = 60^o$, z_{max} is

decreased to 4.875mm. The relationship between the maximum measurable range and the rotation angles, and the distance between the camera and the light source, are given in figure 3.3, where diagram (a) is when $\theta_1 = 45°$ and $\theta_2 = 30°$, whilst y_s is varied from 5mm to 300mm, and diagram (b) is when $y_s = 100$mm and $\theta_2 = 30°$, whilst θ_1 is varied from a very small value to 90°. It can be concluded that for large distance measurements, small values of θ_1 and θ_2 should be chosen to guarantee that the maximum measurable range is greater than the required distance to be measured.

3.4 Error Analysis

Obviously, any errors in the measurement of the period of the grating, P_0 , the distance from the camera to the grating, z_0, and the distance between the camera and the light source, y_s, and the rotation angles, will cause an error in the measured absolute distance. For simplification, only the error of the absolute distance, which is caused by errors in the rotation angles, is analysed. Assuming that the errors of the four rotation angles are $\Delta\theta_1$, $\Delta\theta_2$, $\Delta\theta_3$, and $\Delta\theta_4$ respectively, the error, Δz, of the absolute distance measured from equation (3-15), can be expressed as follows:

$$\Delta z = \left(\frac{z_0 P_0}{2\pi y_s - P_0\Phi} + \frac{z_0 P_0^2 \Phi}{(2\pi y_s - P_0\Phi)^2} \right) \Delta\Phi \tag{3-19}$$

where

$$\Delta\Phi = -\frac{\Phi\cos\theta_1}{A+B}\left(1 - \frac{2\sin(\Phi A)}{(\cos(\Phi C) - \cos(\Phi D))\sqrt{1 - \left(0.5\frac{\cos(\Phi A) - \cos(\Phi B)}{\cos(\Phi C) - \cos(\Phi D)} \right)^2}} \right) \Delta\theta_1$$

$$-\frac{\Phi\cos\theta_2}{A+B}\left(1+\frac{2\sin(\Phi B)}{(\cos(\Phi C)-\cos(\Phi D))\sqrt{1-\left(0.5\frac{\cos(\Phi A)-\cos(\Phi B)}{\cos(\Phi C)-\cos(\Phi D)}\right)^2}}\right)\Delta\theta_2$$

$$-\frac{2\Phi(\cos(\Phi A)-\cos(\Phi B))(\sin(\Phi C)\cos\theta_3\Delta\theta_3-\sin(\Phi D)\cos\theta_4\Delta\theta_4)}{(A+B)(\cos(\Phi C)-\cos(\Phi D))^2\sqrt{1-\left(0.5\frac{\cos(\Phi A)-\cos(\Phi B)}{\cos(\Phi C)-\cos(\Phi D)}\right)^2}} \quad (3\text{-}20)$$

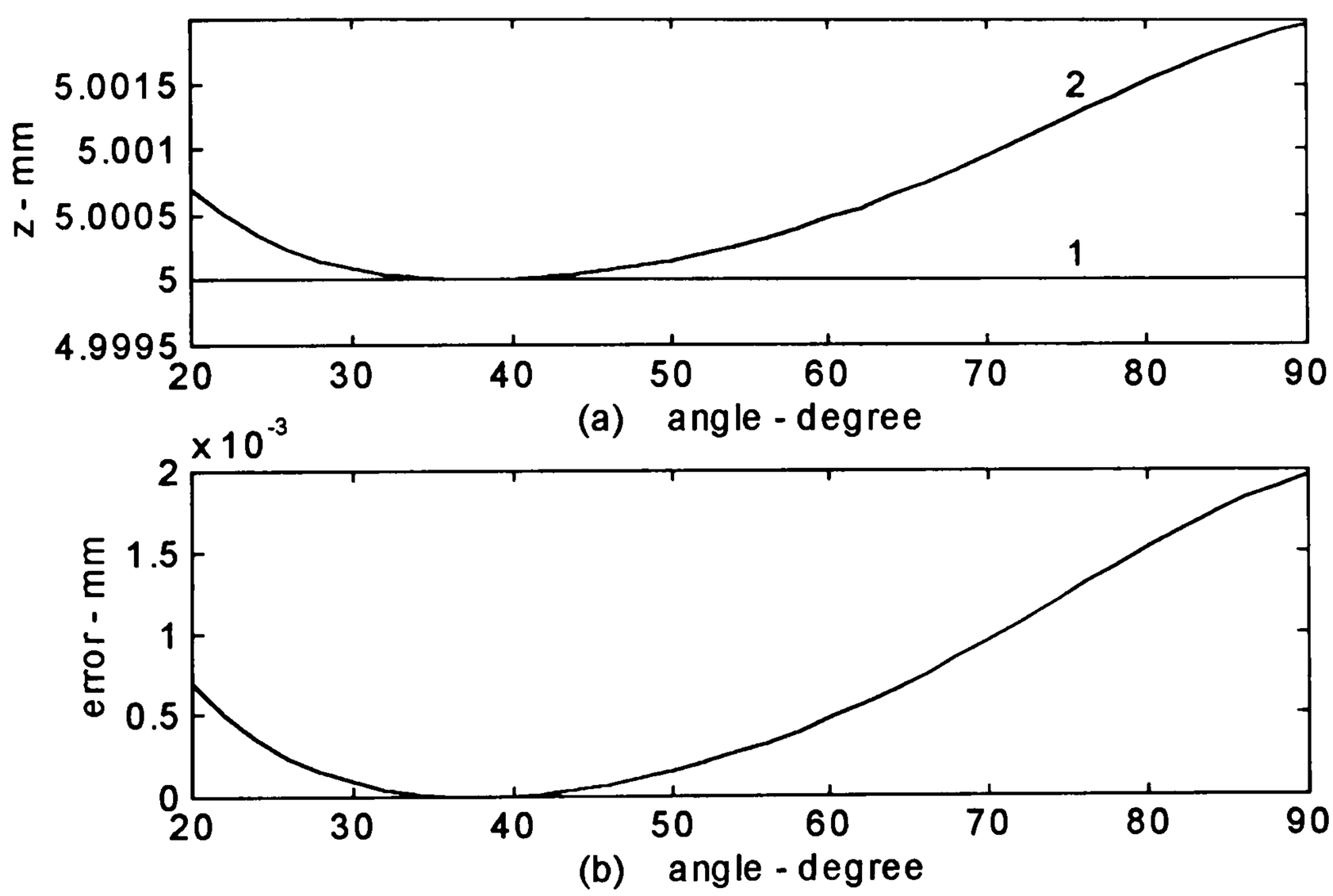

Figure 3.4 The Relationship of the Measured Absolute Distance With and Without Errors of Rotation Angles when θ_1 is Varied From 20° to 90°, z_0 = 450mm, y_s = 100mm, P_0 = 1.0mm, and θ_2 = 30°. (a) 1-the measured distance without rotation angle error; and 2-the measured distance with error in the rotation angles, (b) errors of the measured distance, caused by the errors in the rotation angles (0.01°)

If it is assumed that the errors of the four angles are $\Delta\theta_1 = \Delta\theta_2 = \Delta\theta_3 = \Delta\theta_4 = 0.01°$, and the experimental parameters are z_0 = 450mm, P_0 = 1.0mm, y_s = 100mm, z = 5mm. θ_1 is varied from 20° to 90° when θ_2 = 18°, the simulated absolute distance and the

errors, Δz, are shown in figure 3.4. Figure 3.4(a) shows the relationship of the calculated absolute distance and the value of θ_1, where diagram (1) is that without error in the rotation angles and diagram (2) is that with 0.01° error in every angle. Figure 3.4(b) shows the difference caused by the errors in the four angles. It is clear that the error is small and related to the values of the angle θ_1 when the other three angles are constants. Therefore, an appropriate value of θ_1 should be chosen to reduce the measurement error. If θ_1 is fixed and θ_2 is varied over a certain range, the result will be similar to that described above.

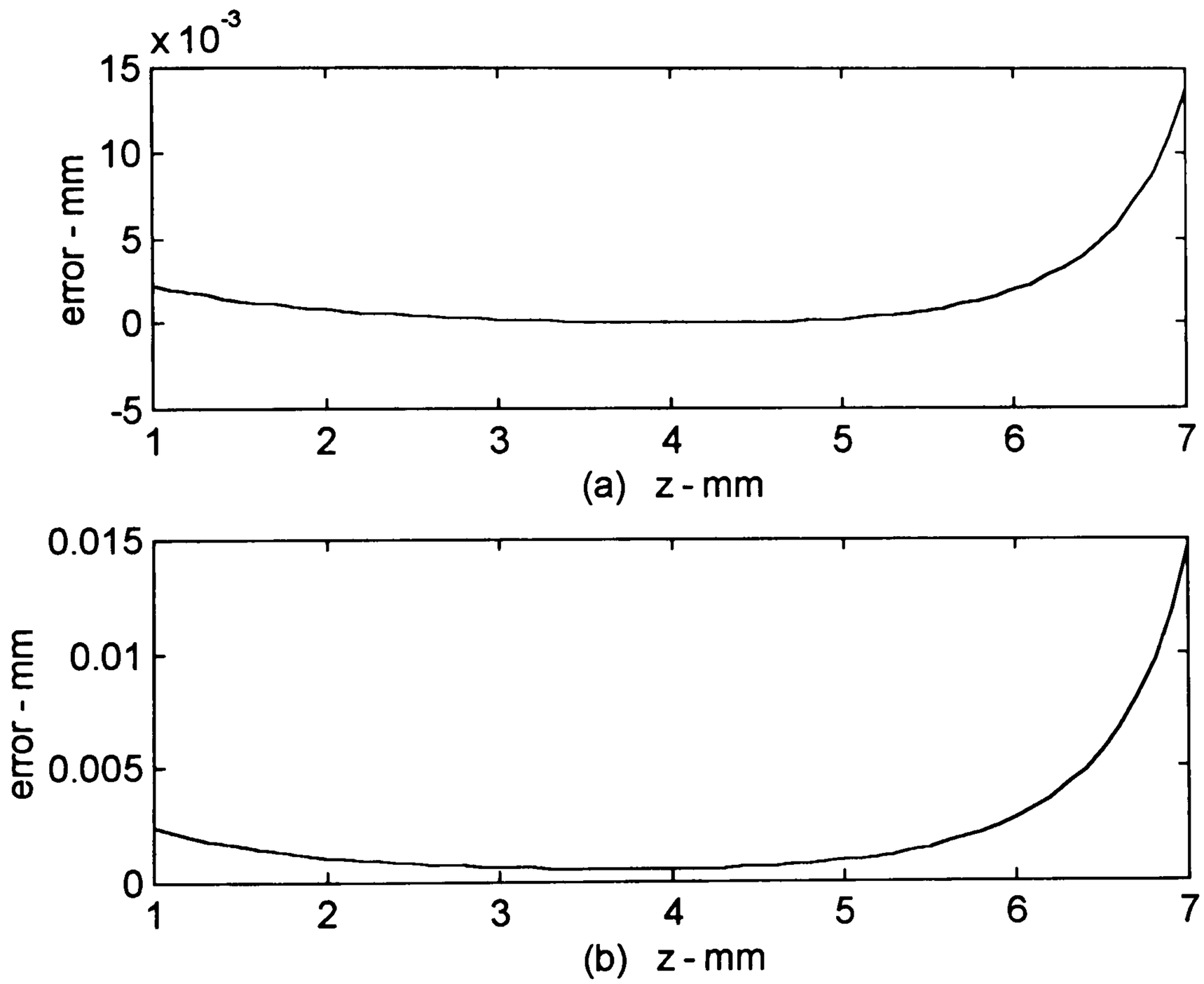

Figure 3.5 Errors of the Measured Distance, Caused by Errors in Rotation Angles for Different Values of Distance, when z_0 = 450mm, y_s = 100mm, P_0 = 1.0mm, θ_1 = 40°, θ_2 = 30°, Z is Varied from 1mm to 7mm. (a) the errors when four angles have the same error (0.01°) (b) the errors when θ_1 has an error of 0.01° and the others are correct.

For the same parameters given above, but assuming θ_1=40°, θ_2=30°, the errors of the four angles remain 0.01°, and z is varied from 1mm to 7mm, the simulated results are shown in figure 3.5. Diagram (a) shows the error of the measured absolute distance

when all four angles have the same error (0.01°), and diagram (b) shows the error when only one angle, θ_1, has an error and the others are correct. It was found from the results that the error in this case, depends upon the values of the distance. The errors are larger when z is small, or is close to the value of the maximum measurable range, (here z_{max} = 8.106mm). The results also show that the errors are approximately of the same order when all four angles have the same errors or only one has an error and the others are correct. In order to obtain more accurate results, the mid-range should be chosen by selecting suitable geometric parameters or rotation angles, to achieve a certain maximum measurable range for a given range of distance to be measured.

3.5 Summary

The four-image absolute distance contouring method proposed is described in this chapter. The theoretical analysis of this method shows that it is possible to use this method for the measurement of absolute distance and object height. It requires fewer images than the method described in chapter two, and as a result, it is faster. The maximum measurable range is directly proportional to the distance between the grating and the camera, and the grating period. It is inversely proportional to the distance from the camera to the light source, and the sum of the sinusoidal values of the first two rotation angles, θ_1 and θ_2. It can be adjusted by choosing different parameters of the system and rotation angles to suit various ranges to be measured. The error in absolute distance caused by errors in the rotation angles is small, and depends on the values of the rotation angles themselves, and the actual distance to be measured. The simulation results have verified this analysis. If suitable parameters are chosen, accurate results of absolute distance and object height can be obtained.

Chapter 4

Theory of Three-Image Absolute Distance Contouring

4.1 Introduction

It is possible to use a three image system to measure absolute distance and object height similar to those methods described in chapters two and three. The theoretical analysis of the method is based on that described in chapter two. Only three images are required for each measurement, so that it is faster than the previous methods and computationally less intensive. Like the four-image method, the calculated distance is a periodic function and the maximum measurable range, which depends on the rotation angle and the parameters of the experimental geometry, is limited. The mathematical analysis for this method as well as the relationship between the maximum measurable range, the geometric parameters and the rotation angles, are given in sections 4.2 and 4.3. An analysis of errors caused by errors in the rotation angles is depicted in the followed sections. The method is verified by the results of simulation, as a accurate and fast technique.

4.2 Three-Image Absolute Distance Contouring

The three-image absolute distance contouring method is based on the method previously described in chapter two, but different from that described in chapter three. For convenience, it is still assumed that the grating used in the absolute distance contouring system shown in figure 2.2, is a sinusoidal wave intensity grating. Therefore, the contour term can be rewritten as follows:

$$M'' = \frac{RI_0}{8}\cos\left(\frac{2\pi}{P_0}\frac{zy_s}{(z+z_0)}\sin\theta'\right) \tag{4-1}$$

When the grating is rotated to three different positions, three images with different intensity distributions are obtained, which depend upon the absolute distance and the rotation angles, as well as the experimental parameters of the system. The three corresponding contour terms are given by equations (4-2), (4-3), and (4-4) respectively.

$$M''_1 = \frac{RI_0}{8}\cos\left(\frac{2\pi}{P_0}\frac{zy_s}{(z+z_0)}\sin\theta'_1\right) \tag{4-2}$$

$$M''_2 = \frac{RI_0}{8}\cos\left(\frac{2\pi}{P_0}\frac{zy_s}{(z+z_0)}\sin\theta'_2\right) \tag{4-3}$$

$$M''_3 = \frac{RI_0}{8}\cos\left(\frac{2\pi}{P_0}\frac{zy_s}{(z+z_0)}\sin\theta'_3\right) \tag{4-4}$$

Let $A' = \sin\theta'_1$, $B' = \sin\theta'_2$, $C' = \sin\theta'_3$ and

$$\Phi' = \frac{2\pi}{P_0}\frac{zy_s}{(z+z_0)} \tag{4-5}$$

Using a similar analysis to the four-image method, then

$$\frac{M''_1 - M''_2}{M''_2 - M''_3} = \frac{\cos(A'\Phi') - \cos(B'\Phi')}{\cos(B'\Phi') - \cos(C'\Phi')}$$

$$= \frac{\sin\left(\frac{A'+B'}{2}\Phi'\right)\sin\left(\frac{A'-B'}{2}\Phi'\right)}{\sin\left(\frac{B'+C'}{2}\Phi'\right)\sin\left(\frac{B'-C'}{2}\Phi'\right)} \tag{4-6}$$

If the sinusoidal values of the three angles satisfy the following conditions:

$$A'+B' = 2(B'+C') \tag{4-7}$$

$$A'-B' = B'-C' \tag{4-8}$$

then

$$A' = 5C' \tag{4-9}$$

and

$$B' = 3C' \tag{4-10}$$

Equation (4-11) results by substituting equations (4-9) and (4-10) into equation (4-6).

$$\frac{M''_1 - M''_2}{M''_2 - M''_3} = 2\cos(0.4A'\Phi') \tag{4-11}$$

For convenience, let

$$H' = 0.5 * \frac{M''_1 - M''_2}{M''_2 - M''_3} \tag{4-12}$$

From equations (4-11) and (4-12), Φ' can be determined as a function of H'.

$$\Phi' = \frac{1}{0.4A'}\cos^{-1}(H') \tag{4-13}$$

The absolute distance can be determined from equations (4-5) and (4-13) as follow:

$$z = \frac{z_0 P_0 \Phi'}{2\pi y_s - P_0\Phi'} = \frac{z_0 P_0 \cos^{-1}(H')}{0.8\pi A' y_s - P_0 \cos^{-1}(H')}$$

$$= \frac{z_0 P_0 \cos^{-1}\left(0.5\frac{M''_1 - M''_2}{M''_2 - M''_3}\right)}{0.8\pi A' y_s - P_0 \cos^{-1}\left(0.5\frac{M''_1 - M''_2}{M''_2 - M''_3}\right)} \tag{4-14}$$

If $z_0 >> z$, then equation (4-14) can be simplified to equation (4-15).

$$z = \frac{z_0 P_0}{2\pi y_s}\Phi' = \frac{z_0 P_0}{o.8\pi_s A' y_s}\cos^{-1}(H') = \frac{z_0 P_0}{0.8\pi A' y_s}\cos^{-1}\left(0.5\frac{M''_1 - M''_2}{M''_2 - M''_3}\right) \tag{4-15}$$

In equation (4-14) or (4-15), P_0, z_0, y_s are known values of the experimental arrangement. If the value of $A'(\theta'_1)$ is chosen, then the values of $B'(\theta'_2)$ and $C'(\theta'_3)$ can be determined by equations (4-9) and (4-10). Three images are captured at the positions determined by the values of the three rotation angles. The absolute distance, z, and the object's height, can be calculated from equation (4-14).

4.3 Relationships of the Parameters and Rotation Angles

From the analysis in the above section, it can be seen that H' and Φ' are periodic functions, so that the calculated absolute distance from equation (4-14) would also be a periodic function. The relationship of H', Φ', the calculated absolute distance and the simulated value of z, are shown in figures 4.1(a) to 4.1(c), when $z_0 = 450$mm, $y_s = 100$mm, $P_0 = 1.0$mm, $\theta'_1 = 90^\circ$, and z is varied from zero to 30mm. Figure 4.1(d) shows the error between the simulated and the calculated absolute distance.

The figures show that because H', Φ' and the calculated distance are periodic functions of the simulated distance, z, similar to that discussed in four-image analysis, following the first half cycle the error between the calculated distance and the simulated distance is increased dramatically such that the results obtained by equation (4-14) would be incorrect from the second half cycle onwards. Therefore, this method can only be effectively used to measure a limited range of distance and object height. The maximum measurable range is the maximum value of the calculated absolute distance. This is called z'_{max}, in order to distinguish it from the maximum measurable range obtained using the four-image method. The maximum value of the calculated absolute distance is achieved when the conditions imposed by equation (4-16) are satisfied.

$$\Phi' = \Phi'_{max} = \frac{2.5\pi}{A'} \tag{4-16}$$

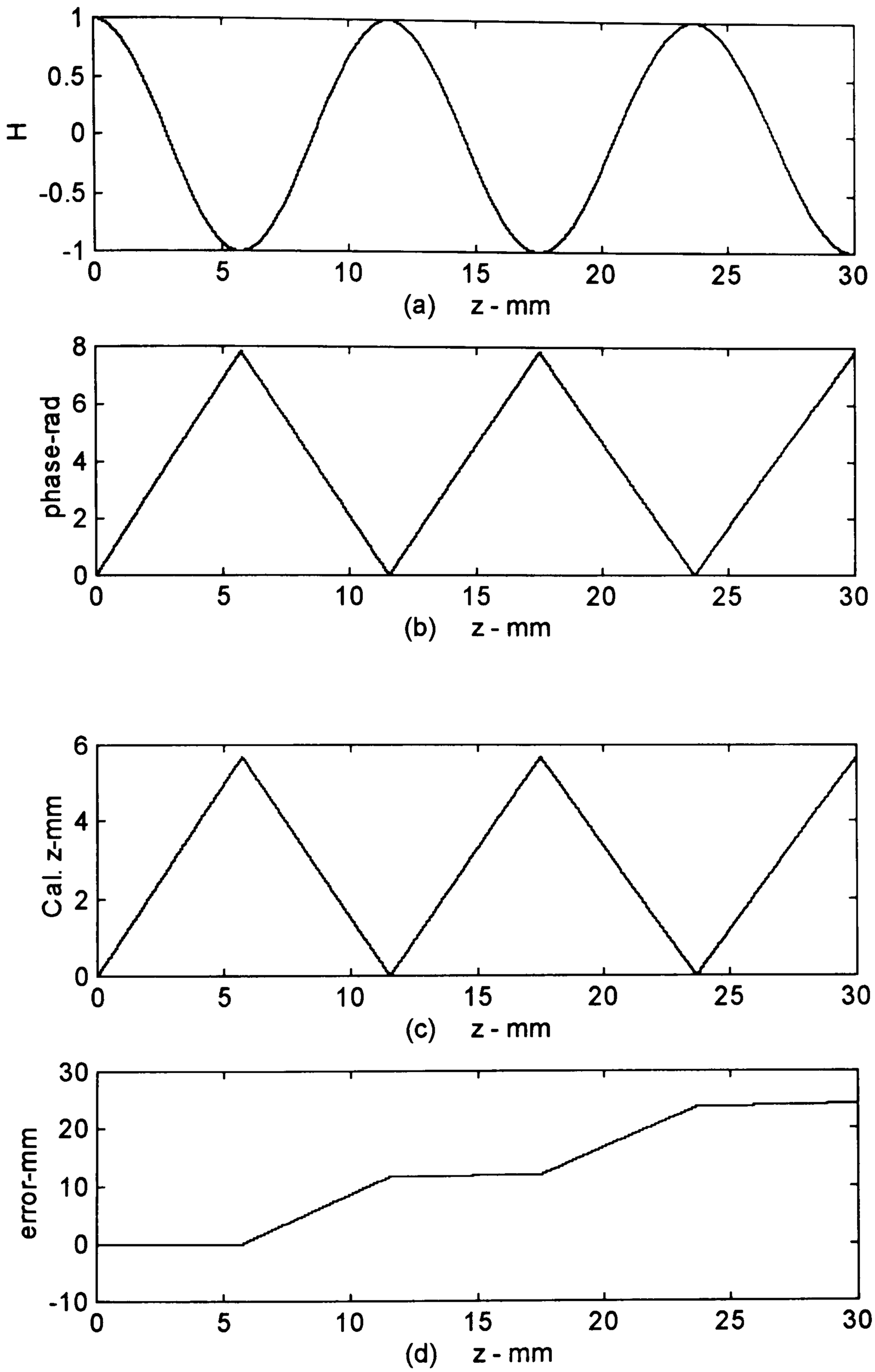

Figure 4.1 The Relationship of H', Φ', the Calculated Absolute Distance and the Simulated Distance, z, and the Error Between the Simulated and Calculated z. when $z_0 = 450$mm, $y_s = 100$mm, $P_0 = 1.0$mm, $\theta'_1 = 90°$ and Z is Varied from zero to 30mm.

The maximum value of the calculated absolute distance, z'_{max}, which is the maximum measurable range obtained from equation (4-14), is given by equation (4-17).

$$z'_{max} = \frac{2.5 z_0 P_0}{2A' y_s - 2.5 P_0} \tag{4-17}$$

From this analysis, it can be concluded that the three-image contouring method can be used to measure absolute distance values less than or equal to z'_{max}. This is a limitation of the method, but when used within the maximum measurable range, it provides accurate results. When z_0 = 450mm, y_s = 100mm, P_0 = 1.0mm, and θ'_1 = 90°, the simulated results of the calculated absolute distance, and the error between the simulated distance, z, and the calculated absolute distance, are shown in Figure 4.2.

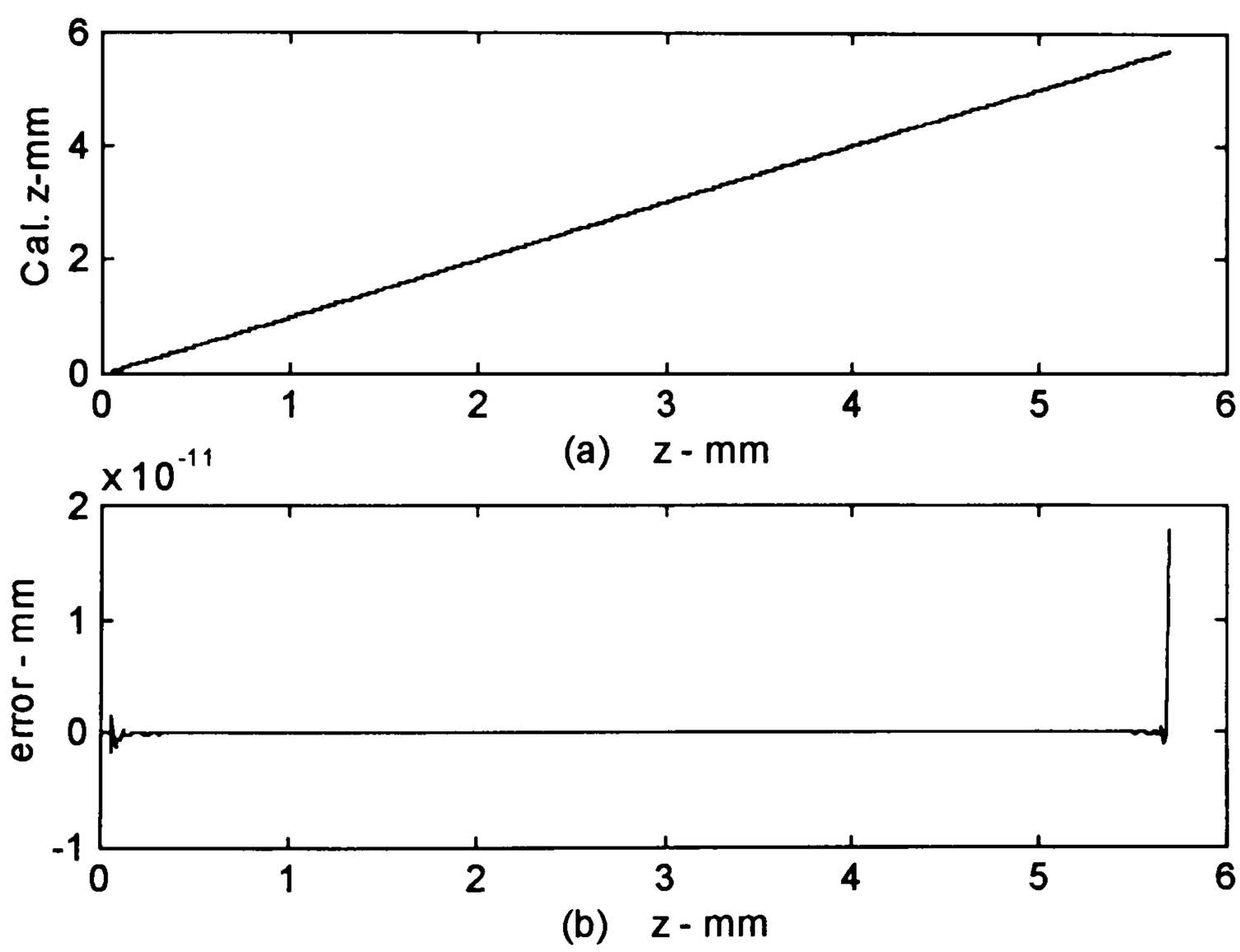

Figure 4.2 The Calculated Absolute Distance from 0 to z'_{max} (here z'_{max} =5.696mm) and Error Between the Calculated and Simulated Distance, z_0 = 450mm, y_s = 100mm, P_0=1.0mm and θ'_1 =90°.

From this diagram, it was found that the calculated absolute distance is very close to the value of the simulated absolute distance, the difference between them being less than 0.1nm. This verified that the three-image absolute distance contouring method

can be applied for the measurement of absolute distance and object height, over some limited range, with good accuracy.

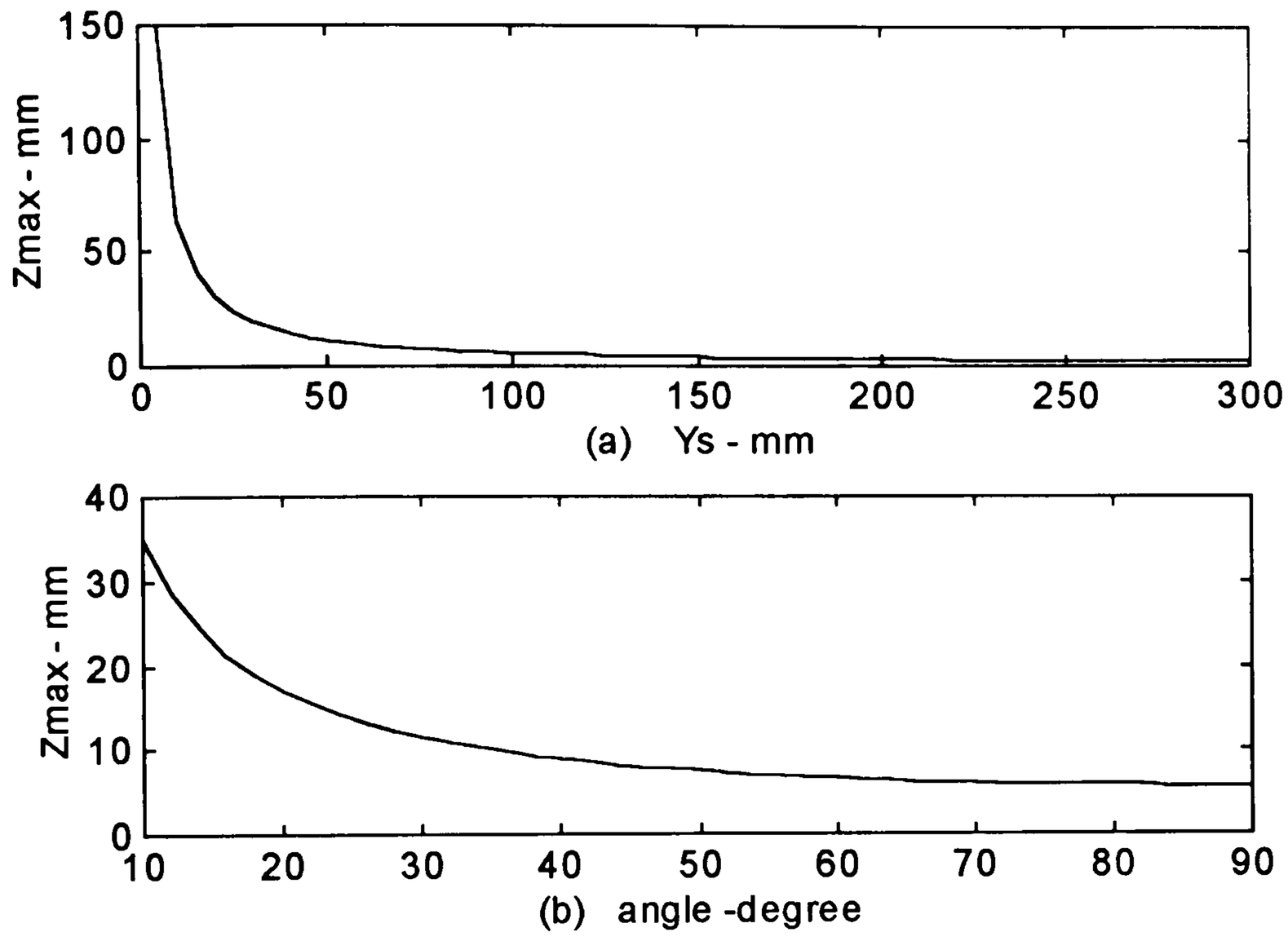

Figure 4.3 Variation of the Maximum Measurable Range, Whilst Varying y_s from 5mm to 300mm and θ'_1 from 10° to 90°, where $z_0 = 450$mm and $P_0 = 1.0$mm (a) $\theta'_1 = 90°$ (b) $y_s = 100$mm.

The maximum measurable range, z'_{max}, is related to the parameters of the experimental geometry and the rotation angle, θ'_1. It is directly proportional to the distance from the camera to the grating, z_0, and the period of the grating, P_0. It is inversely proportional to the distance between the camera and the light source, y_s, and the sinusoidal value of the angle, θ'_1. Therefore, it is possible to change the maximum measurable range by varying the values of the parameters of the system and the rotation angle, θ'_1. In this case, it is easier to change the rotation angle than to vary any of the other parameters. Consider the case, when $z_0 = 450$mm, $y_s = 100$mm, $P_0 = 1.0$mm, $\theta'_1 = 90°$, $z'_{max} = 5.696$mm. If θ'_1 is changed to 30°, then z'_{max} changes to 11.538mm. When z_0=450mm and P_0=1.0mm, figure 4.3 shows the maximum measurable range when the distance from the camera to the light source is varied from 5mm to 300mm when θ'_1=90°; and when y_s=100mm when θ'_1 is varied from

10° to 90°. For a large distance to be measured, small values of y_s and θ'_1 should be used to ensure the maximum measurable range is greater than the distance to be measured.

4.4 Error Analysis

Any errors in the measurement of the absolute distance obtained by the three-image method, depend on the errors of the parameters of the system geometry and the rotation angles. To simplify the mathematical analysis, only differences caused by errors in the rotation angles, will be discussed. If the errors in the three angles are $\Delta\theta'_1, \Delta\theta'_2, \Delta\theta'_3$ respectively, then the error in the measured absolute distance, Δz, can be expressed as:

$$\Delta z = \left(\frac{z_0 P_0}{2\pi y_s - P_0\Phi'} + \frac{z_0 P_0^{\,2}\Phi'}{(2\pi y_s - P_0\Phi')^2} \right)\Delta\Phi' \tag{4-18}$$

$$\begin{aligned}\Delta\Phi' = &-\frac{\cos\theta'_1}{A'}\Phi'\left(1 - \frac{1.25\sin(\Phi' A')}{(\cos(\Phi' B') - \cos(\Phi' C'))\sqrt{1-\left(0.5\dfrac{\cos(\Phi' A') - \cos(\Phi' B')}{\cos(\Phi' B') - \cos(\Phi' C')}\right)^2}}\right)\Delta\theta'_1 \\ &- \frac{1.25\sin(\Phi' B')\cos\theta'_2\Phi'\left(1 - \dfrac{\cos(\Phi' A') - \cos(\Phi' B')}{\cos(\Phi' B') - \cos(\Phi' C')}\right)}{A'(\cos(\Phi' B') - \cos(\Phi' C'))\sqrt{1-\left(0.5\dfrac{\cos(\Phi' A') - \cos(\Phi' B')}{\cos(\Phi' B') - \cos(\Phi' C')}\right)^2}}\Delta\theta'_2 \\ &+ \frac{1.25\Phi'\sin(\Phi' C')\cos\theta'_3(\cos(\Phi' A') - \cos(\Phi' B'))}{A'(\cos(\Phi' B') - \cos(\Phi' C'))^2\sqrt{1-\left(0.5\dfrac{\cos(\Phi' A') - \cos(\Phi' B')}{\cos(\Phi' B') - \cos(\Phi' C')}\right)^2}}\Delta\theta'_3\end{aligned} \tag{4-19}$$

If the errors in the three rotation angles are $\Delta\theta'_1 = \Delta\theta'_2 = \Delta\theta'_3 = 0.01^\circ$, and the values of the parameters of the system are $z_0 = 450$mm, $y_s = 100$mm, $P_0 = 1.0$mm, $z = 5.0$mm, and the first angle, θ'_1 is varied from 20° to 90°, then the simulated absolute

distance and the differences caused by the these angle errors, are shown in figure 4.4. Figure 4.4(a) shows the absolute distance obtained from equation (4-14), where (1) shows that without errors in the rotation angles, and (2) shows that when each angle has the same error of 0.01°. Figure 4.4(b) shows the differences caused by the errors in the three angles. This shows that the error in the measured absolute distance, is dependent on the value of angle θ'_1. It can be seen that the error is large when θ'_1 is greater than 60°, but is less than 3μm when θ'_1 is in the range of 20° to 60°. Therefore, an appropriate value of θ'_1 should be chosen to reduce the measurement error caused by the rotation angles.

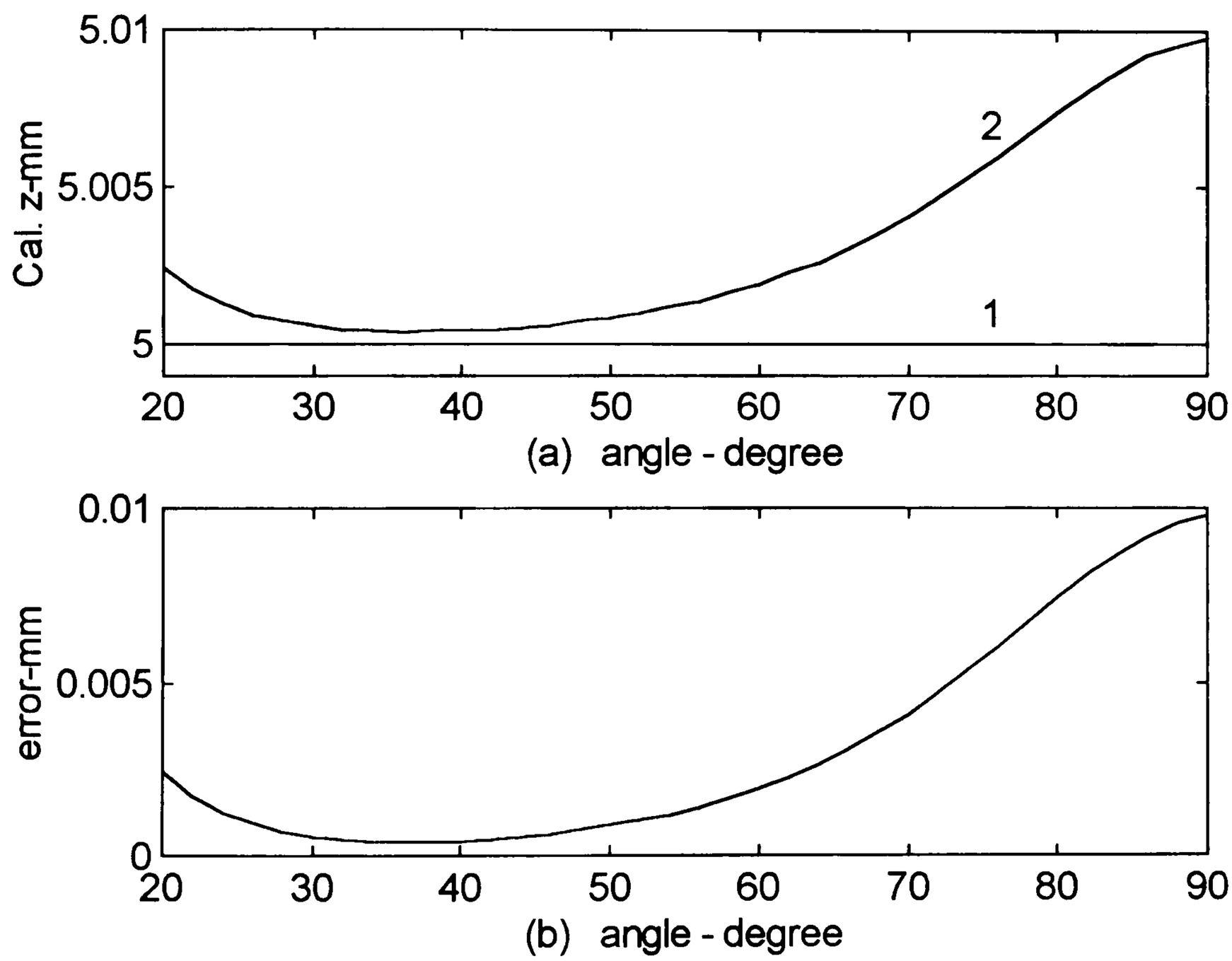

Figure 4.4 The Measured Absolute Distance and Error Caused by the Rotation Angles when θ'_1 is varied from 20° to 90°, z_0= 450mm, y_s=100mm, P_0=1.0mm, z=5.0mm and $\Delta\theta'_1 = \Delta\theta'_2 = \Delta\theta'_3$=0.01°. (a) the measured absolute distance (1)without and (2)with errors. (b) the differences caused by errors in rotation angles

Using the parameters as above, but varying z from 1.0mm to 8.0mm, whilst θ'_1 =40°, the error in the measured absolute distance, caused by the rotation angle errors, are shown in figure 4.5. Diagram (a) shows the error when $\Delta\theta'_1 = \Delta\theta'_2 = \Delta\theta'_3 = 0.01°$, the value of the error being dependent on the value of the measured distance. When the distance is less than 7.5mm, the error reduces to less than 10μm. When the measured distance is larger than 7.5mm and tends to the maximum measurable range, z'_{max}, (here z'_{max} = 8.924mm), the error becomes significant. Figure 4.5(b) shows the error when $\Delta\theta'_1 = 0.01°$ but $\Delta\theta'_2 = \Delta\theta'_3 = 0$. In this case, the overall error is smaller than 5μm when the absolute distance is less than 7.5mm, but increases when the distance is greater than 7.5mm. Figure 4.5(c) shows the errors for the condition when $\Delta\theta'_1 = \Delta\theta'_3 = 0$ and $\Delta\theta'_2 = 0.01°$. In this case, the error is large when the distance is large or small. The error caused by $\Delta\theta'_3 = 0.01°$ but $\Delta\theta'_1 = \Delta\theta'_2 = 0$ is shown in figure 4.5(d). It is less than 10μm when the distance is less than 7.5mm, but increases when the distance is greater than this value.

From the above analysis, it can be concluded that if there are errors in the rotation angles, there will be an error in the measured absolute distance. There are different relationships between the errors in the measured absolute distance and those in the rotation angles. The total error in the measured absolute distance depends on the values of θ'_1, the errors in the three angles, and the values of the absolute distance itself. For a given distance to be measured, the error can be very small if a suitable value of θ'_1 is chosen. The geometry of the system and measurement of its parameters must be carefully undertaken to minimise all other possible error sources.

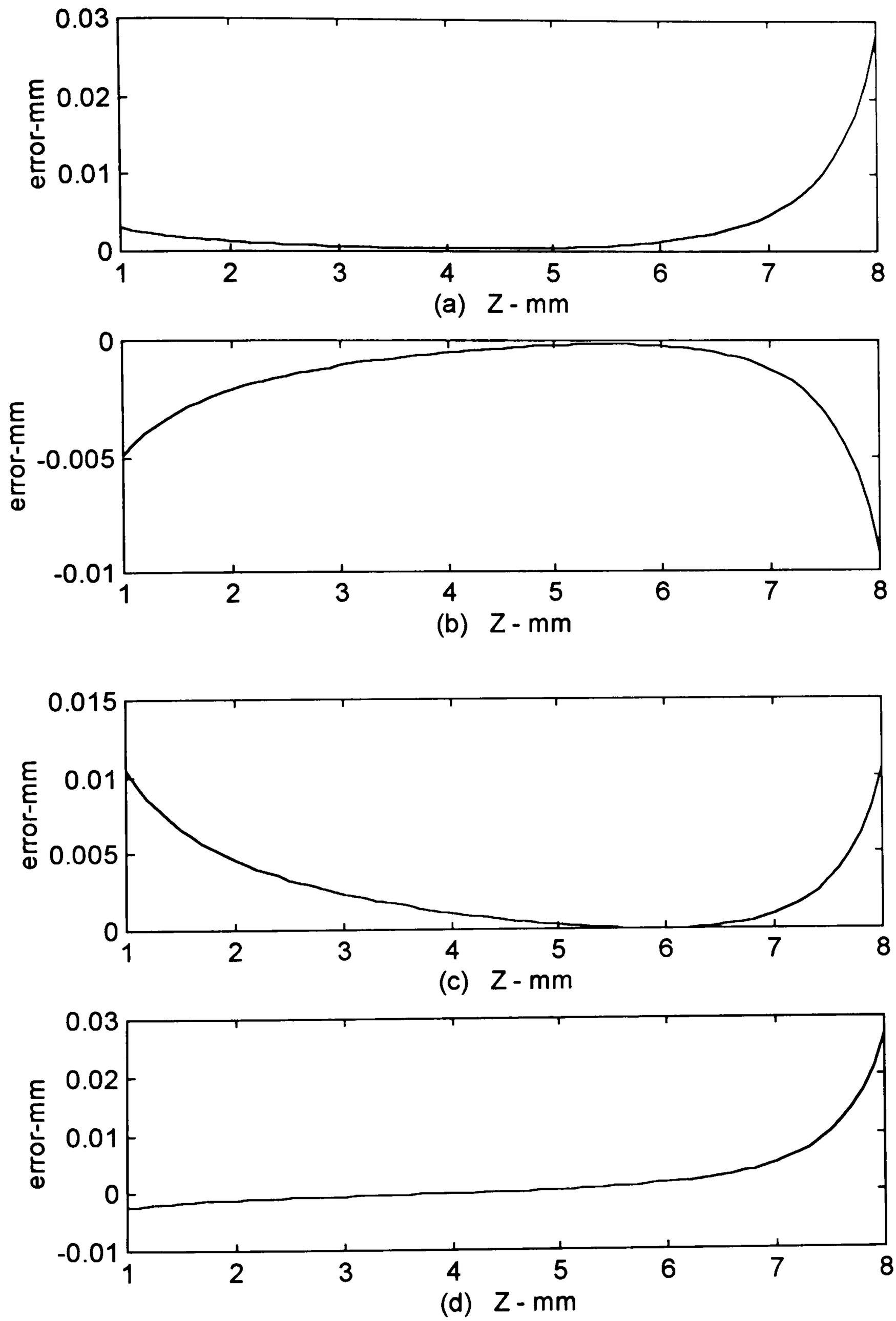

Figure 4.5 The Errors in the Measured Absolute Distance, Caused by Errors in the Rotation Angles, when z_0=450mm, y_s=100mm, P_0=1.0mm, z is Varied from 1.0mm to 8.0mm, θ'_1=40°. (a) $\Delta\theta'_1=\Delta\theta'_2=\Delta\theta'_3$=0.01° (b) $\Delta\theta'_1$=0.01° and $\Delta\theta'_2=\Delta\theta'_3$=0 (c) $\Delta\theta'_1=\Delta\theta'_3$=0 and $\Delta\theta'_2$=0.01° (d) $\Delta\theta'_1=\Delta\theta'_2$=0 and $\Delta\theta'_3$=0.01°

4.5 Summary

A new three-image absolute distance contouring system has been proposed. The analysis is based on that given in chapters two and three. However, it only requires three images for each measurement, therefore being less computationally intensive and offering a reduced signal processing time. The theoretical analysis has confirmed that the proposed method can be used for measurement of absolute distance and object height with good accuracy, provided that appropriate parameters and rotation angles are chosen. In the same way as the four-image contouring method, the maximum measurable range depends upon the parameters of the system and the rotation angle, θ'_1. The simulation results have confirmed the above conclusions.

Chapter 5

Experiments and Results of Absolute Distance Contouring

5.1 Introduction

The proposed three absolute distance contouring methods described in chapters two, three, and four, have been shown by experiment to be accurate and fast contouring techniques. An accuracy of better than 10μm has been achieved. These methods could be used for the measurement of absolute distance and surface topography in many applications. This chapter describes the experiments carried out and the results obtained for each method. Firstly, the experimental system, used to verify each of the methods, is discussed in section 5.2. The instruments and test objects used in the system are outlined in section 5.2. In section 5.3, the details of the signal processing procedures for each method are given. The experiments, results, and discussions about the factors which affect the accuracy of the measurement, are described in section 5.4. Sections 5.5 and 5.6 outline the experiments and results of the four-image and three-image contouring methods.

5.2 Experimental System

Following the theoretical analysis of each of the contouring methods, it is necessary to verify the conclusions obtained, by experiment. Figure 5.1 shows a diagram of the absolute distance contouring system which was used in the experiments for each of the three different methods.

In these experiments, the grating used is a sinusoidal wave intensity grating which is mounted on a bearing such that it can rotated about an axis normal to the plane of the rulings. The test object is located behind the grating and illuminated by a light source which need not be coherent. The distance from the grating to the object can be adjusted by the micrometer. The bearing is driven by a stepper motor which is controlled by a computer equipped with a VFG frame grabber. The images of the moiré patterns, obtained when the grating is rotated to different positions, are captured by a CCD camera. The image data is sent to the computer for processing. The whole experimental process is controlled by specially designed software.

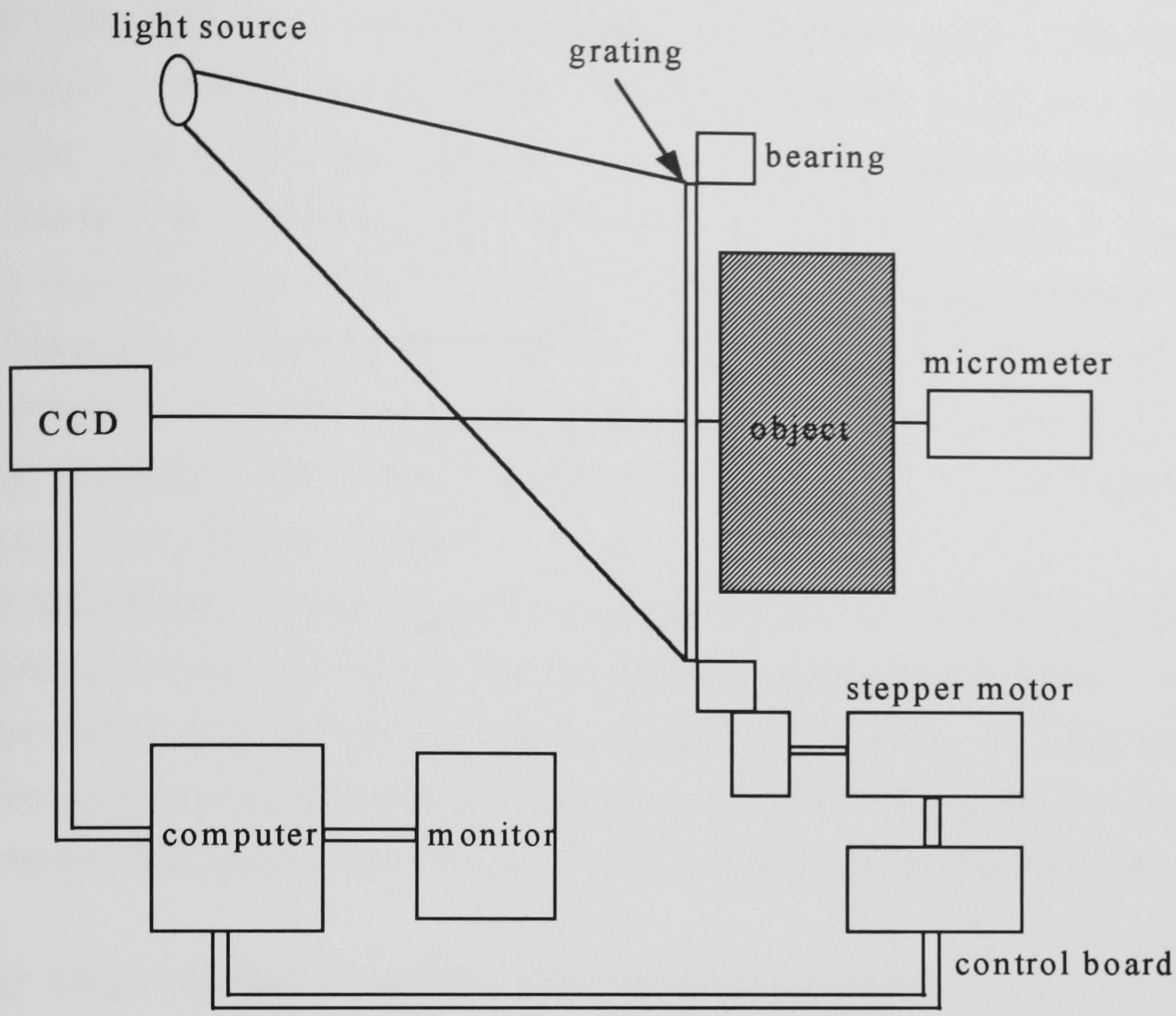

Figure 5.1 Absolute Distance Contouring System

The instruments and components used in the experimental system are as follow:

(1) **Light Source** - a white light source from AG Electro-Optics Ltd, model IL 410 illumination system.

(2) **CCD Camera -** Model CCIR monochrome CCD camera, COHU INC.

(3) **Computer -** IBM PC 486DX2 66MHZ 16M RAM.

(4) **Frame Grabber** - ITEX variable-scan frame grabber, model VFG 1.0, Imaging Technology Inc..

(5) **Stepper Motor** - four-phase 7.5° stepper motor, RS Components.

(6) **Stepper Motor Control Board -** Programmable Single Axis Stepping Motor Controller with On-Board Motor Driver, RS Components, step rate variable between 48 - 3072 steps per revolution.

(7) **Sinusoidal wave intensity gratings** - Manufactured using a photographic enlargement process. The high quality commercially available square wave intensity grating, with a small period, is used as a master and its image is enlarged. The holographic plate, (Holotest plates - 8F75HD, Laza Holograms Limited), is placed in the image plane. By varying the distance between the master and the image plane, different periods of grating can be obtained. If the image of the square wave grating is appropriately defocused, gratings with an approximate sinusoidal intensity distribution can be obtained. The periods of the sinusoidal gratings used in these experiments, ranged from 0.5mm to 1.36mm.

(8) **Test objects** - The objects used in the experiments are made of wax or metal. The surface is painted matt white in order to increase the reflectivity and reduce the noise. The objects' shapes are concave, convex, concave-convex, groove, and other profiles. The concave objects have different dimensions, with heights ranging from 1.858mm to 7.600mm. The convex objects' heights are in the range of 1.470mm to 3.017mm.

5.3 Experimental Procedure and Signal Processing

The experiments for each of the contouring methods are carried out using the system shown in figure 5.1. All the captured images are in a 64x64 pixel format. The programs used to control the experiment and signal processing are written in Microsoft C version 6.0. The signal from the CCD camera is digitized and stored in the frame memory for processing. There are different procedures and signal processing methods for each of the contouring systems.

5.3.1 Absolute Distance Contouring

For the absolute distance contouring method described in chapter two, the measured distance and accuracy depend on the parameters of the experimental system and the rotation angle. For a given distance or object height to be measured, the appropriate parameters and rotation angles should be selected to ensure the highest accuracy. The experimental procedure for this method firstly requires a choice in the parameters of the system geometry, such as the distance from the grating to the object , z_0, the

distance between the light source and the camera, y_s, and the grating's period, P_0. It is then required to determine the value of the rotation angle, θ_n, and the required steps through which the grating will be rotated from zero to θ_n, or the number of required images to be captured through the grating's rotation. If the grating is rotated from zero to θ_n in N steps, the number of the images will be N+1. After these parameters are entered into the computer, the first image is captured when $\theta = 0$, and the image data is read to an array in the computer's memory. The grating is rotated step by step by an interval of θ_n/N. Following each step, another image is captured and the data is read to memory. In these experiments, the grating was rotated from zero to θ_n in 20 steps, acquiring a total of 21 images for each measurement. The rotation angles, θ_n, used are 15°, 30°, 60°, and 90°, giving a rotation angle interval of each step of 0.75°, 1.5°, 3.0°, and 4.5° respectively, for each of the four different rotation angles.

After 21 images are captured, the values of the image intensity at pixel (i,j) for all 21 images, are read to an array having 21 elements. If the maximum and minimum values in the array are $M_{max}(i,j)$ and $M_{min}(i,j)$, then the background signal can be removed and the phase value for these 21 positions at pixel (i,j) can be calculated from equation (5-1).

$$\varphi_m(i,j) = \arccos\left(\frac{M_m(i,j) - \dfrac{M_{max}(i,j) + M_{min}(i,j)}{2}}{\dfrac{M_{max}(i,j) - M_{min}(i,j)}{2}}\right) \tag{5-1}$$

where m = 0 to 20, and i, j vary from 1 to 64.

The absolute value of the phase change from position m to m+1 is

$$\Delta\varphi_{m+1,m}(i,j) = |\varphi_{m+1}(i,j) - \varphi_m(i,j)| \tag{5-2}$$

The total phase variation seen at pixel (i,j) when the grating is rotated from zero to θ_n is the sum of the 20 phase differences:

$$\Delta\varphi(i,j) = \sum_{m=0}^{20} \Delta\varphi_{m+1,m}(i,j) \tag{5-3}$$

Therefore, the fringe number for pixel (i,j) can be obtained from equation (5-4).

$$n(i,j) = \frac{\Delta\varphi(i,j)}{2\pi} \tag{5-4}$$

In this case, n(i,j) may not necessarily be an integer value. The absolute distance can now be obtained by substituting the values of z_0, y_s, P_0, θ_n and n(i,j) into equation (2-11). If the maximum distance is found, then the object's height can be achieved by subtracting the value of the distance from the value of the maximum distance. Figure 5.2 shows a flow diagram of the whole experimental procedure.

Note that the value of n(i,j) must be greater than or at least equal to 0.5. This is because the phase at each position is calculated by equation (5-1), where the maximum and minimum values are the maximum and minimum values of the cosine function. Therefore, if n(i,j)<0.5, the minimum value is not the actual minimum value of the cosine function, and this would lead to incorrect results.

5.3.2 Four-Image Absolute Distance Contouring

The experimental procedure for four-image contouring method is relatively simple compared with that described in section 5.3.1. Using this method, only four images are required for each measurement so that the grating is only rotated to four different positions rather than 21 as above. It requires less memory to store the image data and less time to process the signal.

The procedure is similar to that for the absolute distance contouring method. Firstly, the parameters, z_0, y_s, and P_0, are determined according to the maximum distance to be measured. The maximum measurable distance, z_{max}, for the given parameters must be larger than the distance to be measured. Therefore, the appropriate rotation angles, θ_1

and θ_2, should be chosen to ensure the above condition. After θ_1 and θ_2 have been chosen, the values of θ_3 and θ_4 are obtained from equations (3-10) and (3-11). Four images are captured at each of the four different grating positions.

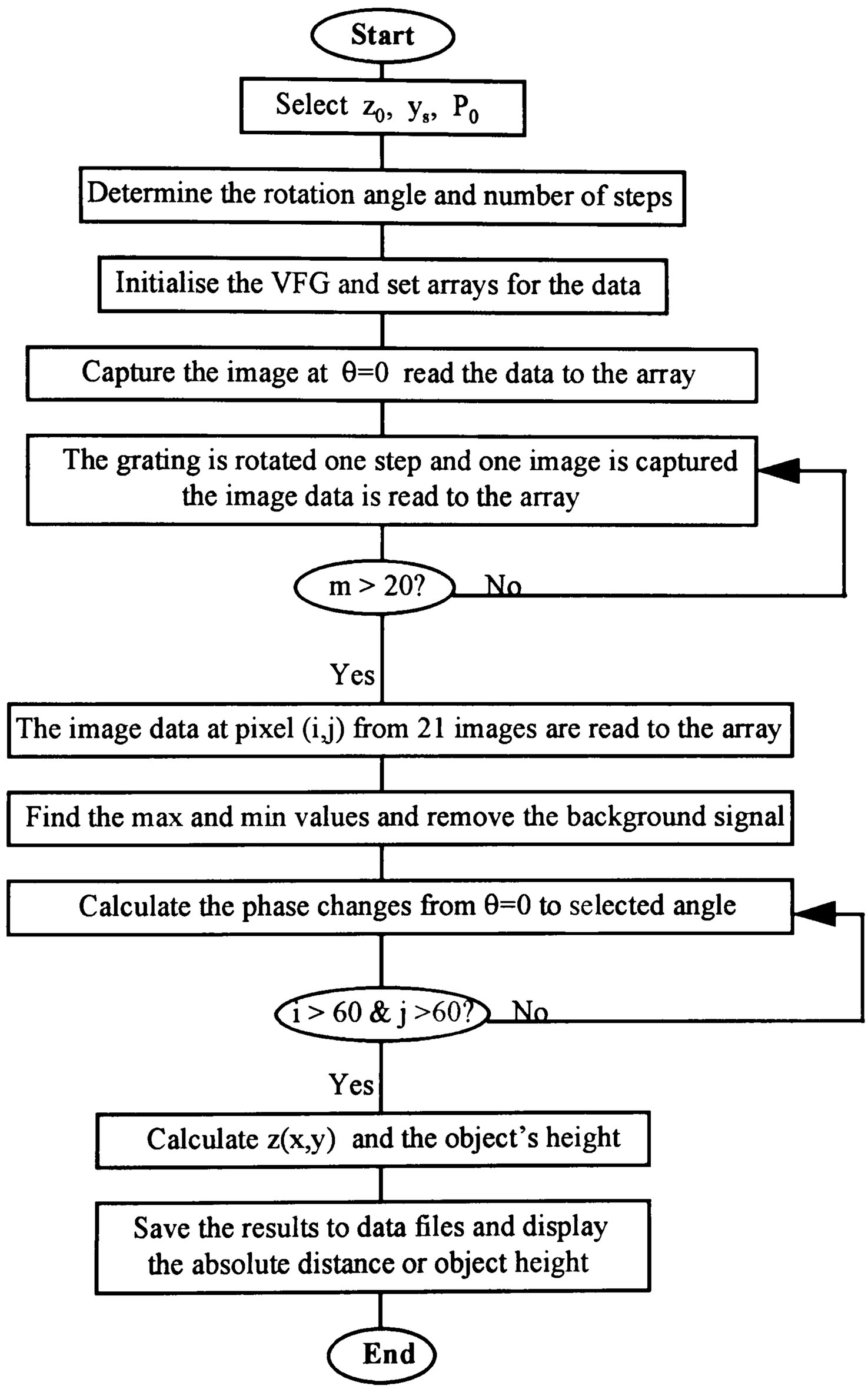

Figure 5.2 Flow Diagram of the Experimental Procedure for the Absolute Distance Contouring Method

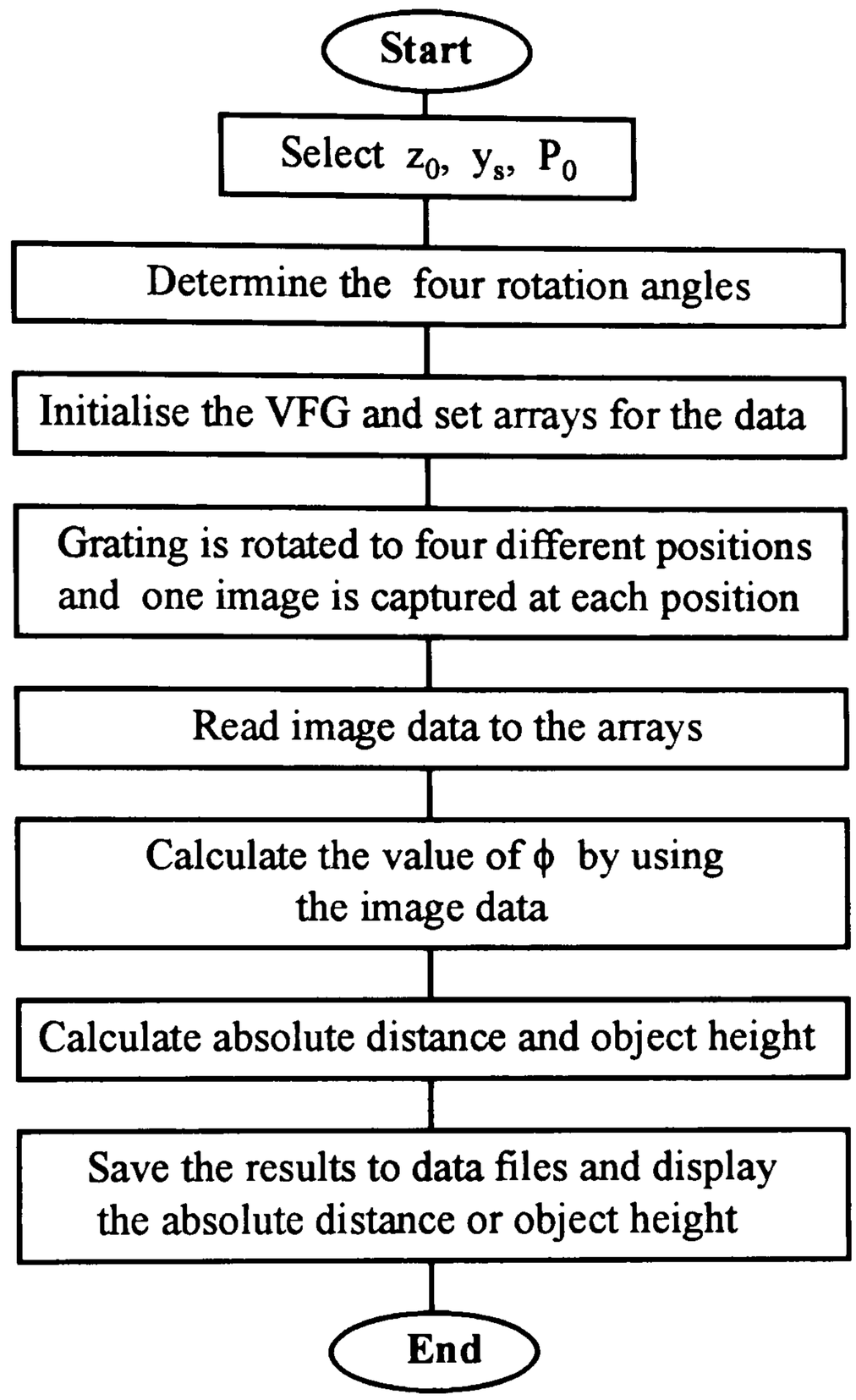

Figure 5.3 Flow Diagram of the Experimental Procedure for the Four-Image Absolute Distance Contouring Method

The value of Φ can be calculated by using the data from the four captured images, and by using equation (3-13). Note that if it is assumed that each image has the same background signal, this will be removed when the data from the four images is substituted into equation (3-13). The absolute distance can be obtained by substituting the values of Φ into equation (3-15). The object's height can be achieved using the same method as that described in 5.3.1, where the object height is equal to the difference between the maximum absolute distance and the actual absolute distance. The whole experimental procedure is shown in figure 5.3.

5.3.3 Three-Image Absolute Distance Contouring

The experimental procedure for the three-image contouring method is similar to that for the four-image contouring method. The advantage that the three-image system offers, is that it is only required to choose the value of the rotation angle, θ'_1, after the other parameters of the experimental system have been determined. The other two angles, θ'_2 and θ'_3, are determined by equations (4-9) and (4-10). In a similar fashion to the four-image method, the maximum measurable range, z'_{max}, determined by equation (4-17), is to be considered when determining the parameters of the system and the rotation angle for a given accuracy and distance to be measured. After the data from each of the three images has been captured, the value of Φ' is calculated from equation (4-13). By substituting the values of the parameters, rotation angle and Φ', the absolute distance can be obtained from equation (4-14). The object's height also can be calculated in the same way as that used for the four-image method.

5.4 Experiments and Results of Absolute Distance Contouring

The experiments carried out for the absolute distance contouring method are based on the experimental system and procedures described in sections 5.2 and 5.3. A C program was designed to control the system and handle signal processing routines.

5.4.1 Experiments of Absolute Distance Contouring

In these experiments, the distance, z_0, from the grating to the camera, is set at 320mm, 370mm, 420mm and 470mm. The distance, y_s, between the camera and light source, is 100mm. Both sinusoidal and square wave intensity gratings are used in the experiments. The periods of the gratings, P_0, measured using a co-ordinate measuring machine, (SIP MU-214B, Switzerland), are:

sinusoidal wave intensity grating - 0.763mm, 0.985mm, 1.360mm and 1.80mm;
square wave intensity gratings - 0.508mm, 0.980mm, 1.386mm and 1.800mm.

The rotation angles, θ_n, used are 15°, 30°, 60° and 90°. The measured dimensions and areas of the objects, for different values of z_0, are shown in figure 5.4 and table 5.1.

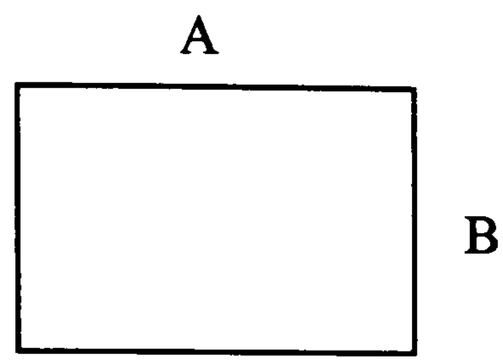

Figure 5.4 The Measured Area

Table 5.1 The Measured Dimensions and Areas

Z_0(mm)	A(mm)	B(mm)	S=AxB(mm^2)
320	24	20	480
370	30	25	750
420	36	30	1080
470	42	36	1512

The objects used for this method are prepared as that described in section 5.2. The maximum heights of the objects, as measured by the contact gauge (Three-Axis Measuring Machine, SIP 414M, Switzerland), are listed in table 5.2.

Table 5.2 Object Shape and Maximum Height as Measured by Contact Gauge

Object Shape	**Maximum Heights** (mm)
Convex1	1.470
Convex2	3.017
Concave1	1.858
Concave2	3.102
Concave3	3.417
Concave4	5.210
Concave5	7.600
Groove	2.661
Concave&Convex	1.421/1.690

All images are defocused (this is explained in section 5.4.3(i)) and in a 64x64 pixel format. However, only a 60x60 pixels image is used in the signal processing. In all of the experiments, 21 images are used for each measurement. In these experiments, the measured distance or the object height is displayed on the screen and saved in data files. The data is condensed into 30x30 and 15x15 arrays for convenience.

5.4.2 Experimental Results

Figure 5.5 shows the focused and defocused images of the object called concave3, when the grating is at a position of 15°. Figure 5.6 shows the measured results for this object when $z_0 = 420$mm, $y_s = 100$mm, $P_0 = 0.763$mm and $\theta_n = 30^0$. In figure 5.6, (a) is a 3-D plot of the measured absolute distance from the grating to the object's surface for the measured area; (b) is a 3-D plot of the object's height, whilst (c) and (d) are the side views of the 3-D plots when the data is in a 30x30 and 60x60 pixel format respectively. Figure 5.7 shows the three-dimensional plots from the measured results, of the other tested objects listed in table 5.2, when $z_0 = 420$mm, $y_s = 100$mm, $P_0 = 0.763$mm and $\theta_n = 30^0$. The data is in a 30x30 pixel format. In figure 5.7, from (a) to (h), the objects are convex1, convex2, concave1, concave2, concave4, concave5, groove and concave&convex, respectively.

The maximum heights of the objects, measured by the contouring method, are listed in table 5.3. The heights measured by the contact method are shown for comparison purposes.

From the results given in table 5.3, it can be seen that the contouring method is accurate, the difference being typically less than 10μm. Each measurement takes approximately 16 seconds.

The results obtained using different parameters of the system and different rotation angles are similar to that described above, but there are some differences when different parameters and rotation angles are used in the experiments. This will be discussed in section 5.4.3.

(a) focused

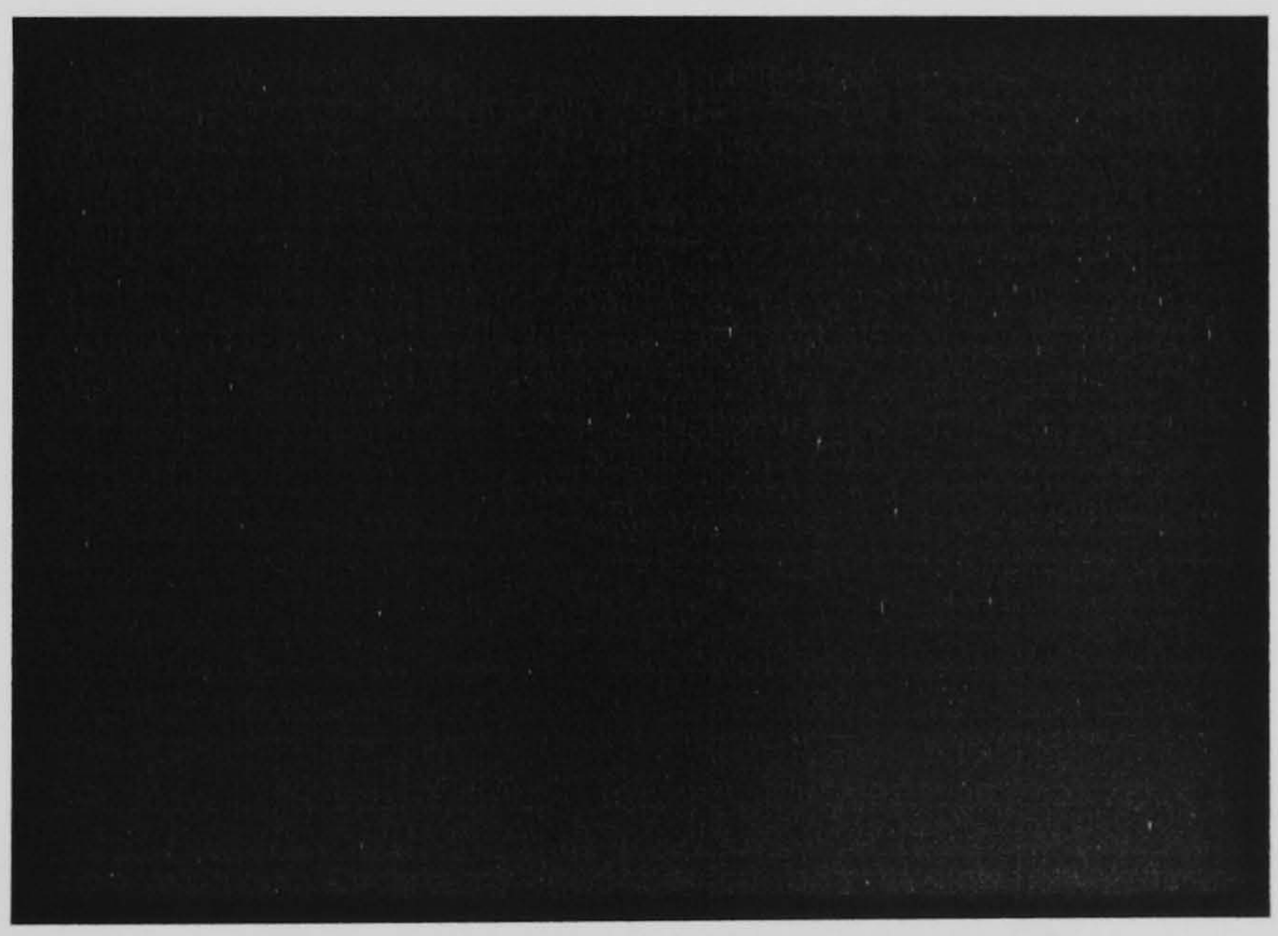

(b) defocused

Figure 5.5 The Images of Object Concave3 when the Grating is at 15°

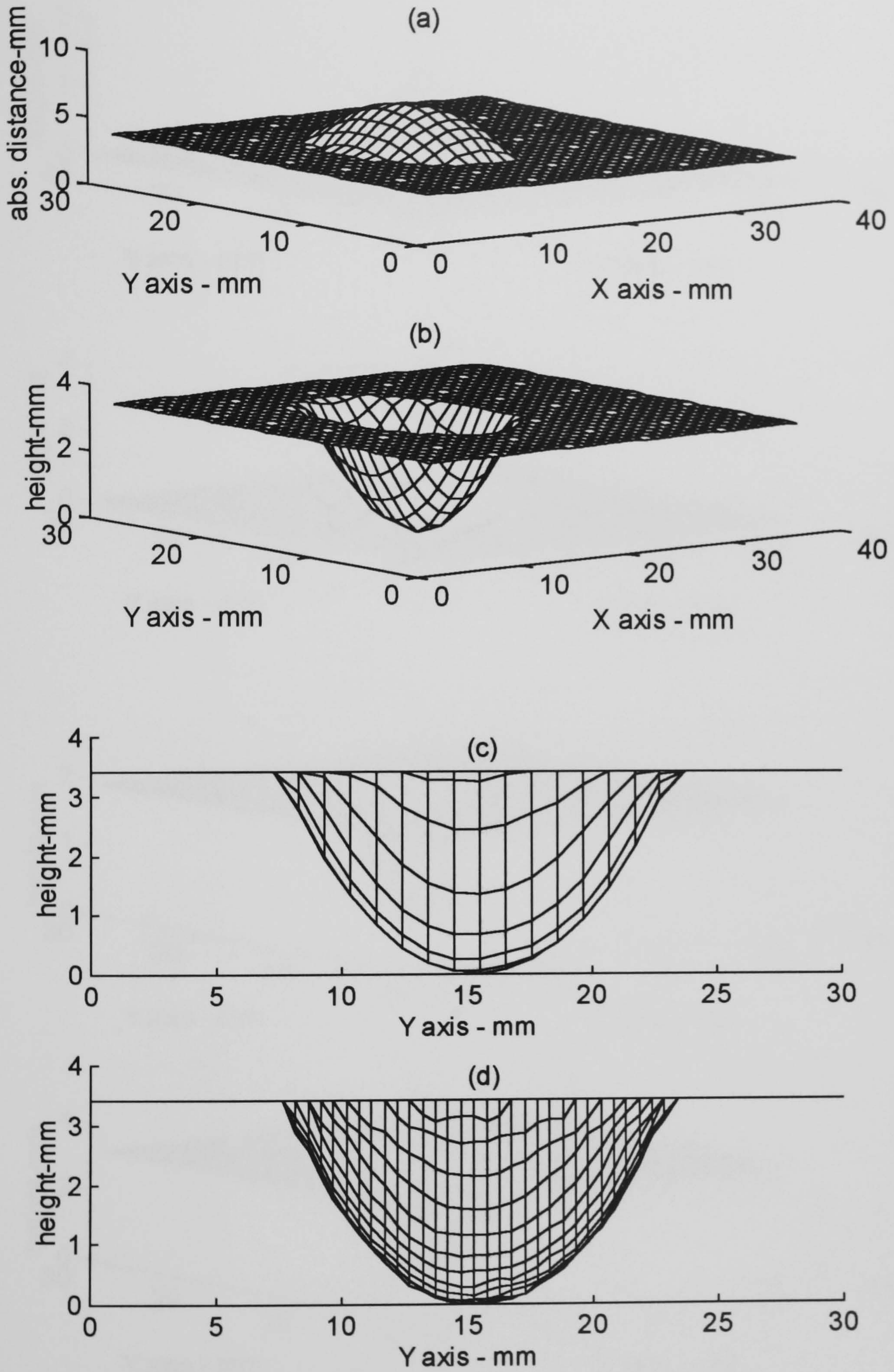

Figure 5.6 3-D Plots of Absolute Distance (a) and Height of Object Concave3 (b) Side View of the Object Height (c) and (d)

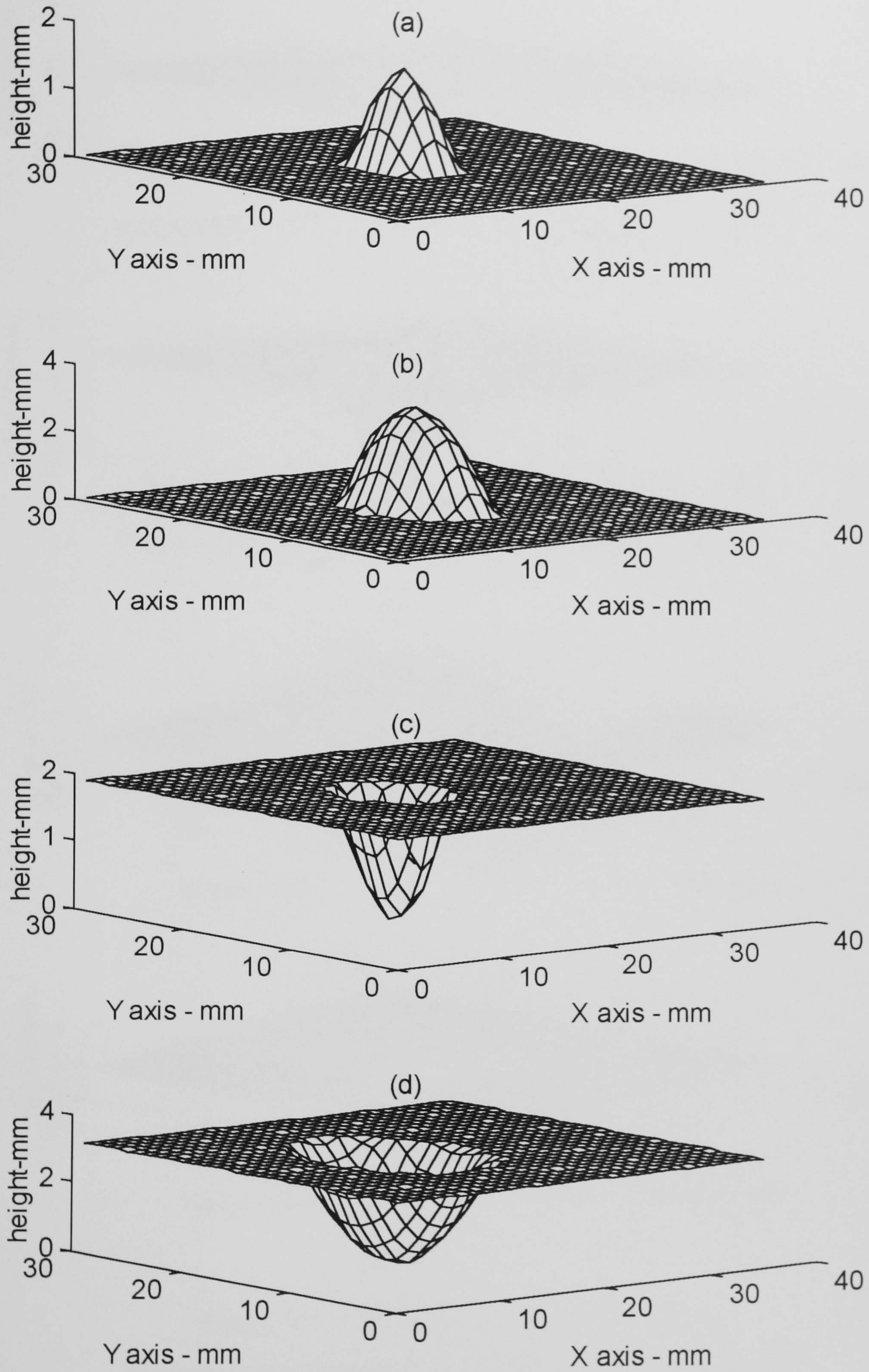
(a)
height-mm
2
1
0
30
20
10
0
Y axis - mm
0
10
20
30
40
X axis - mm
(b)
height-mm
4
2
0
30
20
10
0
Y axis - mm
0
10
20
30
40
X axis - mm
(c)
height-mm
2
1
0
30
20
10
0
Y axis - mm
0
10
20
30
40
X axis - mm
(d)
height-mm
4
2
0
30
20
10
0
Y axis - mm
0
10
20
30
40
X axis - mm

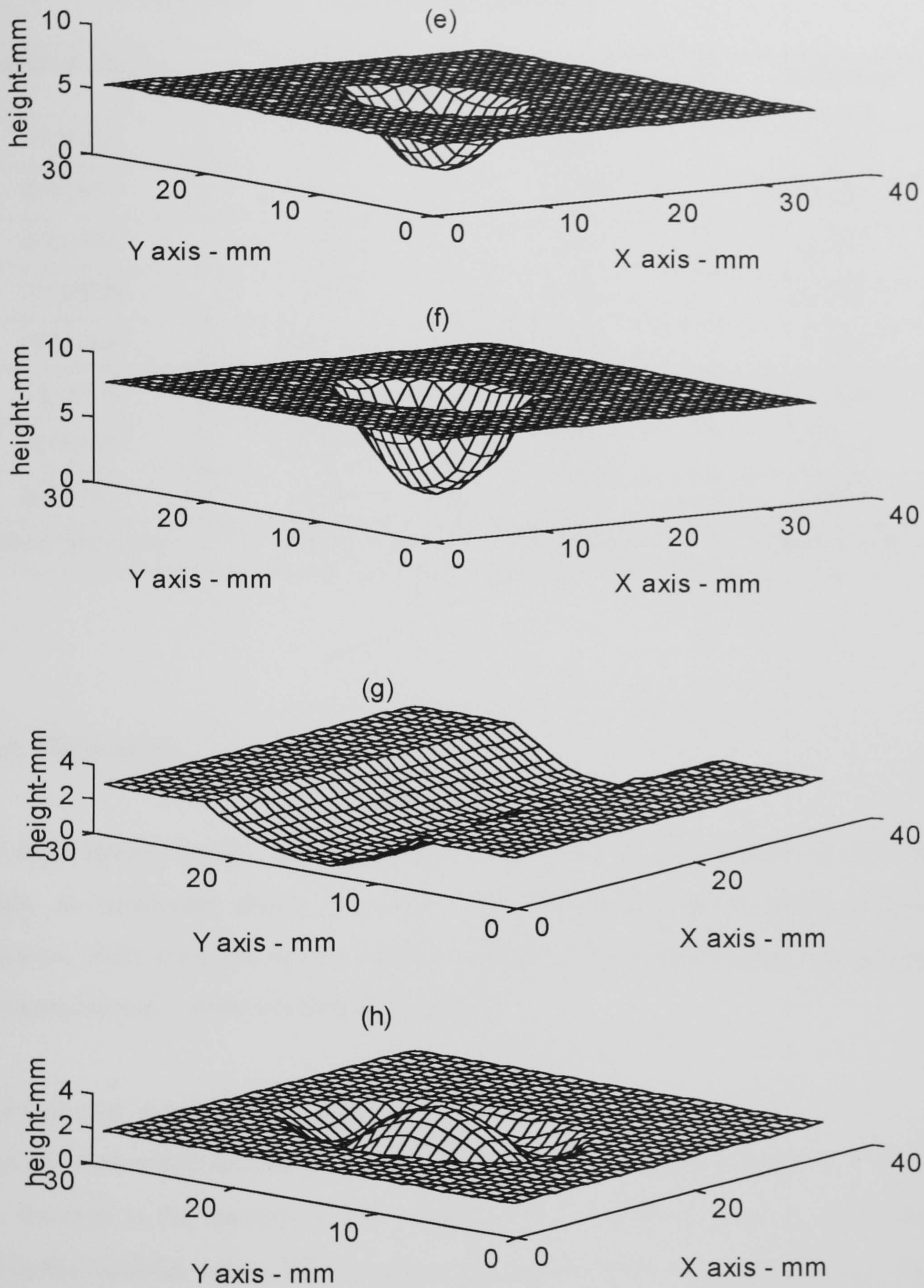

Figure 5.7 3-D Plots of the Test Objects

From (a) to (h) are convex1, convex2, concave1, concave2, concave4 concave5, groove, and concave&convex respectively

Table 5.3 Comparison of the Maximum Heights of the Objects Measured by Two Different Methods

shape of objects	height(mm) (contact method)	height(mm) (contour method)	Difference (mm)
convex1	1.470	1.461	+0.009
convex2	3.017	3.010	+0.007
concave1	1.858	1.865	-0.007
concave2	3.102	3.101	+0.001
concave3	3.417	3.421	-0.004
concave4	5.210	5.206	+0.004
concave5	7.600	7.578	+0.002
groove	2.661	2.668	-0.007
concave&convex	1.421/1.690	1.412/1.698	0.000/-0.008

5.4.3 Discussions

The experimental results for the different parameters of the system and the rotation angles, as mentioned above, are similar for all objects used in these experiments. However, there are a few factors which could affect the resolution and the accuracy of the measurement, which are discussed below.

(i) period and profile of the grating

From the theoretical analysis of the absolute distance contouring method, it is known that the data of the captured image contains a dc and high frequency components, as well as the required terms. The dc component can be easily removed from the signal as described in section 5.3.1, but the high frequency components will affect the results. Therefore, they should be removed as much as possible. The technique used to minimise the high frequency terms is to defocus the image before it is captured, and low-pass filter it after the image is stored in the VFG memory. Figure 5.5 shows two typical images of focused and defocused samples.

From equation (2-8), for the sinusoidal grating, there are three terms which are unwanted, with frequencies higher than that of the contour term. The unwanted terms could be removed using the method just described. For a sinusoidal grating, if the period of the grating is not too large, say less than 1.5mm, it is effective for minimizing the high frequency terms in this experiment. It is not easy to achieve when the period of the grating is larger than about 1.5mm. Test results have confirmed this conclusion, when a grating with a period of 1.8mm was used.

However, for the square wave grating, it is difficult to remove the unwanted terms from the whole signal. It can be seen, from equation (2-14), that the signal contains an infinite number of terms. Experience shows that, if the period of the square wave grating is small, say less than 1.0mm, it could be treated as a sinusoidal grating. The unwanted terms can be removed in the same way as that used for the sinusoidal grating. For square wave gratings with periods of 1.386mm and 1.800mm, the unwanted terms are difficult to remove. Although theoretically, if a square or circular aperture of certain dimensions is used with the square wave grating, the visibility of the primary fringes would be zero for certain values of θ and the unwanted modulation is zero, but it is not easy to achieve.

The period of the grating also has an effect on the resolution and accuracy of the measurement, which is related to the analysis of the minimum absolute distance given above. From equation (2-11), it can be seen that for a given absolute distance, geometrical parameters, and rotation angles, the fringe number is inversely proportional to the grating's period. For a given fringe number, the absolute distance is directly proportional to the grating's period. Table 5.4 lists the measured absolute distance values when different grating periods and values of z_0 are used, where y_s=100mm, $\theta_n = 15^\circ$, and fringe number n = 1.

The fringe number for different absolute distance and grating periods when $\theta_n = 30^\circ$, $z_0 = 420$mm and $y_s = 100$mm is given in table 5.5.

Table 5.4 The Measured Absolute Distance with Different z_0 and P_0 (unit-mm)

Z_0/P_0	0.508	0.763	0.985	1.360
320	6.407	9.720	12.660	17.747
370	7.407	11.239	14.638	20.520
420	8.400	12.758	16.616	23.293
470	9.400	14.277	18.595	26.066

Table 5.5 The fringe number for different z and P_0 (unit-mm)

Z/P_0	0.508	0.763	0.985	1.360
2.0	0.4665	0.3106	0.2458	0.1742
4.0	0.9285	0.6182	0.4789	0.3468
6.0	1.3863	0.9229	0.7149	0.5178
8.0	1.8397	1.2249	0.9488	0.6782
10.0	2.8890	1.5239	1.1805	0.8550
20.0	4.4738	2.9786	2.3073	1.6711

(ii) rotation angles

The measured absolute distance is inversely proportional to the rotation angle, θ_n, as analyzed in chapter two. For a given absolute distance and system parameters, the fringe number is directly proportional to the sinusoidal value of the rotation angle. When z_0=420mm, y_s=100mm, and fringe number, n=1, the measured absolute distance for different grating periods and rotation angles are listed in table 5.6. As described in section 5.3.1, the parameters and rotation angles should be carefully chosen for a given absolute distance to ensure that the fringe number, n(i,j), is greater than 0.5 in order to obtain correct results. If z_0=420mm, y_s=100mm and n=0.5, the minimum absolute distance, which can be measured, is the half of those values listed in table 5.6.

Table 5.6 The Measured Absolute Distance with Different θ_n and P_0 (unit-mm)

θ_n/P_0	0.508	0.763	0.985	1.360
15°	8.400	12.758	16.616	23.293
30°	4.311	6.508	8.440	11.743
60°	2.478	3.733	4.830	6.699
90°	2.142	3.229	4.178	5.792

(iii) the number of images

The total phase variation for pixel (i,j) is the sum of the individual phase differences obtained between steps, when the grating is rotated from zero to the selected rotation angle, θ_n. The accuracy of the complete measurement depends upon the accuracy obtained at each step. The phase difference between steps is determined by the parameters of the system, rotation angle and the absolute distance to be measured. Table 5.7 shows the fringe number, n, total phase variation, $\Delta\varphi$, and average phase change at each step, $\Delta\varphi_m$, when z_0 = 420mm, y_s = 100mm, P_0 = 1.0mm, z = 10mm and the image number is 21 for different rotation angles. If the phase difference between steps is too large, errors will result. For example, it may miss the maximum or minimum value of the cosine function. For this reason, the image number should be as large as possible. However, when the number of images is large, more computer memory is required to store the image data, and more time is needed for processing. The average phase change at each step, when the image number is 21, gives that z_0 = 420mm, y_s = 100mm, θ_n = 30°, for different gratings and absolute distance values, is listed in table 5.8.

Table 5.7 Fringe Number, Total Variation and Average Phase Change for Each Step

θ_n	n	$\Delta\varphi$	$\Delta\varphi_m$
15°	0.6019	216.68°	10.83°
30°	1.1628	418.60°	20.93°
60°	2.0140	725.04°	36.25°
90°	2.3256	837.21°	41.86°

Table 5.8 The Average Phase Change for Different P_0 and z (unit-mm)

Z/P_0	0.508	0.763	0.985	1.360
2.0	8.40°	5.59°	4.42°	3.14°
4.0	16.71°	11.13°	8.62°	6.24°
6.0	24.59°	16.61°	12.83°	9.32°
8.0	33.11°	22.05°	17.08°	12.37°
10.0	52.00°	27.43°	21.25°	15.39°
20.0	80.53°	53.61°	41.53°	30.08°

(iv) accuracy

It is known that the error of the measured absolute distance can be caused by inaccuracies in the parameters of the system and the rotation angle, as analyzed in chapter two. From these experiments, it was also found that, an imperfect grating and the remaining unwanted terms in the signal can also cause errors in the measured distance. All of these facts will affect the accuracy of the overall results.

In these experiments, the accuracy of the measured distance or the object height is better than 10μm, when compared with measurement made by the contact method. The maximum height of the objects, measured by the absolute distance contouring method and contact method, are listed in table 5.3. The height distribution along one central line of object concave3 and their difference measured by two methods are shown in figure 5.8.

From the above discussions, it can be concluded that the technique of absolute distance contouring, is an accurate method of measurement. To ensure the greatest accuracy, appropriate parameters of the system, rotation angle and image number should be chosen. For a given absolute distance and system parameters, a small rotation angle can reduce the fringe number and a large image number can reduce the average phase change between steps, such that the error of the measurement can be minimised.

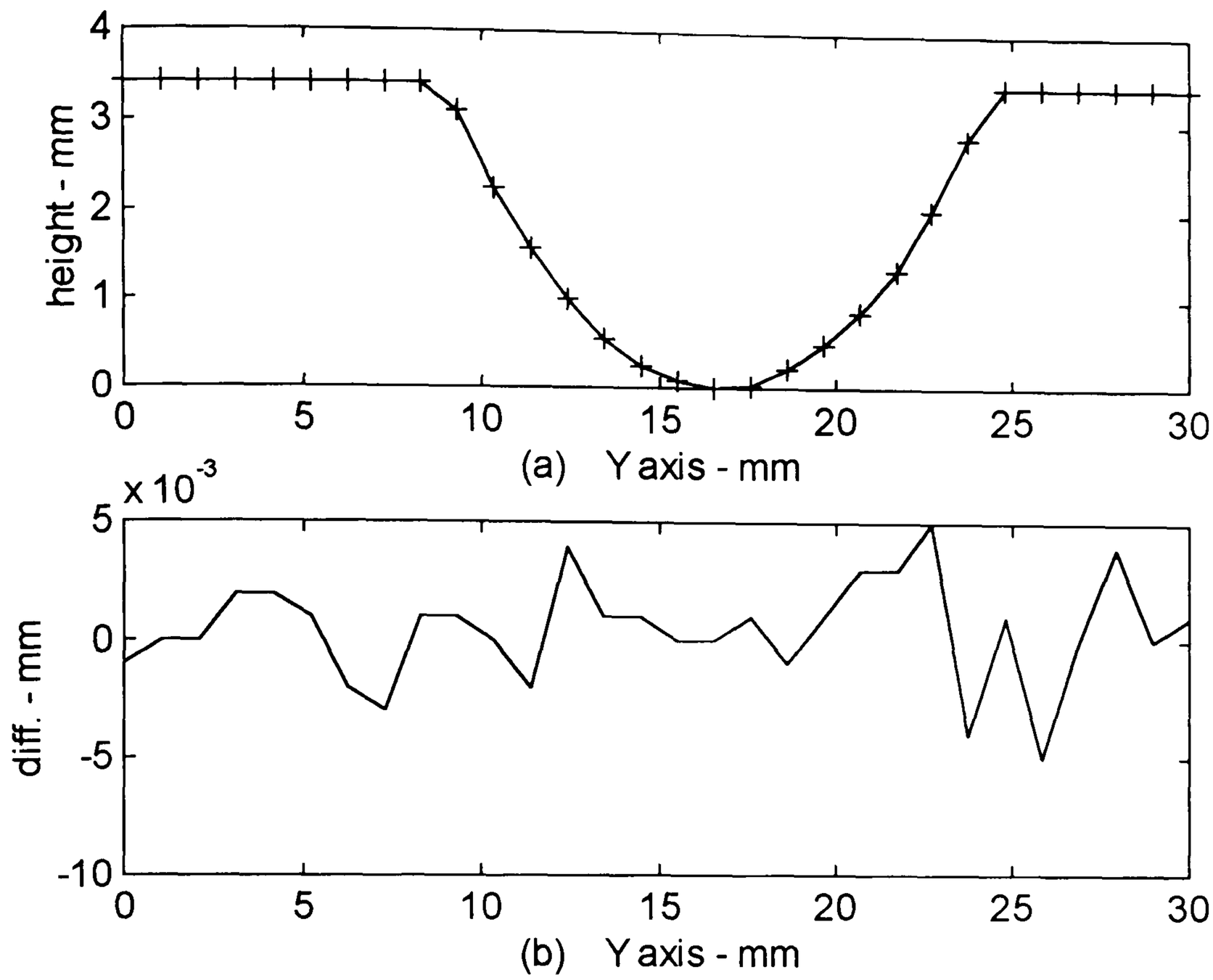

Figure 5.8 The Height Distribution Along One Central Line of Object Concave3 Measured by Two Methods and Their Difference (a) the height distributions obtained by contact method(+) and absolute distance contouring method (b) difference between contact and contour method

5.5 Experiments and Results of the Four-Image Contouring Method

In the experiments of the four-image contouring method, the grating used is a sinusoidal grating, its period being 0.763mm. The objects used in the experiments are concave1, concave3, convex1 and convex2. The distance from the grating to the camera, z_0, is 450mm and the distance between the camera and the light source, y_s, is 100mm. The four captured images are defocused and in a 64x64 pixel format. A 60x60 pixel format is used in the signal processing. The rotation angles used are $\theta_1 = 90°$, 60°, 45° and 30°, $\theta_2 = 60°$, 45°, 30° and 20° respectively. Angles θ_3 and θ_4 are determined by equations

(3-10) and (3-11), and the corresponding maximum measurable ranges calculated by equation (3-18), are listed in table 5.9.

Table 5.9 Rotation Angles and Measurable Ranges of the Four-Image Method

θ_1	θ_2	θ_3	θ_4	z_{max}(mm)
90.00°	60.00°	32.24°	23.55°	3.710
60.00°	45.00°	28.21°	18.29°	4.408
45.00°	30.00°	23.91°	11.43°	5.762
30.00°	20.00°	16.83°	7.56°	8.306

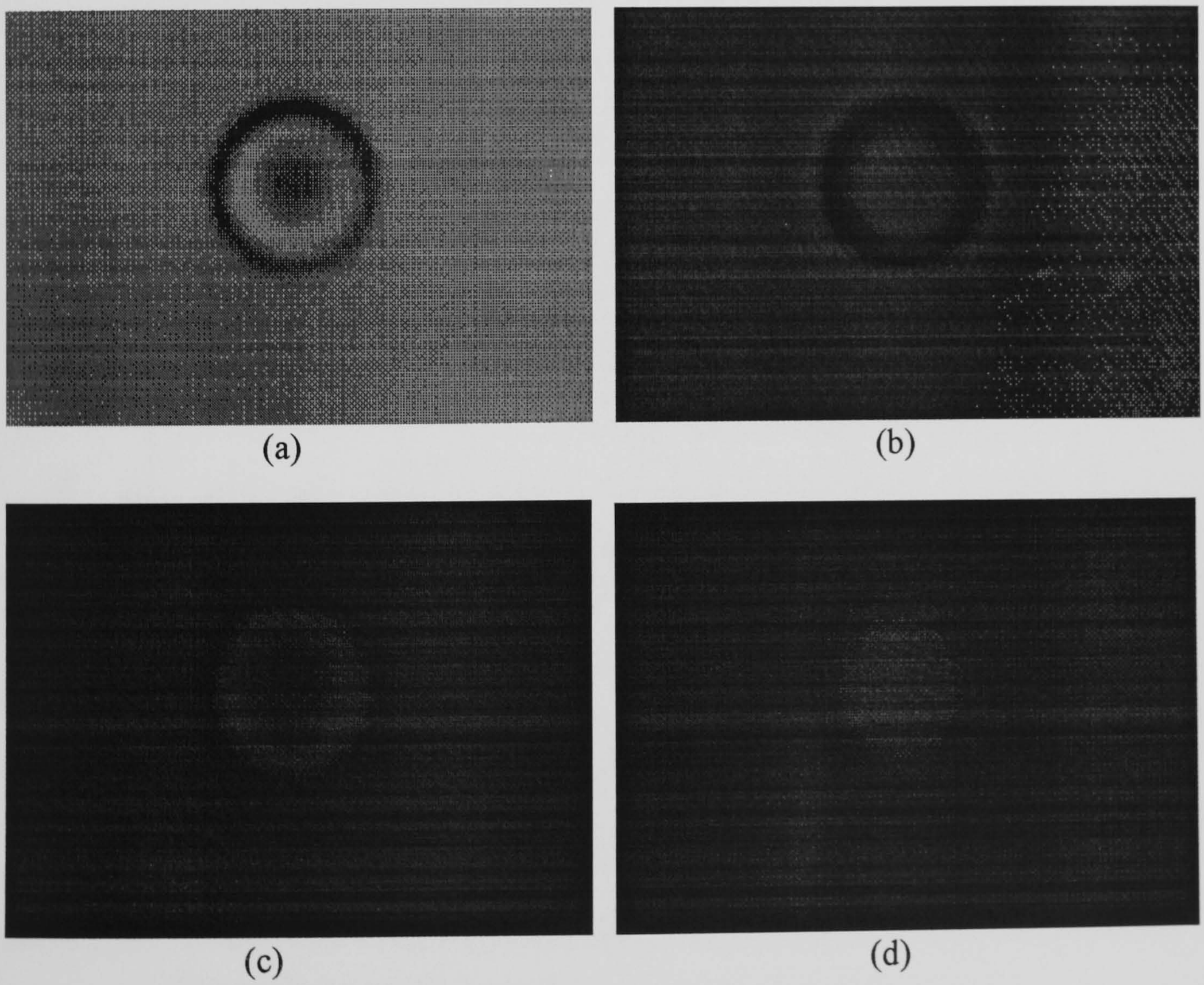

Figure 5.9 Images from Four-Image Absolute Distance Contouring when the grating is at (a) 90°, (b) 60°, (c) 32.24°, and (d) 23.55°

Figure 5.9 shows the four images captured when the grating is rotated to four different positions, determined by the values of the four rotation angles, where $\theta_1=90°$, $\theta_2=60°$, $\theta_3=32.24°$ and $\theta_4=23.55°$. The maximum heights of four objects measured by this method are concave1 - 1.858mm, concave3 - 3.417mm, convex1 - 1.472mm and convex2 - 3.019mm. The height distributions along one central line of object convex2, measured using the contact method(+) and four-image contouring method are shown in figure 5.10(a). Figure 5.10(b) shows the height difference between them. The results show that the difference between the height distributions and the maximum heights of the objects, obtained by the contact method and the four-image method, are within 10μm of each other.

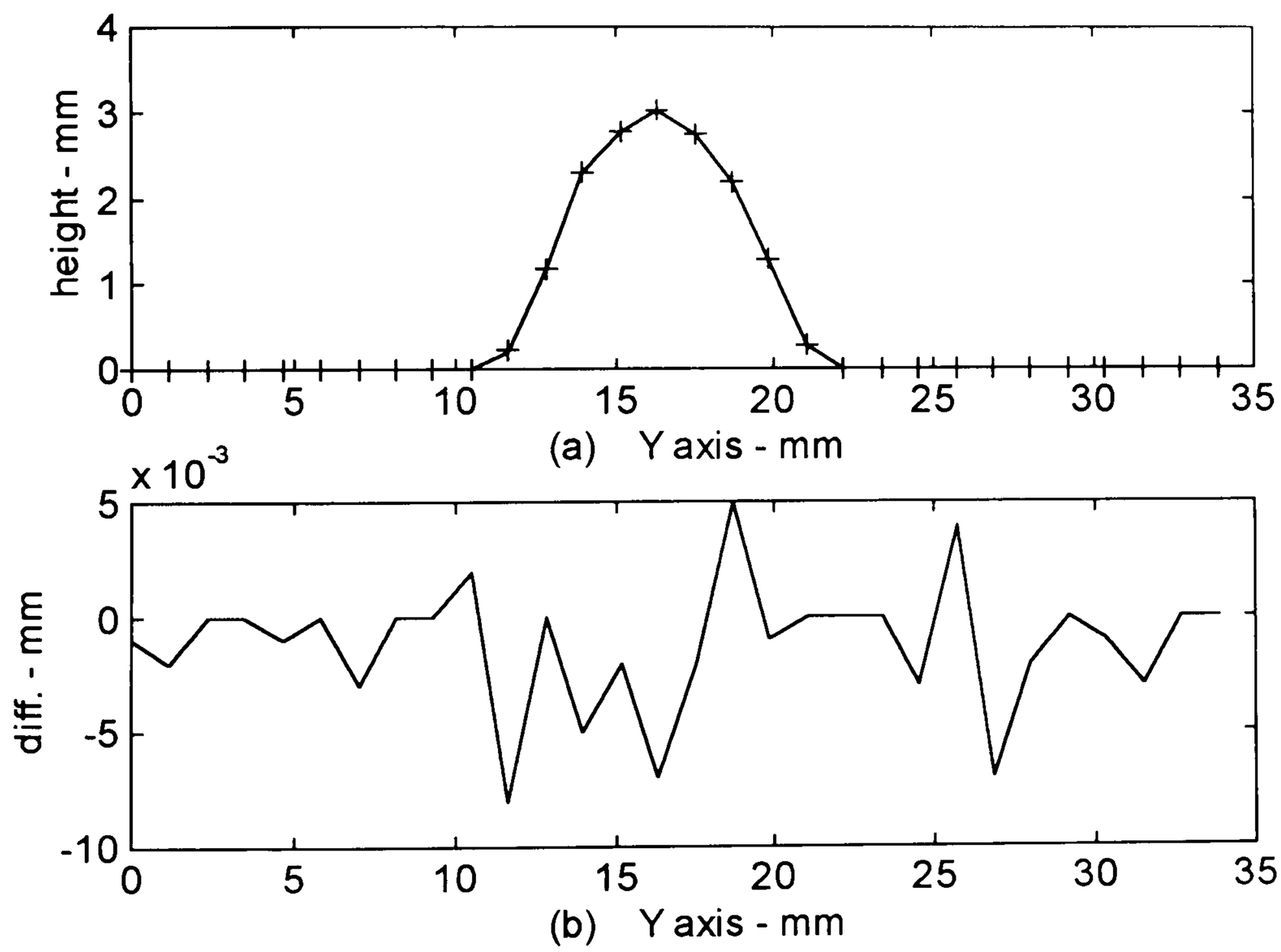

Figure 5.10 Height Distribution Along One Central Line of Object Convex2
(a) measured by contact method(+) and four-image methods
(b) the difference between the two methods

5.6 Experiments and Results of the Three-Image Contouring Method

The parameters of the experimental system for the three-image contouring method are set as, z_0=450mm, y_s=100mm, P_0=0.763mm. The objects used are concave1, concave3, concave4, convex1 and convex2. The rotation angles are set to θ'_1=90°, 60°, 45°, 30° and 20°. The rotation angles, θ'_2 and θ'_3, as determined by equations (4-9) and (4-10). The maximum measurable ranges, z'_{max}, obtained from equation (4-17) for different values of θ'_1, are listed in table 5.10.

Table 5.10 Rotation Angles and Measurable Ranges of the Three-Image Method

θ'_1	θ'_2	θ'_3	z'_{max} (mm)
90.00°	36.87°	11.54°	4.333
60.00°	31.31°	9.97°	5.011
45.00°	25.10°	8.13°	6.153
30.00°	17.46°	5.74°	8.751
20.00°	11.84°	3.92°	12.909

Figure 5.11 shows three images of object concave3 when the grating has been rotated to θ'_1=45°, θ'_2=25.10° and θ'_3=8.13° respectively. The height distribution along one central line of object concave3, measured by the contact method and the three-image contouring method, and their differences, are shown in figure 5.12.The maximum heights of the objects used in this experiment are concave1=1.862mm, concave3=3.421mm, concave4=5.215mm, convex1=1.469mm and convex2=3.019mm. Each measurement takes about three seconds.

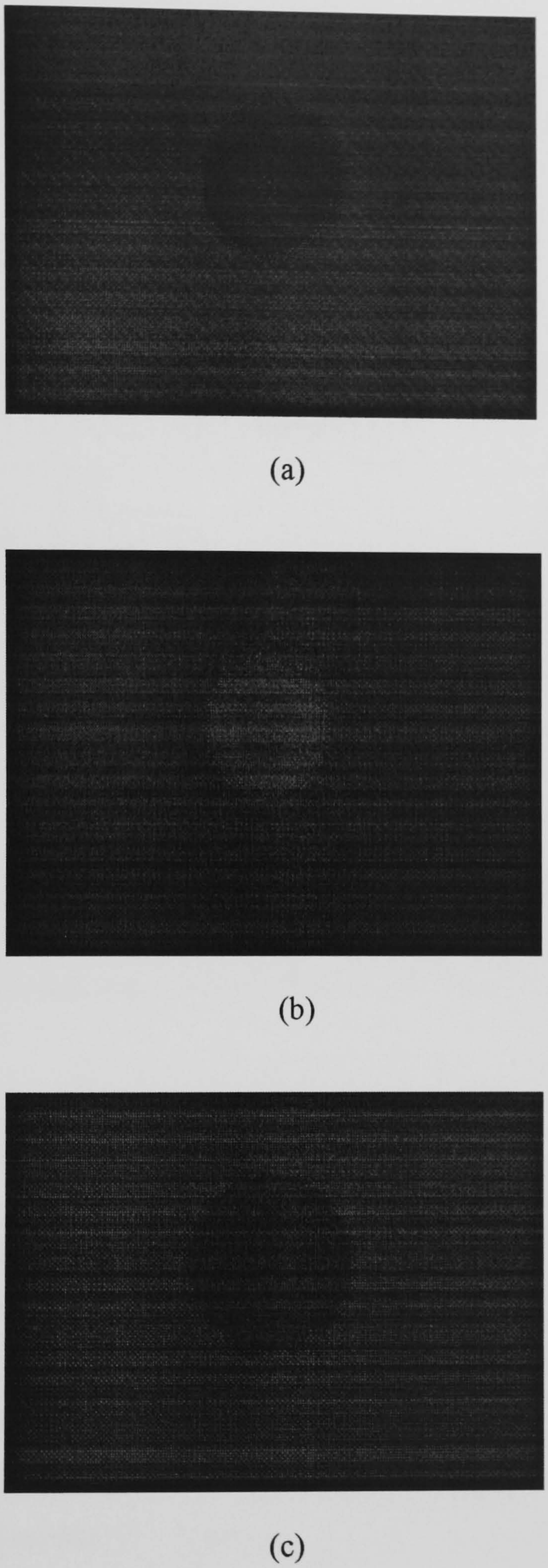

(a)

(b)

(c)

Figure 5.11 Images from Three-Image Absolute Contouring when the grating is at (a) 45.00° (b) 25.10° (c) 8.13°

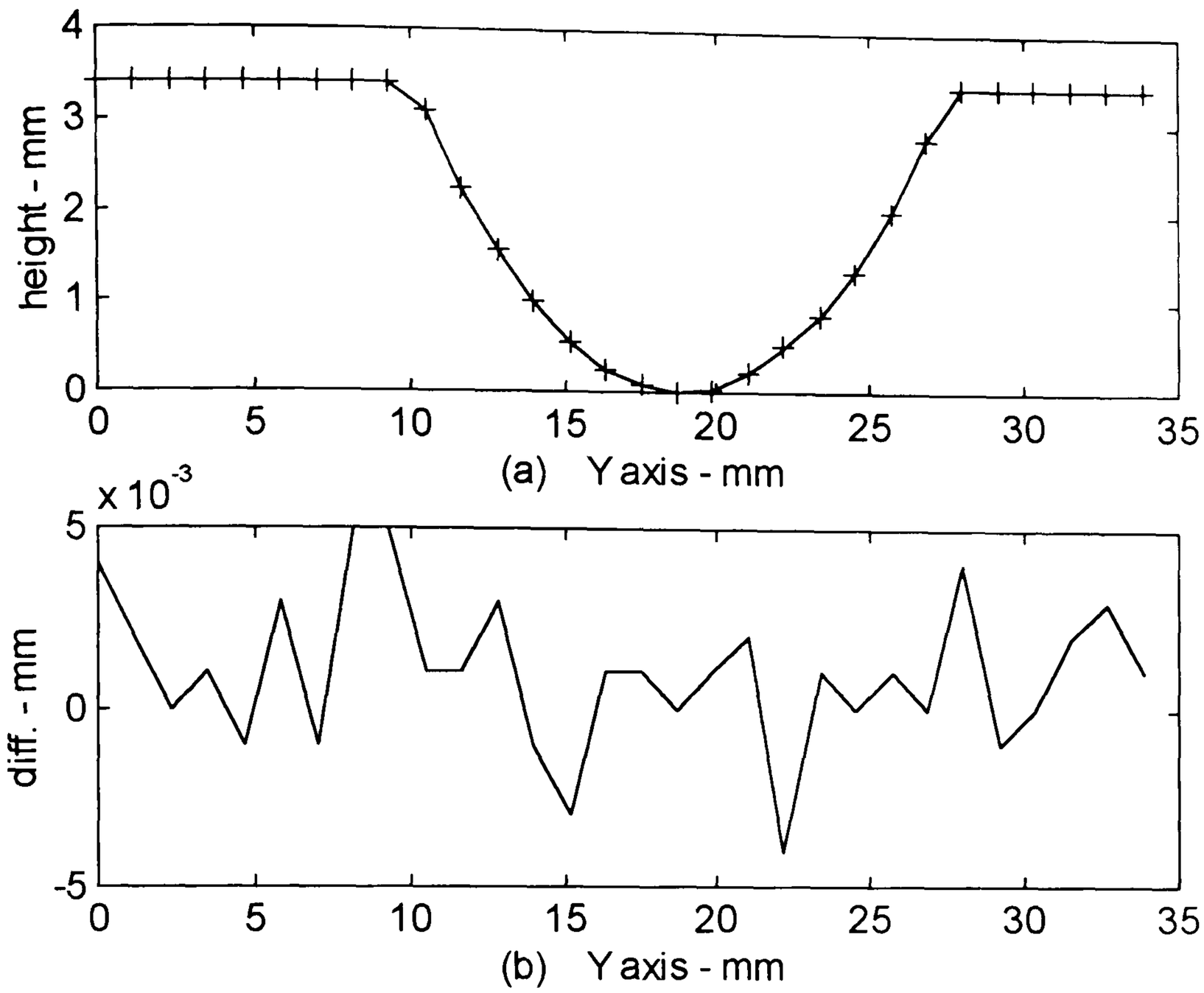

Figure 5.12 The Height Distribution Along One Central Line of Object Concave3, Measured by Contact(+) and Three-Image Methods and Their Difference

5.7 Summary

The experimental results of the three absolute distance contouring methods, as well as the factors which affect their accuracy, have been described in this chapter. All experiments were carried out using the same basic experimental system. The whole process is automated and controlled by specially designed software. Each method requires a different number of images for each measurement, resulting in a significant difference in the time needed for capturing images, data processing and computer storage. The absolute distance contouring method requires more images and takes significantly longer to process results than the four-image and three-image methods, but there is no maximum measurable limit. The period and profile of the grating and the rotation angles have an effect on the accuracy of the measurements obtained using each of the methods. The results from the three contouring methods show that the

difference between the maximum heights or height distributions along a central line of the object, obtained by the contact method and each of the three contouring methods, is less than 10μm. It can be concluded that these three new contouring methods are accurate and fast, and can be used for non-contact topographic measurement of engineering components in many applications.

Chapter 6

Comparison Between the Three Absolute Distance Contouring Methods

6.1 Introduction

The three different absolute distance contouring methods, as analysed in chapters two to four and reported in chapter five, are all based on the shadow moiré technique and the rotation of the grating. The three different absolute distance contouring methods have different features and individual requirements. This chapter will analyse and compare the contouring methods in terms of the relationships between the absolute distance and the parameters of the system, the rotation angles, maximum measurable ranges and the factors which affect the accuracy of each measurement.

6.2 Comparison Between the Three Absolute Distance Contouring Methods

Three absolute distance contouring methods are all based on the rotation of the grating such that its equivalent period is varied as a function of the rotation angle. Different relationships exist between the absolute distance, the parameters of the system, and rotation angles, resulting in different measurable ranges, for each method. Each is analysed and compared in terms of their common features and major differences.

6.2.1 Relationship between the Absolute Distance and the Parameters of the System

From the theoretical analysis of each of the contouring methods, three equations describe the relationship between the absolute distance to be measured and the distance from the grating to the camera, z_0, the distance between the light source and the camera, y_s, and the grating's period, P_0. They are expressed by equations (2-11), (3-15), and (4-14) respectively. The distance measured by each of the contouring methods, is directly proportional to z_0 and P_0, and inversely proportional to y_s.

However, the distance measured using the absolute distance contouring method also depends on the fringe number, which represents the total phase variation at the given measuring point when the grating is rotated through the rotation angle, θ_n. For the

four-image and three-image methods, the measured distance depends on the values of Φ and Φ' respectively. The equivalent fringe number given in equations (3-15) and (4-14) for each of these methods are $\Phi/2\pi$ and $\Phi'/2\pi$ respectively. The measured distance for specified parameters of z_0, y_s and P_0, is directly proportional to the fringe number, (or equivalent fringe number), for all three methods. However, the fringe number for a specified distance, as measured by the absolute distance contouring method, is directly proportional to $\sin\theta_n$, and the equivalent fringe number for the four-image and three-image methods are fixed values for a given absolute distance.

6.2.2 Rotation Angles

The three different contouring methods all depend upon the rotation of the grating to vary the phase distribution of the images. However, the relationships between the measured absolute distance and the rotation angles in each case, are different.

Using absolute distance contouring method, only one rotation angle is required to be chosen and the angle to be rotated in each step is decided by this chosen angle, θ_n, and the number of the images required for each measurement. It does not matter whether the angles rotated at each step are equal or not. In the four-image method, there are two angles to be chosen, the other two angles are determined by equations (3-10) and (3-11). There is only one angle to be chosen for the three-image method, the other two angles being determined by equations (4-9) and (4-10). This means that for the four-image and three-image methods, the grating must respectively be rotated to four and three exact positions. In the absolute distance contouring method, the only requirement is that the grating is rotated to the chosen angle exactly through N steps.

6.2.3 Measurable Ranges

The measurable ranges of each of the three different contouring methods are related to the optical arrangement of the system and the rotation angles. Theoretically, there is no measurable range limit for the absolute distance contouring method. This is because for

the given parameters, z_0, y_s, and P_0, the measured distance is directly proportional to the fringe number and inversely proportional to $\sin\theta_n$. Therefore, for a given distance to be measured, if the image number is large, a large rotation angle can be used. This will result in a large fringe number and corresponding small phase difference between steps, tending to limit the overall measurement error. If the number of images is limited, a small rotation angle should be chosen to limit the fringe number, the total phase variation, and the phase difference between steps. In this way, any errors caused by missing the maximum or minimum values of the consine function, as analysed in section 5.4.3, can be avoided. It should also be noted that the fringe number must be equal to or greater than 0.5.

There are measurable range limits for each of the four-image and three-image contouring methods. This is due to the relationship between the calculated absolute distance, the parameters of the experimental system, and the rotation angle(s) expressed by equations (3-15) and (4-14). As seen in the simulated results, the measured distance is a periodic function of the simulated absolute distance. As expressed in equations (3-18) and (4-17), the maximum measurable ranges are the values of the calculated absolute distance when Φ is at its maximum value given by equation (3-17) for the four-image method, and Φ' is at its maximum value given by equation (4-16) for the three-image method, respectively. The maximum measurable ranges for both methods are directly proportional to z_0 and P_0, and inversely proportional to y_s. The maximum measurable range is inversely proportional to the sum of the sinusoidal values of the first two rotation angles for the four-image method, and to the sinusoidal value of the first angle for the three-image method. If the first angle is given for the four-image method, the maximum measurable range for specified values of z_0, y_s and P_0, is decided by the value of the second angle. For the same value of the first angle, which method provides the maximum measurable range, depends upon the value of the second angle in the four- image method. For example, if z_0 = 450mm, y_s = 100mm, P_0 = 1.0mm, $\theta_1 = \theta'_1 = 90^\circ$, $\theta_2 = 30^\circ$, then z_{max} = 6.081mm and z'_{max} = 5.696mm. However, when $\theta_2 = 45^\circ$, z_{max} = 5.335mm. Figure 6.1(a) shows the maximum measurable ranges of the two methods when the first angle of each of the methods is varied from 20° to 90°, and the second angle for the four-image method is 30°, based

on the above parameters. When the first angle is 90° and the second angle is varied from 20° to 90°, the maximum measurable range using the four-image method is shown in figure 6.1(b).

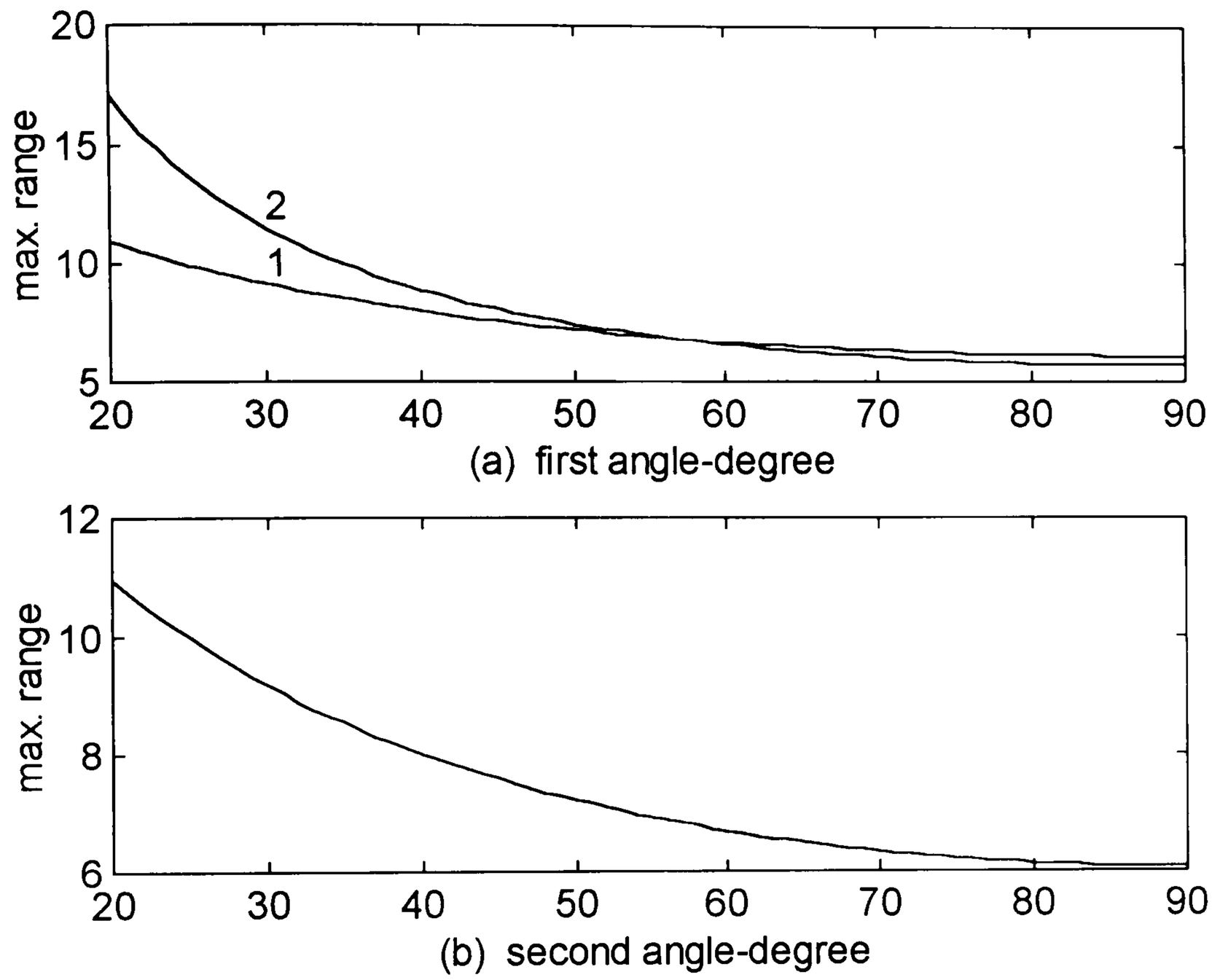

Figure 6.1 Variation of the Maximum Measurable Ranges of the Four-Image and Three-Image Methods with the Rotation Angle(s), when z_0 = 450mm, y_s = 100mm, P_0 = 1.0mm. (a) 1 - four-image method when $\theta_2 = 30°$ 2 - three-image method (b) four-image method when θ_1=90°

6.2.4 Factors Which Affect Measurement Accuracy

It should be noted that the measurement accuracy offered by all three methods, depends upon the accuracy of the system's parameters and the rotation angles. Similar relationships exist describing the accuracy of the measurement to the accuracy of the parameters, z_0, y_s and P_0. However, they are different for the rotation angles.

Only one sinusoidal function of the rotation angle, θ_n, given in equation (2-11), is used by the absolute distance contouring method. The difference in the measurement caused

by the error in the rotation angle, θ_n, is expressed by equation (2-28). In this method, the grating is rotated N steps from zero to the selected angle, and N+1 images are captured for each measurement. However, any errors in the angles at each successive step do not have any effect on the accuracy of the measurement. Calculation of the absolute distance is dependent on the grey level recorded at each pixel in the image. The inverse cosine function is used, so the absolute distance to be measured must be greater than that represented by half a fringe, as explained in section 5.4.3, otherwise significant errors will result. The number of images used in this method is a very important factor to ensure high accuracy. This is because for a given distance to be measured, system parameters, and rotation angle, the total phase difference is fixed, so that the average phase change between steps is inversely proportional to the image number. If the image number is small, the average phase change must be large, so that some of the peak values of the cosine function may be missed, resulting in errors. In essence, the greater the number of images used, then the better will be the accuracy.

The four-image method differs from the absolute distance contouring method by the relationship between the accuracy of the measurement and the rotation angles. As the image number is fixed, two of the four rotation angles are chosen, the other two being determined by equations (3-10) and (3-11). The corresponding four images are captured when the grating is rotated to these four positions. The measured distance is directly dependent on the grey levels at each pixel in the image. Any inaccuracy in angles will cause an error in distance measurement. The error analysis of the four-image method, given in section 3.4, showed that for the stated parameters of the system, the error in the measured absolute distance for the given angle inaccuracy is different for each of the first two rotation angles. Appropriate rotation angles should be chosen to reduce the error in the measurement.

The three-image contouring method is similar to that of the four-image method regarding the relationship between the measurement accuracy and the accuracy of the rotation angles. In this case, the image number is fixed at three. The first angle is chosen, the other two being determined by equations (4-9) and (4-10). Like the four-image method, calculation of the absolute distance relies on the values of the images' grey

level, and any inaccuracy in the three positions will produce an error in the result. This error will be different for different rotation angles for any given system parameters. Choosing suitable rotation angles, the error in the measurement can be minimised.

In addition, if the grating used in the system is not perfect, the images' intensity distributions will be affected. If the illumination of the system and the aperture of the camera are not correctly adjusted, for example, if the intensity of the illumination is too strong or too weak or the camera aperture is too large or too small, then the transmitted intensity through the sinusoidal grating, will be a distorted version, leading to an incorrect image intensity distribution. These facts would affect all contouring systems.

Table 6.1 Comparisons of Three Different Absolute Distance Contouring Methods

	absolute method	four-image method	three-image method
maximum measurable range	no limit $\propto Z_0\ P_0\ n$ $\propto \frac{1}{y_s}$ $\propto \frac{1}{\sin(\theta_n)}$	limited $\propto Z_0\ P_0$ $\propto \frac{1}{y_s}$ $\propto \frac{1}{\sin(\theta_1)+\sin(\theta_2)}$	limited $\propto Z_0\ P_0$ $\propto \frac{1}{y_s}$ $\propto \frac{1}{\sin(\theta'_1)}$
number of images	it is not fixed more better	4	3
memory needed	large(331KB)	small(234KB)	smaller(226KB)
measuring speed	slow(16 seconds)	fast(4 seconds)	faster(3 seconds)
factors which affect the accuracy	$\Delta Z_0\ \Delta P_0\ \Delta y_s$ $\Delta\theta_n$	$\Delta Z_0\ \Delta P_0\ \Delta y_s$ $\Delta\theta_1\ \Delta\theta_2\ \Delta\theta_3\ \Delta\theta_4$	$\Delta Z_0\ \Delta P_0\ \Delta y_s$ $\Delta\theta'_1\ \Delta\theta'_2\ \Delta\theta'_3$
accuracy	5μm	5μm	5μm

6.3 Summary

From the above analysis and comparisons, it can seen that each of the methods, has different relationships between the absolute distance and the parameters of the system.

the rotation angles, different maximum measurable ranges, and different accuracy effects based on errors in the rotation angles. Each method requires a different number of images so that the time taken for signal processing and data storage are different. The relationships between the measured absolute distance, the parameters of the system, and the rotation angles are listed in table 6.1.

Each of the contouring methods has its own advantages and disadvantages and can be used for different applications. Different methods and parameters can be chosen to ensure the highest accuracy and speed of measurement.

The characteristics of the three different contouring methods have been analysed and compared in this chapter. All three methods are based on the shadow moiré technique and the rotation of the grating to vary the images' intensity distribution and used to measure the absolute distance. Similar relationships exist between the absolute distance and the parameters, z_0, y_s, P_0, of the system for each of the three methods. However, the relationships between the absolute distance and the rotation angles, as well as the number of images required for each measurement, the maximum measurable ranges, and the factors which affect the accuracy of the measurement, are different in each case. Each method offers its own specific features and can be used to advantage in many situations.

Chapter 7

Phase Unwrapping in the Presence of Discontinuities

7.1 Introduction

Phase unwrapping is an important step in three-dimensional measurement using Fourier transform or phase shifting techniques, especially when there are discontinuities in the phase map. As described in chapter one, none of previous techniques seems to offer a perfect solution for the problem of discontinuities in the phase map. To solve this issue, it is proposed to use a phase unwrapping algorithm with the use of a crossed grating in the projection system. The crossed grating has two sets of lines in different directions so that two phase maps can be obtained, each with different precision. By using these phase maps, the correct object height distribution can be obtained , even in the presence of height steps. Only one image is required for each measurement using this technique, rather than those of four or more images required by other methods. The proposed algorithm has been verified by simulation and experiment as a fast algorithm which could be used for the measurement of object profiles with height steps, or phase maps with discontinuities caused by other reasons.

In the following section of this chapter, the basic principle of the Fourier transform method and phase unwrapping will be described. The crossed grating is described in section 7.3 and the details of the proposed phase unwrapping algorithm in the presence of discontinuities is explained in section 7.4. Section 7.5 details the simulation of the algorithm and the corresponding results obtained. Section 7.6 provides a summary of the chapter.

7.2 Principle of the Fourier Transform and Phase Unwrapping

7.2.1 Fourier Transform

In the fringe projection system, when a sinusoidal intensity grating or fringe pattern is projected onto an object's surface, the shadow of the grating deformed by the surface, can be expressed in the general form as follows:

$$I(x,y) = a(x,y) + b(x,y)\cos[2\pi f_0 x + \Phi(x,y)] \tag{7-1}$$

where $a(x,y)$ and $b(x,y)$ represent unwanted irradiance variations arising from the non-uniform light reflection or transmission by a test object; in most cases $a(x,y)$, $b(x,y)$ and $\Phi(x,y)$ vary slowly compared with the variation introduced by the spatial-carrier frequency f_0. The phase function $\Phi(x,y)$ characterizes the fringe deformation and is related to the object's shape $z = h(x,y)$.

The fringe pattern can be rewritten as:

$$I(x,y) = a(x,y) + c(x,y)\exp(2\pi i f_0 x) + c^*(x,y)\exp(-2\pi i f_0 x) \tag{7-2}$$

where $$c(x,y) = \frac{1}{2}b(x,y)\exp[i\Phi(x,y)] \tag{7-3}$$

Equation (7-2) is Fourier transformed with respect to x by the use of the Fast-Fourier-Transform (FFT) algorithm resulting in equation (7-4).

$$I(f,y) = A(f,y) + C(f - f_0,y) + C^*(f + f_0,y) \tag{7-4}$$

where $A(f,y)$ is the transform of $a(x,y)$, and $C(f - f_0,y)$ and $C^*(f + f_0,y)$ are the positive and negative frequency spectra of the modulated carrier fringes. As the spatial variations of $a(x,y)$, $b(x,y)$, and $\Phi(x,y)$ are slow compared with f_0, the function $I(f,y)$ will be a trimodal function with peaks at $-f_0$, f_0 and the origin. The function $C(f - f_0,y)$ can be isolated using a filter centered at f_0. The carrier frequency can be removed by shifting $C(f - f_0,y)$ by f_0 to the origin to give $C(f,y)$. From the inverse Fourier transform of $C(f,y)$ with respect to f, the phase distribution, $\Phi(x,y)$, can be obtained.

Assuming that the phase of the reference plane is $\Phi_r(x,y)$, then the phase distribution,

$\Phi_0(x,y)$, produced by the object's shape, $h(x,y)$, can be expressed as:

$$\Phi_0(x,y) = \Phi(x,y) - \Phi_r(x,y) \tag{7-5}$$

7.2.2 Phase Unwrapping

The phases obtained from equation (7-5) are indeterminate to a factor of 2π because the inverse tangent function is defined over a range from $-\pi$ to π. The full phase is given by:

$$\varphi(x,y) = \Phi_0(x,y) + 2n(x,y)\pi \tag{7-6}$$

where $n(x,y)$ is an integer which may be positive or negative.

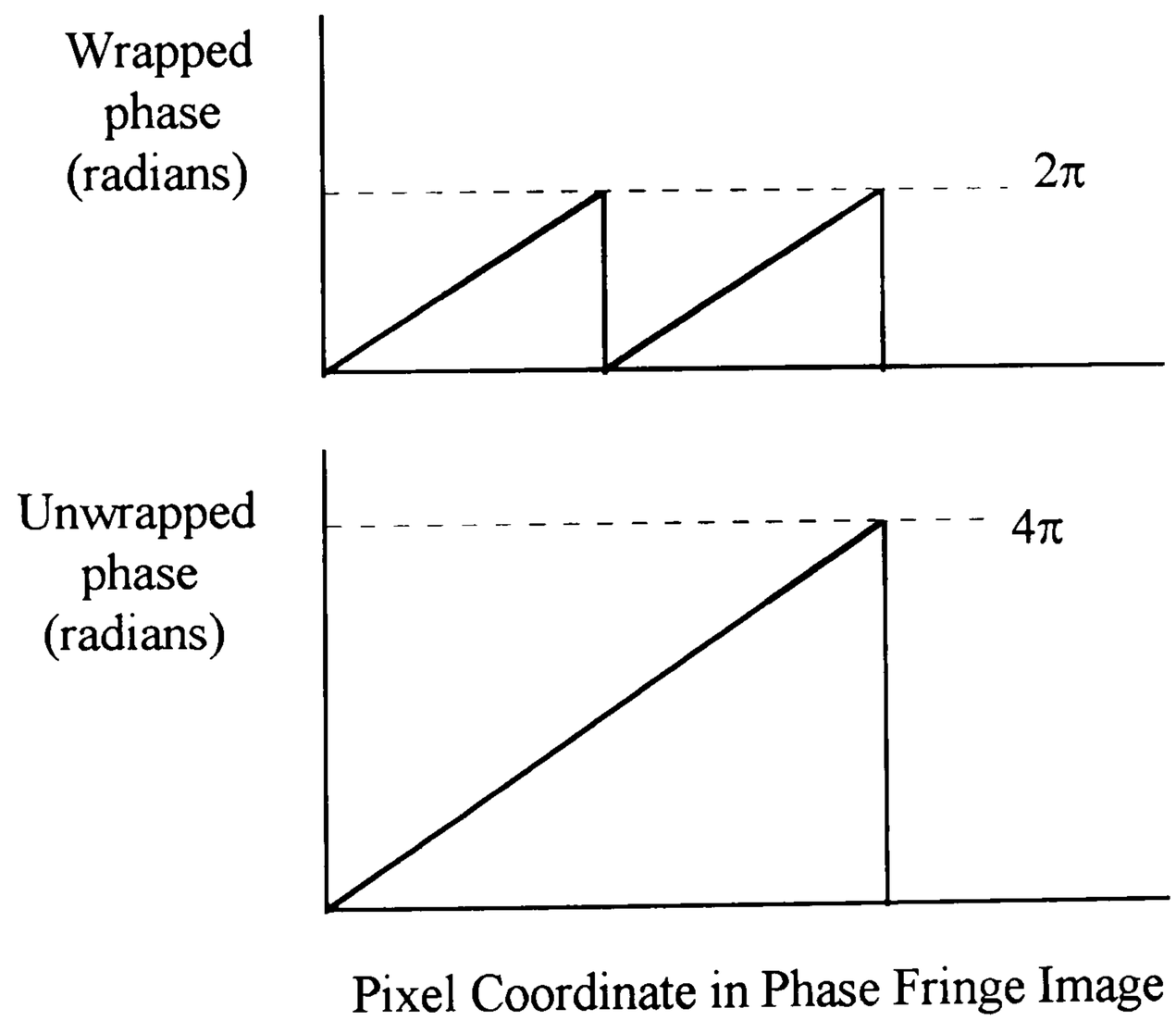

Figure 7.1 Wrapped and Unwrapped Phase

The whole purpose of phase unwrapping is to determine the value of $n(x,y)$ by comparing the phase values between adjacent pixels. Since the variation of the phase is slow compared with the sampling interval, the absolute value of the phase difference

between two adjacent pixels is much less than 2π, at points where the phase distribution is continuous. Therefore, it becomes almost 2π at points where the 2π phase jump occurs, as shown in figure 7.1. Hence, by setting an appropriate criterion for the absolute difference, all the points at which the 2π phase jump takes place and also the direction of each phase jump, positive or negative, can be specified.

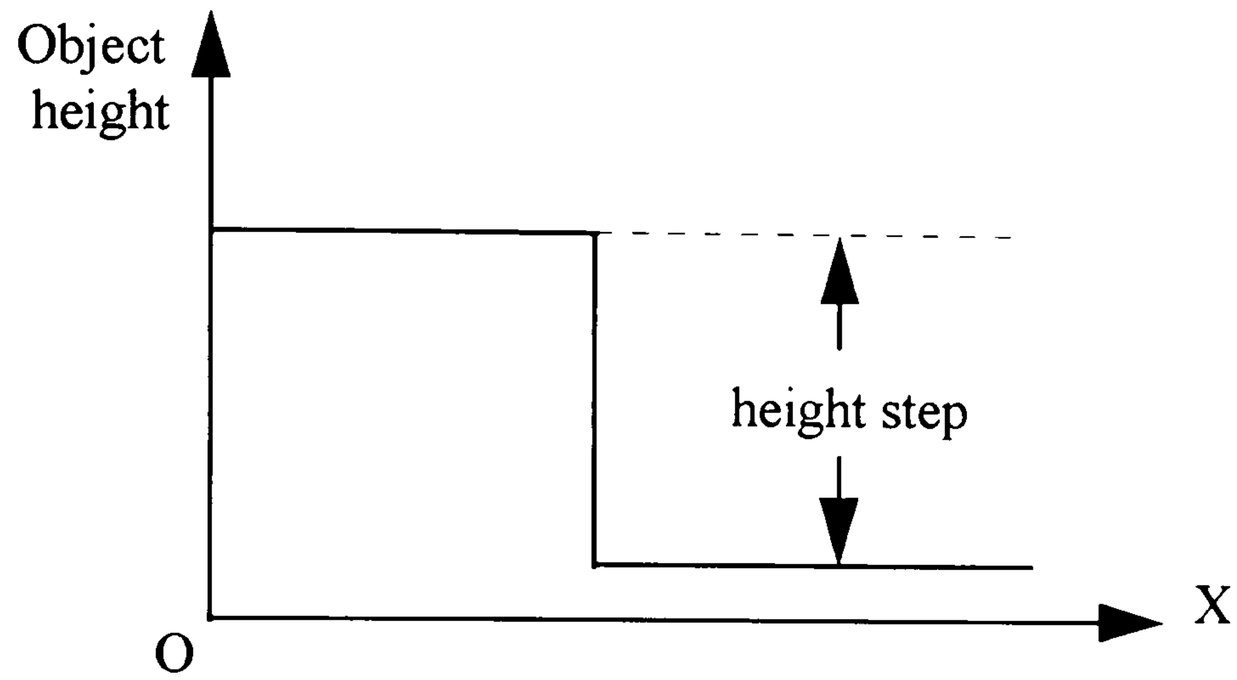

Figure 7.2 Object with a Height Step

The phase unwrapping routine described above can only specify the phase jump modulo 2π, when the phase distribution is discontinuous. If the phase jump is greater than 2π, correct phase unwrapping could not be obtained using this method. For example, if there are height steps to be measured on the object's surface as shown in figure 7.2, the corresponding phase jump may be $2n\pi$ for a certain period of grating used, where n is an integer greater than one. This means that it is not possible to determine how many fringes have been moved from the top of the step height relative to the bottom. Therefore, only adding 2π to the phase at that point is not sufficient to give the correct phase. Another problem is that as the phase value obtained using the inverse tangent function is in the range from $-\pi$ to π, it cannot be used to give the correct result for the cases given in figure 7.3. These show two images of the object with height steps, where figure 7.3(a) is when the phase jump between the two parts of the surface is less than π, it does not require phase unwrapping and the correct result can be achieved, as shown in figure 7.3 (c). However, in the case of figure 7.3 (b), the phase jump is bigger than π

but smaller than 2π, the correct phase value can still not be obtained. For example, if the phase jump in this case is from 0 to 1.2π, the phase jump calculated by the inverse tangent function is from 0 to -0.8π. One may set the appropriate criterion for the absolute phase difference to add 2π to the phase at the point of measurement to obtain the phase value of 1.2π, but it may not always be correct since it is not known what the exact phase jumps should be for different height steps.

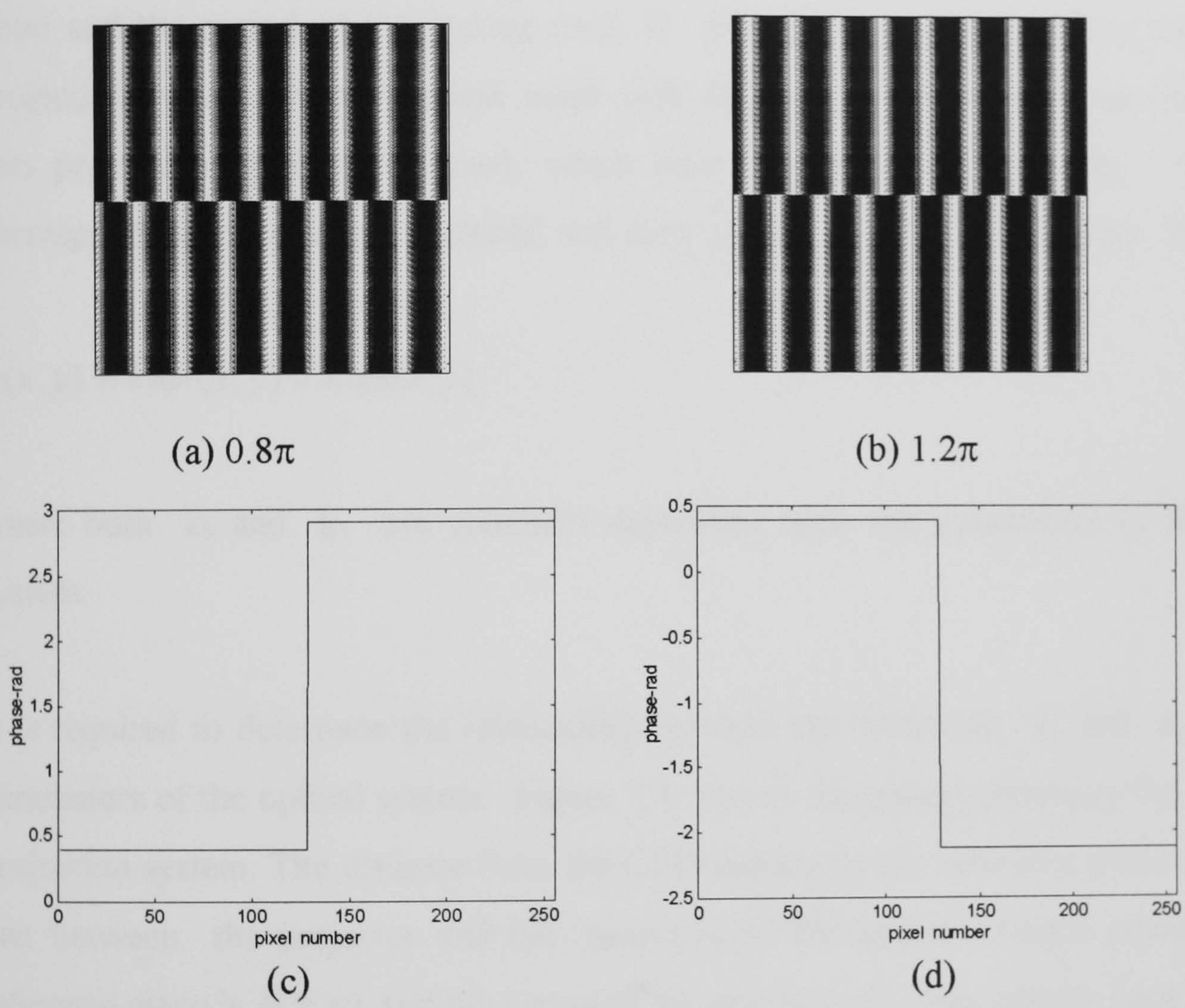

Figure 7.3 Fringe Patterns on an Object's Surface with Height Steps and the Corresponding Calculated Phase Distributions Along One Line

7.3 Phase Unwrapping in the Presence of Discontinuities

A method is needed to solve the problems previously described. From equation (7-1), it is seen that the value of phase $\varphi(x,y)$ is related to the object height distribution,

$h(x,y)$. This means that the relationship between the phase distribution and object height distribution can be expressed as:

$$h(x,y) = k\varphi(x,y) \tag{7-7}$$

where k is a constant which depends on the geometry of the optical system.

The values of phase at different points are dependent upon the object's height at each point and the period of the grating used. If different grating periods are used in the projection system, different phase maps with different precisions can be obtained. If two projection gratings are used, which have periods P_0 and P_1, then the corresponding phase maps obtained are $\varphi_0(x,y)$ and $\varphi_1(x,y)$ respectively. Therefore,

$$h(x,y) = k_0\varphi_0(x,y) = k_1\varphi_1(x,y) \tag{7-8}$$

where both k_0 and k_1 are constants depending upon the parameters of the optical system.

It is required to determine the relationship between the constants, k_0 and k_1, and the parameters of the optical system. Figure 7.4 shows the optical geometry for a general projection system. The distance from the CCD camera to the reference plane is L, and that between the projector and the camera is d. The object's height relative to the reference plane is $h(x,y)$ and the period of the grating is P_0. The grating lines projected onto the object or the reference plane are normal to the plane of the figure.

The difference in phase values between points C and D, φ_{CD}, observed by the same camera, can be related to the geometric distance AC as follows:

$$AC = \frac{P_0}{2\pi}\varphi_{CD} \tag{7-9}$$

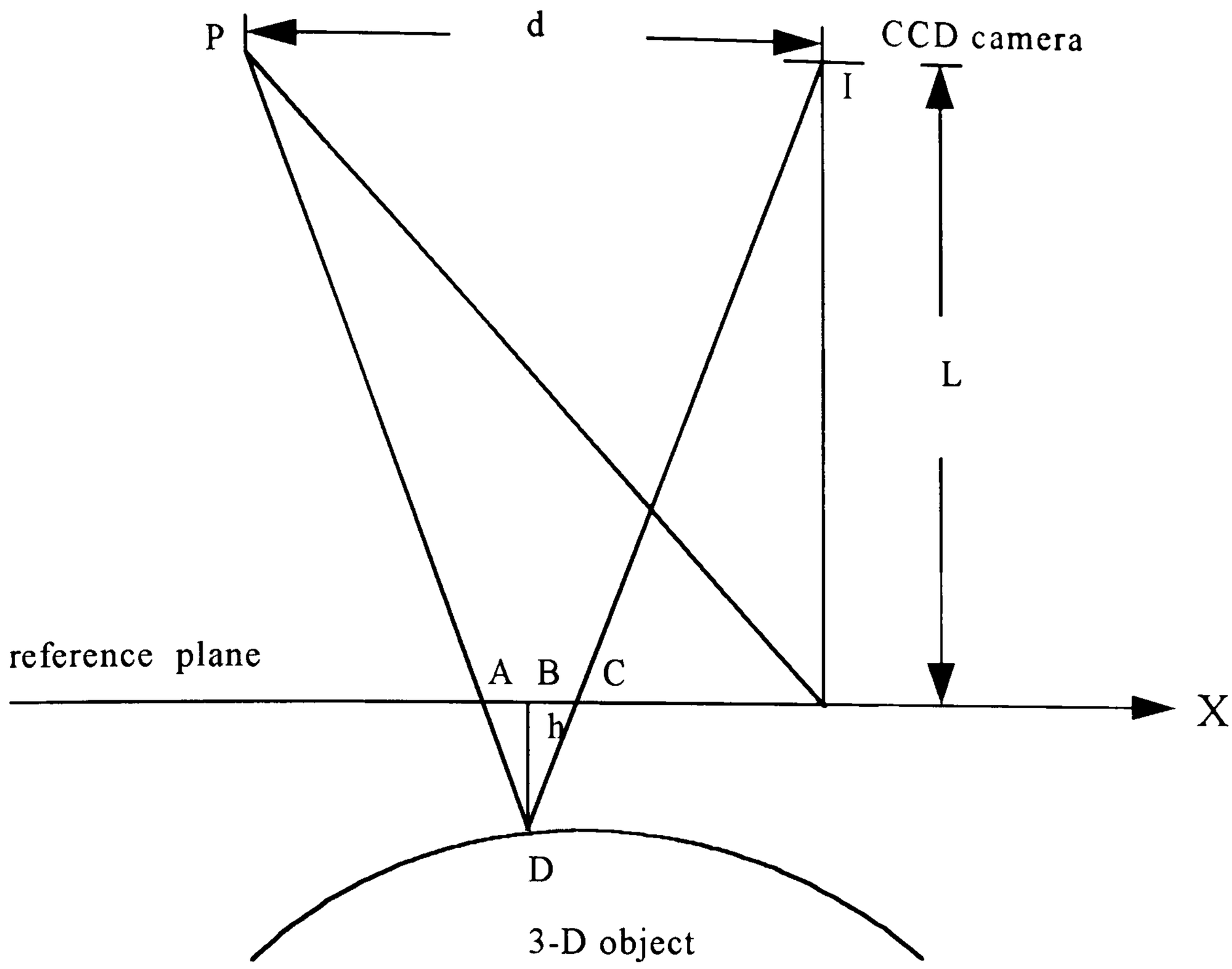

Figure 7.4 Optical Geometry of a General Projection System

From the relationship between the triangles, ACD and IDP, the object's height can be expressed as:

$$h(x,y) = \frac{AC}{d - AC} L = \frac{AC}{d\left(1 - \frac{AC}{d}\right)} L \tag{7-10}$$

Since for most cases, d >>AC, equation (7-10) can be simplified to:

$$h(x,y) = \frac{AC}{d} L = \frac{P_0 L}{2\pi d} \varphi_{CD} \tag{7-11}$$

From equation (7-9), coefficients, k_0 and k_1, are determined as:

$$k_0 = \frac{P_0 L}{2\pi d} \tag{7-12}$$

$$k_1 = \frac{P_1 L}{2\pi d} \tag{7-13}$$

Substituting equations (7-12) and (7-13) into equation (7-8), the phase values at the same point for different grating periods, results in equation (7-14):

$$\frac{\varphi_0(x,y)}{\varphi_1(x,y)} = \frac{P_1}{P_0} = \frac{f_0}{f_1} \tag{7-14}$$

where f_0 and f_1 are the spatial frequencies of the gratings with periods P_0 and P_1, respectively.

Equation (7-14) indicates that the phase value for the same object height is inversely proportional to the period of the grating, or is directly proportional to the spatial frequency of the grating. This confirms that, with the projection method and by using different grating periods, the phase maps obtained will have different precisions. Therefore, the shape of the object with height steps can be correctly measured by using two gratings having different periods in the projection system to obtain two phase maps with different sensitivities. To obtain the correct phase distribution from the two phase maps requires a comparison of the phase differences between corresponding pixels for each of the phase maps. This is explained in sections 7.3.1 and 7.3.2.

7.3.1 Phase Jumps Less Than 2π

As described above, when the phase jump is between π and 2π, the correct phase values may be obtained by the use of the normal phase unwrapping algorithm, but a correct result is not always guaranteed. Using the two phase map technique, it is

assumed that the periods of the two gratings used in the projection system are P_0 and P_1, and further that $2P_0 < P_1$. The phase jumps, between adjacent sample points, (i, j) and (i+1, j), are $\Delta\varphi_0$ and $\Delta\varphi_1$ for the two phase distributions respectively. So for the true phase jump, if $\pi < |\Delta\varphi_0| < 2\pi$, then:

$$\Delta\varphi_1 = \frac{P_0}{P_1}\Delta\varphi_0 < \pi \tag{7-15}$$

When $|\Delta\varphi_1| \geq (P_0 / P_1)\pi$ and $(\Delta\varphi_1 / \Delta\varphi_0) < 0$, this means the real phase jump is in the range of π to 2π, so that $\pm 2\pi$ should be added to the phase values for all the sample points which have an index number greater than i as follows:

$$\varphi(x_{i+1}, y_j) = \varphi_0(x_{i+1}, y_j) \pm 2\pi \tag{7-16}$$

Here the sign is decided by the sign of $\Delta\varphi_0$ and $\Delta\varphi_1$. For example, if $\Delta\varphi_0 < 0$ and $\Delta\varphi_1 > 0$, 2π should be added, and if $\Delta\varphi_0 > 0$ and $\Delta\varphi_1 < 0$, then -2π should be added. This is related to the direction of the height steps. Using this method the error can be corrected.

7.3.2 Phase Jumps Greater Than 2π

When the real phase jump between two adjacent sample points is greater than 2π, the correct phase value is obtained by firstly going through the procedure for the condition when the phase jump is in the range of π to 2π as the phase jump may be in the range of $(2n+1)\pi$ to $2(n+1)\pi$. Then the phase difference between two adjacent sample points in the phase map, obtained from the projection of the grating with a period of P_1, is calculated. If the absolute value of the phase difference, $|\Delta\varphi_1|$, is greater than $2(P_0 / P_1)\pi$, then the integer value of $n(x, y)$ is calculated as follows:

$$n = INT\left(\frac{\Delta\varphi_1 P_1}{2\pi P_0}\right) \tag{7-17}$$

where INT is an operator to obtain the integer value. The integer value obtained is less than or equal to the absolute value in the brace.

After obtaining the value of n, $2n\pi$ is added to the phase value of $\varphi(x,y)$ for all sample points which have an index number bigger than i as follows:

$$\varphi(x_{i+1},y_j) = \varphi(x_{i+1},y_j) + 2n\pi \tag{7-18}$$

Note that in the above equation, the calculation is only valid for phase jumps of less than or equal to $(P_1 / P_0)\pi$, with a grating period of P_0.

7.4 Use of a Crossed Grating

From the above analysis, it is clear that a simple method of utilizing two phase maps with different sensitivities is required. Although Zhao has studied a method to obtain the required two phase maps [Zhao 1994], using his method a total of eight images are required and accurate grating translation is needed because they use a phase shifting technique. To simplify the process of the measurement, it is proposed to use a crossed grating which has two sets of lines in different directions so that only one image is required for the measurement and no movement of the grating is necessary. It is more convenient and suitable for many applications in which vibration or other movements may occur.

If two fringe patterns with the same spatial frequency but at an angle, α, to each other, are added together, a crossed fringe pattern is formed. If the pattern is viewed along a single direction, the equivalent periods of the two sets of lines will be different. Figures 7.5 (a) and (b) show two separated fringe patterns with lines in the vertical direction and at an angle, α, relative to the vertical direction. Figure 7.5 (c) shows the sum of figures 7.5 (a) and (b). If the original period of the two fringe patterns is P_0, then in the case of (a), the period along the X direction is still P_0. However, in the case of (b), the equivalent period in the X direction is given as:

$$P_1 = \frac{P_0}{\cos\alpha} \tag{7-19}$$

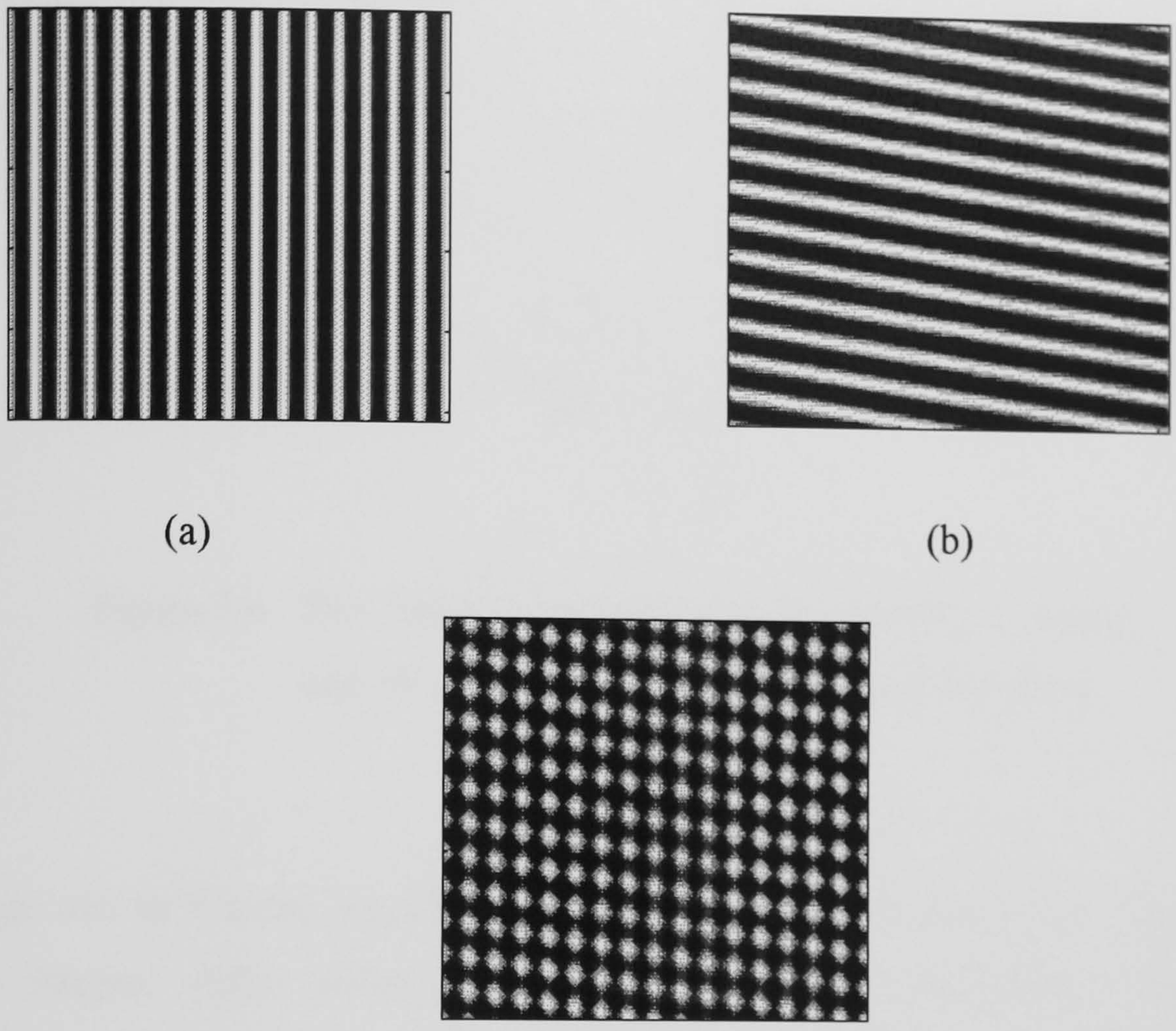

(a) (b)

(c)

Figure 7.5 Single Direction Fringe Patterns (a) and (b) and the Equivalent Crossed Fringe Pattern (c)

This relationship is shown in figure 7.6. If this crossed grating is projected onto the object, the deformed grating image is equal to the superposition of the two individual grating images projected separately. The corresponding spatial frequencies of the two equivalent gratings in the X direction are:

$$f_0 = \frac{1}{P_0} \tag{7-20}$$

$$f_1 = \frac{\cos\alpha}{P_0} \tag{7-21}$$

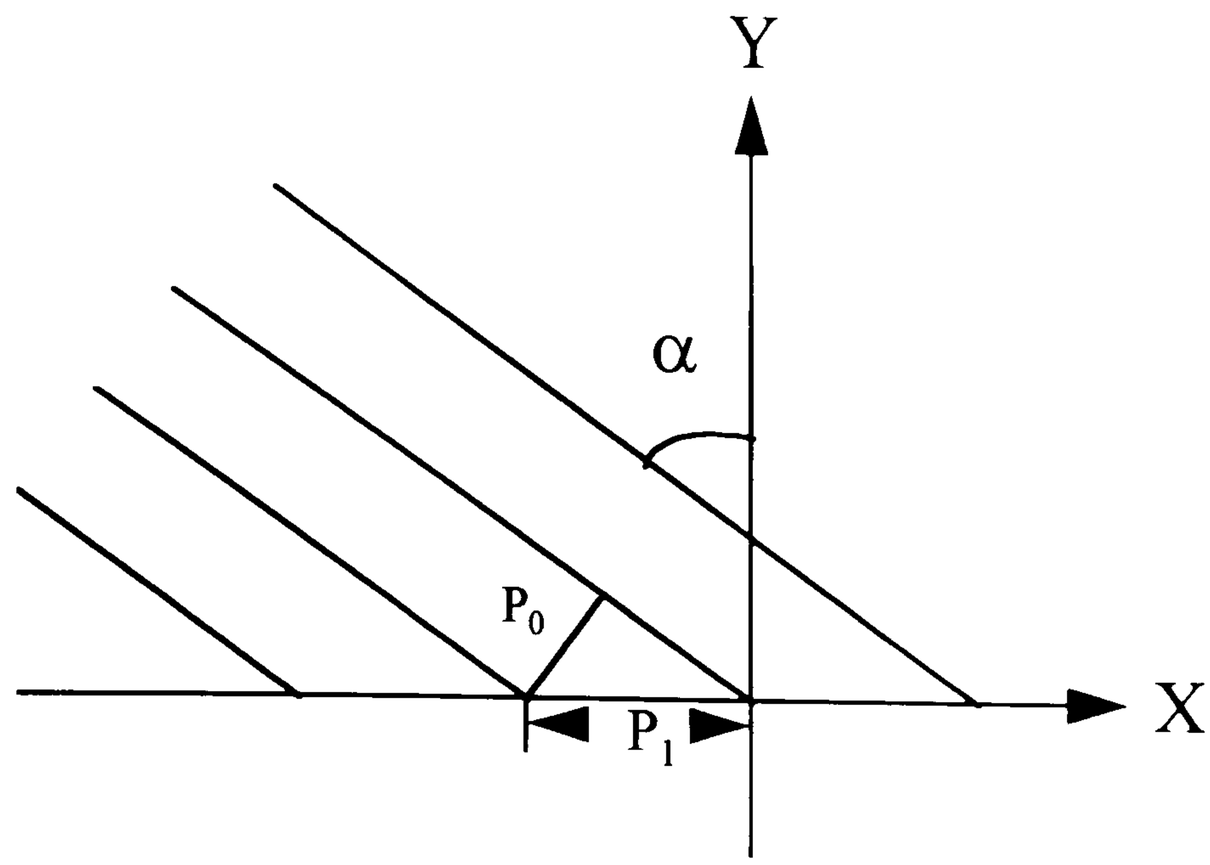

Figure 7.6 The Relationship Between the Grating's Period and the Equivalent Period in the X Direction

The image can be Fourier transformed and separated in the frequency space as two separate images. After performing the inverse Fourier transform, two phase distributions which have different sensitivities are obtained and the correct phase values at each sample point can be determined by the procedures described above.

7.5 Simulation of the Crossed Grating System

To verify the method of using a crossed grating in the projection system and the Fourier transform, as described above, a program was designed to simulate an object with a height step, with a crossed grating projected onto its surface. The simulated three-dimensional object is shown in figure 7.7, which has a height step in the horizontal direction. The simulated crossed grating is the sum of the two sets of lines. The periods of the gratings are P_0 and P_1 respectively, along the horizontal direction where $P_1 = 8P_0$. The phase jump caused by the step height obtained by the grating with a period of P_0, should be -5.6π.

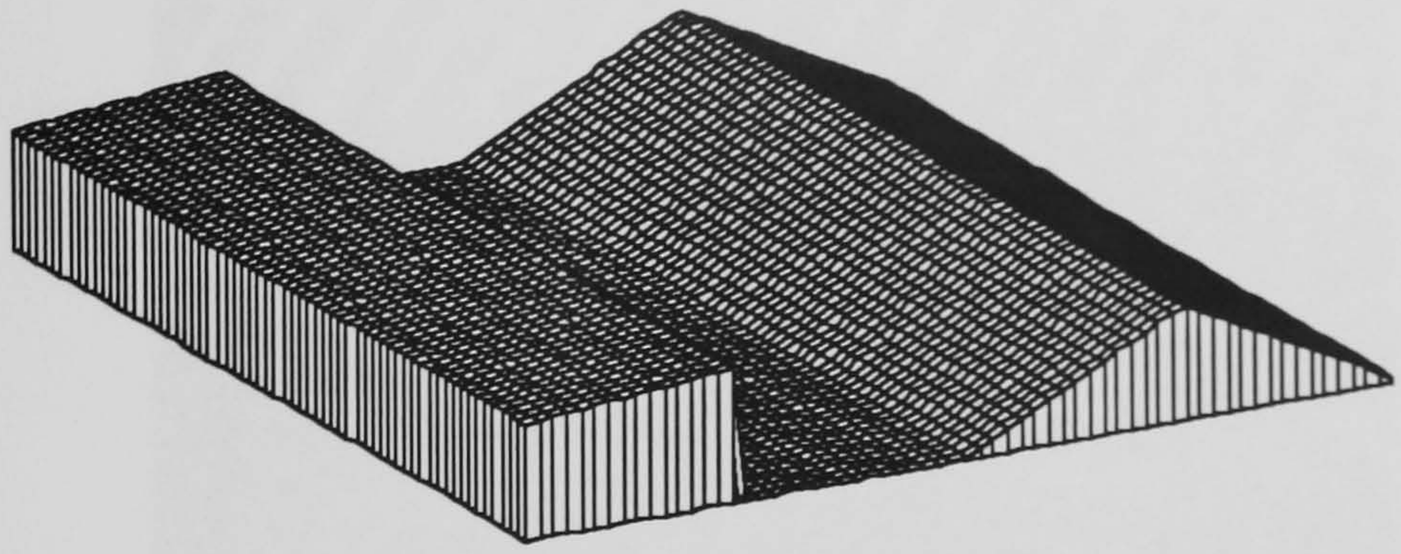

Figure 7.7 The Simulated Object with Height Step

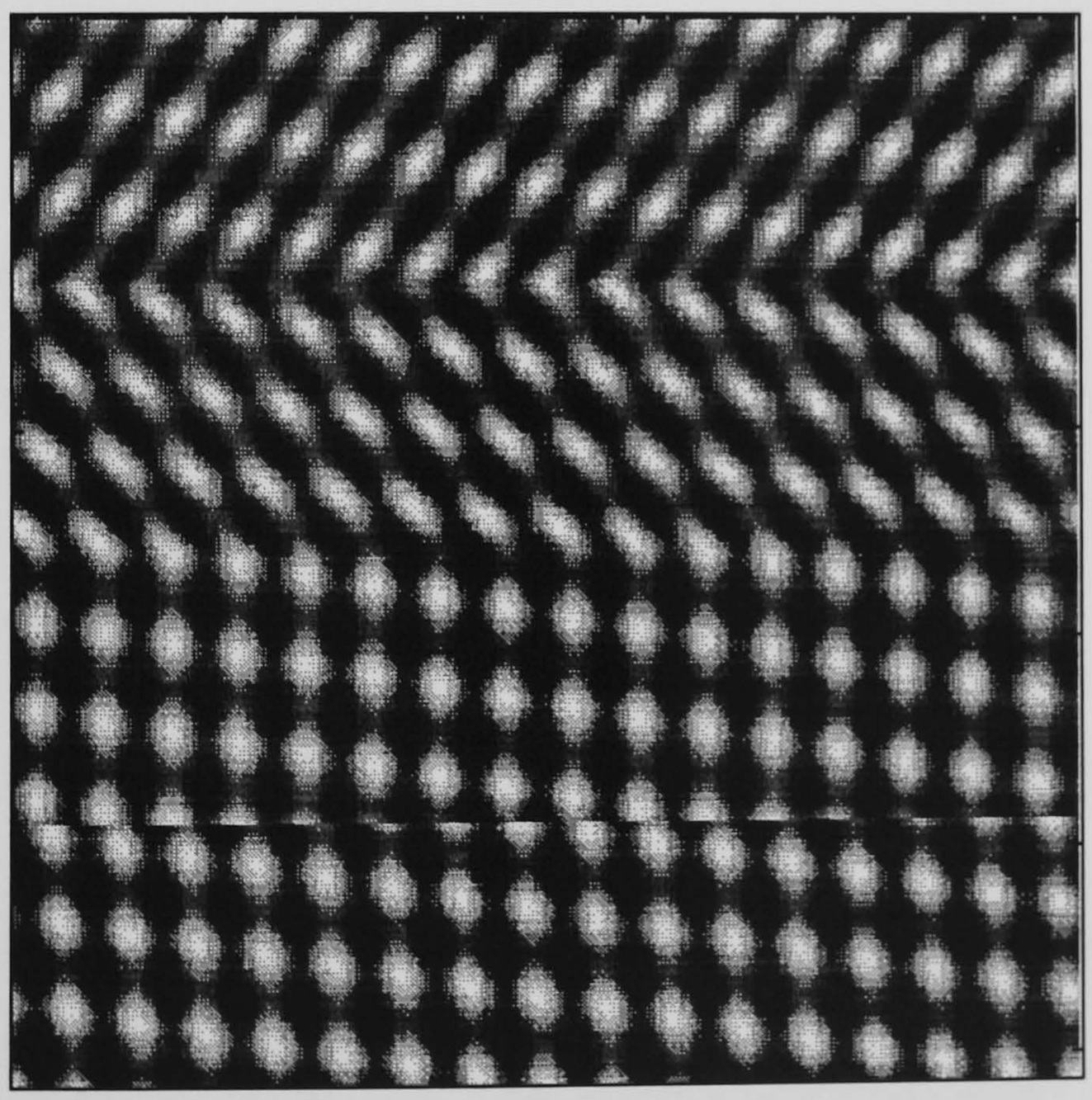

Figure 7.8 The Deformed Crossed Grating Image on the Object in Figure 8.7 in the X direction $P_1 = 8P_0$

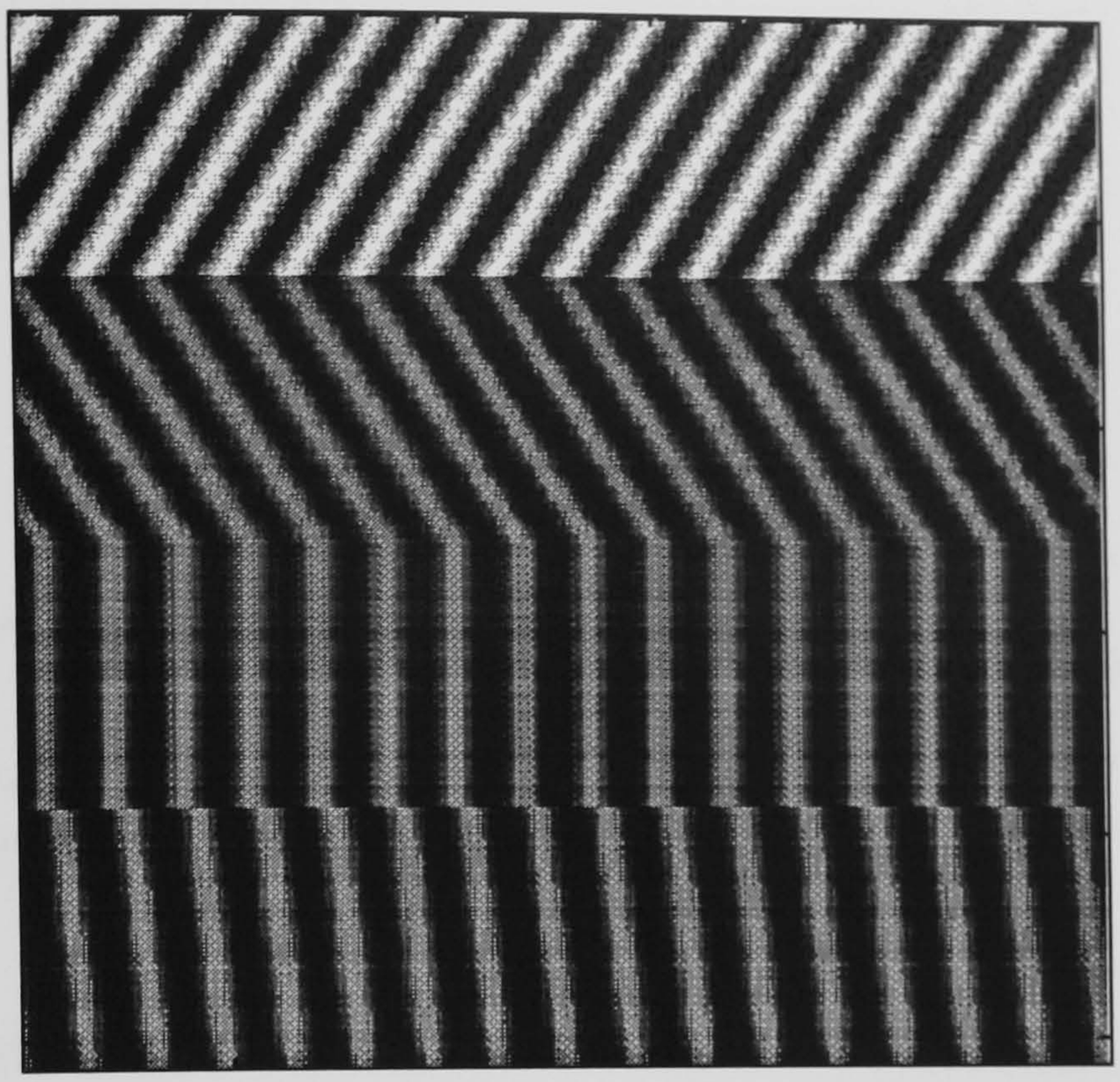

(a)

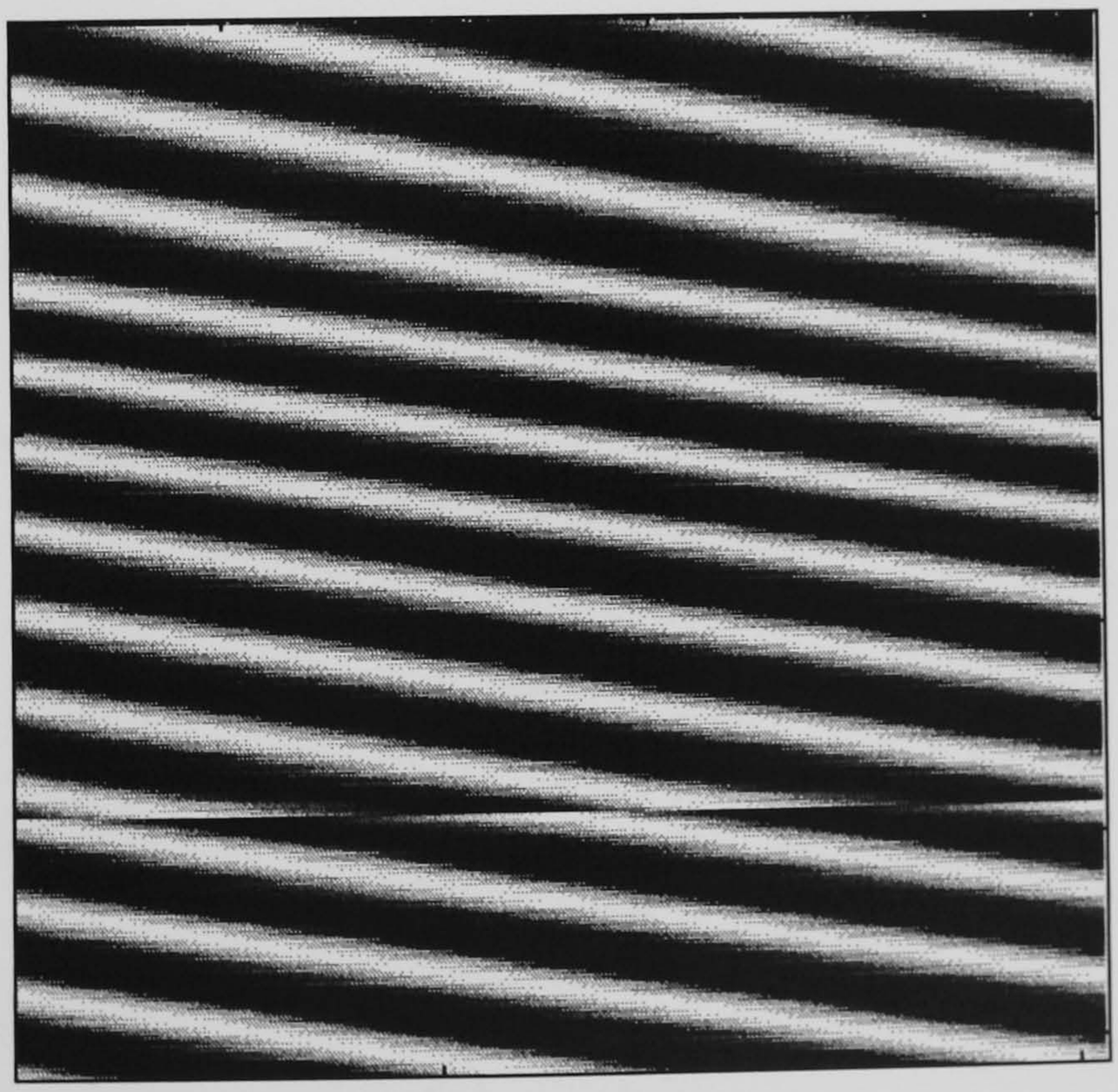

(b)

Figure 7.9 Deformed Grating Images on the Object

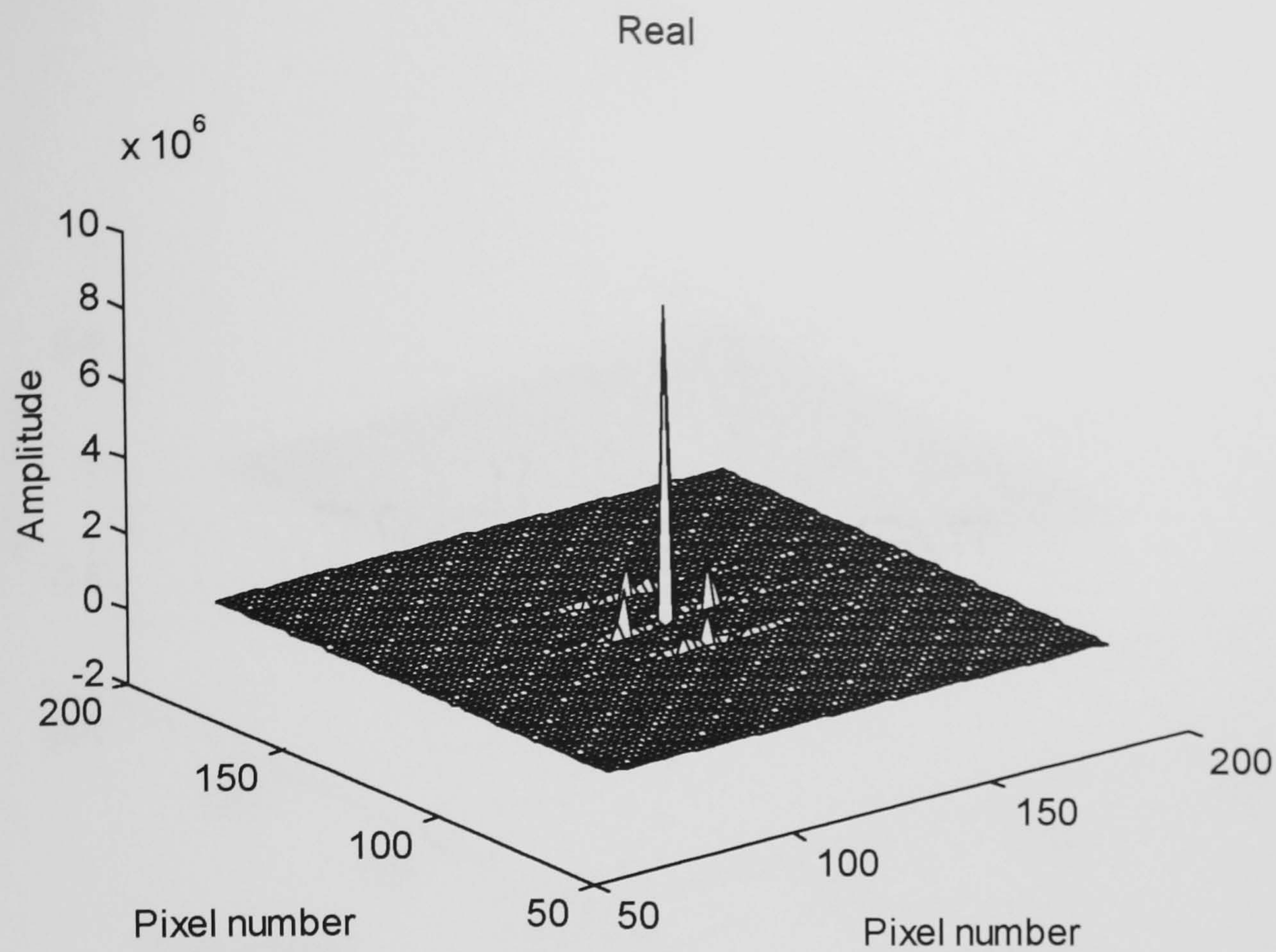

(a)

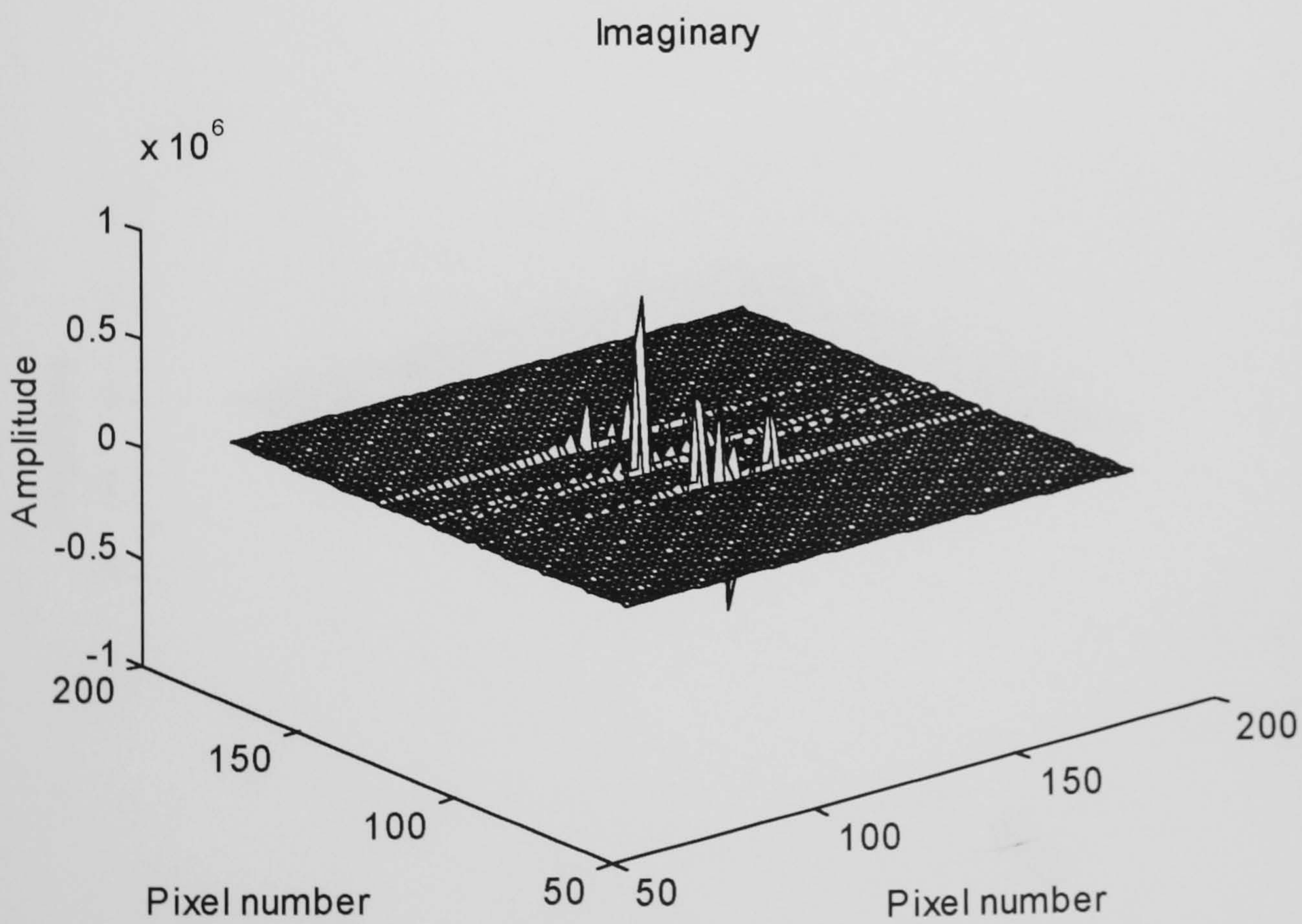

(b)

Figure 7.10 The Fourier Spectra of the Image in Figure 7.8

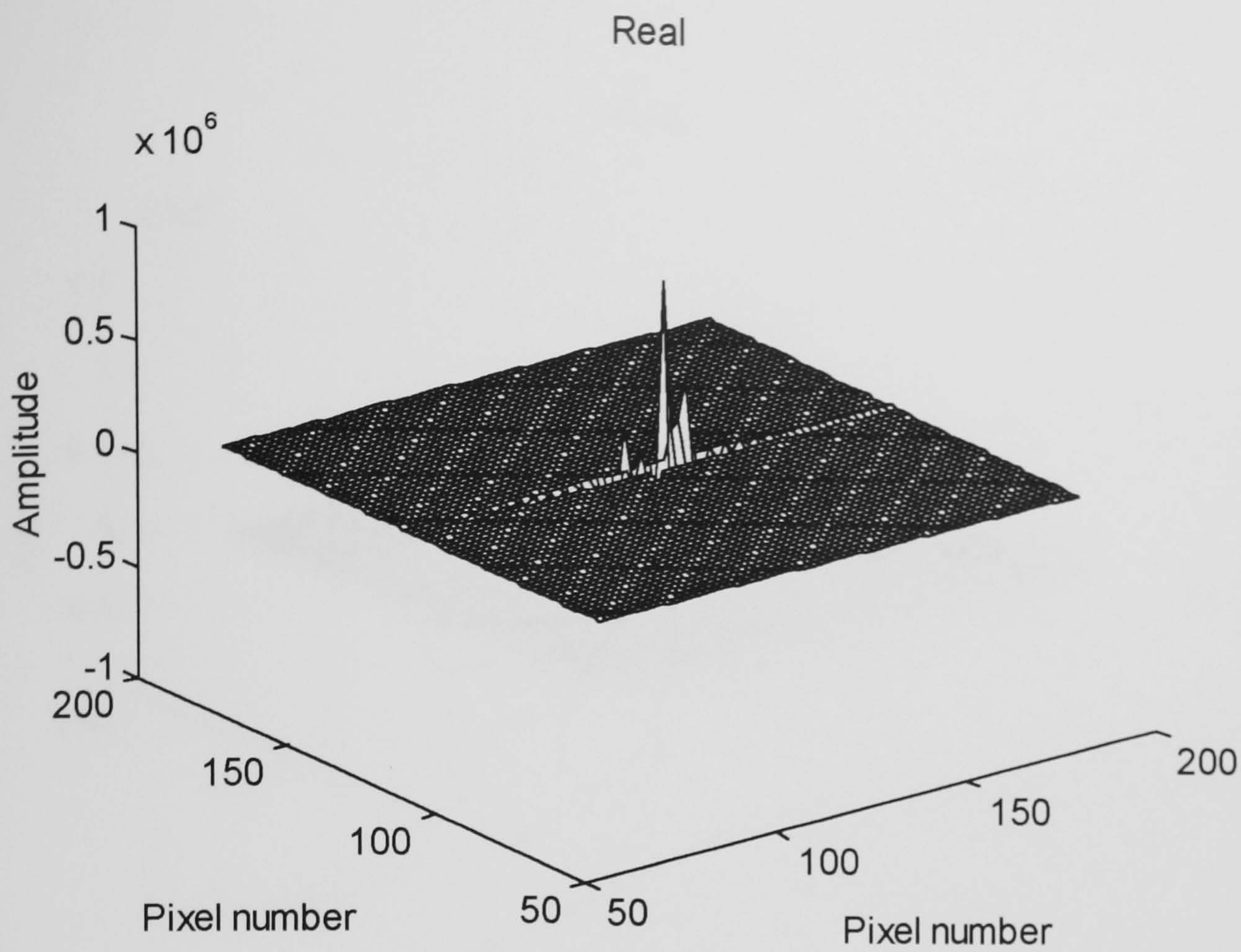

(a)

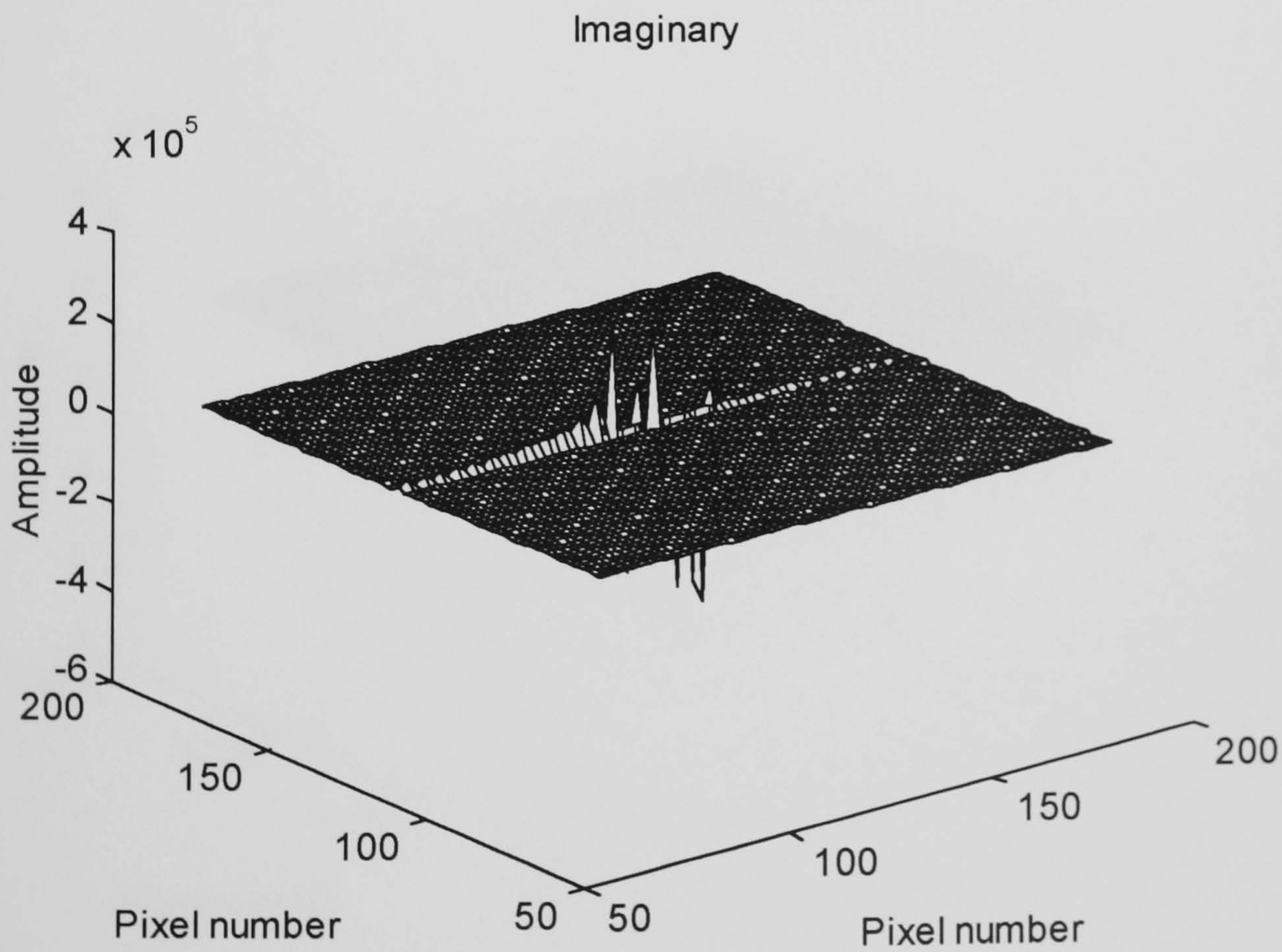

(b)

Figure 7.11 The Fourier Spectra of the Image in Figure 7.9(a)

After Filtering and Frequency Shifting

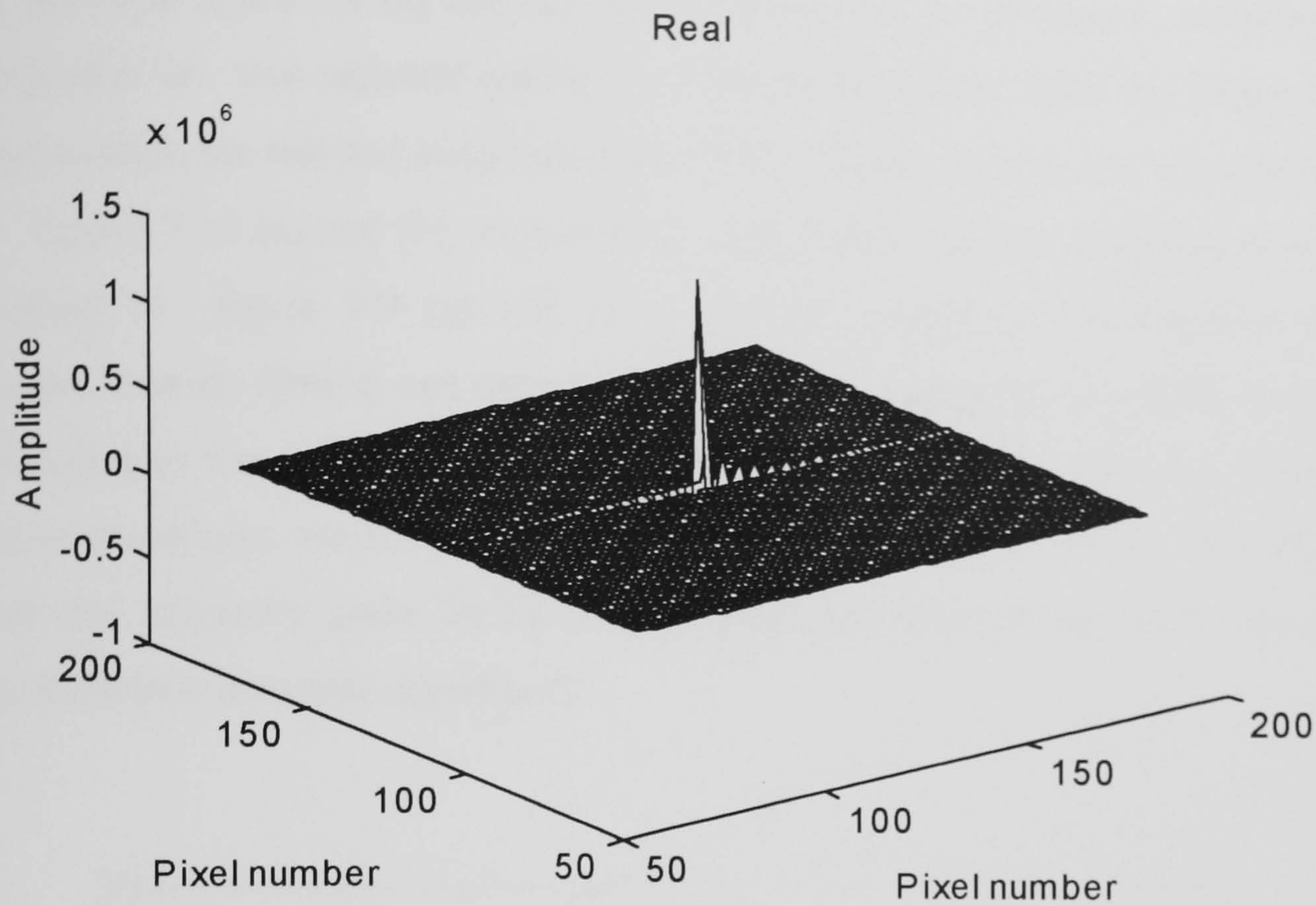

(a)

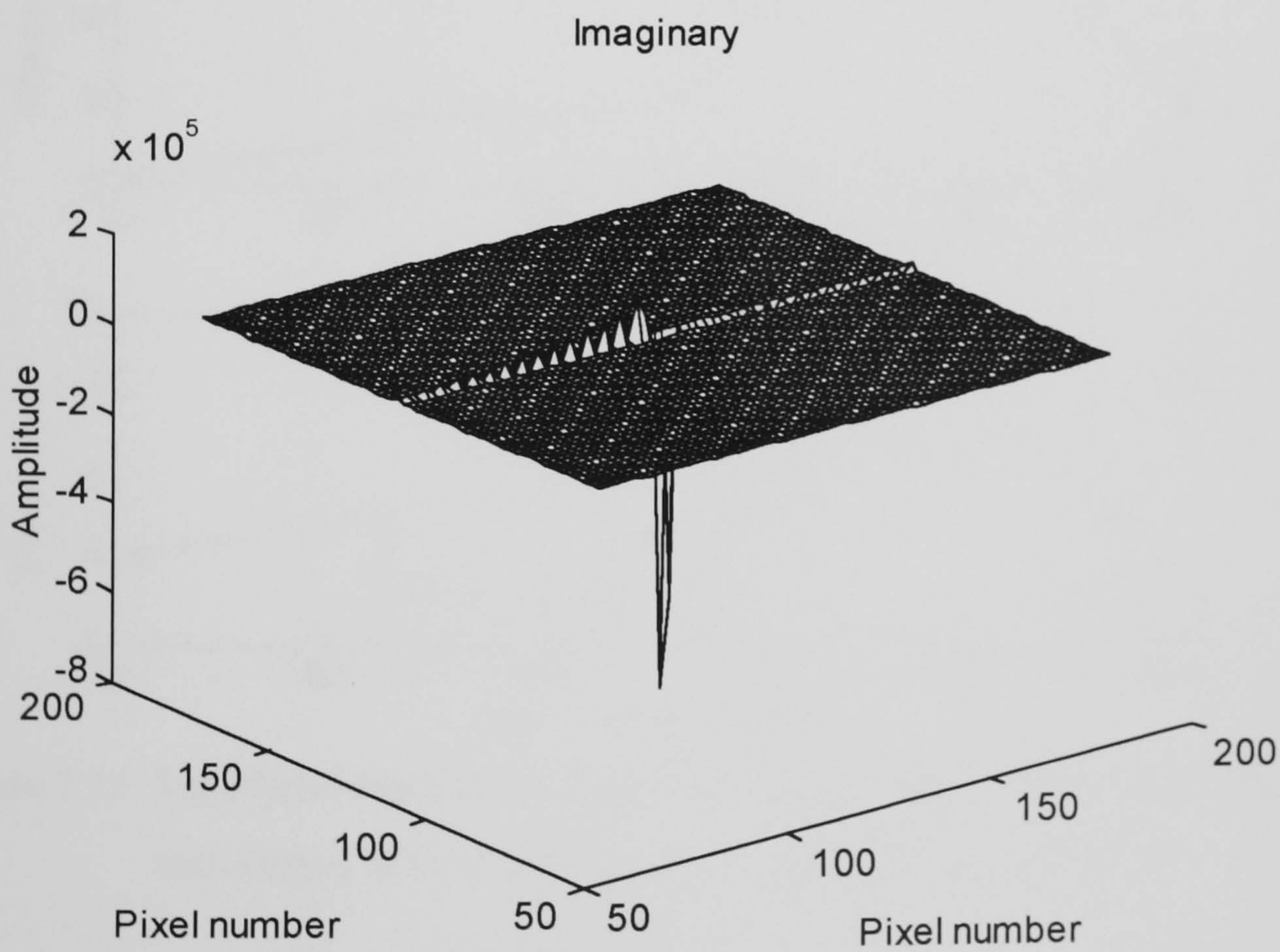

(b)

Figure 7.12 The Fourier Spectra of the Image in Figure 7.9(b)

After Filtering and Frequency Shifting

The image shown in figure 7.8 can be separated in the frequency space as two images as shown in figure 7.9 (a) and (b), which correspond to the images obtained by the projection of two separate gratings in different directions. After the image is Fourier transformed, the real and imaginary parts of the Fourier spectra are obtained as shown in figures 7.10 (a) and (b) respectively. The Fourier spectra contributed by the two gratings in figure 7.9 (a) and (b) are now separated, the negative frequency components are filtered, and the positive frequency components are shifted to the origin according to the frequencies of the two gratings. The spectra obtained following the above procedures are shown in figures 7.11 and figure 7.12, which correspond to the real and imaginary parts for the gratings with equivalent periods of P_0 and P_1, along the horizontal direction respectively.

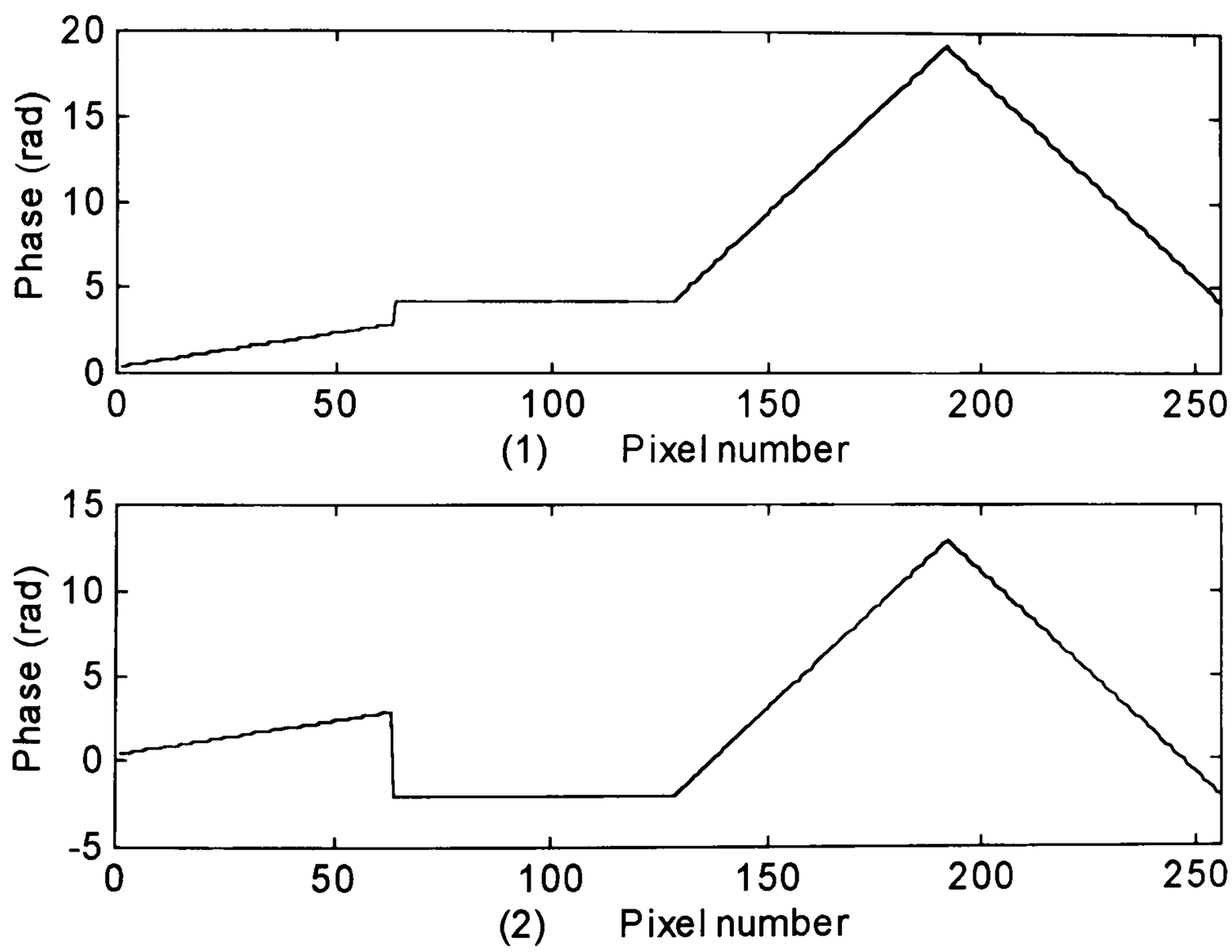

Figure 7.13 The Phase Distribution Along One Line Obtained From the Grating with Period of P_0 in X Direction (1) Original (2) Corrected

After the inverse Fourier transform of the two different spectra and the normal phase unwrapping process, two phase distributions are obtained. Figure 7.13(1) shows the phase distribution along one line obtained from the image shown in figure 7.9(a). It can be seen that the calculated phase jump caused by the object's height step in the

figure is only 0.4π rather than -5.6π, thereby giving an incorrect result. To correct this error, the procedure designed in section 7.3.1 is followed. From the phase differences of the two phase maps at these points, the condition of $|\Delta\varphi_1| \geq (P_0 / P_1)\pi$ and $(\Delta\varphi_1 / \Delta\varphi_0) < 0$ is satisfied and also $\Delta\varphi_0 > 0$ and $\Delta\varphi_1 < 0$. Therefore, -2π is added to the phase value as required by equation (7-17). Figure 7.13(2) shows the phase distribution along one line after this correction, the phase jump is -1.6π, rather than 0.4π.

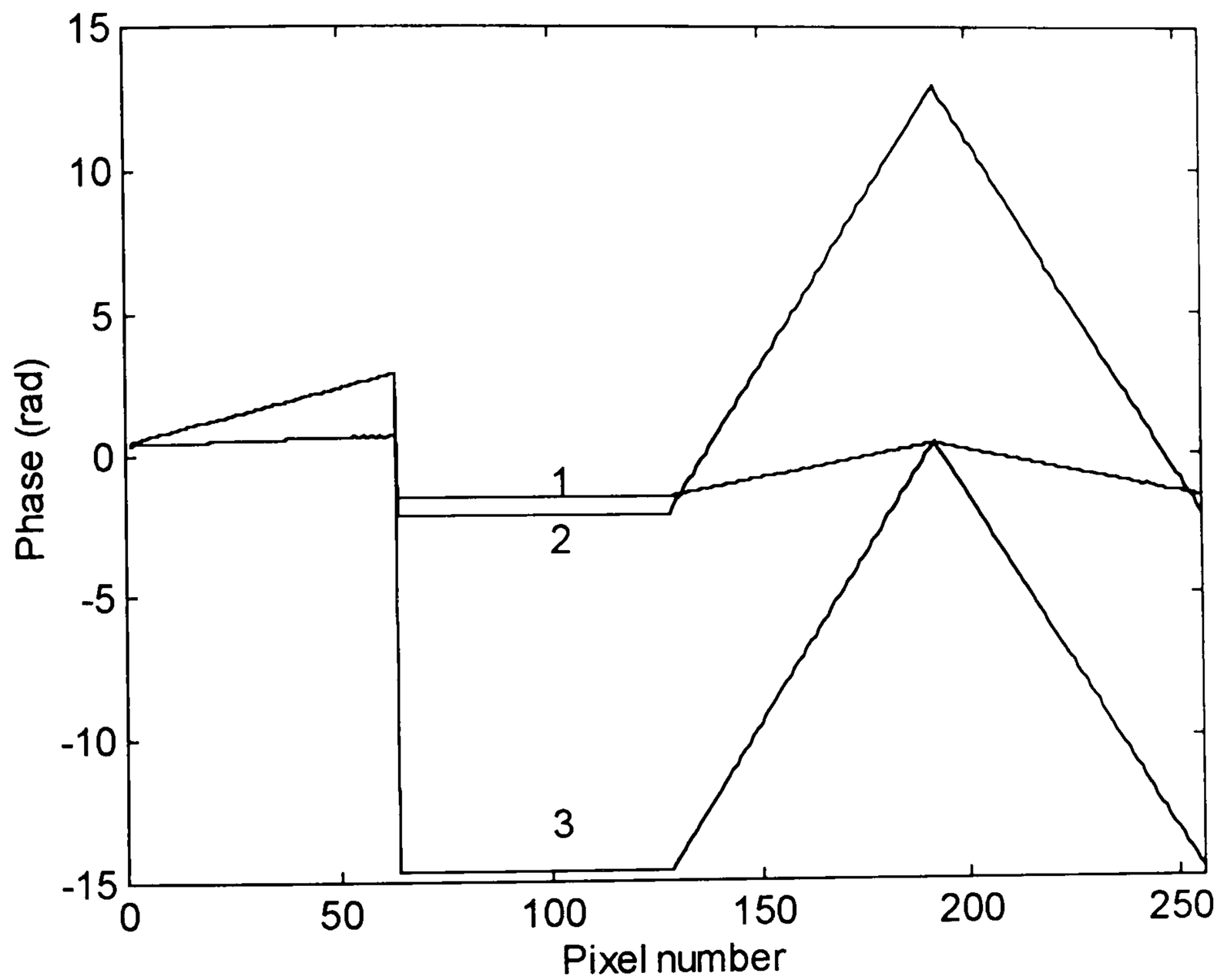

Figure 7.14 The Phase Distribution Along One Line Obtained From Different Gratings
1 - From the Image in Figure 7.9(b) 2 - From the Image in Figure 7.9(a) 3 - Corrected

The second step of correction as described in section 7.3.2, is to check that the true phase jump is bigger than 2π or not. In this simulation, the absolute value of the phase difference, $|\Delta\varphi_1|$, is larger than $2(P_0 / P_1)\pi$. By using equation (7-17), the calculated integer value is -2, so that 2nπ = - 4π is added, as required by equation (7-18). At this stage, the phase values are all corrected and the actual phase jump of -5.6π is obtained. To compare the phase distributions from different phase maps, three

different phase distributions along one line are drawn in figure 7.14, where (1) is that obtained from the lines which have an equivalent period of P_1 in the horizontal direction, (2) is that given in figure 7.13(2), and (3) gives the correct result.

7.6 Summary

In this chapter, the basic Fourier transform and phase unwrapping technique are reviewed. To solve the problem of phase unwrapping in the presence of discontinuities caused by the object's height steps or other reasons, a new phase unwrapping algorithm has been proposed. The two phase maps are obtained by the projection of a crossed grating and use of the Fourier transform technique. Only one image is required for each complete measurement so that vibrations have no effect and accurate grating translations are not required during the process. The theoretical analysis and simulation results have shown that the proposed algorithm is fast and could be used in many applications, for the measurement of three-dimensional object profile.

Chapter 8

Experiments and Results of Phase Unwrapping

8.1 Introduction

In the previous chapter, the theoretical analysis of the proposed phase unwrapping algorithm was described for a phase map with discontinuities, by the use of a crossed grating, and the algorithm is verified by the results of simulation. In this chapter, an experimental system which is used to verify the technique and the corresponding procedure for signal processing, will be described. A crossed grating is projected onto an object with height steps and the deformed grating image is captured by a CCD camera. The signal is processed by the specially designed software. The experimental results show that the phase unwrapping algorithm, compared with previous techniques, is fast and can be used for the measurement of three-dimensional object profile in many application areas. The following section details the experimental arrangement and the instruments used in the system. The signal processing procedure and the design of the software are described in section 8.3, and the experimental results and their discussion are contained in section 8.4. Section 8.5 gives a summary of the chapter.

8.2 Experimental Arrangement

The theoretical analysis and simulation in chapter seven have shown that the proposed phase unwrapping algorithm is able to unwrap phase images with discontinuities caused by height steps. To verify this theoretical conclusion, an experimental system which includes a crossed sinusoidal grating, CCD camera, projector and computer, as shown in figure 8.1, is designed. The camera and the projector have the same perpendicular distance to the object. The distance between the camera and the object is large compared with the object height. The crossed grating is projected onto the surface of the object, the deformed grating image is captured by the CCD camera and the data is read to the computer memory for processing. The image is in a 128 x 128 pixel format.

In this arrangement, the crossed grating used is a commercially available crossed sinusoidal grating from Technolink (Europe) Ltd. The effect is the same as the sum of

two separate gratings of the same period, projected at an angle α, to each other The original period of the grating is $P_0 = 0.25$mm, and the angle between the two sets of lines, $\alpha \cong 80^\circ$. When the period of one set of lines along the horizontal direction is P_0, the equivalent period of the other set of lines is $P_0/\cos\alpha = 5.5\ P_0$. The size of the grating is 50mm x 50mm. The projector is a standard 35mm slide projector, (Prado Universal, Germany). The CCD camera is a CCIR monochrome camera, (COHU INC.), with Nikon lens, (f = 55mm, 1:2.8). The computer is an IBM PC 486DX2 computer, equipped with a frame grabber, (ITEX Variable-Scan Frame Grabber, VFG 1.0, Imaging Technology Inc.).

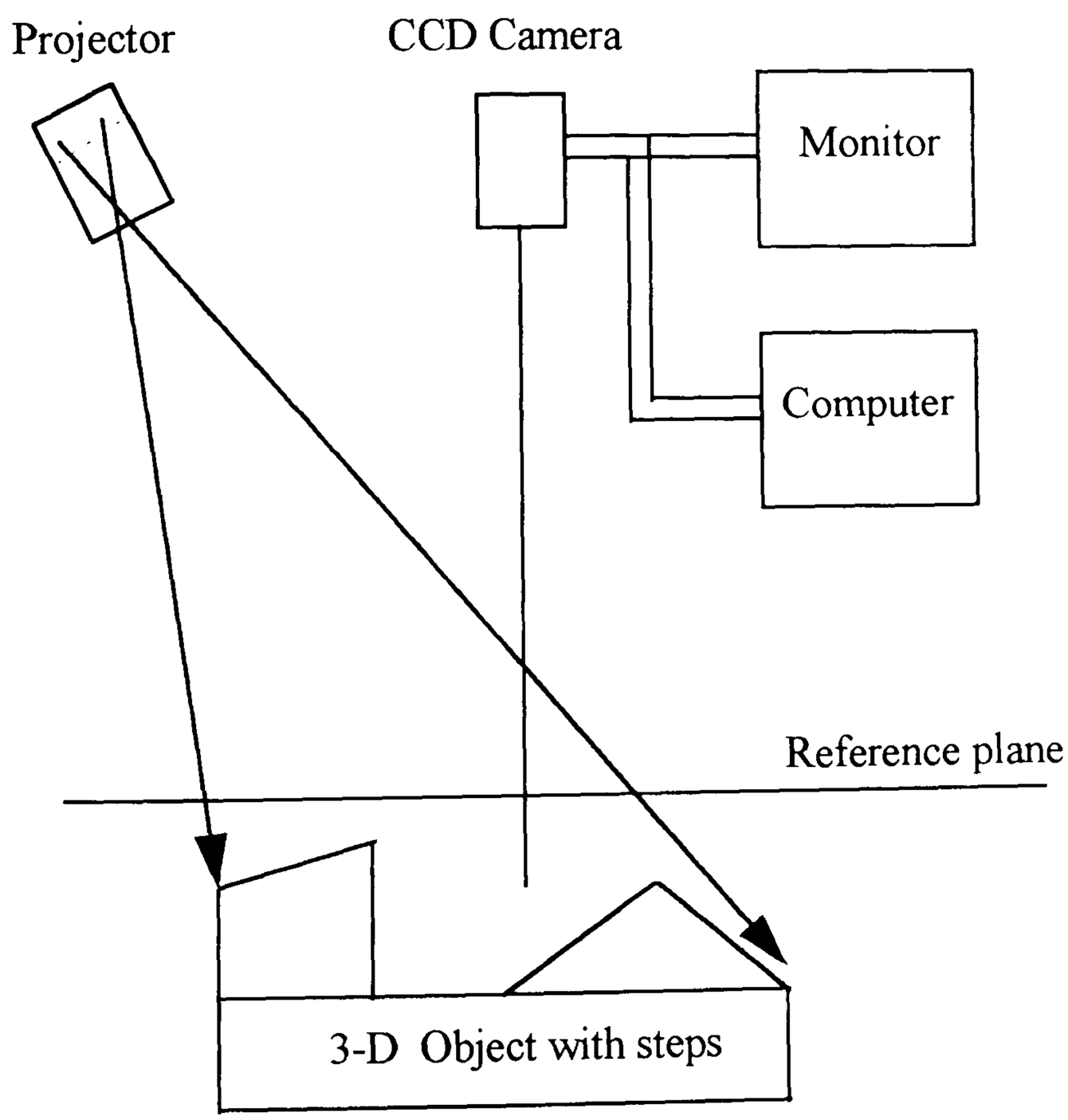

Figure 8.1 Schematic Diagram of an Experimental System for the Phase Unwrapping Algorithm

8.3 Signal Processing Procedure

For the convenience of the frequency shifting process, a suitably deformed grating image on the surface of the object is chosen to ensure that both fringe numbers for each set of grating lines along the horizontal direction, are integer values. This is adjusted by altering the distance between the camera and the object before the image is captured. After the image is captured, it is digitized and saved in computer memory for processing. The image is then Fourier transformed by the use of the FFT. The Fourier spectra contain frequency components from both sets of grating lines. Since there is an angle, α, between them, the corresponding frequency components, except the dc component, are separated in the frequency space by an amount proportional to the angle between the two sets of lines. The whole Fourier spectra of the deformed image is separated into two individual spectra which correspond to each separate grating. If these two spectra are now inverse Fourier transformed, two deformed images, similar to those shown in figure 7.9 (a) and (b), will be obtained. After the negative frequency and dc components have been removed, the remaining positive frequency components are shifted to the origin and inverse Fourier transformed. Two wrapped phase maps with different precisions will be obtained.

These two wrapped phase maps contain information about the object's height distribution. However, if there are any discontinuities in these phase maps, it would not be possible to obtain the correct distribution of the object's height. Therefore, the normal phase unwrapping procedure is utilised to obtain the correct phase distribution when the phase discontinuities are caused by a continuos height variation, which may cause a 2π phase jump. When the object's height steps or the noise spikes are large enough to cause a phase jump greater than π, as explained in section 7.3, the normal phase unwrapping technique may not be used to obtain the correct phase distribution. The problem can be solved by the algorithm described in chapter seven. Therefore, the next stage is to follow the procedures described in section 7.3.1 to correct the error in the phase distribution, when the phase jump is between π and 2π. A phase jump of $2n\pi$ would be corrected by the technique described in section 7.3.2 using two phase

maps with different sensitivities. At this point, all phase discontinuities should be corrected and the resulting phase distribution should represent the correct height distribution of the measured object. The complete algorithm is shown in figure 8.2.

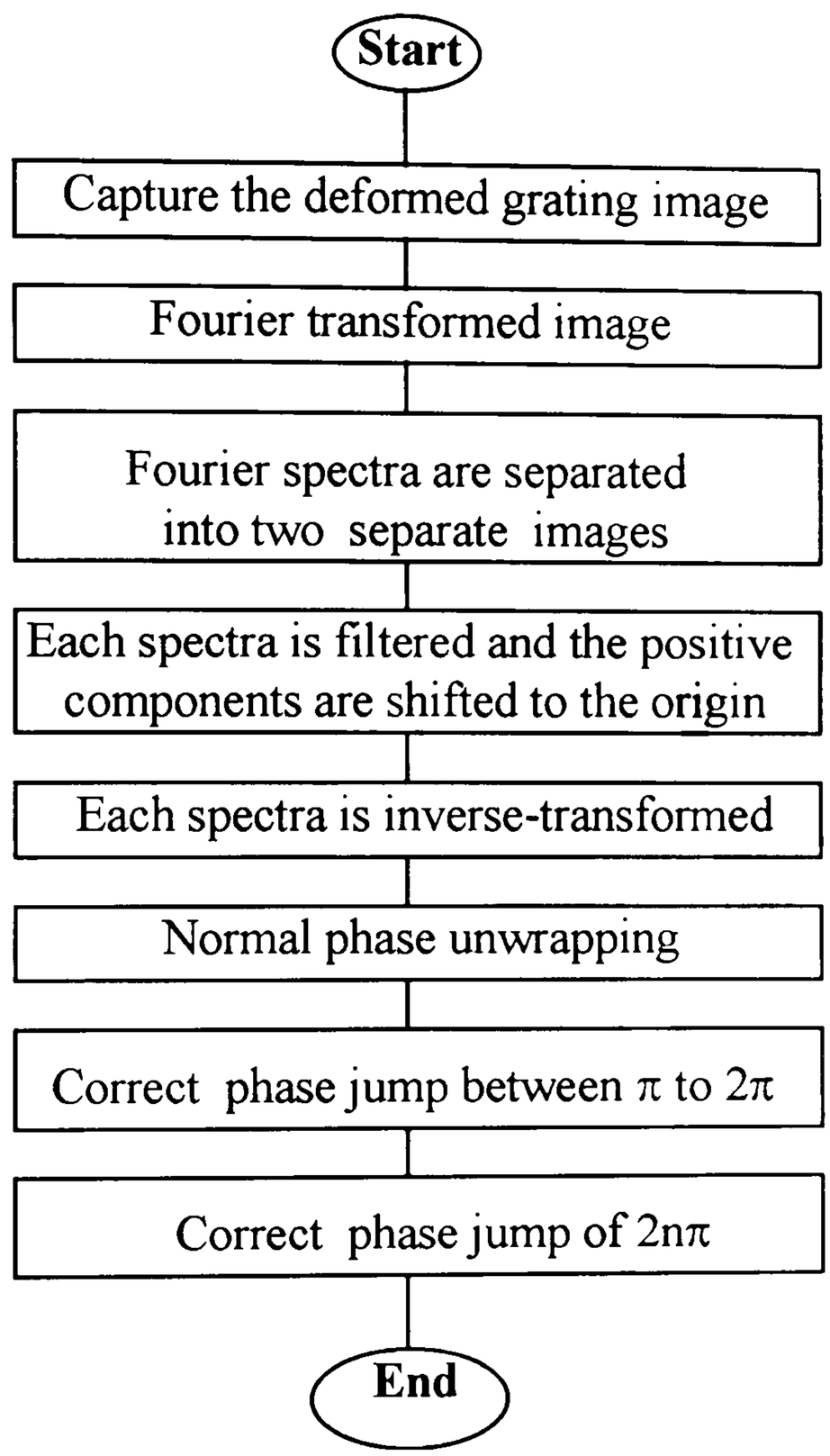

Figure 8.2 Flow Diagram of the Signal Processing Procedure

8.4 Experimental Results

The experiments to verify the proposed phase unwrapping algorithm were carried out using the experimental system described in figure 8.1. The signal is processed using the

procedure described in section 8.3. The experiments are carried out in two stages. Firstly, it is required to verify the relationship between the values of the phase jump and the periods of the gratings for a given object height step, and that between different height steps and the periods of the gratings, as described by equation (7-15). Secondly, the crossed grating is used to measure the height distribution of the three dimensional object containing height steps. To obtain a good quality image, the objects used in the experiments are painted matt white. The experiments and the corresponding results obtained are described in sections 8.4.1 and 8.4.2.

8.4.1 The Phase Jump for Different Grating Periods

The purpose of the experiments is to verify the relationship between the phase jump and the periods or spatial frequencies of the gratings, and compare them with those obtained by the theoretical analysis given in section 7.3. In these experiments, the objects used have two flat parts with different height steps. The height difference between the two flat parts varies between 1.5mm and 11.5mm. The largest height step causes the phase jump, for large period of grating, is less than π, and it is bigger than $n\pi$ ($n > 2$) for the small period of grating. The number of fringes in the image varies from 2 to 16. The corresponding values of the phase jumps caused by different height steps are obtained by the procedure described in section 8.3.

When the object height step is 5mm, and the number of fringes in the image are 16, 7, 4, and 2, respectively, the deformed grating images for the same fixed distance between the object and the camera, and that between the camera and the projector, are shown in figures 8.3 (a) to (d). The calculated values of the phase jump caused by the 5mm height step are 5.10, 2.21, 1.24 and 0.62 radians, for fringe numbers of 16, 7, 4, and 2 respectively. The relationship between the fringe number in the image and the values of the phase jump for the same height step are shown in figure 8.3 (e). It can be seen that the relationship is linear and confirms the conclusion expressed by equation (7-15).

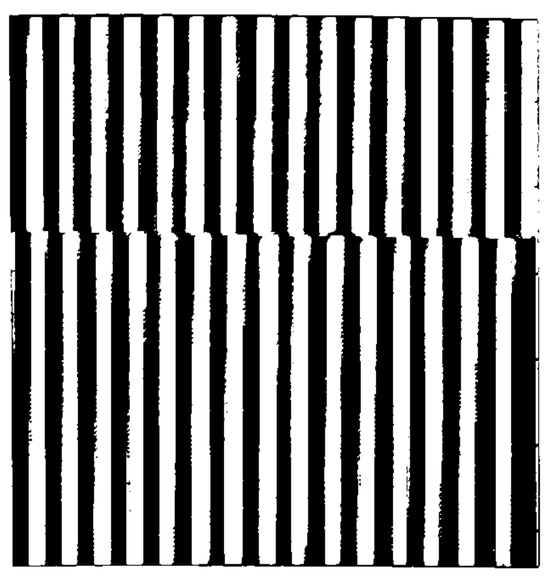

(a) sixteen fringes

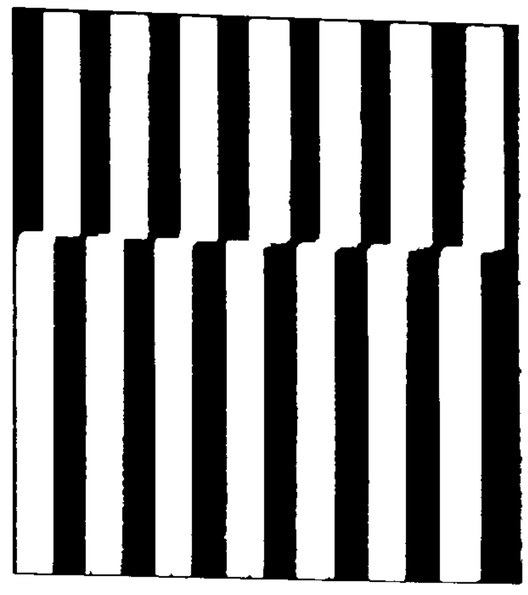

(b) seven fringes

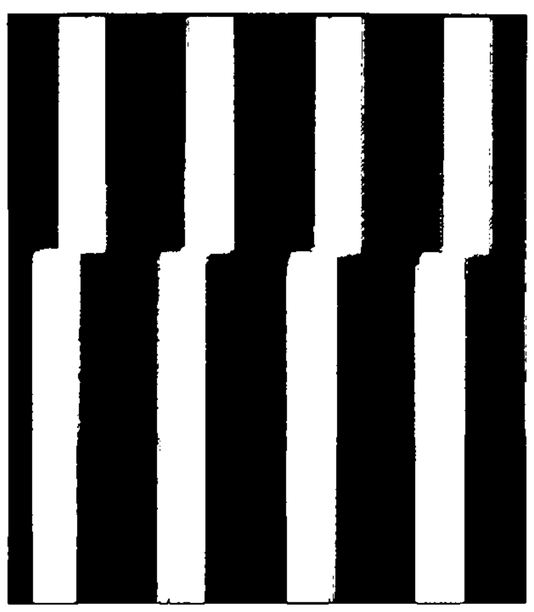

(c) four fringes

(d) two fringes

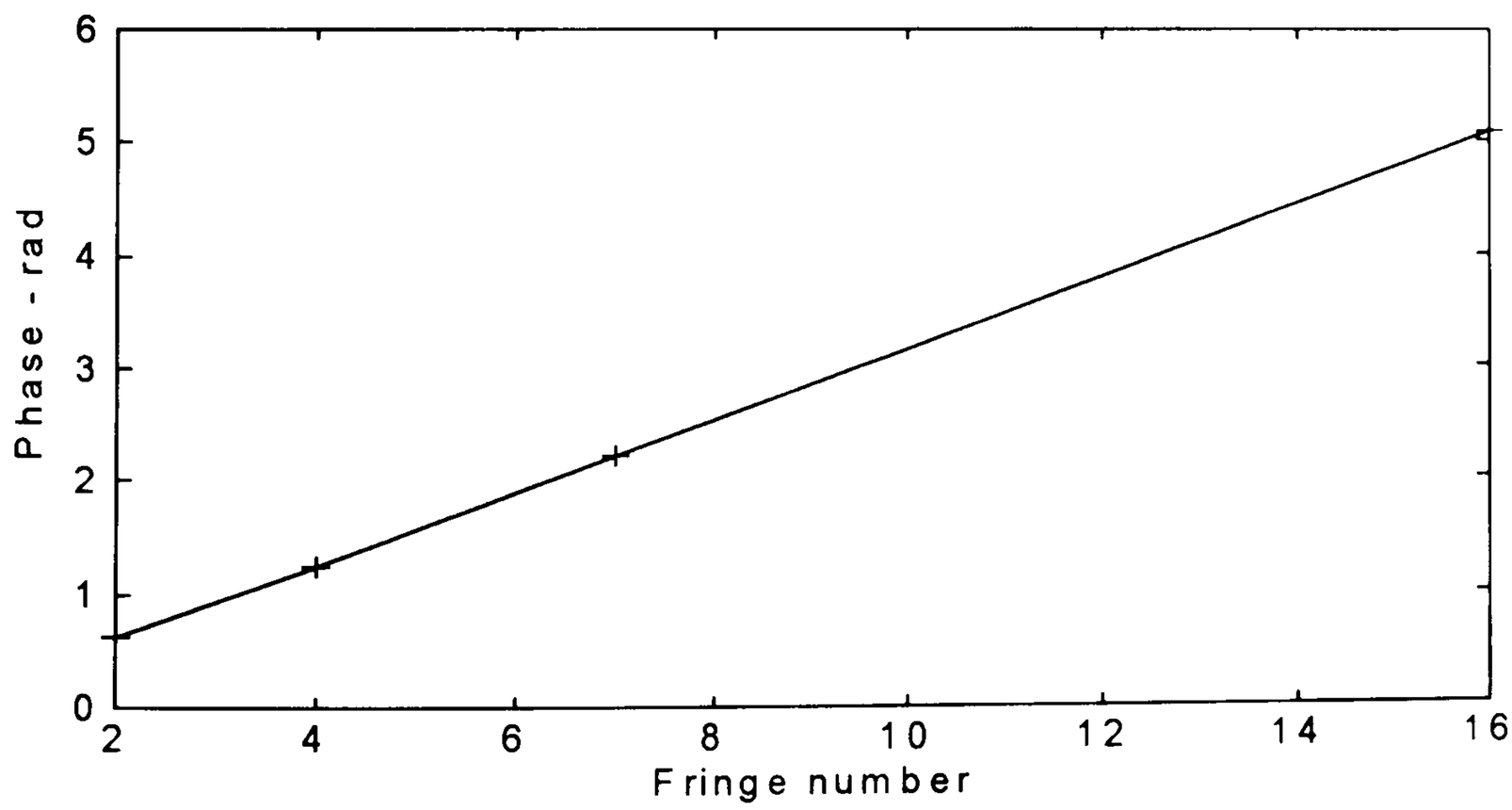

(e) the phase jumps for different number of fringes

Figure 8.3 The Images and Phase Jumps Caused by the 5mm Height Step for Different Numbers of Fringes in the Image

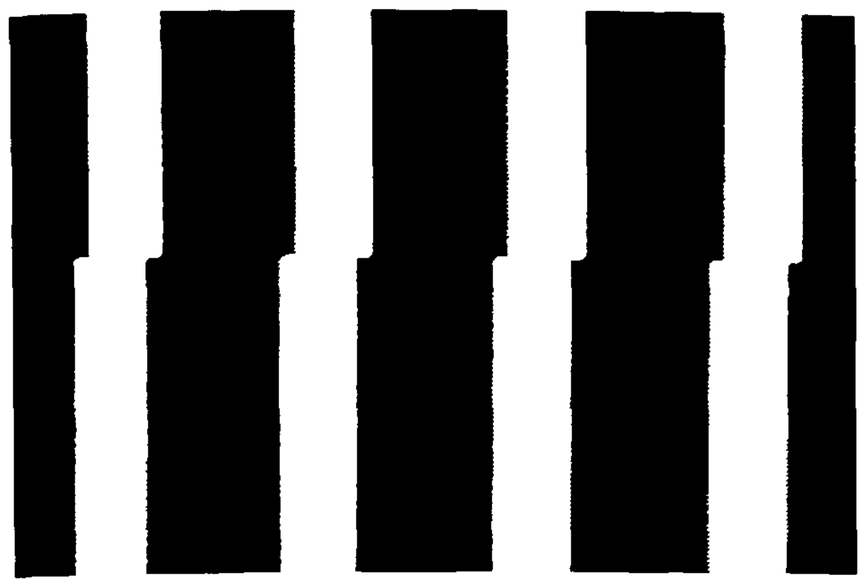

(a) 4 fringes and 1.5mm height step

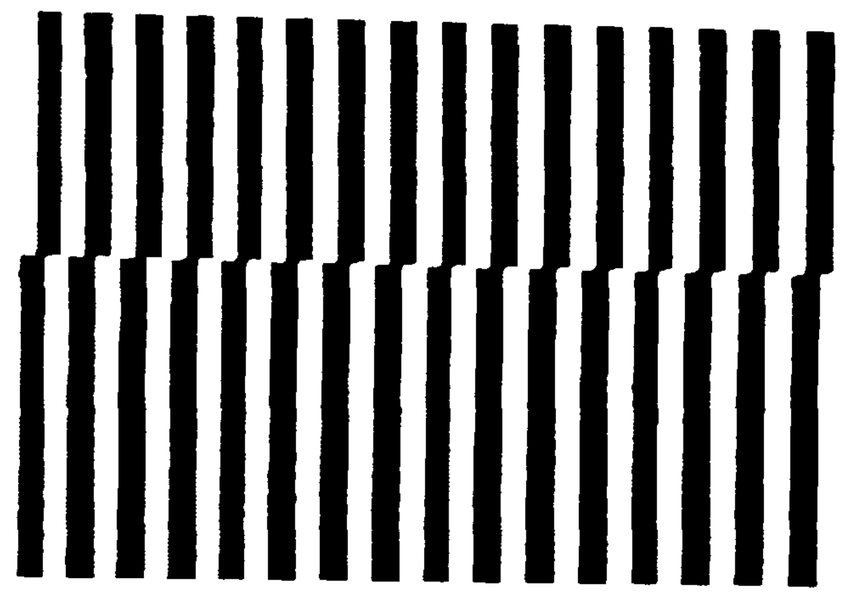

(b) 16 fringes and 1.5mm height step

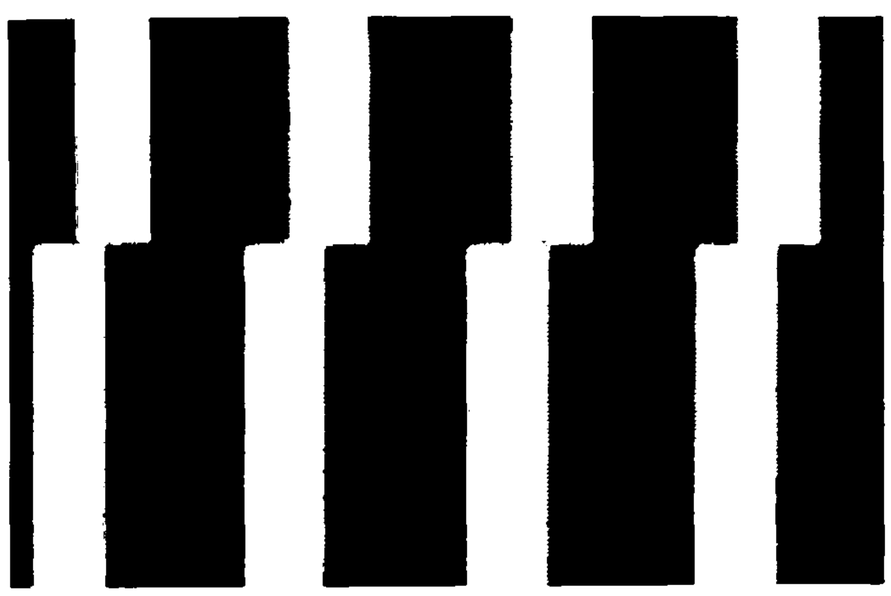

(c) 4 fringes and 6.5mm height step

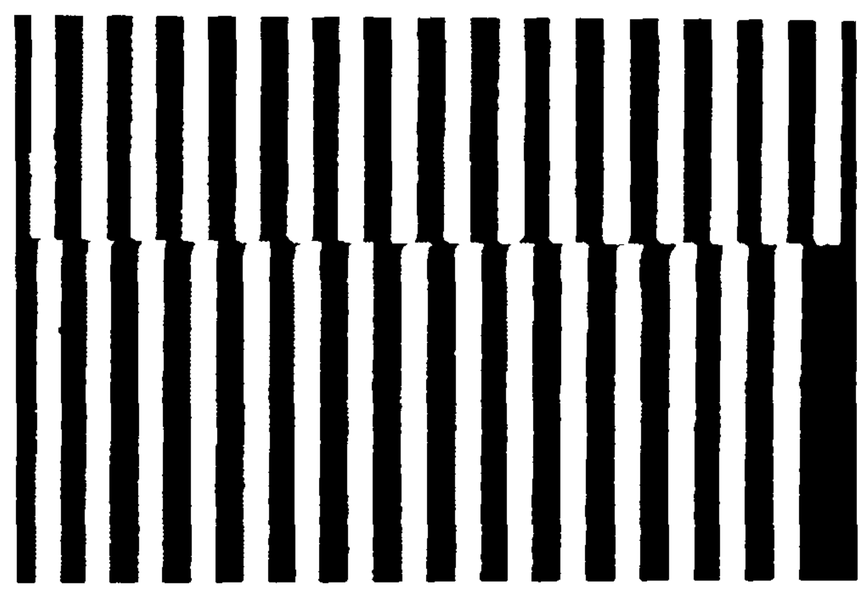

(d) 16 fringes and 6.5mm height step

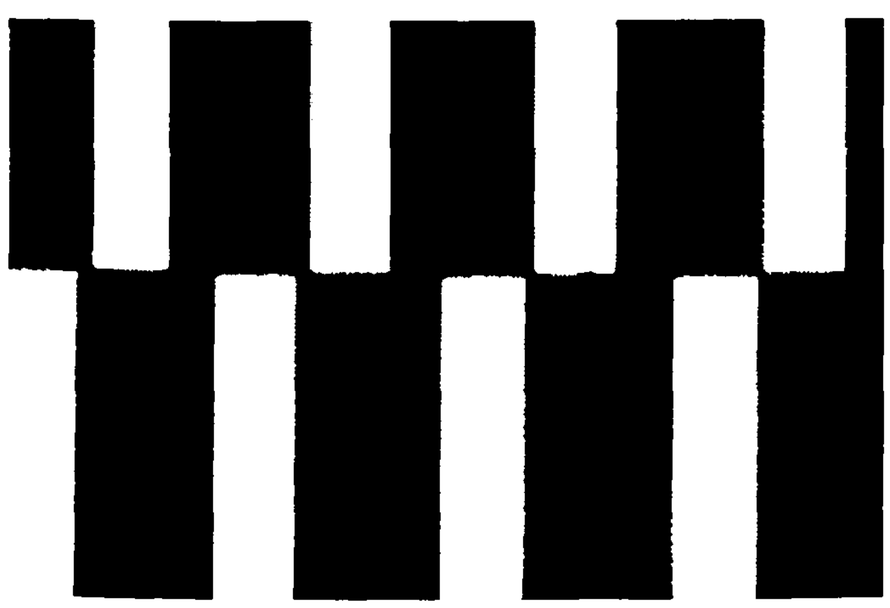

(e) 4 fringes and 11.5mm height step

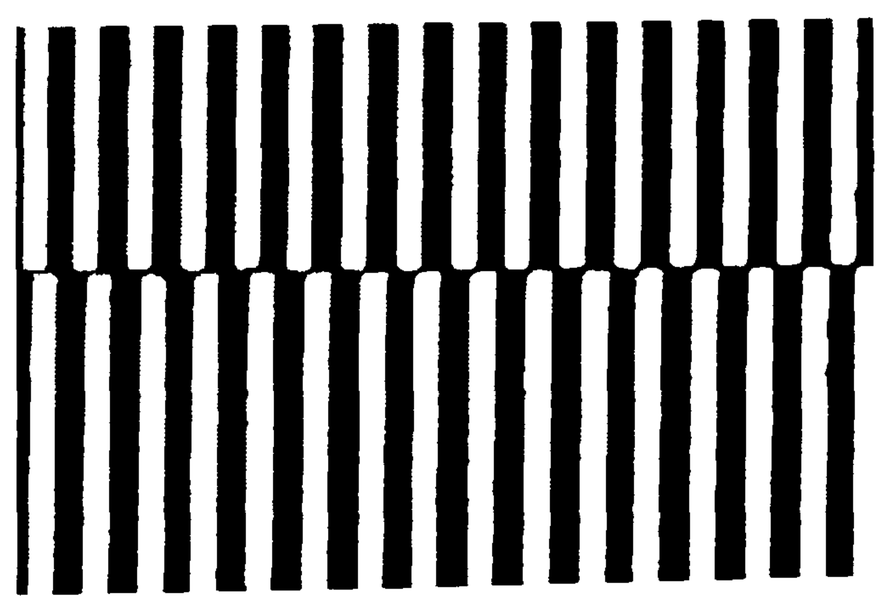

(f) 16 fringes and 11.5mm height step

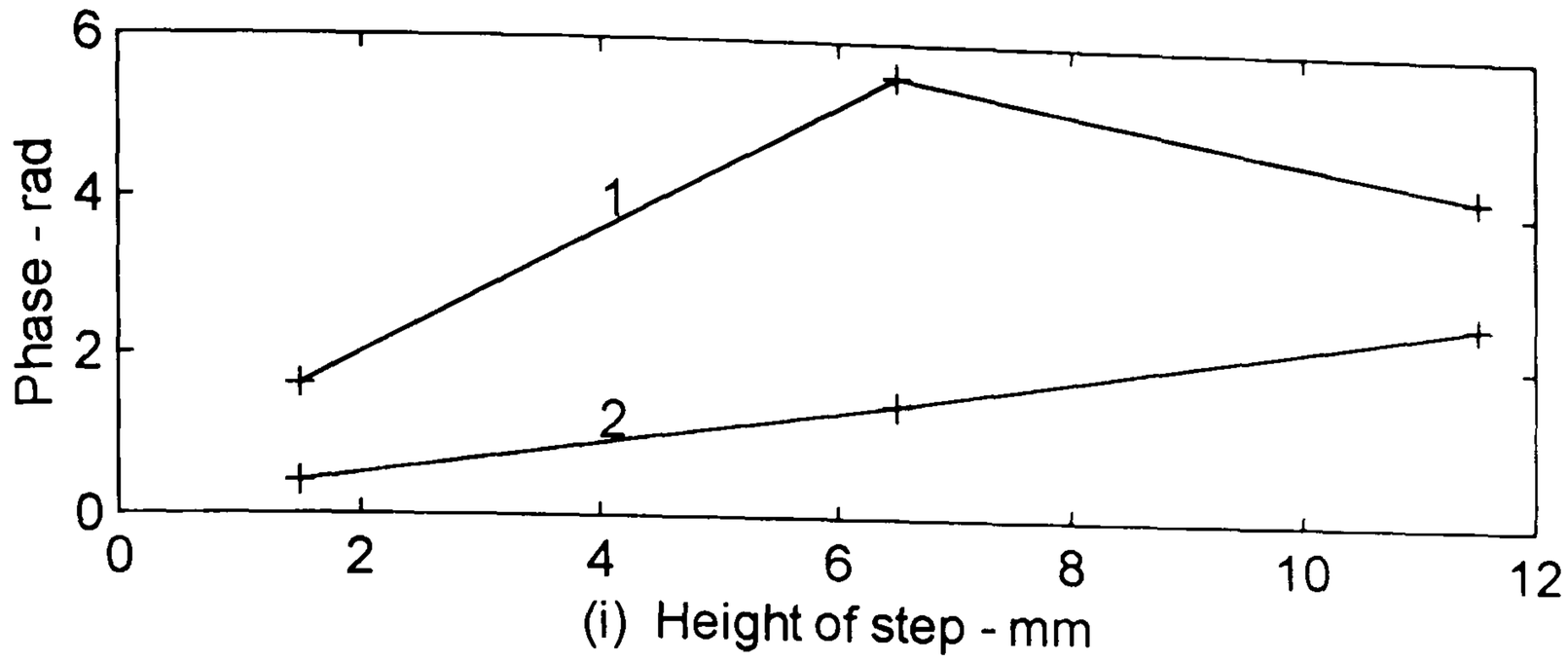

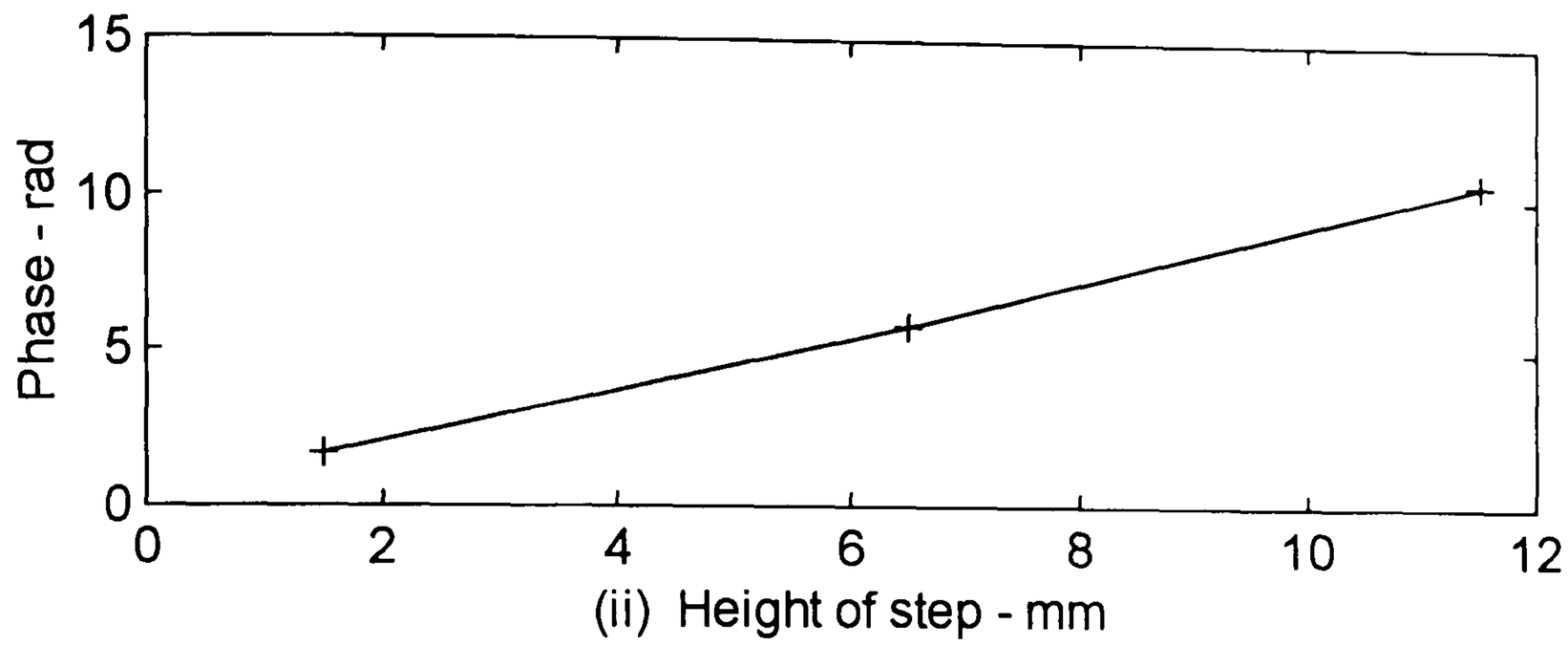

(g) the phase values obtained by different fringe number and after the correction

Figure 8.4 The Images and Phase Jumps Caused by Different Height Steps for a Fringe Number of 4 and 16 respectively

Different phase jumps will be obtained when the grating used has a different period for the same height step, as that obtained above. If the object has different height steps, different values of the phase jump can be obtained by using the same grating. To verify the conclusion obtained from the theoretical analysis, two gratings with a spatial frequency ratio of 4 are used for the projection, and the object height steps are 1.5mm, 6.5mm and 11.5mm respectively. The number of fringes in the image for both gratings are 16 and 4 respectively. The images obtained are shown in figures 8.4 (a) to (f). The corresponding values of the phase jumps with different object height steps are shown in figure 8.4 (g), where in (i), 1 - the phase jumps obtained by the grating which has 16 fringes in the image, 2 - the phase jumps obtained by the grating with 4

fringes in the image, and (ii), the correct values of the phase jumps obtained by the proposed phase unwrapping algorithm. From this figure, it can be seen that for the given parameters of the experimental system, the correct value of the phase jump should be directly proportional to the height step. The results obtained by the large period grating satisfies this condition. However, those obtained by the small period grating do not. Though the phase values obtained by the use of a large period grating are correct, it is not sufficiently sensitive. The inverse condition is true when considering the small period grating. By using both gratings, phase values which are correct and accurate, can be obtained.

8.4.2 Measurement of 3-D Objects Containing a Height Step Using a Crossed Grating

A crossed grating used for the projection in our experiments is formed by two sets of grating lines at an angle of about 80° and an original period of 0.25mm It has a frequency ratio of 5.5 along the horizontal direction. The numbers of fringes along the horizontal direction are 22 and 4 respectively. The three dimensional object to be measured has a height step of 10mm in the vertical direction.

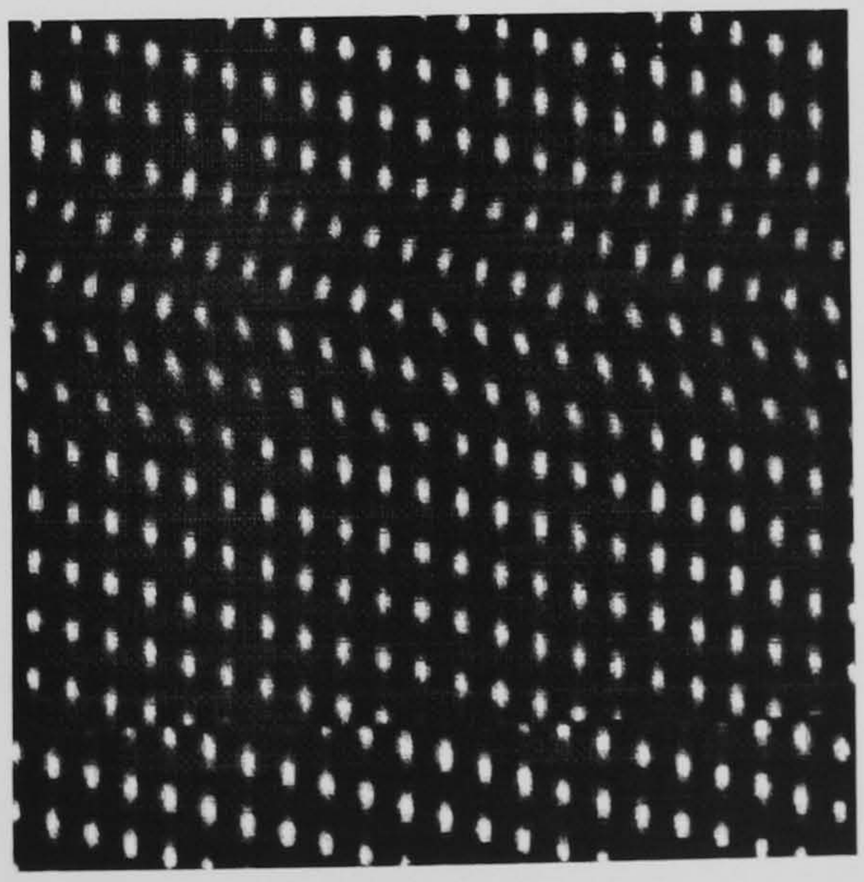

Figure 8.5 The Deformed Crossed Grating Image

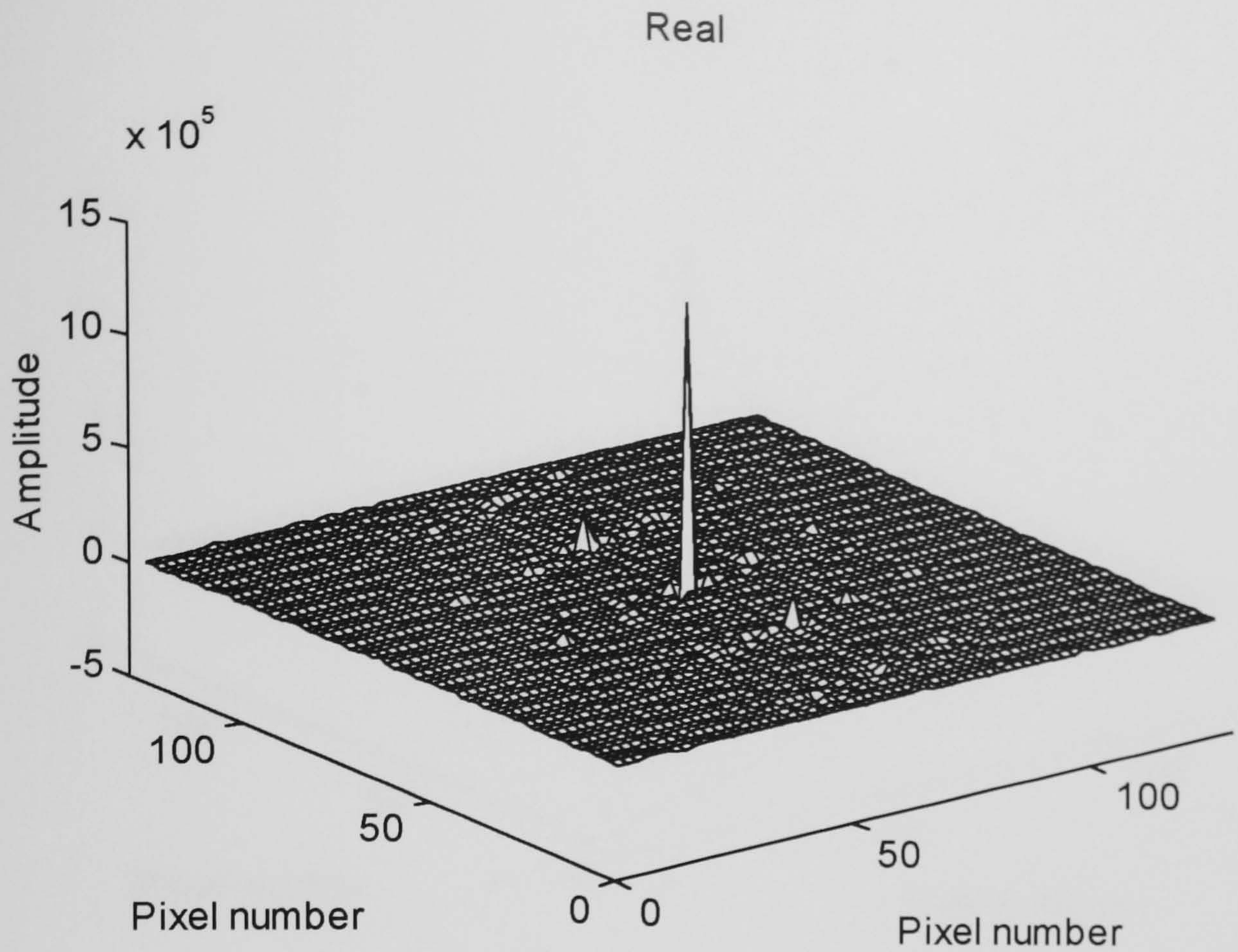

(a)

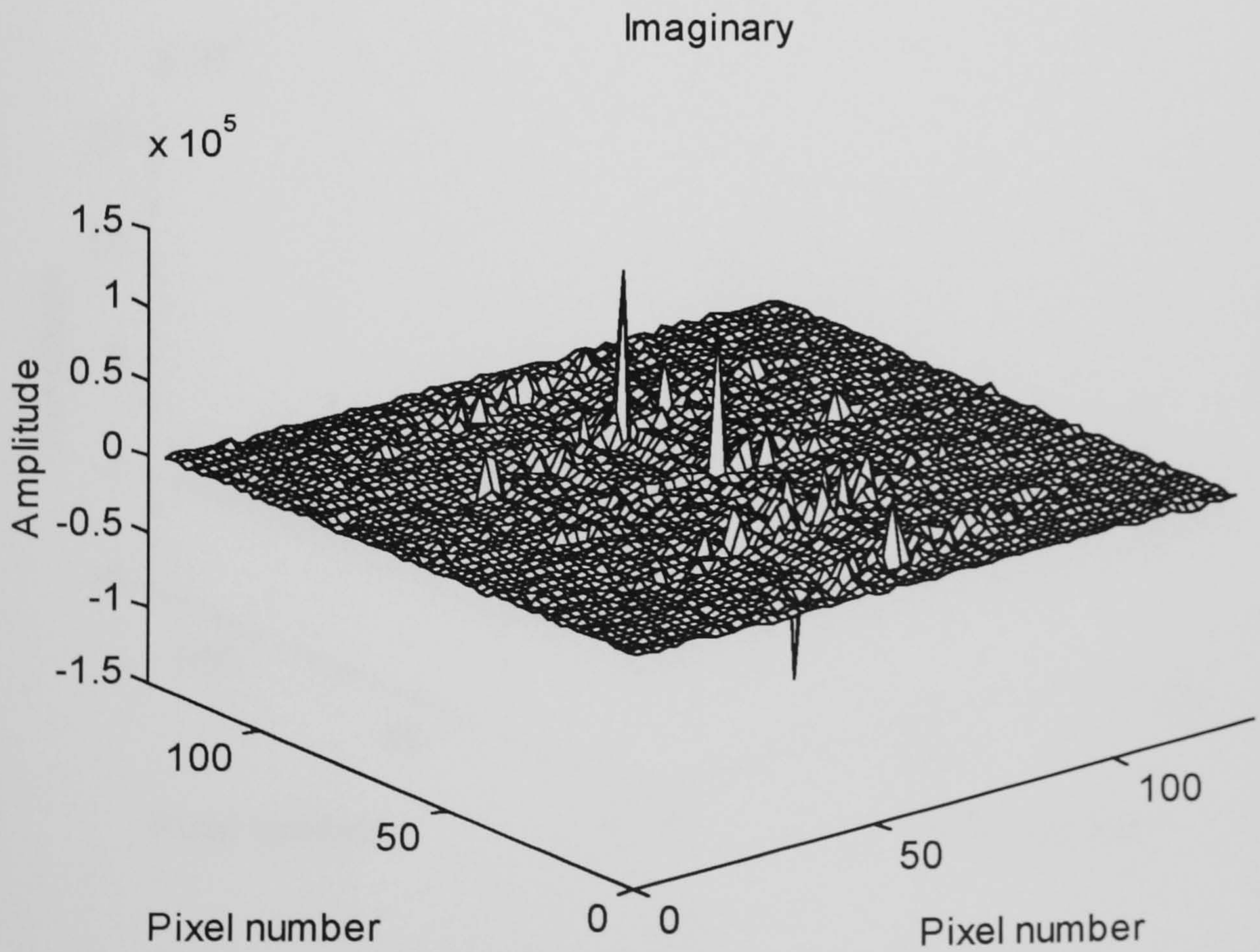

(b)

Figure 8.6 The Fourier Spectra of the Image in Figure 8.5

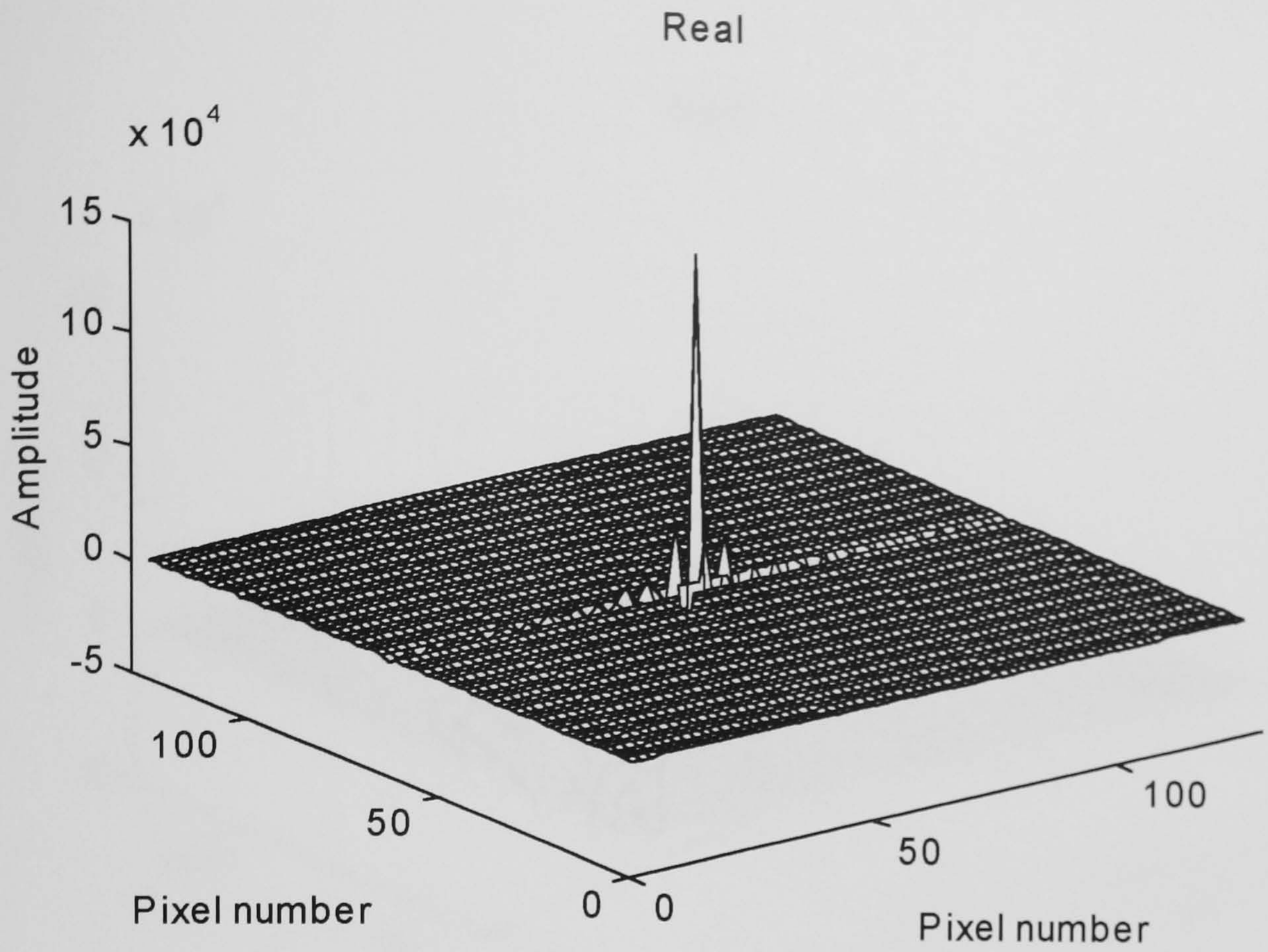

(a)

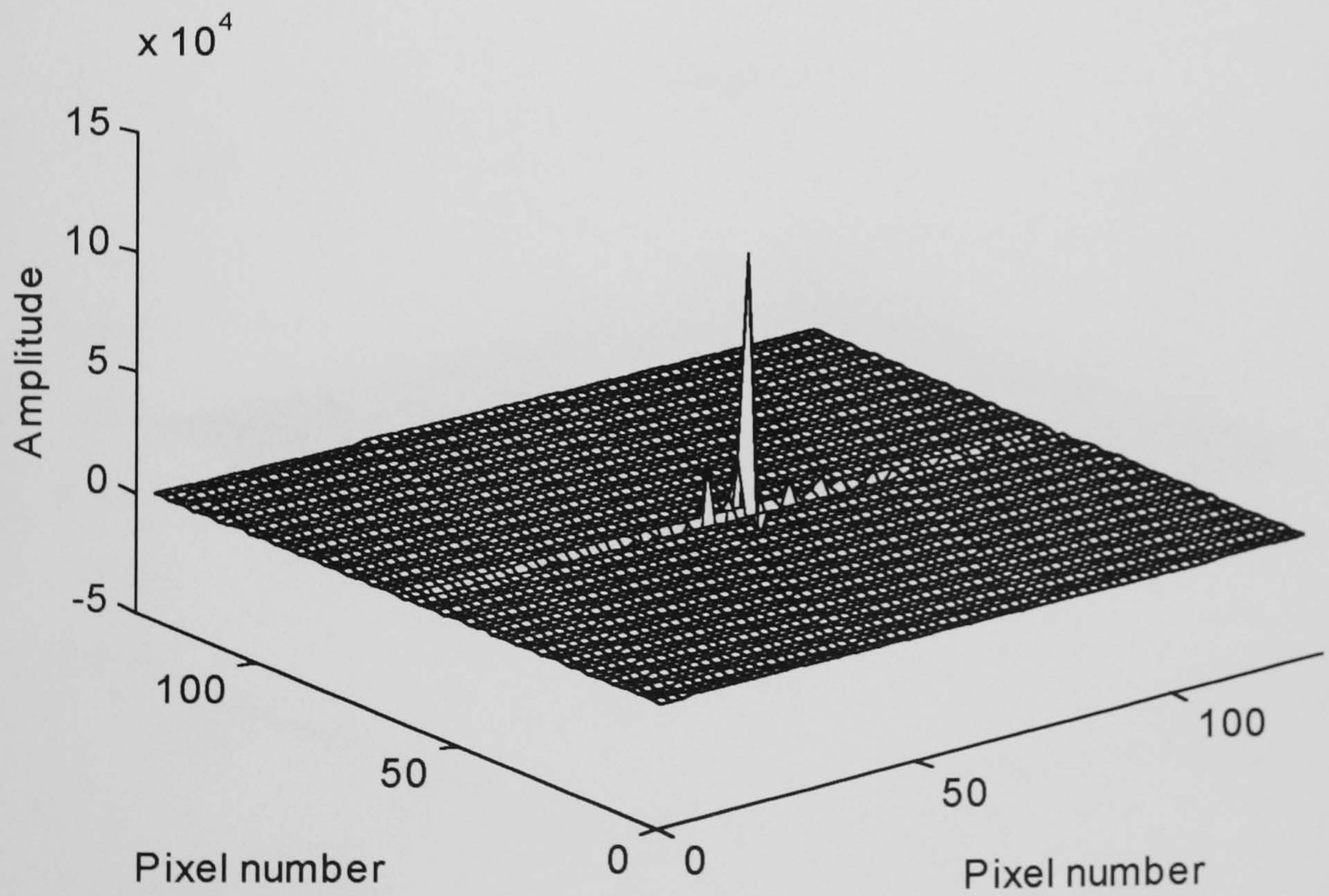

(b)

Figure 8.7 The Fourier Spectra of the Image in Figure 8.5, after filtering and frequency shifting for the grating with 22 fringes in the horizontal direction

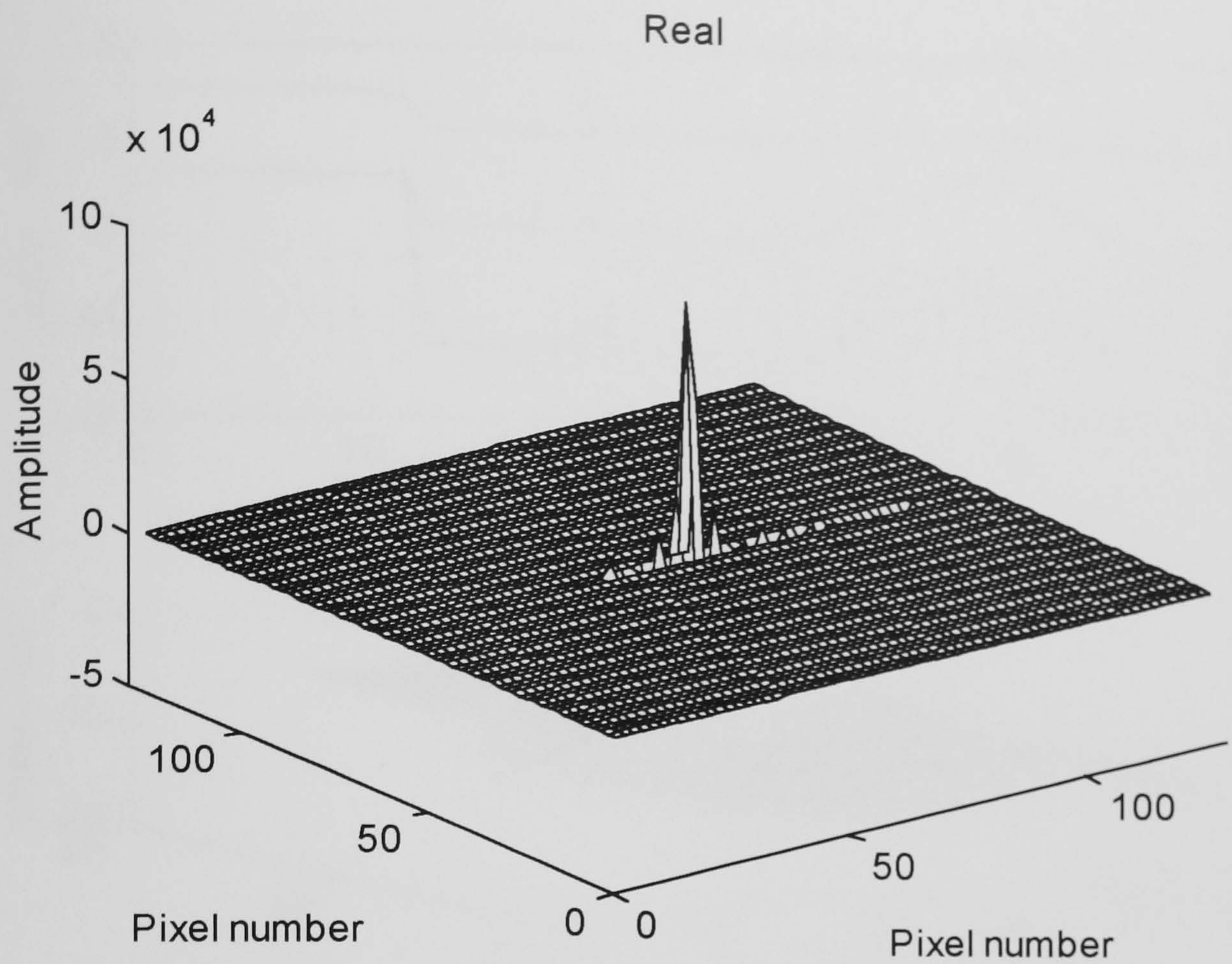

(a)

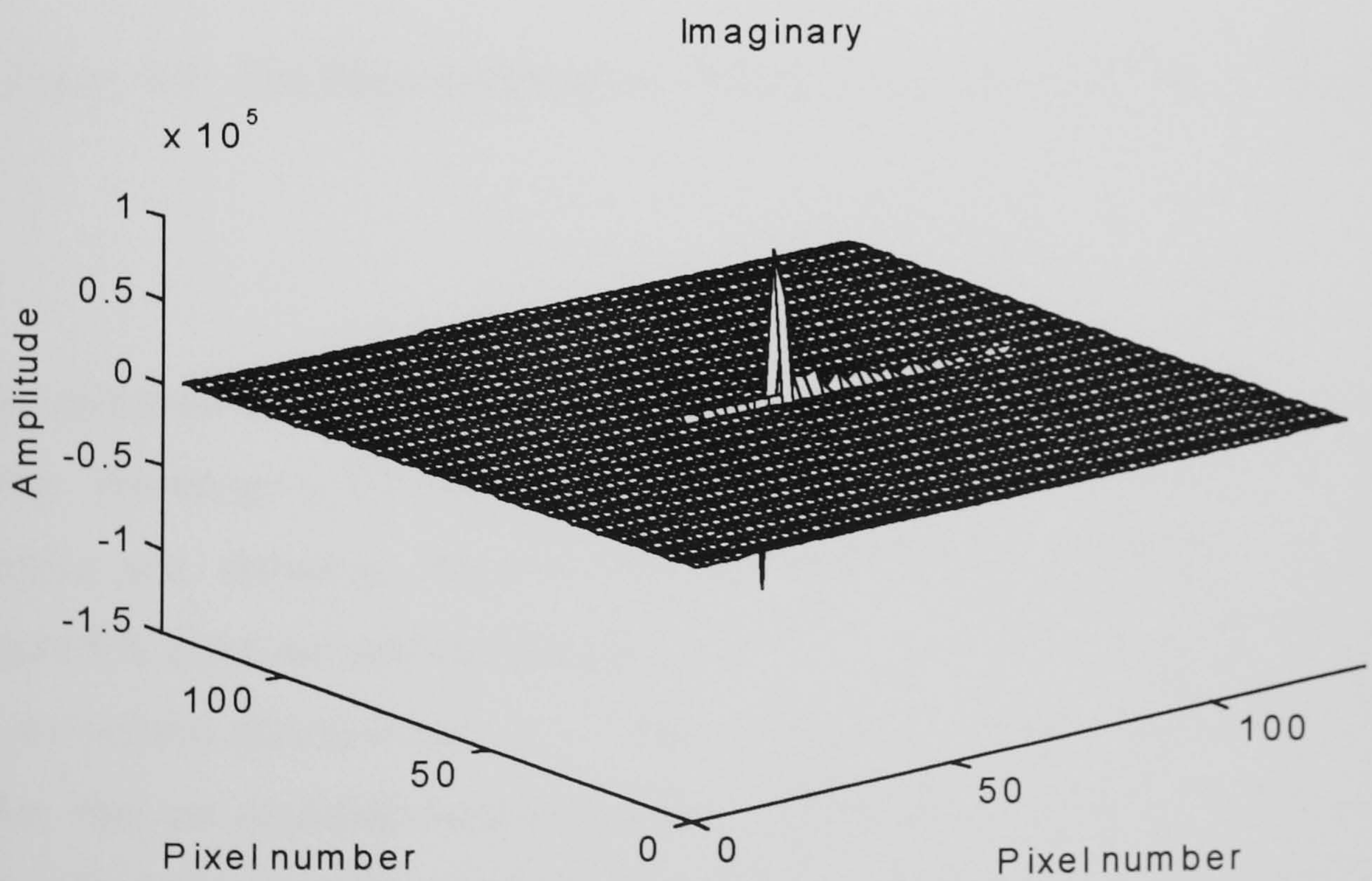

(b)

Figure 8.8 The Fourier Spectra of the Image in Figure 8.5, after filtering and frequency shifting for the grating with 4 fringes in the horizontal direction

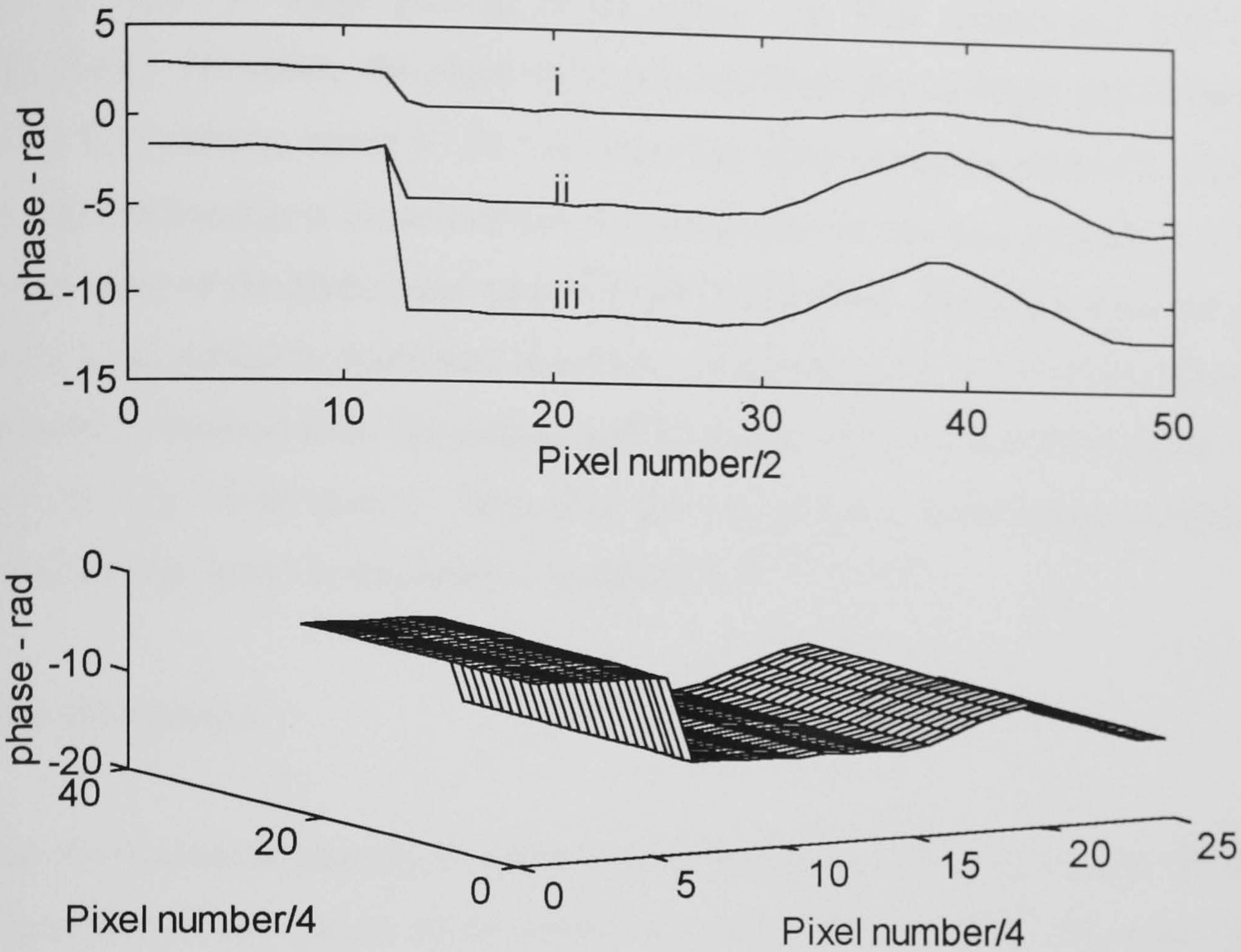

Figure 8.9 The Phase Distribution Along One Line and 3-D Plot of the Object

The deformed crossed grating image captured by the camera, is shown in figure 8.5. After the image is Fourier transformed, the real and imaginary parts of the Fourier spectra are shown in figure 8.6 (a) and figure 8.6 (b) respectively. Figure 8.7 and figure 8.8 show the real and imaginary parts of the Fourier spectra for the grating lines in the vertical direction and at an angle of about 80° relative to the vertical direction, after they are separated from each other, filtered and frequency shifted to the origin. The calculated phase distribution along one line, obtained from two separate spectra and that after phase unwrapping, are shown in figure 8.9, where (i) to (iii) are the phase distributions obtained from the gratings with 4 and 22 lines in the horizontal direction and that after correction, respectively. The three dimensional plot using the final correct phase distribution is shown in figure 8.9.

From the results of this work, the object height step of 10mm causes phase jumps for the 22 and 4 fringe gratings in the image, of 9.66 radians and 1.76 radians respectively. However, the phase value obtained from the 22 fringe map in the image is only 3.32 radians, which is 2π less than that which would be expected. Assuming that the relationship is linear and the frequency ratio of the two gratings is 5.5, the correct value of the phase jump caused by this height step calculated from the grating with a large period in horizontal direction, should be 1.76 x 5.5=9.68 radians. The phase jump obtained from the grating with 22 fringes in the horizontal direction should be $3.32 + 2\pi = 9.60$ radians. Obviously, there is an error in the results obtained. The reason for this error is discussed in section 8.4.3.

8.4.3 Discussions

From the theoretical analysis, it is known that the values of the phase jumps are directly proportional to the values of the height steps for a given spatial frequency grating. Furthermore, for a given height step, the values of the phase jumps are directly proportional to the spatial frequencies of the gratings. These are confirmed by simulation and the experimental results described above. There are still some errors which are caused by noise or imperfections contained in the grating.

In the theoretical analysis of the phase unwrapping algorithm, to ensure accurate results, it is assumed that the crossed grating is the superposition of two separate sets of lines and the number of fringes in the image are integer values for both gratings. However, in practice, it is not easy to make a crossed grating which actually represents the sum of two separate gratings. In most practical cases, the transmittance of the crossed grating is the multiplication of the individual transmittances of the two separate gratings, and this can be seen from figures 8.6 (a) and 8.6(b). This leads to some extra frequency components appearing in the frequency space in the case of the crossed grating, which do not appear in the case of the two gratings considered separately. This makes it difficult to filter and frequency shift accurately, which results in errors. In the normal Fourier transform technique, the filtering and frequency shifting

are carried out on an integer basis, rather than a fraction basis. Unsuitable filtering will leave some unwanted frequency components in the spectra, which when inverse transformed to obtain the phase distribution, result in noise components in the phase map. The non-integer value of fringes in the image will cause difficulty in the frequency shifting process and will result in errors in the phase map.

To avoid these errors, it is necessary to make the crossed grating as perfect as possible to ensure that the transmittance is the sum of the transmittances of the two individual gratings. It is also necessary to choose a suitable angle between the grating lines to obtain an appropriate frequency ratio for certain height step measurements, and to adjust the distance between the camera and the object to make sure the number of fringes in the image are integer values for both sets of grating lines. In these experiments, the crossed grating is not perfect since the transmittance is not only the sum of the two separate transmittances, but contains some extra components which result in errors.

8.5 Summary

In this chapter, an experimental system to verify the phase unwrapping algorithm and the details of the instruments used in the system, have been described. Experiment and signal processing procedure was explained. The experiments to verify the relationship between the values of the phase jump and the spatial frequency of the grating, as well as the relationship between the object height steps and the corresponding phase jump values, were described. The reasons for any errors and how to minimise their effects, have been discussed. The experimental results show that the proposed phase unwrapping algorithm can be used for the measurement of an object with certain height steps. The maximum measurable height step is determined by the spatial frequency of the grating, which has a large equivalent period in the horizontal direction. The overall accuracy of the measurement is dependent upon the spatial period of the finer grating.

Chapter 9

Conclusions and Recommendations for Further Work

9.1 Introduction

The measurement of absolute distance and three-dimensional object shape is very important in many applications. The primary purpose of this research work is, firstly, to develop an original concept proposed for the optical non-contact measurement of absolute distance and 3-D shape, based on the shadow moiré method and rotation of a grating, and to make improvements to the previous methods. Secondly, it is required to develop a phase unwrapping algorithm using a crossed grating and Fourier transform analysis, to obtain the correct phase distribution for phase maps containing discontinuities.

This thesis has described the content and progression of three different contouring methods, which are used for the measurement of absolute distance and three-dimensional object shape. It also discusses a phase unwrapping algorithm using a crossed grating and Fourier transform analysis. The height distribution of an object can be accurately measured in the presence of discontinuities caused by height steps, or noise contained in the phase map.

The earlier techniques of shadow moiré contouring, and projection moiré contouring including phase shifting, Fourier transform, and phase unwrapping, were reviewed in chapter one. Chapters two, three, and four specified the principles of each of the proposed new absolute distance contouring techniques. The experimental system used to verify the proposed methods, as well as the experimental results obtained, were given in chapter five. The features of the three different methods were analysed and compared in chapter six.

The theoretical analysis of the proposed phase unwrapping algorithm was given in chapter seven, and the corresponding experimental system, signal processing, and results obtained, were described in chapter eight. The proposed techniques have been verified by theoretical analysis, simulation and experiments. In this chapter, the

conclusions obtained by this research work are presented and recommendations for further work in these areas are made.

9.2 Conclusions

Absolute distance contouring, which is based on shadow moiré contouring and the rotation of a grating, is a new technique for the measurement of absolute distance and three-dimensional object shape. In this system, the effective period of the grating is varied by its rotation, so that the phase of the moiré pattern is also changed. By the selection of suitable rotation angles, images are captured at different positions of the grating to obtain the absolute distance from the grating to the object, as well as the object's height, through an examination of the phase differences between each of the resulting fringe patterns.

This absolute distance contouring technique is divided into three different methods. They are known as: (i) absolute distance contouring, (ii) four-image absolute distance contouring, and (iii) three-image absolute distance contouring, according to the number of images required for each measurement. In the first method, the number of images required for each measurement is not fixed and depends on the distance to be measured and the required resolution. A maximum rotation angle needs to be chosen and the number of steps to be rotated by the grating is decided by the image number. In the four-image method, two angles need to be chosen and these determine the remaining two angles according to a fixed relationship. In the three-image method, only one angle is to be chosen, the other two being decided by the relevant equations.

The maximum measurable ranges for each of the three different methods, are related to the parameters of the experimental arrangement and the rotation angles. The maximum measurable ranges are all directly proportional to the distance between the camera and the grating and the period of the grating itself. However, they are inversely proportional to the distance from the camera to the light source and the sinusoidal value of the rotation angles. In the first method, the measurable range is inversely proportional

to the sinusoidal value of the maximum rotation angle. In the four-image and three-image methods, it is inversely proportional to the sum of the sinusoidal values of the two chosen angles and the sinusoidal value of the chosen angle, respectively.

Theoretically, there is no measurable range limit for the first method. For a fixed arrangement, the measured absolute distance is directly proportional to the fringe number and inversely proportional to the sinusoidal value of the maximum rotation angle. Thus, for a given distance to be measured, the larger the rotation angle, the larger the fringe number will be. Therefore, a larger image number can be chosen to ensure that the phase difference between steps is not too great, which could result in a significant measurement error. If the image number is limited, a small rotation angle can be chosen. In this case, the fringe number and the phase difference between steps, is small. In this way, any errors caused by missing the maximum or minimum values of the cosine function, can be avoided.

The accuracy of the measurement obtained by the three different methods depends upon the accuracy of the system parameters and the rotation angles. The relationships describing these functions are similar, but they differ when considering the rotation angles. For the first method, only the accuracy of the maximum rotation angle will affect the accuracy of the measurement and despite any error in the angles between each step, it does not have any effect on the overall accuracy of the measurement. However, for the four-image and three-image methods, any error in the angles will have some effect on the measurement.

Using these methods, the absolute distance and object height can be accurately ascertained. The advantages over the previous methods are that it is not necessary to determine the absolute fringe order and there is no ambiguity between the hills and valleys of the object's surface. Therefore, some of the problems of the previous shadow moiré methods can be solved and their inconvenience can be overcome. These methods have been verified by theoretical analysis and corresponding experiments as accurate and fast techniques, offering an accuracy of better than 10μm, taking only 16, 4, and 3

seconds for the three methods respectively. They offer robust techniques for topographic inspection in many engineering areas.

The phase unwrapping algorithm, through the use of a crossed grating and the Fourier transform, is an algorithm to be used to solve the problems caused by the presence of discontinuities in the phase map, especially when measuring objects containing height steps. The algorithm is sufficiently different from, and significantly simpler than previous techniques. Using this algorithm, only simple computation is involved and only cheap equipment is required.

A crossed grating is projected onto the object's surface. The deformed grating image is equivalent to the superposition of two separate conventional grating images. After the image is Fourier transformed, the Fourier spectra are separated into two images. The inverse Fourier transform of the two images, after filtering and frequency shifting, results in two phase maps with different sensitivities. Phase unwrapping of each pixel is carried out independently. By comparing the phase differences between adjacent pixels in the two phase maps, the phase discontinuities which may be caused by object height steps or noise, can be identified and corrected. The maximum measurable phase jump depends on the original period of the grating and the angle between the two sets of grating lines. Alternatively, this is considered as the ratio of the equivalent periods of the two sets of grating lines. This has been confirmed by theoretical analysis, simulation, and experiment.

Using this algorithm, only one image is required for each measurement and no grating translation is required. This provides an advantage over the previous techniques. This method is tolerant of discontinuities and noise in the phase map. It is faster and especially suitable for the measurement of three-dimensional object profiles in the presence of height steps and in cases where there is vibration. This new technique will find applications in many new areas, for example, for the inspection of components on a production line, or in robotic vision systems.

9.3 Recommendations for Further Work

The theoretical and experimental analysis of absolute distance contouring and the phase unwrapping algorithm has been the fundamental aim of this research program. Although much investigation has been undertaken into the theoretical concepts, practical operation and analysis of data, much work is still required to develop the instrument to the stage where it may be successfully used as a stand-alone device capable of making accurate measurement of absolute distance and three-dimensional profile.

Using the absolute distance contouring technique, it has been shown that discrepancies in the measurements obtained, are caused by errors in the parameters of the experimental system, measurement of the rotation angles, and imperfections contained in the grating. Imperfections in the grating will cause incorrect phase distributions in the fringe pattern. The accuracy of the rotation angles has a direct effect on the accuracy of the whole measurement. If the grating is to be relied upon in the future for this purpose, it is essential that its transmission profile be as accurate as possible. To achieve this, one possible arrangement is to make a high quality grating through the use of two mono-mode optical fibres forming two arms of an interferometer, producing a sinusoidal intensity distribution, or Young's fringes. The disadvantage of this method is that the available light output from such a system, is likely to be small. Alternatively, a grating could be manufactured using a non-optical technique. One of these methods would be to generate mathematically perfect fringes on a computer system, the grey-scale density of which would then be printed onto an appropriate substrate. The accuracy of this method is limited by the resolution of the printing device and it may be difficult to achieve the very high resolutions obtainable by modern photographic processes.

One of the most interesting developments would be to use more advanced versions of C++ which can be used under Windows. The advantage is that they make more efficient use of computer memory for data storage so that the resolution and speed of

the measurement can be improved. The number of images required by the absolute distance contouring method can therefore be increased to improve the accuracy of the measurement. It is also more appropriate to run the program within a Windows environment, rather than under DOS as at present. The software associated with the system should, therefore, be redesigned as a Windows graphical user interface.

The most obvious development for absolute distance contouring, is to integrate the system into a self-contained instrument to be used for real world applications. To achieve this, the system should be miniaturised, using components which are as small as possible, to minimise the size of the instrument.

In the case of the phase unwrapping algorithm, since a crossed grating is used in the projection system, the quality of the grating is most important to ensure an accurate measurement. In practice, this is not so easy to achieve. It is necessary to improve the quality of the crossed grating to ensure the transmittance of the crossed grating is exactly equal to the sum of the individual transmittances of the two separate gratings. In this way, the accuracy of the measurement will be greatly enhanced. Once the crossed grating is manufactured, the angle between the two sets of lines, or the ratio of the two equivalent periods, as well as the maximum measurable phase jump, is fixed. A possible alternative technique to solve this problem is to project two interference fringe patterns of which the direction and period of the fringes can be adjusted. This could be achieved, for example, by using an optical fibre interferometer, producing fringes in two different directions. In this way, the ratio of the two equivalent spatial frequencies could be easily varied to suit the measurement of a particular range, or height step in order to optimise the accuracy. This type of technology lends itself very well to the manufacture of such optical systems using a modular approach. Fringe patterns can most readily be produced using laser diodes and pig-tailed fibres. The spacing of the fringes can be adjusted by altering the spacing between the fibre ends, which act as spatial filters, thereby producing clean interferograms. Rotation of the fringes is achieved by the simple expedient of rotating the fibres themselves. A suitable crossed grating could also be produced by using a system of three fibres, the characteristics of the pattern being dependant upon the relative positions of the fibres. Using three unpolarised fibre sources

would result in the production of a three-pattern system. Whilst this may be suitable for measurement purposes, it would require a significant amount of analysis to develop it to the stage of a usable technique. This should be examined as part of any future work programme. However, to generate a standard crossed grating system as described earlier, two of the fibre sources would need to use light which was polarised at 90 degrees to each other, thereby producing no interference pattern. Introducing a third fibre source, such that all three fibre ends are oriented in a triangular arrangement, would allow the production of a twin pattern crossed interferogram, provided the third source was polarised at 45 degrees to each of the other light sources. A system such as this is currently under development elsewhere within the University and has shown significant promise. However, it does suffer from various problems, especially from the small amount of useful light which is available at the output of the system. The interferometer and camera should be packed together as a detecting head of the whole instrument, fixing many of the geometric relationships of the system.

References

Allen, J. B. and Meadow, D. M. (1971) Removal of Unwanted Patterns from Moire Contour Maps by Grid Translation Techniques, Appl. Opt., **10**(1), 210-212

Andrews, D. R. (1982) Shadow Moiré Contouring of Imapct Craters, Opt. Eng., **21**(4), 650-654.

Arai, Y., Yokozeki, S., and Yamada, T. (1995) Fringe-Scanning Method Using a General Function for Shadow Moiré, Appl. Opt., **34**(22), 4877-4882.

Atkinson, J. T. and Lalor, M. J. (1986) A Novel Approach to Optical Range Finding, SPIE, **701**, ECOOSA, 237-243.

Beynet, P. and Plunkett, R. (1971) Plate Impact and Plastic Deformation by Projectiles, Exp. Mench., **11**(2), 64-73.

Bhat, G. K. (1994) A Fourier Transform Technique to Obtain Phase Derivatives in Interferometry, Opt. Comm., **110**, 279-286.

Bone, D. J., Bachor, H. A., and Sandeman, R. J. (1986) Fringe-Pattern Analysis Using a 2-D Fourier Transform, Appl. Opt., **25**(10), 1653-1660.

Bone, D. J. (1991) Fourier Fringe Analysis: The Two-Dimensional Phase Unwrapping Problem, Appl. Opt., **30**(25), 3627-2632.

Bryngdahl, O. (1976) Characteristics of Superposed Patterns in Optics, J. Opt. Soc. Am., **66**, 87-94.

Burton, D. R. and Lalor, M. J. (1994) Multichannel Fourier Fringe Analysis as an Aid to Automatic Phase Unwrapping, Appl. Opt., **33**(14), 2939-2948.

Butters, I. N. (1970) The Engineering Uses of Holography, Cambridge University Press, London.

Butters, J. N. and Leendertz, J. A. (1971) Speckle Pattern and Holographic Techniques in Engineering Metrology, Opt. Laser Technol., **3**, 26.

Chang, M., Hu, C. P., Lam, P., and Wyant, J. C. (1985) High Precision Deformation Measurement by Digital Phase Shifting Holographic Interferometry, Appl. Opt., **24**, 3780-3783.

Chang, M. and Wand, D. S., (1991) On-Line Automated Phase-Measuring Profilometry, Opt. Lasers Eng., **15**, 127-139.

Chang, M. and Ho, C. S. (1993) Phase-Measuring Profilometry Using Sinusoidal Grating, Exp. Mech., 117-122.

Chiang, C. (1969) Moiré Patterns From the Surface and Their Application in Measuring Topography, Btit. J. Appl. Physics (J. Physics D) Series 2, **2**, 287-292.

Chiang, C. (1975) Moiré Topography, Appl. Opt., **14**(1), 177-179.

Chu, J. and Bloch, P. (1981) Application of Moiré Patterns for Obtaining Surface Contour Information on Patients Receiving Radiotherapy, SPIE, **283**, 2-6.

Cline, H. E., Holik, A. S., and Lorensen, W. E. (1982) Computer-Aided Surface Reconstruction of Interference Contours, Appl. Opt., **21**, 4481.

Cline, H. E., Lorensen, W. E., and Holik, A. S. (1984) Automatic Moiré Contouring, Appl. Opt., **23**(10), 1454-1459.

Creath, K. (1985) Phase-Shifting Speckle Interferometry, Appl. Opt., **24**, 3053-3058.

Cusack, R., Huntley, J. M., and Golderin, H. T. (1995) Improved Noise-Immune Phase-Unwrapping Algorithm, Appl. Opt., **34**(5), 781-789.

Datta, S. K. (1926) Trans. Opt. Soc., **28**, 214.

Ding, X. H. and Pekelsky, J. R. (1987) Photometric Ordering of Ordinary Moiré Fringes, Surface Topography and Spinal Deformity IV, Gustav Fischer, Stuttgart, New York.

Dirckx, J. J. J., Decraemer, W. F., and Dielis, G. (1988) Phase Shift Method Based on Object Translation for Full Field Automatic 3-D Surface Reconstruction From Moiré Topograms, Appl. Opt., **27**(6), 1164-1169.

Dirckx, J. J. J. and Decraemer, W. F. (1989) Phase Shift Moiré Apparatus for Automatic 3D Surface Measurement, Rev. Sci. Instrum., **60**(12), 3698-3701.

Dirckx, J. J. J. and Decraemer, W. F. (1990) Automatic Calibration Method for Phase Shift Shadow Moiré Interferometry, Appl. Opt., **29**(10), 1474-1476.

Dirckx, J. J. J., Decraemer, W. F., and Eyckmans, M. M. K. (1990) Grating Noise Removal in Moiré Topography, Optik, **86**(3), 107-110.

Durelli, A. D. and Parks, V. J. (1970) Moiré Analysis of Strain (Prentice-Hall, Engle Wood Cliffs, N. J. 1970).

Dykes, B. C. (1970) Analysis of Displacements in Large Plates by the Grid-Shadow Moiré Technique, Experimental Stress Analysis and Its Influence on Design, Proc. of the 4th Inter. Conf. on Exper. Stress Analysis, Cambridge.

Ennos, A. E. (1975) Speckle Interferometry in Laser Speckle and Related Phenomena, J. C. Dainty, Ed. (Springer, Berlin, 1975), **9**, 203-253.

Gasvik, K. J. (1983) Moiré Technique by Means of Digital Image Processing, Appl. Opt., **22**(23), 3543-3548..

Gasvik, K. J. and Fourney, M. E. (1986) Projection Moiré Using Digital Video Processing: A Technique for Improving the Accuracy and Sensitivity, Transactions of the ASME, **53**, 652-656.

Gasvik, K. J. (1987) Optical Metrology, John Wiley & Sons, Chichester, 125-144.

Gasvik, K. J. and Hovde, T. (1989) Moiré Technique in 3-D Machine Vision, Opt. Lasers Eng., **10**, 241-249.

Gierloff, J. J. (1987) Phase Unwrapping by Regions, Current Developments in Optical Engineering II, SPIE , **818**, 2-9.

Ghiglia, D. C., Mastin, G. A., and Romero, L. A. (1987) Cellular-Automata Method for Phase Unwrapping, J. Opt. Soc. Am., **4A**, 267-280.

Goldstein, R. M., Zebker, H. A., and Werner, C. L. (1988) Satellite Radar Interferometry Two-Dimensional Phase Unwrapping, Radio Science, **23**(4), 713-720.

Graham, S. M. (1990) Sensitivity and Resolution Limitations of Various Moiré Methods, Opt. Lasers Eng., **12**, 119-133.

Green, R. J. and Walker, J. G. (1988) Phase Unwrapping Using a Priori Knowledge About the Band Limits of a Function, Industrial Inspection, SPIE, **1010**, 36-43.

Gruber, M. and Hausler, G. (1992) Simple, Robust and Accurate Phase-Measuring Triangulation, Optik, **89**(3), 118-122.

Halioua, M., Krishnamurthy, R. S., Liu, H., and Chiang, F. P. (1983) Projection Moiré With Moving Grating for Automated 3-D Topography, Appl. Opt., **22**(6), 850-855.

Hariharan, P., Oreb, B. F., and Brown, N. (1983) Reai-time Holographic Interferometry: A Microcomputer System for the Measurement of Vector Displacements, Appl. Opt., **22**, 876.

Hariharan, P., Oreb, B. F., and Eiju, T. (1987) Digital Phase-Shifting Interferometry: A Simple Error-Compensating Phase Calculation Algorithm, Appl. Opt., **26**, 2504-2506.

Heiniger, F. and Tschudi, T. (1979) Moiré Depth Contouring, Appl. Opt., **18**(10), 1577-1581.

Hovanesian, J. D. and Hung, Y. Y. (1971) Moiré Contour-Sum Contour-Difference and Vibration Analysis of Objects, Appl. Opt., **10**(12), 2734-2738.

Huntley, J. M. (1989) Noise-Immune Phase Unwrapping Algorithm, Appl. Opt., **28**(15), 3268-3270.

Ibrahim, M. D. (1982) Formation of Unsymmetric Moiré Fringes and Their Use in Moiré Topography, Opt. Lasers Eng., **3**, 65-72.

Ibrahim, M. D. and Takasaki, H. (1985) Two-Frequency Moiré Topography, Japanese J. of Appl. Phys., **24**(9), 1181-1182.

Idesawa, M. and Yatagai, T. (1977) General Theory of Projection-Type Moiré Topography, Sci. Papers I. P. C. R., **71**, 57-90.

Idesawa, M., Yagitai, T., and Soma, T. (1977) Scanning Moiré Method and Automatic Measurement of 3-D Shapes, Appl. Opt., **16**(8), 2152-2162.

Ivnitsky, A. and Voloshin, A. S. (1990) Measurement of the Face's Topography by Digitally Enhanced Shadow Moiré, SPIE, Close-Range Photogrammetry Meets Machine Vision, **1395,** 1043-1049.

Jin, G. C. and Tang, S. H. (1989) Automatic Moiré Contouring of Diffuse Surfaces, Opt. Eng., **28**(11), 1211-1215.

Judge, T. R., Quan, C., and Bryanston-Cross, P. J. (1992) Holographic Deformation Measurements by Fourier Transform Technique with Automatic Phase Unwrapping, Opt Eng., **31**(3), 533-543.

Judge, T. R. and Bryanston-Cross, P. J. (1994) A Review of Phase Unwrapping Techniques in Fringe Analysis, Opt. Lasers Eng., **21**, 199-239.

Kaezer, J. and Kroupa, F. (1952) The Determination of Strains by Mechanical Inteference, Czech. J. of Appl. Physics, **1**(2), 80-85.

Kafri, O. and Livnat, A. (1979) Tunable Moiré Grating for Optical Mapping, Opt. Lett., **4**(10), 314-316.

Kafri, O., Band, Y. B., and Chin, T. (1985) Real-Time Moiré Vibration Analysis of Diffusive Objects, Appl. Opt., **24**(2), 240-242.

Kafri, O. and Glatt, I. (1989) The Physics of Moiré Metrology, Wiley, New York.

Krumm, J. and Shafer, S. A. (1991) Sampled-Grating and Crossed-Grating Models of Moiré Patterns From Digital Imaging, Opt. Eng., **30**(2), 195-206.

Lamy, F., Liegeois, C., and Meryrueis, P. (1982) Three-Dimensional Automated Pattern Recognition Using the Moiré Techniques, SPIE, **360**, 345-351.

Li, J., Su, X. Y., and Guo, L. R. (1990) Improved Fourier Transform Profilometry for the Automatic Measurement of Three-Dimensional Object Shapes, Appl. Opt., **29**(12), 1439-1444.

Liao, J. E. A. ans Voloshin, A. S. (1993) Enhancement of the Shadow Moiré Method Through Digital Image Processing, Exp. Mech., 59-63.

Lim, J. S., Kim, J., and Chung, M. S. (1989) Additive Type Moiré with Computer Image Processing, Appl. Opt., **28**(13), 2677-2680.

Lim, J. S., Kim, J., and Chung, M. S. (1989) Automatic Shadow Moiré Topography: a Moving-Light-Source Method, Opt. Lett., **14**(22), 1252-1253.

Lin, J. F. and Su, X. Y. (1995) Two-Dimensional Fourier Transform Profilometry for the Automatic Measurement of Three-Dimensional Object Shapes, Opt. Eng., **34**(11), 3297-3302.

Livant, A., Kapi, O., and Erez, G. (1980) Hills and Valleys in Optical Mapping and its Application to Moiré Contouring, Appl. Opt., **19**(19), 3396-3401.

Macy, W. W. (1983) Two-Dimensional Fringe-Pattern Analysis, Appl. Opt., **22**(23), 3898-3901.

Marasco, J. (1975) Use of a Curved Grating in Shadow Moiré, Exp. Mech., 464-470.

Mauvosin, G. (1994) Three-Dimensional Shape Reconstruction by Phase-Shifting Shadow Moiré, Appl. Opt., **33**(11), 2163-2169.

Meadows, D. M., Johnson, W. O., and Allen, T. B. (1970) Generation of Surface Contours by Moiré Patterns, Appl. Opt., **9**(4), 942-947.

Morimoto, Y. and Fujisawa, M. (1994) Fringe Pattern Analysis by a Phase-Shifting Method Using Fourier Transform, Opt. Eng., **33**(110, 3709-3714.

Mulot, M. (1925) Application of the Moiré to the Study of Mica Deformations, Rev. Opt. Theor. Instrum, **4,** 252-259.

Murakami, K. and Murekami, Y. (1978) A Study of Moiré Topography. A Method for Discriminating Between the Concave and Convex Regions of an Object., Bul. of the JSME, **21**(152), 196-202.

Nakadate, S., Magome, N., Honda, T. and Tsuliuchi, J. (1981) Hybrid Holographic Interferometer for Measuring Three-Dimensional Deformations, Opt. Eng., **20**, 246.

Nakadate, S., Yatagai, T. and Saito, H. (1983) Computer-Aided Speckle Pattern Interferometry, Appl. Opt., **22**, 237.

Nakadate, S. and Saito, H. (1985) Fringe Scanning Speckle-Pattern Interferometry. Appl. Opt. **24**(14), 2172-2180.

Ning, P. T. and Peng, W. L. (1988) Automatic Analysis of Moiré Fringe Patterns by Using an Image-Processing System, Exp. Mech., 350-354.

Oreb, B. F. and Dorsch, R. G. (1994) Profilometry by Phase-Shifted Talbot Images, Appl. Opt., **33**(34), 7955-7962.

Patoski, K. and Kujawinska, M. (1985) Three-Way gratings for Moiré Interferometry, Opt. Comm., **53**(5), 285-291.

Pekelsky, J. R. (1987) Automated Contour Ordering in Moiré Topograms, Opt. Eng., **26**(6), 479-486..

Peng, X., Gao, Z., and Zhou, S. M. (1995) Surface Contouring by a new Type of Digital Moiré Technique, Optik, **100**(20, 63-67.

Perrin, J. C. and Thomas, A. (1979) Electronic Processing of Moiré Fringes: Application to Moiré Topography and Comparison with Photogrammetry, Appl. Opt., **18**(4), 563-574.

Perry, K. E. and McKelvie, J. (1993) A Comparison of Phase Shifting and Fourier Methods in the Analysis of Discontinuous Fringe Patterns, Opt. Lasers Eng., **19**, 269-284.

Pirodda, L. (1969) Principi e Applicazione di un Mteoto Fotogrammetrico Basatto Sull'impiego del Moiré, Rivista di Ingegnria, **12,** 1-129.

Pirodda, L. (1982) Shadow and Projection Moiré Techniques for Absolute or Relative Mapping of Surface Shapes, Opt. Eng., **21**(4), 640-649.

Poon, C. Y., Kujawinska, M., and Ruiz, C. (1993) Automated Fringe Pattern Analysis for Moiré Interferometry, Exp. Mech., 234-241.

Post, D. (1982) Developments in Moiré Interferometry, Opt. Eng., **21**(3), 458-467.

Post, D. (1991) Moiré Interferometry: Advances and Applications, Exp. Mech., 276-280.

Quiroga, J. A., Gonzalez-Cano, A., and Bernabeu, E. (1995) Stable-Marriages Algorithm for Preprocessing Phase Maps with Discontinuity Sources, Appl. Opt., **34**(23), 5029-5038.

Rayleigh, L. (1874) On the Manufacture and Theory of Diffraction Gratings, Philos. Mag., **47**(4th series), 18-93 and 193-205.

Redner, A. S. (1985) Shadow Moiré Method-Principles and Applications, Bulletin SM-2, July 1985. Strainoptic Technologies, Inc., North Wales, PA.

Redner, A. S. (1990) Shadow Moiré Surface Inspection, Materials Evaluation, **48**, 873-878.

Reid, G. T. (1984) Moiré Fringes in Metrology, Opt. Lasers Eng., **5**, 63-93.

Reid, G. T., Rixon, R. C., and Messer, H. I. (1984) Absolute and Comparative Measurements of Three-Dimensional Shape by Phase Measuring Moiré Topography, Opt. Lasers Tech., **16**(6), 315-319.

Reid, G. T., Rixon, R. C., Marshall, S. J., and Stewart, H. (1986) Automatic On-Line Measurements of Three-Dimensional Shape by Shadow Casting Moiré Topography, Wear, **109**, 297-304.

Reid, G. T. (1986/7) Automatic Fringe Analysis -A Review, Opt. Lasers Eng.,7, 37-68.

Roddier, C. and Roddier, F. (1987) Interferogram Analysis Using Fourier Transform Techniques, Appl. Opt., **26**(9), 1668-1673.

Roger, R. (1979) Moiré Contouring-A Re-interpretation, Univ. of Oxford Dept. of Energ. Sci., OUL Rpt., 1294.

Sciammarella, C. A., Ross, B. E., and Sturgeon, D. (1965) Basic Optical Law in the Interpretation of Moiré Patterns Applied to the Analysis of Strains, Part 1 and 2, Exp. Mech., **5**(5,6), 154-166.

Sciammarella, C. A. (1981) Proc. I.U.T.A.M. on Optical Methods in Mechanics of Solids, Poitiers, France(1979), Ed. A. Lagarde, Sijthoff and Noordhoff.

Sciammarella, C. A. (1982) Holigraphic Moiré, An Optical Tool for the Determination of Displacements, Strains, Contours and Slopes of Surfaces. Opt. Eng., **21**(3), 447-457.

Sciammarella, C. A. (1982) The Moiré Method-A Review, Exp. Mech., 418-433.

Singh, H. and Sirkis, J. S. (1994) Direct Extraction of Phase Gradients From Fourier Transform and Phase-Step Fringe Patterns, Appl. Opt., **33**(22), 5016-5020.

Sommargren, G. E. (1977) Double-Exposure Holographic Interferometry Using Common Path Reference Waves, Appl. Opt., **16**, 1736.

Srinivasan, V., Liu, H. C., and Halioua, M. (1984) Automated Phase Measuring Profilometry of 3-D Diffuse Objects, Appl. Opt., **23**, 3105-3108.

Srinivasan, V., Liu, H. C., and Halioua, M. (1985) Automated Phase-Measuring Profilometry: A Phase Mapping Approach, Appl. Opt., **24**(2), 185-188.

Strand, T. C. (1985) Optical Three-Dimensional Sensing for Machine Vision, Opt. Eng., **24**(1), 33-40.

Strobel, B. (1996) Processing of Interferometric Phase Maps as Complex-valued Phasor Image, Appl. Opt., **35**(13), 2192-2198.

Su, X. Y., Zhou, W. S., Bally, G. V., and Vukicevic, D. (1992) Automated Phase-Measuring Profilometry Using Defocused Projection of a Ronchi Grating, Opt. Comm., **94**, 561-573.

Suganuma, M. and Yoshizawa, T. (1991) Tree-Dimensional Shape Analysis by Use of a Projected Grating Image, Opt. Eng., **30**(10), 1529-1533.

Surrel, Y. (1993) Phase Stepping: A New Self-Calibrating Algorithm, Appl. Opt., **32**(19), 3598-3600.

Takeda, M., Ina, H., and Kobayashi, S. (1982) Fourier-Transform Method of Fringe Pattern Analysis for Computer-Based Topography and Interferometry, J. Opt. Soc. Am., **72**(1), 156-160.

Takeda, M. and Mutoh, K. (1983) Fourier Transform Profilometry for the Automatic Measurement of 3-D object Shapes, Appl. Opt., **22**(24) 3977-3982.

Takeda, M. Nagatome, K., and Watanabe, Y. (1993) Phase Unwrapping by Neural Network, Proc. 2nd Int Workshop on Automatic Processing of Fringe Patterna, 136-141.

Takeda, M. and Yamamoto, H. (1994) Fourier Transform Speckle Profilometry: Three-Dimensional Shape Measurements of Diffuse Objects with Large Height Steps and /or Spatially Isolated Surface, Appl. Opt., **33**(34), 7829-7837.

Takasaki, H. (1970) Moiré topography, Appl. Opt., **9**(6), 1457-1472.

Takasaki, H. (1973) Moiré Topography, Appl. Opt., **12**(4), 845-850.

Takasaki, H. (1974) Moiré Topography, Proc. of the ISP Biostereometrics, 74 Symp..

Takasaki, H. (1979) Moiré Topography Systems and Applications, Handbook of Non-Topographic Photogrammetry, Amer. Soc. of Photogrammetry, 167-184.

Takasaki, H. (1982) Moiré Topography from its Birth to Practical Application, Opt. Lasers Eng., **3**, 3.

Theocaris, P. S. (1964) Moiré Method in Plates, Non-Classical Shell Problems, Proc. of the IASS Symp., Warsaw, 877-889.

Toyooka, S. and Iwaasa, Y. (1986) Automatic Profilometry of 3-D Diffuse Objects by Spatial Phase Detection, Appl. Opt., **25**(10), 1630-1633.

Valera, J. D. and Jones, J. D. C. (1993) Phase Stepping in Projected-Fringes Fibre-Based Moiré Interfermetry, Elec. Lett., **29**(20) 1789-1791.

Walker, C. A. (1994) A Historical Review of Moiré Interferometry, Exp. Mech., 281-299.

Wegdam, A. M. F., Podzimek, O., and Bosing, H. T. (1992) Simulation of Shadow Moiré Systems Containing a Curved Grating Surface, Appl. Opt., **31**(280), 5952-5955.

Weller, R. and Shephard, B. M. (1948) Displacement of Measurement by Mechanical Interferometry, Pro. of the SESA, **6**(1), 3538.

Wykes, C. (1995) Surface Topography Measurement Using Digital Moiré Contouring-Errors and Limitations, Proc. Instn. Mech. Engrs., **209**, 317-325.

Yasuhiko, A., Yokozeki, S., and Yamada, T. (1995) Fringe Scanning Method Using a General Function for Shadow Moiré, Appl. Opt., **34**(22), 4877-4882.

Yatagai, T., Idesawa, M., and Saito, S. (1982) Automatic Topography Using High Precision Digital Moiré Methods, Proc. Soc. Photo-Opt. Instrum. Eng., **361**, 81.

Yoshino, Y. and Takasaki, H. (1976) Doubling and Visibility Enhancement of Moiré Fringes of the Summation Type, Appl. Opt., **15**, 1124-1126.

Yoshizawa, T. (1993) Shadow Moiré Topography by Means of the Phase Shift Method, Opt. Eng., **32**(7), 1668-1674.

Yuk, K. C., Heung, J., and Chang, S. (1994) Determination of the Absolute Order of Shadow Moiré Fringes by Using Two Differently Colored Light Sources, Appl. Opt., **33**(1), 130-132.

Zhao, H., Chen, W., and Tan, Y. (1994) Phase Unwrapping Algorithm for the Measurement of Three-Dimensional Object Shapes, Appl. Opt., **33**(20), 4497-4500.

Appendix

Publications

(1) X. Xie, J. T. Atkinson, M. J. Lalor and D. R. Burton, *Three-Map Absolute Moiré Contouring*. Applied Optics, **35**(35), 6990-6995(1996).

(2) X. Xie, J. T. Atkinson, M. J. Lalor and D. R. Burton, *Absolute Shadow Moiré Contouring by Rotating the Grating*. SPIE Vol. 2778, Proceeding of 17th Congress of the International Commission for Optics, August 1996, Korea. pp. 485-486.

(3) X. Xie, J. T. Atkinson, M. J. Lalor and D. R. Burton, *Analysis and Comparison of Three Different Absolute Moiré Contouring Methods*. The proceeding of the applied optics divisional conference of the Institute of Physics, Reading, UK. Sept. 1996. pp.222-227

(4) X. Xie and J. T. Atkinson, *Absolute Moiré Contouring*. Optics and Lasers in Engineering, **27**(2), 149-159(1997).

(5) X. Xie, J. T. Atkinson, M. J. Lalor and D. R. Burton, *Effects on Absolute Moiré Contouring by Using Gratings with Different Profile and Period and Rotating Angles*. Optics and Lasers Engineering, **27**(3), 247-257(1997).

(6) X Xie, M J Lalor, D R Burton, and M M Shaw, *Four-Map Absolute Distance Contouring*. Optical Engineering, in press 1997.

(7) X. Xie, M J Lalor, D R Burton, and M M Shaw, *Phase-Unwrapping Algorithm in the Presence of Discontinuities Using a System with Crossed Grating*. Submitted to Optics and Lasers in Engineering, 1997.

Four-Map Absolute Distance Contouring

Abstract

A new method called four-map absolute distance contouring, based on the shadow moiré technique, is described in this paper. In this system, the period of a sinusoidal grating is varied through its rotation, with the effect that the phase of the moiré pattern is also changed. By selecting suitable rotation angles, four images at different grating positions are acquired, from which the absolute distance from the object to the grating can be determined. The theoretical analysis is presented for the method, which has been verified by suitable laboratory experimentation. The measurable range is directly proportional to the period of the grating and inversely proportional to the angles through which the grating is rotated. The results show that the method is fast and accurate.

Phase-Unwrapping Algorithm in the Presence of Discontinuities Using a System with Crossed Grating

Abstract

A new phase-unwrapping algorithm for the phase map containing discontinuities by the use of a system with crossed grating is described in this paper. A crossed grating is projected onto the object in the usual way, the deformed grating image acquired is Fourier transformed and the frequency spectra for the individual gratings are separated. Using both phase distributions which have different sensitivities, the correct phase values in the presence of discontinuities, especially those caused by the object with height steps, can be obtained. This algorithm is fast and accurate. The results of the measurement of a three-dimensional object with height steps are presented.

Full Papers

Three-map absolute moiré contouring

Xinjun Xie, John T. Atkinson, Michael J. Lalor, and David R. Burton

In the shadow-moiré system, the period of the grating is varied by rotation of the grating, so the phase of the moiré pattern is changed as well. By the selection of suitable rotation angles, three images at different positions of the grating are acquired to obtain the absolute distance from the object to the grating. A theoretical analysis is presented for the method, and some experiments have been done to verify the theoretical analysis. The results show that the method is fast and the accuracy is better than 10 μm. The measurable range is directly proportional to the period of the grating and inversely proportional to the angles at which the grating is rotated. © 1996 Optical Society of America

Key words: Three map, absolute moiré contouring, projection moiré, shadow moiré, phase shifting, sinusoidal intensity grating, rotating grating.

1. Introduction

In the past decades, moiré techniques have been widely used as a simple and powerful means of three-dimensional shape analysis for various applications, including contouring large objects and living bodies, obtaining differences in object shapes, etc.[1–10] There are projection-moiré and shadow-moiré methods for determining the objects' contouring. Although shadow moiré suffers certain limitations, the main benefits of this method in terms of potential accuracy tend to outweigh these problems. The main limitation of shadow moiré is that the measurement-field size is limited by the cross-sectional size of the grating itself. There are also potential problems arising from issues such as the diffraction effect, but this occurs only when the grating is some distance from the object being measured or the grating spacing is fine.

Several techniques have been introduced to increase the accuracy and resolving power of the contouring method.[11–14] Projection moiré itself becomes a phase-shifting method by the use of one or two gratings in the system. Also, some investigations have been done by the use of the interference fringes of a laser to replace the projection of the grating[15] and by the use of the rotatable polarizer for phase shifting.[16] However, it could be difficult to control the phase of all fringes precisely in a shadow-moiré system, as in a projection-moiré system. In recent years a few techniques[17–22] have been used in shadow moiré to vary the phase of the moiré pattern by a change in the distance between the grating and the camera, or between the camera and light source, and by the movement of the object or grating vertically to get a few frames phase change. All of these methods need accurate control of the movement.

Here, we propose one trial to apply phase shifting to the shadow-moiré process by rotation of the grating. When the grating is rotated, the period of the grating, as well as the phase of the moiré pattern, is changed. By rotation of the grating to three different positions, three moiré patterns with different phase distributions can be obtained. The absolute distance from the object to the grating and the object height distribution can be obtained directly. The experiment has verified the proposed method as a fast and accurate method.

2. Theoretical Analysis

Figure 1 is a diagram of the absolute moiré-contouring arrangement. The sinusoidal wave-intensity grating is mounted on a bearing such that it can be rotated about an axis normal to the plane of the rulings. The object is illuminated by a light source, which need not be coherent. The shadow of the grid is cast onto the surface through an angle α. Hence the shadow on the object is shifted in the y direction by a distance $z(x, y)\tan\alpha$ relative to the grating. Light from this scene passes through a grating and a lens, forming an image in the region of the sensor, as depicted. The light source and the

The authors are with the Coherent and Electro-Optics Research Group, Liverpool John Moores University, Byrom Street, Liverpool L3 3AF, United Kingdom.

Received 29 February 1996; revised manuscript received 13 August 1996.

0003-6935/96/356990-06$10.00/0

© 1996 Optical Society of America

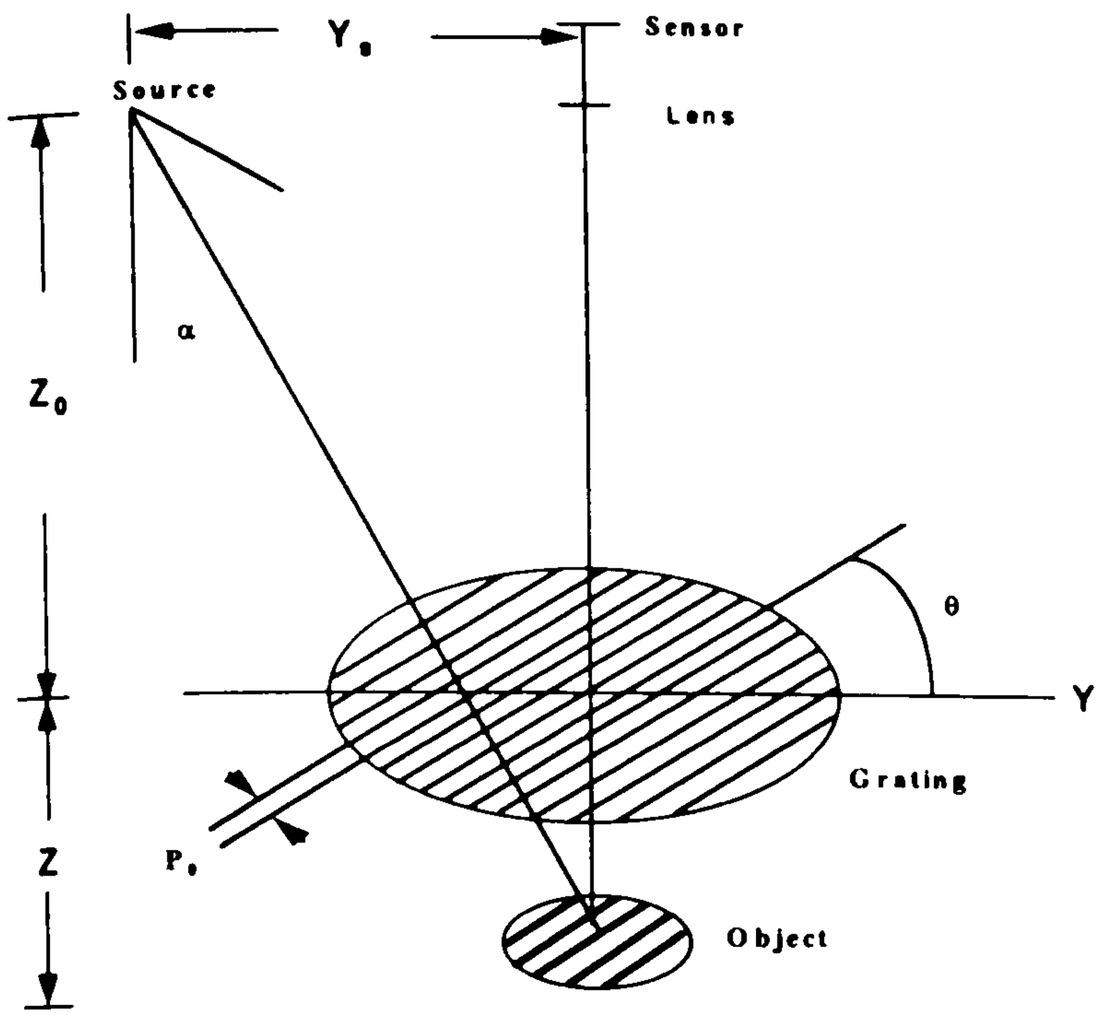

Fig. 1. Schematic diagram of absolute moiré contouring.

lens are the same perpendicular distance z_0 from the grating. Together with the object point at z they define a plane. The intersection of this plane with the grating defines the line along which the period p of the grating is measured. This line also serves as the datum for the rotation of the grating. When the rulings are parallel to it, the angle θ is zero. The system can be analyzed as follows.

For a sinusoidal wave grating, the transmission function is

$$T(y) = \frac{1}{2} + \frac{1}{2}\sin\left(\frac{2\pi}{P_0}y\right), \tag{1}$$

where p_0 is the period of the grating. The intensity incident on the object at point z may be represented by

$$T(y - z\tan\alpha) = T\left(y - \frac{zy_s}{z + z_0}\right). \tag{2}$$

The observed moiré pattern M can be found by the multiplication of Eqs. (1) and (2):

$$M = I_0 T(y) T\left(y - \frac{zy_s}{z + z_0}\right).$$

The intensity of the moiré pattern can be written as

$$M = \frac{I_0}{4}\left\{1 + \sin\left(\frac{2\pi}{P}y\right) + \sin\left[\frac{2\pi}{P}\left(y - \frac{zy_s}{z + z_0}\right)\right] - \frac{1}{2}\cos\left[\frac{2\pi}{P}\left(2y - \frac{zy_s}{z + z_0}\right)\right] + \frac{1}{2}\cos\left(\frac{2\pi}{P}\frac{zy_s}{z + z_0}\right)\right\}, \tag{3}$$

where I_0 is the amplitude of the incident light intensity. The contour item could be expressed as

$$M' = \frac{I_0}{4}\left[1 + \frac{1}{2}\cos\left(\frac{2\pi}{P}\frac{zy_s}{z + z_0}\right)\right]. \tag{4}$$

As the grating is rotated at an angular velocity ω, the measured period of the grating changes such that

$$P = \frac{P_0}{\sin\theta}, \qquad \theta = \omega t, \tag{5}$$

So Eq. (4) can be rewritten as

$$M' = \frac{I_0}{4}\left[1 + \frac{1}{2}\cos\left(\frac{2\pi}{P_0}\frac{zy_s}{z + z_0}\sin\theta\right)\right]. \tag{6}$$

So at three different position of θ, we can get different values of P, as well as M:

$$M_1' = K'\left[1 + k''\cos\left(\frac{2\pi}{P_0}\frac{zy_s}{z + z_0}\sin\theta_1\right)\right], \tag{7}$$

$$M_2' = K'\left[1 + k''\cos\left(\frac{2\pi}{P_0}\frac{zy_s}{z + z_0}\sin\theta_2\right)\right], \tag{8}$$

$$M_3' = K'\left[1 + k''\cos\left(\frac{2\pi}{P_0}\frac{zy_s}{z + z_0}\sin\theta_3\right)\right], \tag{9}$$

where $K' = I_0/4$ and $k'' = 1/2$.

If we let $A = \sin\theta_1$, $B = \sin\theta_2$, $C = \sin\theta_3$, and

$$\Phi = \frac{2\pi}{P_0}\frac{zy_s}{z + z_0}, \tag{10}$$

then we get

$$\frac{M_1' - M_2'}{M_2' - M_3'} = \frac{\cos(A\Phi) - \cos(B\Phi)}{\cos(B\Phi) - \cos(C\Phi)} = \frac{\sin\left(\frac{A + B}{2}\Phi\right)\sin\left(\frac{A - B}{2}\Phi\right)}{\sin\left(\frac{B + C}{2}\Phi\right)\sin\left(\frac{B - C}{2}\Phi\right)}. \tag{11}$$

If we let $A + B = 2(B + C)$ and $A - B = B - C$, we have $A = 5C$ and $B = 3C$. So Eq. (11) becomes

$$\frac{M_1' - M_2'}{M_2' - M_3'} = 2\cos(0.4A\Phi). \tag{12}$$

For convenience, let

$$H = 0.5 * \frac{M_1' - M_2'}{M_2' - M_3'}. \tag{13}$$

Then we can have

$$\Phi = \frac{1}{0.4A}\cos^{-1}(H). \tag{14}$$

From Eqs. (10) and (14), for simplifying the expression, assume that $z_0 \gg z$, then the object height could

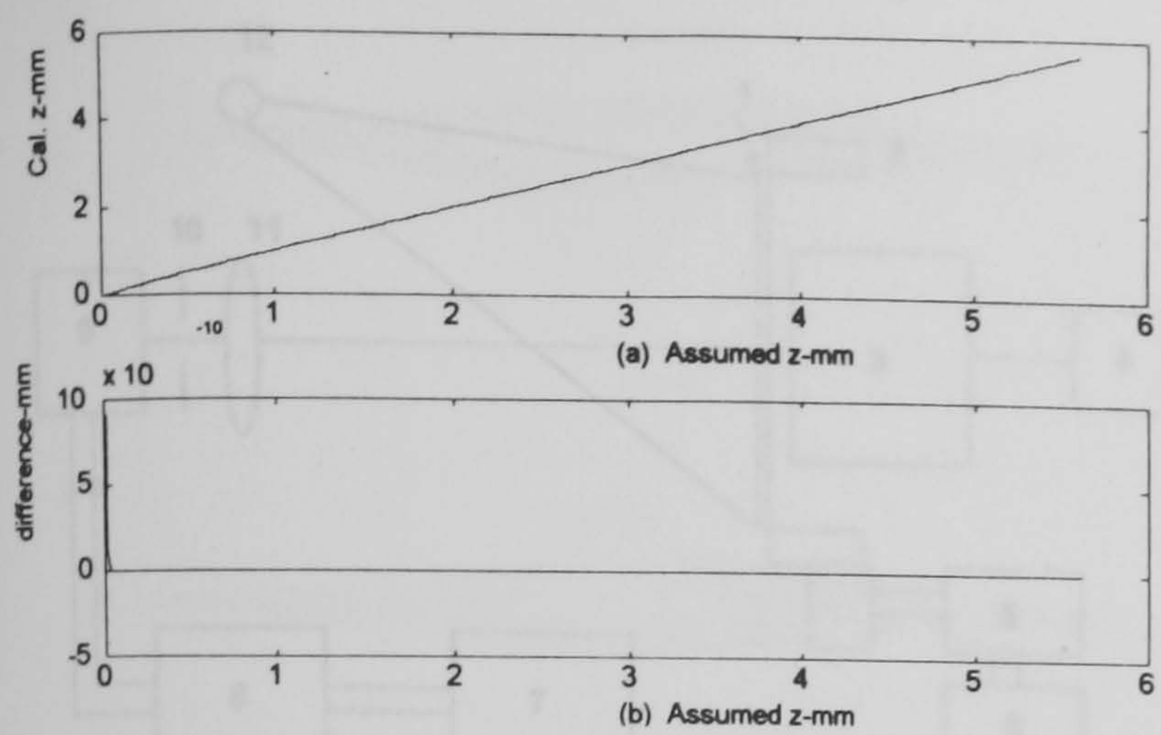

Fig. 2. Relation of the calculated and assumed values of z (0–5.625 mm). Cal., calculated.

be calculated as

$$z = \frac{P_0 z_0}{0.8\pi y_s A} \cos^{-1}(H). \tag{15}$$

In Eq. (15), P_0, z_0, and y_s are known values of the experiment setup, so if we choose the value of $A(\theta_1)$, then the value of z can be calculated from Eqs. (13) and (15). From Eqs. (12) and (13) we can see that H varies between -1 and 1 as a periodical function of the assumed value of z, and the phase Φ varies as a periodical function of the assumed value of z as well. So if we use the Φ values in Eq. (15), the relation between the calculated and assumed values of z is similar to that of Φ. This means that, as the assumed value of z increases, the calculated value of z varies from zero to a maximum value z_{max}, then decreases to zero periodically. The value of z_{max} can be obtained from Eq. (15) when $H = -1$ as

$$z_{max} = \frac{P_0 z_0}{0.8 y_s \sin(\theta_1)}. \tag{16}$$

From the above analysis we can see that this method couldn't be applied directly to the measurement of an object height unless the maximum height of the object were less than or equal to z_{max}. This is because, when $\cos^{-1}(H)$ varies from zero to π, there is a linear relation between the calculated and assumed values of z. So we can use this method for some limited object-height measurements. When we have values of $P_0 = 1.0$ mm, $z_0 = 450$ mm, and $y_s = 100$ mm, then we see the relation of the calculated and assumed values of z for the first linear part (z from zero to $z_{max} - 5.625$ mm, in this case) as drawn in Fig. 2(a). Figure 2(b) shows the difference between the calculated and assumed values of z; it can be seen that the difference is very small.

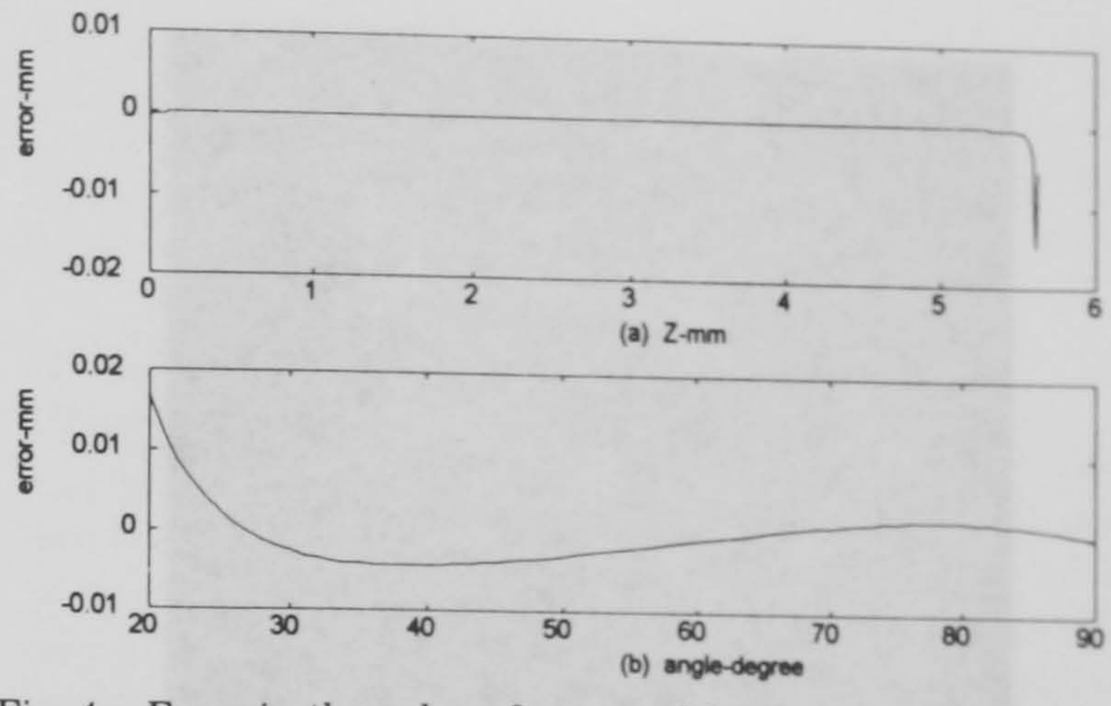

Fig. 4. Error in the value of z, caused by the error in the measurement of θ_1 for $P_0 = 1.0$ mm, $z_0 = 450$ mm, and $y_s = 100$ mm: (a) $\theta_1 = 90°$, $\Delta\theta_1 = 0.05°$, and $z = 0$–5.625 mm; and (b) $\theta_1 = 20$–$90°$, $\Delta\theta = 0.05°$, and $z = 5.0$ mm.

From the theoretical analysis, we also found that z_{max} is directly proportional to the grating's period P_0 and the distance from the camera to the object z_0, and it is inversely proportional to the angle θ_1 and the distance from camera to the light source y_s. From Eq. (16) we obtain the relations among z_{max} and z_0, P_0, y_s, and $A(\theta_1)$, which are shown in Fig. 3. So we can get different values for z_{max} by choosing different parameters of the experiment setup. But it is convenient to choose the angle θ_1 to get the required value of z_{max} for a certain height or depth of the object, e.g., when $\theta_1 = 90°$, 30°, 10°, $z_{max} = 5.625$, 11.25, and 32.393 mm, respectively, under the conditions of $z_0 = 450$ mm, $P_0 = 1.0$ mm, and $y_s = 100$ mm.

From Eq. (15) we can see that any errors from the experimental setup, the period of the grating, or the rotating angles will cause an error in the results. Here we consider only the effects from the rotating

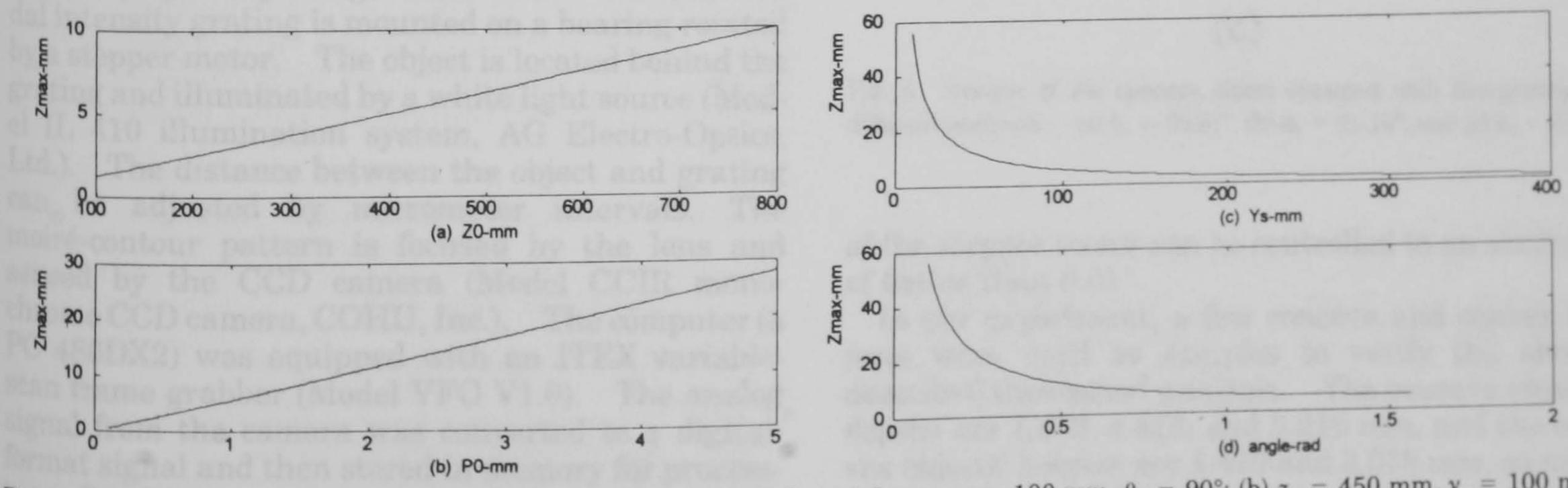

Fig. 3. Relations of z_{max} to z_0, P_0, y_s, and θ_1. Parameters: (a) $P_0 = 1.0$ mm, $y_s = 100$ mm, $\theta_1 = 90°$; (b) $z_0 = 450$ mm, $y_s = 100$ mm, $\theta_1 = 90°$; (c) $P_0 = 1.0$ mm, $z_0 = 450$ mm, $\theta_1 = 90°$; and (d) $P_0 = 1.0$ mm, $z_0 = 450$ mm, $y_s = 100$ mm.

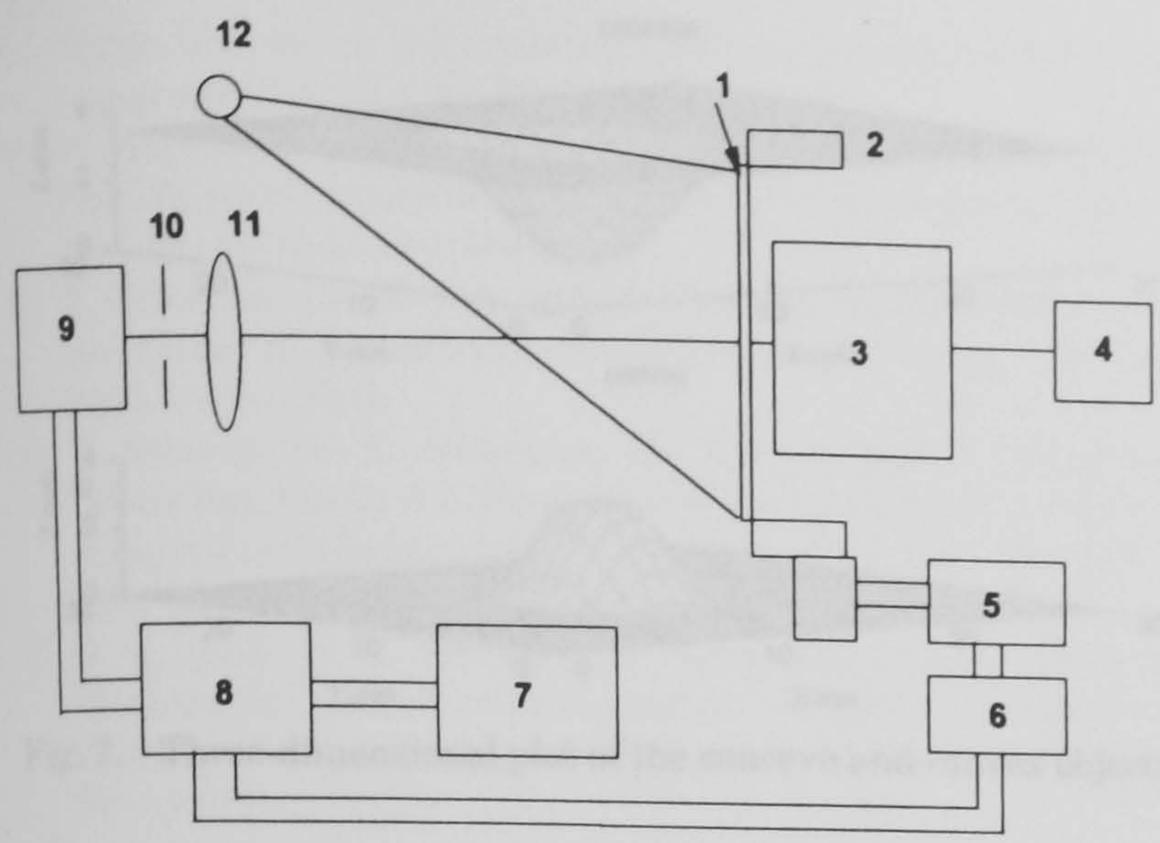

Fig. 5. Diagram of the absolute moiré-contouring instruments: (1) grating, (2) bearing, (3) object, (4) micrometer, (5) stepper motor, (6) control board, (7) monitor, (8) computer, (9) CCD camera, (10) aperture, (11) lens, and (12) light source.

angles. If the error $\Delta\theta_1$ is 0.05° when $\theta_1 = 90°$, $P_0 = 1.0$ mm, $z_0 = 450$ mm, $y_s = 100$ mm, and θ_2 and θ_3 are correct, then we see the simulated error Δz, which is shown in Fig. 4(a). When the value of z is near that of z_{max} (here it is 5.625 mm), the maximum value for Δz is approximately 15 μm. But if $z \leq 5.5$ mm, then Δz is less than 1 μm. From Fig. 4(b) it can be seen that the errors caused by the same value of $\Delta\theta_1$ are related to the value of θ_1. When θ_1 is smaller than 30°, Δz is inversely proportional to the value of θ_1. When $\theta_1 = 20°$ and $z = 5.0$ mm, Δz is approximately 16 μm. And Δz is between ±4 μm when θ_1 is in the range of 30° to 90°. Also, if the errors of θ_1, θ_2, and θ_3 are same, e.g., $\Delta\theta = 0.05°$, and under the same conditions as given for Fig. 4(a), the maximum value of Δz is less than 0.001 μm. So for the measurement of certain-height objects, to reduce the error of the measurement, a suitable rotating angle should be chosen.

3. Experiment and Results

Figure 5 shows a schematic diagram of the experimental system used for the three-map absolute moiré contouring. The whole experimental process is controlled by specially designed software. The sinusoidal intensity grating is mounted on a bearing rotated by a stepper motor. The object is located behind the grating and illuminated by a white light source (Model IL 410 illumination system, AG Electro-Optics, Ltd.). The distance between the object and grating can be adjusted by micrometer intervals. The moiré-contour pattern is focused by the lens and sensed by the CCD camera (Model CCIR monochrome CCD camera, COHU, Inc.). The computer (a PC 486DX2) was equipped with an ITEX variable-scan frame grabber (Model VFG V1.0). The analog signal from the camera was converted to a digital-format signal and then stored in memory for processing. By the rotation of the grating to three different positions, three images are captured. The rotation

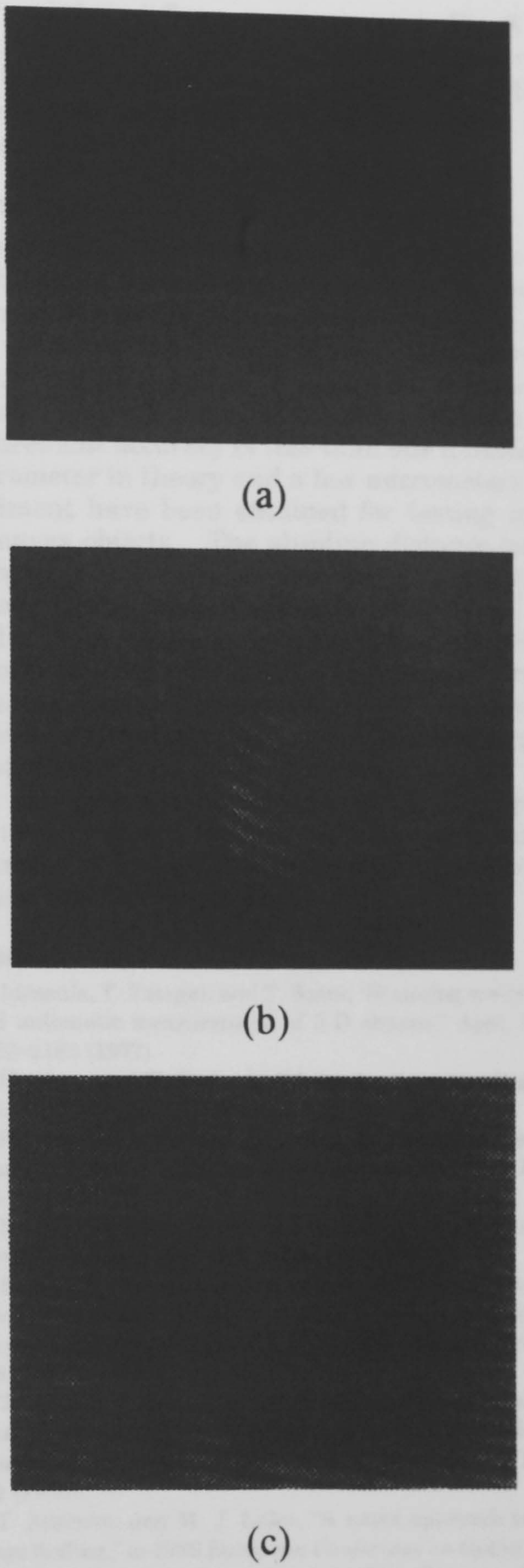

Fig. 6. Images of the concave object obtained with the grating at different positions: (a) $\theta_1 = 36.87°$, (b) $\theta_2 = 21.10°$, and (c) $\theta_3 = 6.89°$.

of the stepper motor can be controlled to an accuracy of better than 0.01°.

In our experiment, a few concave and convex objects were used as samples to verify the above-described theoretical analysis. The concave objects' depths are 1.858, 3.418, and 5.210 mm, and the convex objects' heights are 1.470 and 3.018 mm, as measured with a mechanical gauge. In the experiment, we set $z_0 = 450$ mm, $y_s = 100$ mm, $P_0 = 0.763$ mm,

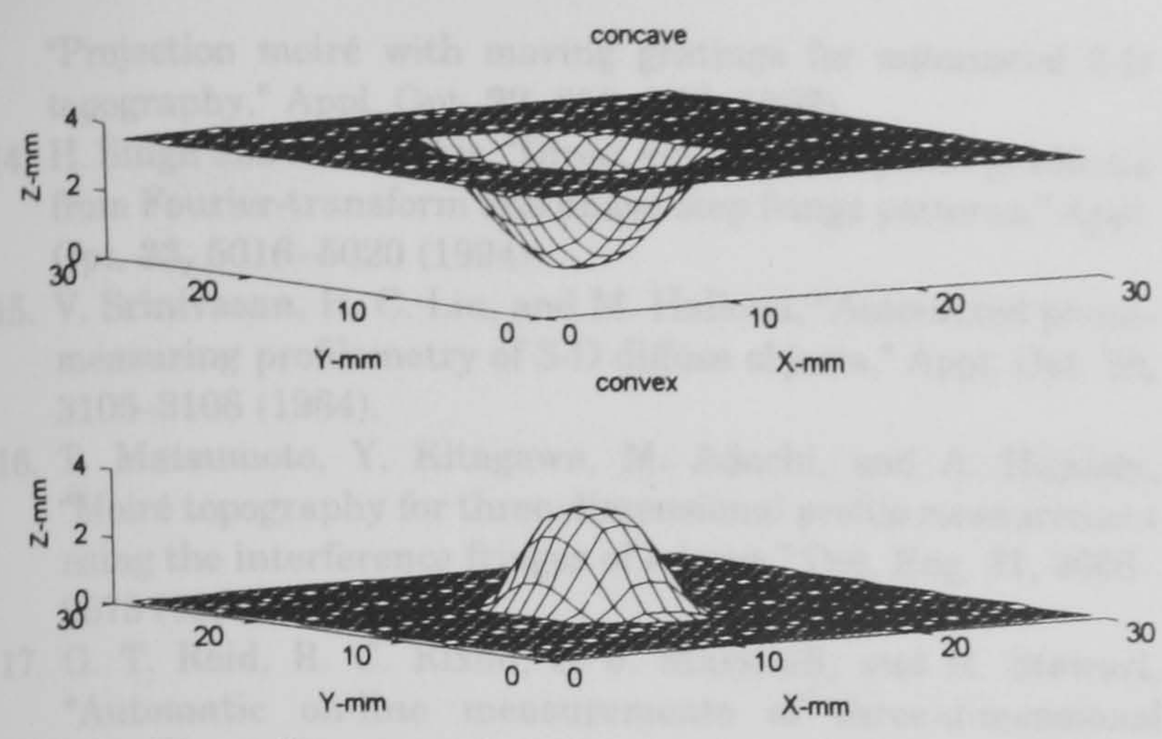

Fig. 7. Three-dimensional plot of the concave and convex objects.

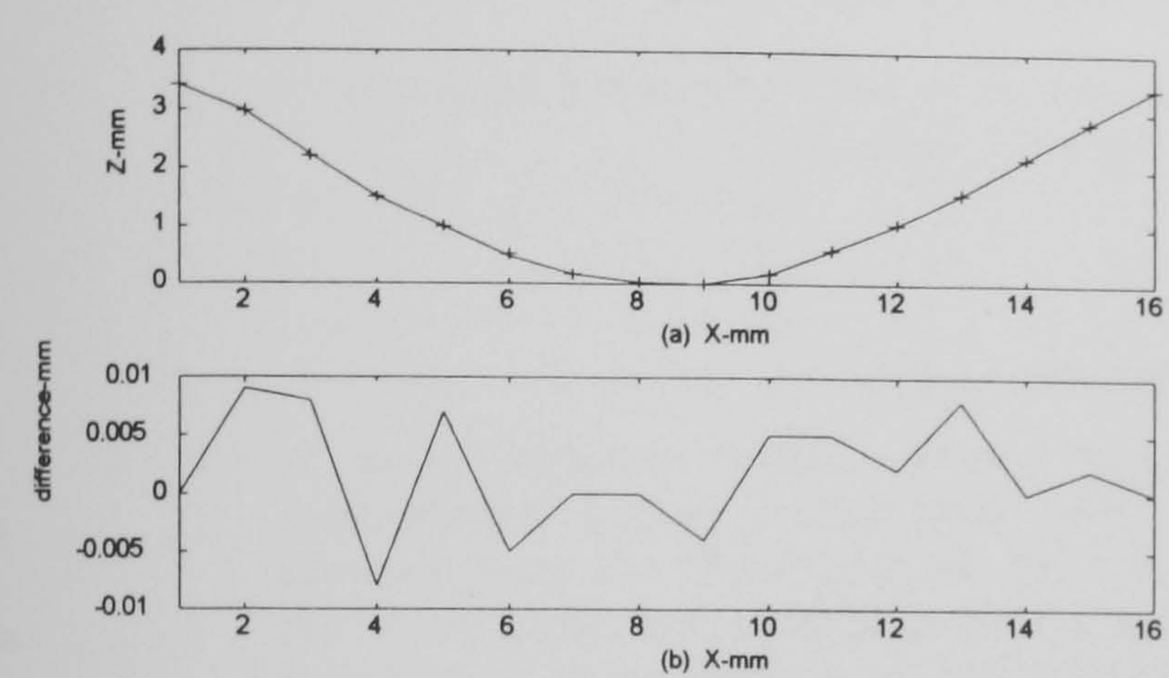

Fig. 8. (a) Results along the central line of the concave object as measured with the contact gauge (+) and the moiré method (−) and (b) the difference of the results in (a).

$A = 1.0, 0.8, 0.6, 0.4, 0.2, 0.1$, and $z_{max} = 4.29, 5.36, 7.15, 10.73, 21.46, 42.92$ mm. For example, when we have $A = 0.4$, the first image is acquired at $\theta_1 = 23.58°$, then the grating is rotated to the next positions, $\theta_2 = 13.89°$ and $\theta_3 = 4.59°$, and another two images are grabbed. The image is divided into 64×64 pixels. Equations (14) and (15) are used for the calculation of the phase and the absolute distance. The result obtained can be output in tabular or graphic format. The whole process of one measurement takes only 3 s.

Figure 6 shows the images of the concave object when the grating is at different positions: $\theta_1 = 36.87°$, $\theta_2 = 21.10°$, and $\theta_3 = 6.89°$. Figure 7 illustrates three-dimensional plots of the concave and convex objects from the experimental results. The results obtained with the mechanical gauge and the moiré method along one central line of the concave object and their differences are shown in Fig. 8. The measured objects' depth or height agreed very well with that measured by the gauge. The difference between them is a few micrometers, as shown in Fig. 8(b) and Table 1.

Table 1. Measurement Results Obtained by the Moiré and Mechanical Techniques[a]

	Object Shape and Number				
Technique	Concave 1	Concave 2	Concave 3	Convex 1	Convex 2
Moiré	1.862	3.414	5.215	1.469	3.019
Mechanical gauge	1.858	3.418	5.210	1.470	3.018

[a]The measurements are in units of millimeters.

4. Conclusion

We have proposed a new method for absolute moiré contouring by the rotation of a grating for the measurement of the three-dimensional profile of an object. It is verified by experiment that three-map absolute moiré contouring is a fast and accurate method. One measurement takes only 3 s. The measurement accuracy of less than one hundredth of a micrometer in theory and a few micrometers in the experiment have been obtained for testing concave and convex objects. The absolute distance between the object and the grating can be acquired directly. The measurable range is directly proportional to the period of the grating used and inversely proportional to the angle at which the grating is rotated. Choosing different periods for the grating or rotation angle yields different measurable ranges. The rotating angle can be controlled to high accuracy, better than 0.01°. The whole experimental process is controlled by specially designed software. This method may be a more efficient means of three-dimensional profile measurement for some relevant application areas.

References

1. M. Idesaula, T. Yatagai, and T. Soma, "Scanning moiré method and automatic measurement of 3-D shapes," Appl. Opt. **16,** 2152–2162 (1977).
2. F. Heiniger and T. Tschudi, "Moiré depth contouring," Appl. Opt. **18,** 1577–1581 (1979).
3. L. Pirodda, "Shadow and projection moiré techniques for absolute or relative mapping of surface shapes," Opt. Eng. **21,** 640–649 (1982).
4. H. E. Cline, W. E. Lorensen, and A. S. Holik, "Automatic moiré contouring," Appl. Opt. **23,** 1454–1459 (1984).
5. F. Lamy, C. Liegeois, and P. Meyrueis, "Three-dimensional automated pattern recognition using the moiré techniques," in *Advances in Infrared Fibers II*, L. D. DeShazer, ed., Proc. SPIE **360,** 345–351 (1982).
6. G. T. Reid, R. C. Rixon, and H. I. Messer, "Absolute and comparative measurements of three-dimensional shape by phase measuring moiré topography," Opt. Laser Technol. **16,** 315–319 (1984).
7. J. T. Atkinson and M. J. Lalor, "A novel approach to optical range finding," in *1986 European Conference on Optics, Optical Systems and Applications (October 1986, Florence, Italy)*, S. Sottini and S. Trigari, eds., Proc. SPIE **701,** 237–243 (1986).
8. S. Toyooka and Y. Iwaasa, "Automatic profilometry of 3-D diffuse objects by spatial phase detection," Appl. Opt. **25,** 1630–1633 (1986).
9. K. Engelhardt and G. Hausler, "Acquisition of 3-D data by focus sensing," Appl. Opt. **27,** 4684–4689 (1988).
10. K. J. Gasvik, T. Hovde, and T. Vadseth, "Moiré technique in 3-D machine vision," Opt. Lasers Eng. **10,** 241–249 (1989).
11. M. Gruber and G. Hausler, "Simple, robust and accurate phase-measuring triangulation," Optik **89,** 118–122 (1992).
12. J. F. Gardenas-Garcia, S. Zheng, and F. Z. Shen, "Implementation and use of an automated projection moiré experimental set-up," Opt. Lasers Eng. **21,** 77–98 (1994).
13. M. Halioua, R. S. Krishnamurthy, H. Liu, and F. P. Chiang,

"Projection moiré with moving gratings for automated 3-D topography," Appl. Opt. **22**, 850–855 (1983).
14. H. Singh and J. S. Sirkis, "Direct extraction of phase gradients from Fourier-transform and phase-step fringe patterns," Appl. Opt. **33**, 5016–5020 (1994).
15. V. Srinivasan, H. C. Liu, and M. Halioua, "Automated phase-measuring profilometry of 3-D diffuse objects," Appl. Opt. **23**, 3105–3108 (1984).
16. T. Matsumoto, Y. Kitagawa, M. Adachi, and A. Hayashi, "Moiré topography for three-dimensional profile measurement using the interference fringes of a laser," Opt. Eng. **31**, 2668–2673 (1992).
17. G. T. Reid, R. C. Rixon, S. J. Marshall, and H. Stewart, "Automatic on-line measurements of three-dimensional shape by shadow casting moiré topography," Wear **109**, 297–304 (1986).
18. J. Dirckx, W. F. Decraemer, and G. Dielis, "Phase shift method based on object translation for full field automatic 3-D surface reconstruction from moiré topograms," Appl. Opt. **27**, 1164–1169 (1988).
19. G. C. Jin and S. Tang, "Automated moiré contouring of diffuse surface," Opt. Eng. **28**, 1211–1215 (1989).
20. T. Yoshizawa and T. Tomisawa, "Shadow moiré topography by means of the phase-shift method," Opt. Eng. **32**, 1668–1674 (1993).
21. G. Mauvoisin, F. Bremand, and A. Lagarde, "Three-dimensional shape reconstruction by phase-shifting shadow moiré," Appl. Opt. **33**, 2163–2169 (1994).
22. Y. Arai, S. Yokozeki, and T. Yamada, "Fringe scanning method using a general function for shadow moiré," Appl. Opt. **34**, 4877–4822 (1995).

ELSEVIER

Optics and Lasers in Engineering 27 (1997) 149–159
© 1997 Elsevier Science Limited
Printed in Northern Ireland. All rights reserved
0143-8166/97/$17.00

PII: S0143-8166(96)00017-6

Absolute Moiré Contouring

X. Xie & J. T. Atkinson

School of Electrical and Electronic Engineering, Liverpool John Moores University, Byrom Street, Liverpool, UK, L3 3AF

(Received 3 November 1995; revised version received 11 January 1996; accepted 22 January 1996)

ABSTRACT

A novel absolute moiré contouring principle and the associated experimental system is described. This system enables the absolute distance from the object point to the reference plane and the height of the object to be measured directly to a high degree of accuracy. It is not necessary to judge the hills or valleys to decide the object's shape. A few objects were used as samples to illustrate the procedure. The objects' height, found by using the moiré technique, compares very well with that found by using a mechanical gage. © 1997 *Elsevier Science Ltd. All rights reserved.*

1 INTRODUCTION

Measurement of the 3D surface geometry of an object has been extensively studied because such topographic information is needed in quality control, robotics, CAD/CAM, medical diagnostics, solid modeling, computer vision, metrology, and many manufacturing applications. The use of optical methods (moiré, holography, etc.) is a desirable alternative to micrometers and dial gages. It is a non-contact method, acquires data rapidly and has a high and adjustable sensitivity. One promising optical method is moiré contouring for which the experiment set-up is quite simple.

An early application of the moiré method was demonstrated in 1925.[1] The method was reintroduced by a number of authors at a later time,[2–4] attempting to use the formation of moiré patterns by the projection of the shadow of a grating on a surface with collimated light. In the last 20 years, a group of authors have generalized the conditions of observation and

illumination,[5-6] and automatic data processing of shadow pattern has been developed.[7-13]

Early methods suffer from some difficulties. Firstly, the observation of moiré fringe contours does not allow the direct determination of whether a fringe pattern indicates a hill or a valley. This judgment can only be made if one knows the object's shape. Surface height data betwen fringes must be extrapolated from the available data. This type of determination could not be applied to an unknown object or in automatic processing. Secondly, the absolute distance between the object surface and the reference plane can only be measured by positioning a continuous object (e.g. a wire) from the surface to the reference plane and counting the fringes along it. The above drawbacks may not be serious for many applications. However, there are limitations for many applications. This paper describes a method called absolute moiré contouring, which can overcome the drawbacks of the previous moiré techniques.

2 ABSOLUTE MOIRÉ CONTOURING

Moiré contouring is a well documented and widely used technique.[5,6] A typical arrangement for producing good quality fringe maps, is similar to that shown in Fig. 1.

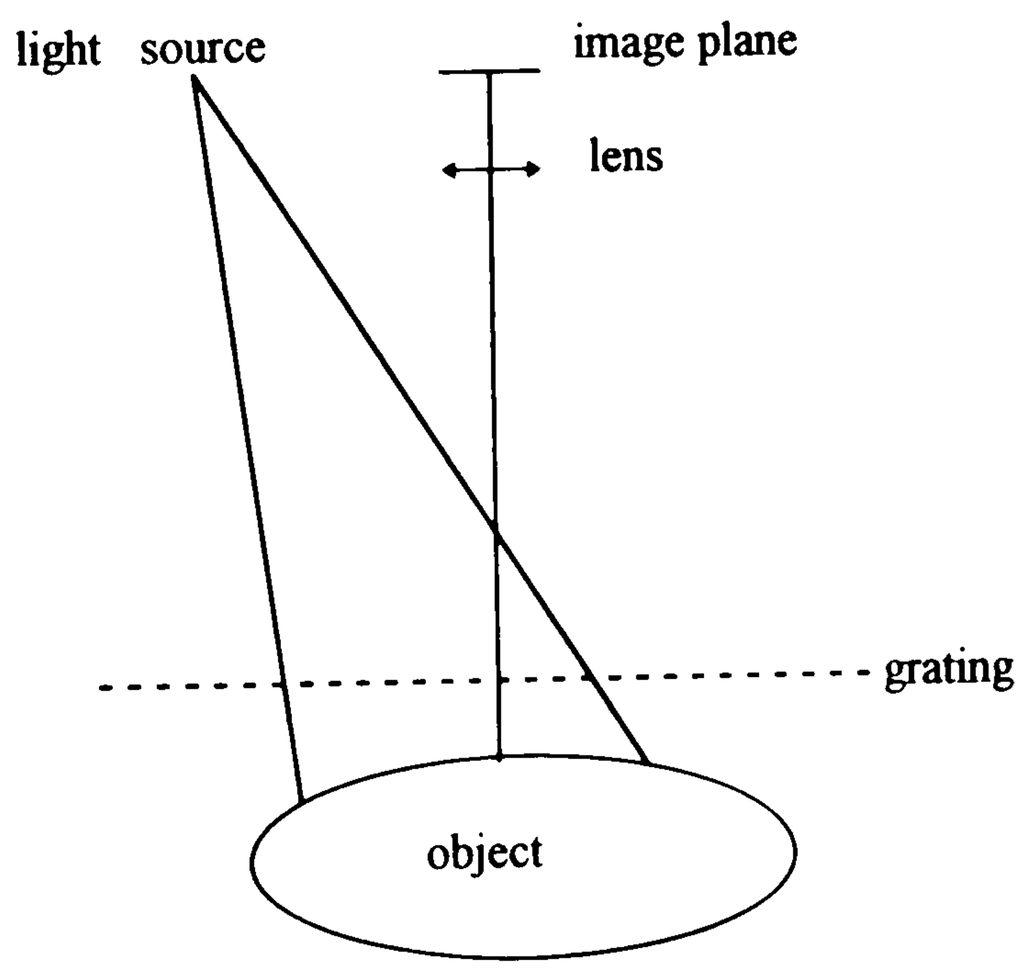

Fig. 1. Shadow moiré contouring.

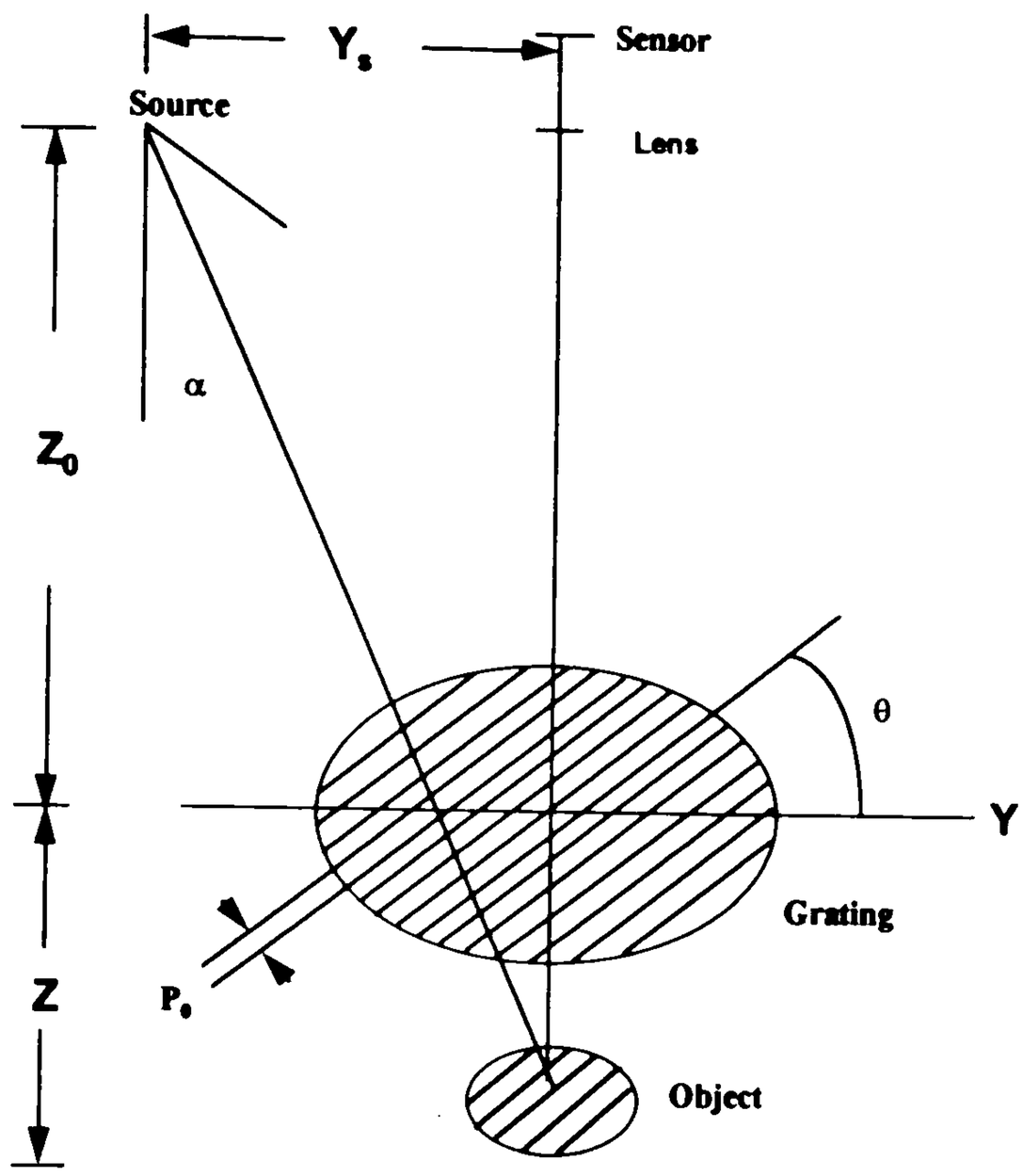

Fig. 2. Absolute moiré contouring.

Figure 2 is a schematic diagram of the absolute moiré contouring apparatus. The sinusoidal wave intensity grating is mounted on a bearing, such that it can be rotated about an axis normal to the plane of the rulings. The object is illuminated by a light source which need not be coherent. The shadow of the grid is cast onto the surface through an angle α. Hence the shadow on the object is shifted in the y direction by a distance $z(x, y) \tan \alpha$ relative to the grating. Light from this scene passes through a grating and a lens, forming an image in the region of the sensor, as depicted. The light source and the lens are the same perpendicular distance, z_0, from the grating. Together with the object point at z they define a plane. The intersection of this plane with the grating defines the line along which the period, p, of the grating is measured. This line also serves as the datum for the rotation of the grating. When the rulings are parallel to it, the angle θ is zero. The system can be analyzed as follows: Let the transmission function of the grating be given by

$$T(y) = \frac{1}{2}\left[1 + \sin\left(\frac{2\pi y}{P}\right)\right] \tag{1}$$

where p is the period of the grating. The intensity incident on the object at z may be represented by

$$T(y - z\tan\alpha) = T\left(y - \frac{zy_s}{z + z_0}\right) \tag{2}$$

The observed moiré pattern, M, can be found by multiplying the expressions:

$$\begin{aligned} M &= T(y)T\left(y - \frac{zy_s}{z + z_0}\right) \\ &= \frac{A}{4}\left[1 + \sin\left(\frac{2\pi y}{P}\right)\right]\left\{1 + \sin\left[\frac{2\pi}{P}\left(y - \frac{zy_s}{z + z_0}\right)\right]\right\} \\ &= \frac{A}{4}\left\{1 + \sin\left(\frac{2\pi y}{P}\right) + \sin\left[\frac{2\pi}{P}\left(y - \frac{zy_s}{z + z_0}\right)\right]\right. \\ &\quad \left. - \frac{1}{2}\cos\left[\frac{2\pi}{P}\left(2y - \frac{zy_s}{z + z_0}\right)\right] + \frac{1}{2}\cos\left(\frac{2\pi}{P}\frac{zy_s}{z + z_0}\right)\right\} \end{aligned} \tag{3}$$

where A is the amplitude of the light intensity.

The last term in eqn (3), $\frac{A}{8}\cos\left(\frac{2\pi}{P}\frac{zy_s}{z + z_0}\right)$, has a single unknown, z, and yields contour lines on the surface.

As the grating is rotated at an angular velocity, ω, the measured period of the grating changes such that:

$$P = \frac{P_0}{\sin\theta} \qquad \theta = \omega t \tag{4}$$

Therefore the above contour term can be rewritten as:

$$M' = \frac{A}{8}\cos\left(\frac{2\pi}{P_0}\frac{zy_s}{z + z_0}\sin\omega t\right) \tag{5}$$

This equation represents a modulated function with respect to time. Each peak of the output trace corresponds to an integer fringe number n. These integer values of n occur at values of θ_n at which the contour depth of the system is the nth fraction of z.

It follows from eqn (5) that the value of θ at which the fringe number is $n(\theta_n)$ is:

$$\sin\theta_n = \frac{nP_0}{zy_s}(z + z_0) \tag{6}$$

So that z can be found from

$$z = \frac{z_0 n P_0}{y_s \sin \theta_n - n P_0} \tag{7}$$

Now z_0, y_s, and P_0 are known values of the optical arrangement. To calculate z from the sensor output a suitable value of n is chosen and the value of θ at which it occurs is measured.

From eqn (6), if assume $\alpha = \pi/4$, we have

$$\sin \theta_n = \frac{n P_0}{z} \tag{8}$$

From eqn (8), consider that the value of z is changed by Δz from z_1 to z_2, then θ_{n1} and θ_{n2} will change as follows:

$$\sin \theta_{n2} = \sin \theta_{n1}\left(1 - \frac{\Delta z}{z_2}\right) \tag{9}$$

and if $\theta_{n1} = 90°$

$$\theta_{n2} = \sin^{-1}\left(1 - \frac{\Delta x}{z_2}\right) \tag{10}$$

If a grating of period 500 μm is used, and z has a initial value of 125 μm (so that $\theta_{n=0{\cdot}25}$ is 90°), then increasing the value of z by 0·1 μm would cause $\theta_{n=0{\cdot}25}$ to change to 87·7°. This means that the technique is very sensitive if n is chosen such that θ_n approaches 90°. Figure 3 is a typical time varying output.

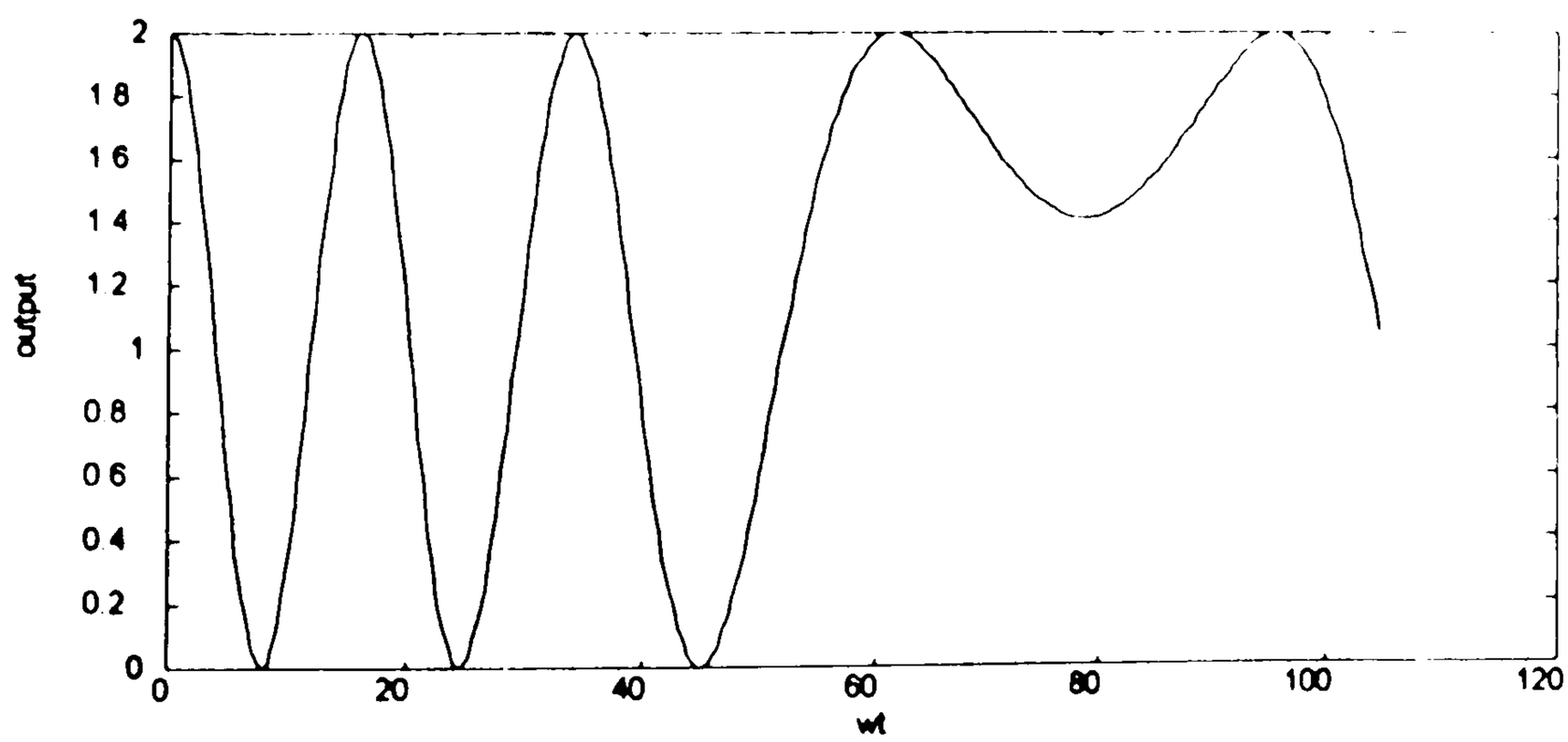

Fig. 3. A typical time varying output.

3 EXPERIMENTAL SYSTEM

Figure 4 is the schematic diagram of the experiment system used for absolute moiré contouring. The grating was a sinusoidal wave intensity grating and was mounted on a bearing rotated by a stepper motor. The object was illuminated by a light source (white light source—IL 410 illumination system). The object was located behind the grating. The distance between the object surface and the reference plane (grating) could be adjusted by a micrometer. The moiré contour pattern was focused by the lens and the image was taken by a CCD camera (CCIR monochrome CCD camera—COHU). The computer was equipped with on ITEX Variable-Scan Frame Grabber (VFG V1·0). The analog signal from the camera was converted to a digital formatted signal then stored in computer memory. By rotating the grating step by step, the images at different positions (θ) of the grating were grabbed by the frame grabber. Using a specially designed software, all the data were processed and the results were displayed in tabular or graphical formats. The moiré fringe pattern images were divided into pixels. When the grating was at the position of $\theta = 0°$, the first image was grabbed into the computer. Then by rotating the grating from 0° to θ_n step by step, more images were taken. After all the images were acquired, the background of the signal was removed and the signal normalized, then the phase changes for each step of the motor's rotation and the total fringe number for each pixel were calculated, and eqn (7) was used to calculate the absolute distance between the object and the grating. By finding out the maximum distance, the object's height which is relative to its deepest point equals max $(z) - z$.

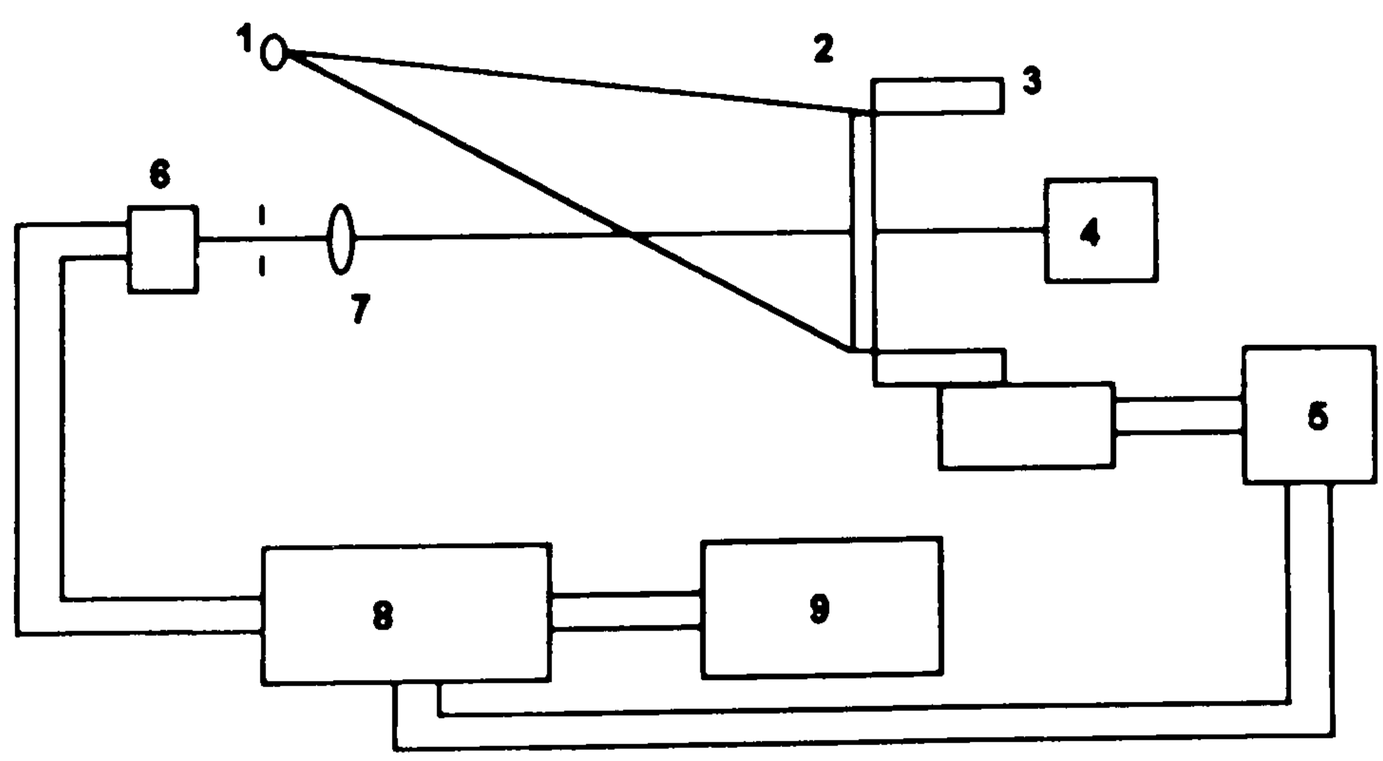

Fig. 4. Absolute moiré contouring instrument: 1—light source, 2—grating, 3—bearings, 4—object, 5—motor, 6—CCD camera, 7—lens, 8—computer, 9—monitor.

4 EXPERIMENTAL RESULTS

In this experiment, the period of the grating is 0·763 mm, $y_s = 100$ mm, $z_0 = 420$ mm. The image was divided into 64×64 pixels. The grating is rotated from 0° to 30°. The rotation of the stepper motor was controlled by the program. For one measurement, 21 images were taken. The data were processed as described above.

Concave and convex objects of different dimensions were used as the samples in the experiment. The object's surfaces were painted white to obtain a good image. Figure 5 is a photograph of the moiré fringe pattern of the concave–convex, and concave objects at $\theta = 30°$. The measured object surface area was about 10 cm^2, limited by the size of the bearing. The measuring time was about 16 s. Figure 6 shows the 3D plots of the

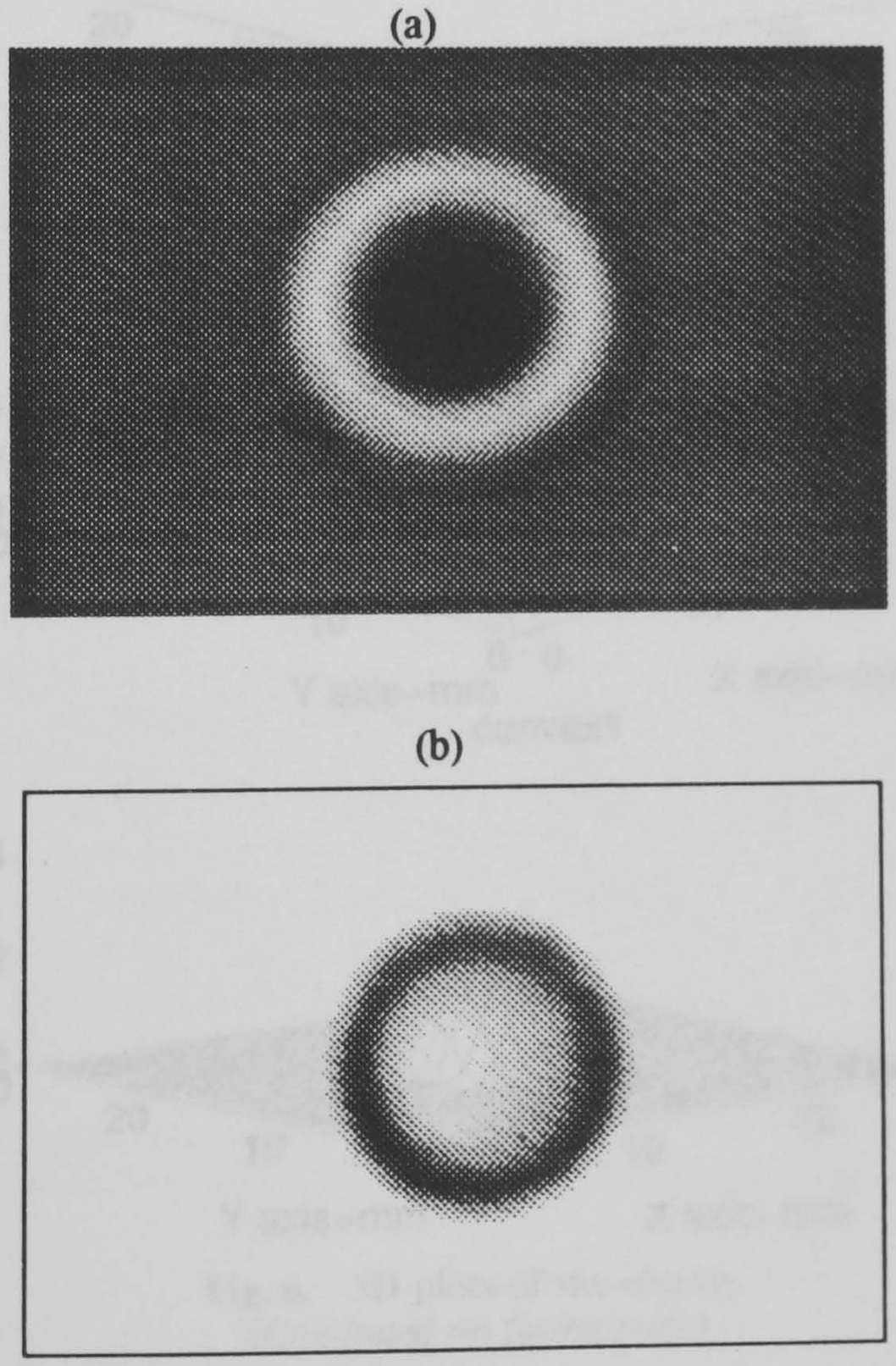

Fig. 5. The photos of the object's moiré fringe pattern: (a) concave–convex object; (b) concave object–both (a) and (b) at $\theta = 30°$.

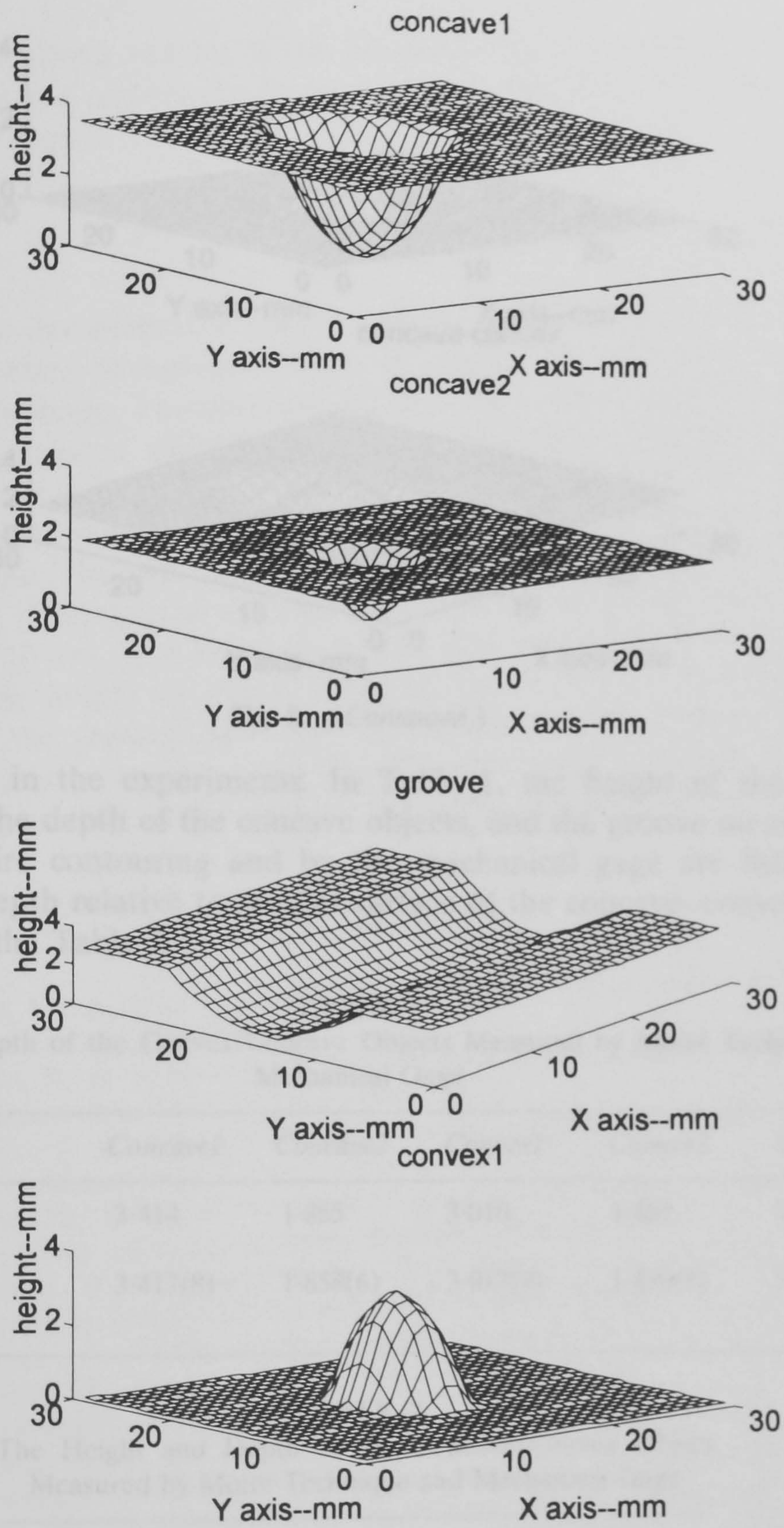

Fig. 6. 3D plots of the objects.
(*Continued on facing page*)

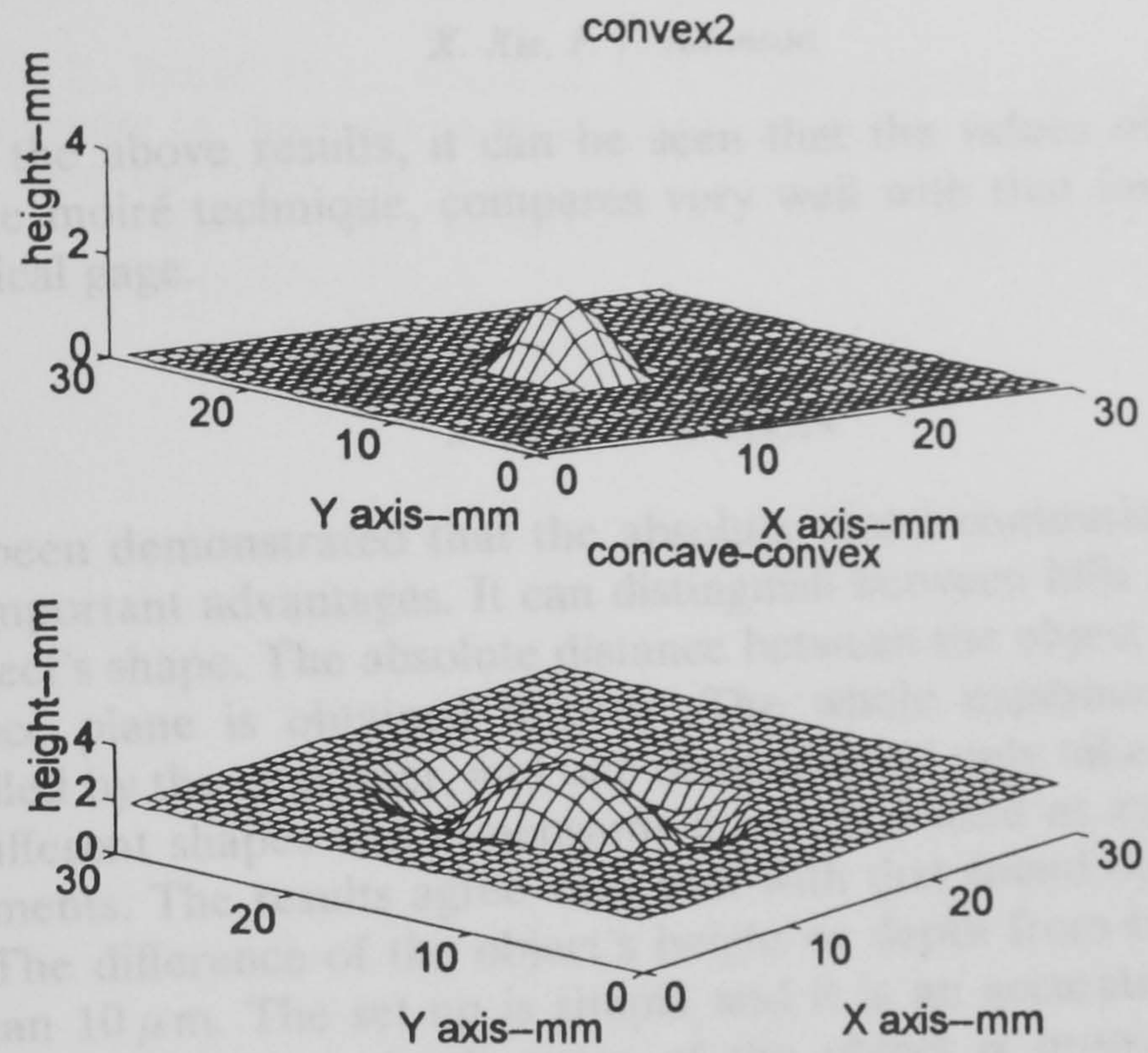

Fig. 6. (*Continued.*)

objects used in the experiments. In Table 1, the height of the convex objects and the depth of the concave objects, and the groove measured by absolute moiré contouring and by the mechanical gage are listed. The height and depth relative to the flat surface of the concave–convex object are listed in the Table 2.

TABLE 1

The Height/Depth of the Convex/Concave Objects Measured by Moiré Technique and Mechanical Gage

	Concave1	*Concave2*	*Convex1*	*Convex2*	*Groove*
Moiré technique	3·414	1·865	3·010	1·461	2·676
Mechanical gage	3·417(8)	1·858(6)	3·017(9)	1·470(7)	2·667(7)

TABLE 2

The Height and Depth of the Concave/Convex Object Measured by Moiré Technique and Mechanical Gage

	Height	*Depth*
Moire technique	1·412	1·711
Mechanical gage	1·421(2)	1·718(5)

From the above results, it can be seen that the values of z found by using the moiré technique, compares very well with that found by using mechanical gage.

5 CONCLUSION

It has been demonstrated that the absolute moiré contouring system has some important advantages. It can distinguish between hills and valleys in the object's shape. The absolute distance between the object point and the reference plane is obtained directly. The whole experiment process is controlled by the computer, and one measurement only takes 16 s. Objects with different shapes and dimensions have been used as examples in the experiments. The results agree very well with that found by a mechanical gage. The difference of the object's height or depth from two methods is less than 10 μm. The set-up is simple and it is an accurate method. The measurable height or depth range of the object is proportional to the period of the grating used. Due to the limits of the contour depth, if the object's relative height is too big, the measuring accuracy will be lower. Also if the grating is not perfect, the measuring accuracy will be affected.

REFERENCES

1. Mulot, M., Application of the moiré to the study of mica deformations. *Rev. D'optique* **4,** (1925) 252–9.
2. Weller, R. & Shephard, B. M., Displacement measurement by mechanical interferometer. *Proc. SESA* **6** (1948) 35–8.
3. Kaezer, J. & Kroupa, F., The determination of strains by mechanical interference. *Czech. J. Appl. Phys.* **1** (1952) 80–5.
4. Theorcaris, P. S., Moiré method in plates. Non-classical shell problem. In *Proc. of the IASS Symposium,* Warsaw, 1964, pp. 887–9.
5. Meadow, D. M., Johnson, W. O. & Allen, T. B., Generation of surface contours by moiré pattern. *Appl. Optics* **9** (1970) 942–7.
6. Takasaki, A., Moiré topology. *Appl. Optics,* **9** (1970) 1457–72.
7. Idesawa, M., Yatagai, T. & Soma, T., Scanning moiré method and automatic measurement of 3-D shapes. *Appl. Optics* **16** (1977) 2152–62.
8. Moore, D. T. & Truax, B. E., Phase-locked moiré fringe analysis for automated contouring of diffuse surface. *Appl. Optics* **18** (1979) 91–6.
9. Cline, H. E., Holik, S. & Lorensen, W. E., Computer aided surface reconstruction of interference contours. *Appl. Optics* 21 (1982) 4481–8.
10. Cline, H. E., Lorensen, W. E. & Holik, A. S., Automatic moiré contouring. *Appl. Optics* 23 (1984) 1454–9.
11. Reid, G. T., Rixon, R. C. & Messer, H. I., Absolute and comparative measurements of three-dimensional shape by phase measuring moiré topography. *Optics Laser Technol.* **December** (1984) 315–9.

12. Reid, G. T., Rixon, R. C., Marshall, S. J. & Stewart, H., Automatic on-line measurements of three-dimensional shape by shadow casting moiré topography. *Wear* **109** (1986) 297–304.
13. Jin, G. G. & Tang, S. H., Automatic moiré contouring of diffuse surface. *Optical eng.*, **28** (1989) 1211–5.

ELSEVIER

Optics and Lasers in Engineering 27 (1997) 247–257
© 1997 Elsevier Science Limited
Printed in Northern Ireland. All rights reserved
0143-8166/97/$17·00

PII: S0143-8166(96)00028-0

Effects on Absolute Moiré Contouring by Using Gratings with Different Period and Profile and Rotating Angles

X. Xie, J. T. Atkinson, M. J. Lalor & D. Burton

Coherent and Electro-optics Research Group, Liverpool John Moores University, Byrom Street, Liverpool, UK, L3 3AF

(Received 23 February 1996; accepted 5 April 1996)

ABSTRACT

Effects on the absolute moiré contouring systems from using different period and profile gratings and rotating angles are described in this paper. It was found that by choosing a different period of the grating or the rotating angle, different resolution and accuracy of the measurement can be obtained. So, for objects with different height or depth, different period of grating or rotating angle should be chosen to ensure accuracy of the measurement. The square wave intensity grating with small period can be treated as a sinusoidal wave intensity grating in the absolute moiré contouring system. A few objects with different shapes and dimensions have been used as samples to verify the above conclusion.
© 1997 *Elsevier Science Ltd. All rights reserved.*

1 INTRODUCTION

Three-dimensional (3D) shape measurement by non-contact optical methods has been extensively studied because of its importance in automated manufacturing, component quality control, medicine, robotics and modelling applications. Among the various types of methods, i.e. light scattering, speckle, holography, moiré etc., the moiré method is popular. The early application of moiré method can be traced back to 1925.[1] In recent years this method has attracted the attention of many workers as an attractive alternative for measuring the shape of 3D objects.[2–17] The methods employed were variations of the principles of shadow moiré and projected fringes, with and without phase shift technique. But in the previous methods, it was not easy to decide whether a contour fringe indicates a hill or a valley or to calculate the absolute distance from the

object's surface to the reference plane unless one knew the shape of the object and used additional techniques.

We have proposed a new method—absolute moiré contouring,[18] which allows a direct determination of hills or valleys and the absolute distance measurement between the object's surface and grating, and the object's height, without any additional information being needed. In this paper the effects on absolute moiré contouring by using the gratings with different profile and period and rotation angle are discussed.

2 EXPERIMENT PRINCIPLE

Figure 1 is a schematic diagram of the absolute moiré contouring arrangement. The grating is mounted on a bearing which can be rotated about an axis normal to the plane of the rulings. The object to be tested is located behind the grating and illuminated by a light source which need not be coherent. The shadow of the grid is cast on to the object's surface with angle α. The moiré fringe pattern is observed through the grating in a direction perpendicular to the plane of the grating's rulings.

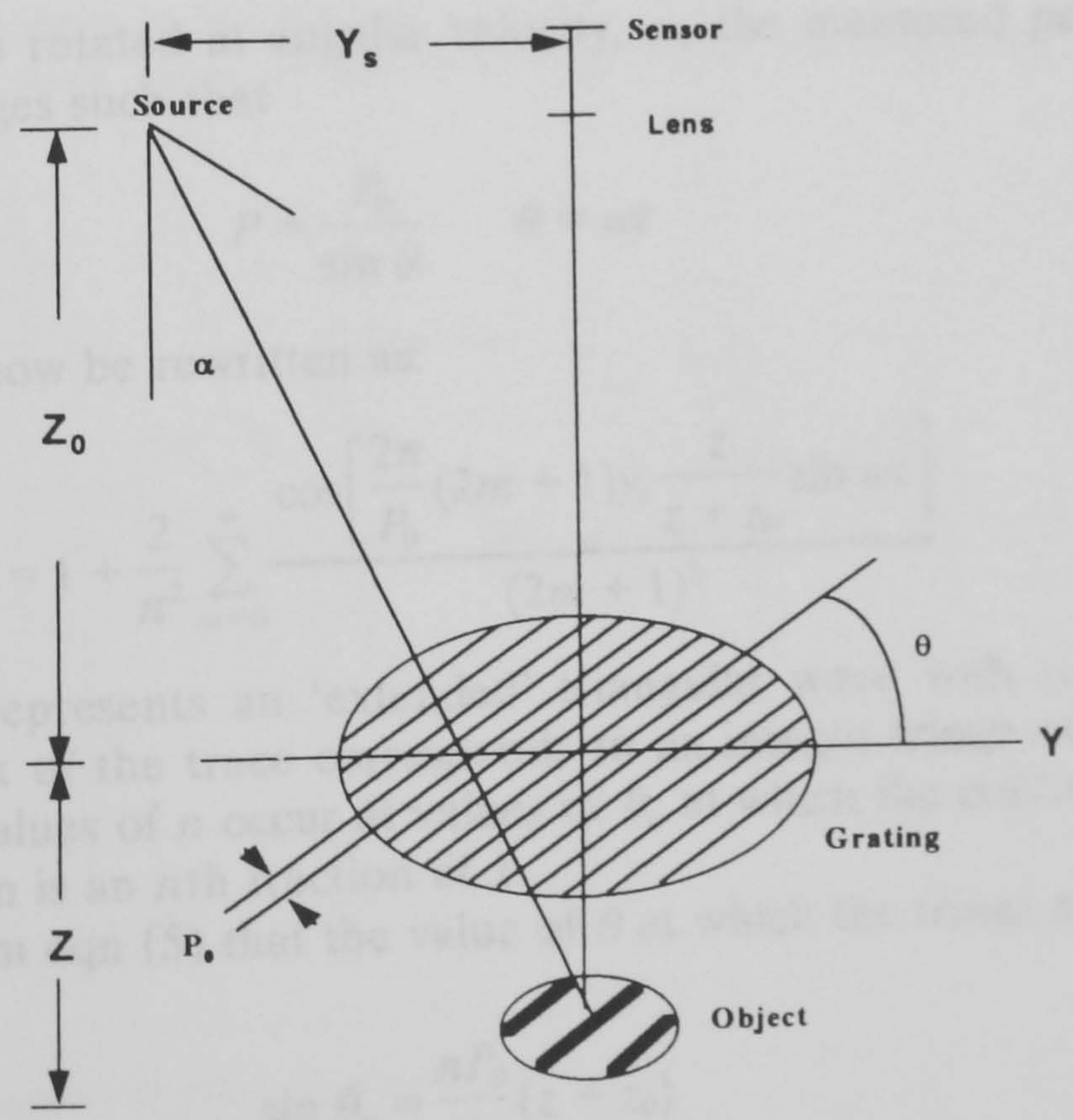

Fig. 1. Schematic diagram of absolute moiré contouring.

If $T(y)$ represents the transmission function of the grating, the intensity incident on the target at z may be represented by

$$T\left(y - z\frac{y_s}{z + z_0}\right)$$

The observed moiré pattern, M, can be found by multiplying these expressions

$$M = T(y)T\left(y - z\frac{y_s}{z + z_0}\right) \tag{1}$$

For a square wave (Ronchi) grating, the transmission function is given by

$$T(y) = \frac{1}{2} + \frac{2}{\pi}\sum_{m=0}^{\infty}\frac{\sin\left[(2m+1)\frac{2\pi}{P}y\right]}{2m+1} \tag{2}$$

The moiré contouring term resulting from substitution of eqn (2) in eqn (1) may be written as:

$$M = 1 + \frac{2}{\pi^2}\sum_{m=0}^{\infty}\frac{\cos\left(\frac{2\pi}{p}(2m+1)\frac{y_s z}{z + z_0}\right)}{(2m+1)^2} \tag{3}$$

As the grating is rotated at angular velocity, ω, the measured period of the grating changes such that

$$P = \frac{P_0}{\sin\theta} \qquad \theta = \omega t \tag{4}$$

So eqn (3) can now be rewritten as:

$$M = 1 + \frac{2}{\pi^2}\sum_{m=0}^{\infty}\frac{\cos\left[\frac{2\pi}{P_0}(2m+1)y_s\frac{z}{z + z_0}\sin\omega t\right]}{(2m+1)^2} \tag{5}$$

This equation represents an 'extended' triangular wave with respect to time. Each peak of the trace corresponds to an integer fringe number n. These integer values of n occur at values of θ_n at which the contour depth Δz of the system is an nth fraction of z.

It follows from eqn (5) that the value of θ at which the fringe number is $n(\theta_n)$ is

$$\sin\theta_n = \frac{nP_0}{zy_s}(z + z_0) \tag{6}$$

so that z can be found from

$$z = \frac{z_0 n P_0}{y_s \sin(\theta_n) - n P_0} \tag{7}$$

For the sinusoidal wave grating, the transmission function can be given as

$$T(y) = \tfrac{1}{2} + \tfrac{1}{2}\sin\left(\frac{2\pi y}{P}\right) \tag{8}$$

The same expression as eqn (6) has been obtained for the sinusoidal wave grating.[18]

Now z, y_s and P_0 are known values of the optical arrangement. To calculate z from the sensor output a suitable value of n is chosen and the value of θ at which it occurs is measured.

3 EXPERIMENTAL PROCEDURE AND SIGNAL PROCESSING

The experimental system of absolute moiré contouring is shown in Fig. 2. The whole experimental process is controlled by specially designed software. The moiré fringe pattern observed through the grating is sensed by a CCD camera (CCIR monochrome CCD camera–COHU). The signal from the camera is digitised and stored in the frame memory. By rotating the grating step by step, the images at different positions (θ) of grating

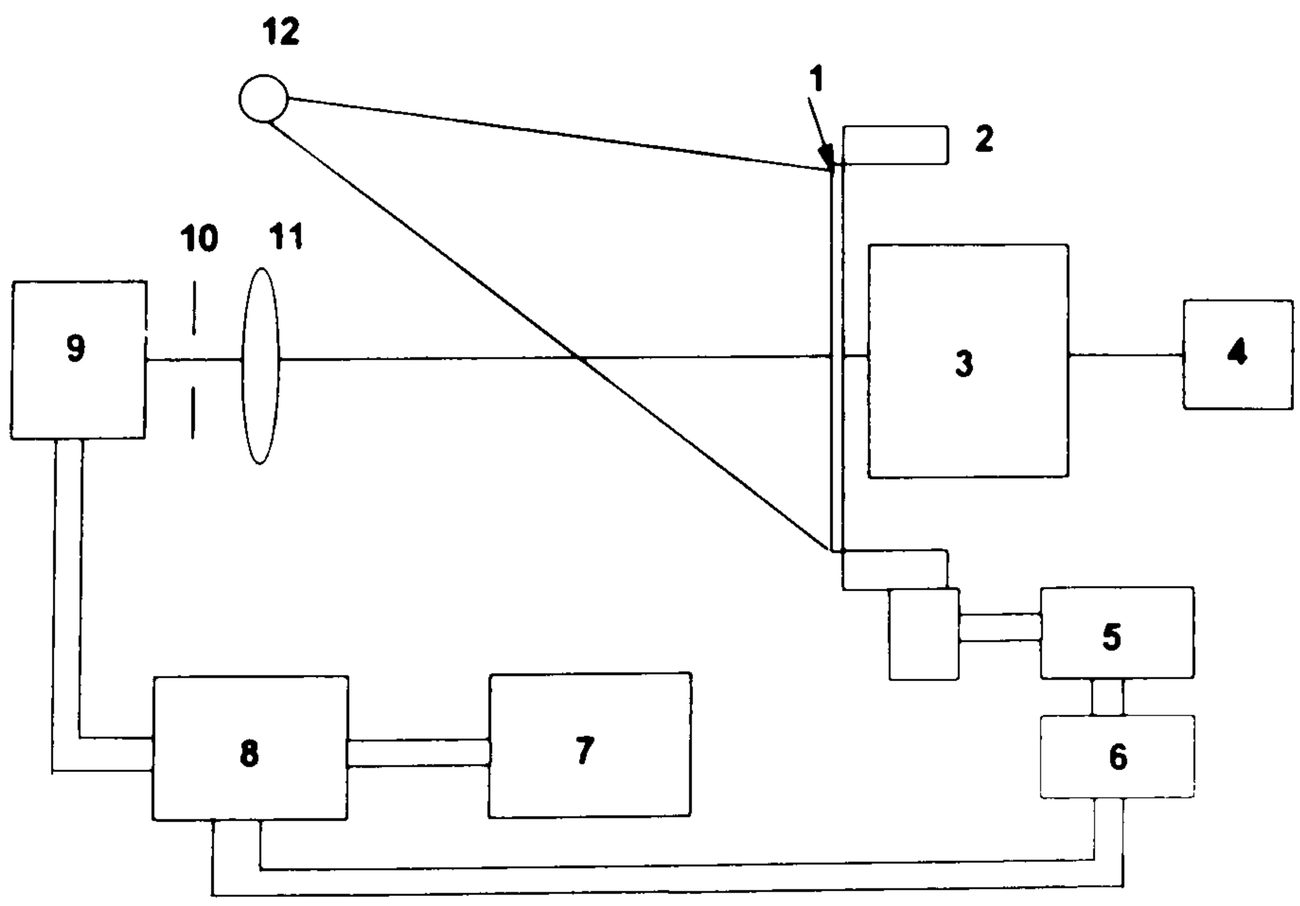

Fig. 2. Diagram of absolute moiré contouring instruments: (1) grating; (2) bearing; (3) object; (4) micrometer; (5) stepper motor; (6) control board; (7) monitor; (8) computer; (9) CCD camera; (10) aperture; (11) lens; (12) light source.

are captured. After capturing all required images, the grey level data of one pixel from a different image is moved to one array, first removing the background from the data, then calculating the total phase varying from $\theta = 0°$ to θ_n as well as the fringe number. The distance z from the object to the grating is calculated from the eqn (7). After the maximum z is found, the object's height can be obtained. A function to eliminate the random noise is used in the program. Figure 3 illustrates the procedure of the experiment and signal processing.

4 EXPERIMENTAL RESULTS AND ANALYSIS

4.1 Results

In our experiments, the whole image is divided into 64×64 pixels. Only 60×60 pixels have been used and 21 images were taken for one measurement. One measurement takes about 16 s. The gratings used were square wave gratings (0·508, 1·386 and 1·800 mm) and sinusoidal wave gratings (0·763, 0·985, 1·360 and 1·800 mm). The grating rotated angles were 15, 30, 60 and 90°. The experimental process control and data processing are as described in Section 3. Concave and convex objects with different dimensions were used as the samples in the experiment. All the objects' surfaces were painted white to increase reflectance. Three-dimensional plots of four typical objects used are shown in Fig. 4. Figure 5 shows the side view of Figs 4(a) and (b). Table 1 lists the objects' maximum height or depth obtained by contact gauge and the absolute moiré contouring system.

4.2 Analysis

The gratings with different period

From eqn (7) we can see that z is directly proportional to the period of the grating used when fringe number, n, is given, and the relation between z and P_0 is non-linear. Figure 6(a) shows the relationship. For different periods of the gratings, different accuracy and resolution of the measurement can be obtained. Table 2 lists the z values for different period of gratings when $n = 1$. From the table we can find that resolution of the system is inversely proportional to the grating's period. This means that for certain z, the smaller the period of grating used, the more the phase (fringe number) varies. If we assume the object's maximum depth or height is $z_h = 5$ mm, the shortest distance from the object to the grating is $z_{0\cdot5}$, $z = z_h + z_{0\cdot5}$, and the grating rotates 20 steps for one measurement,

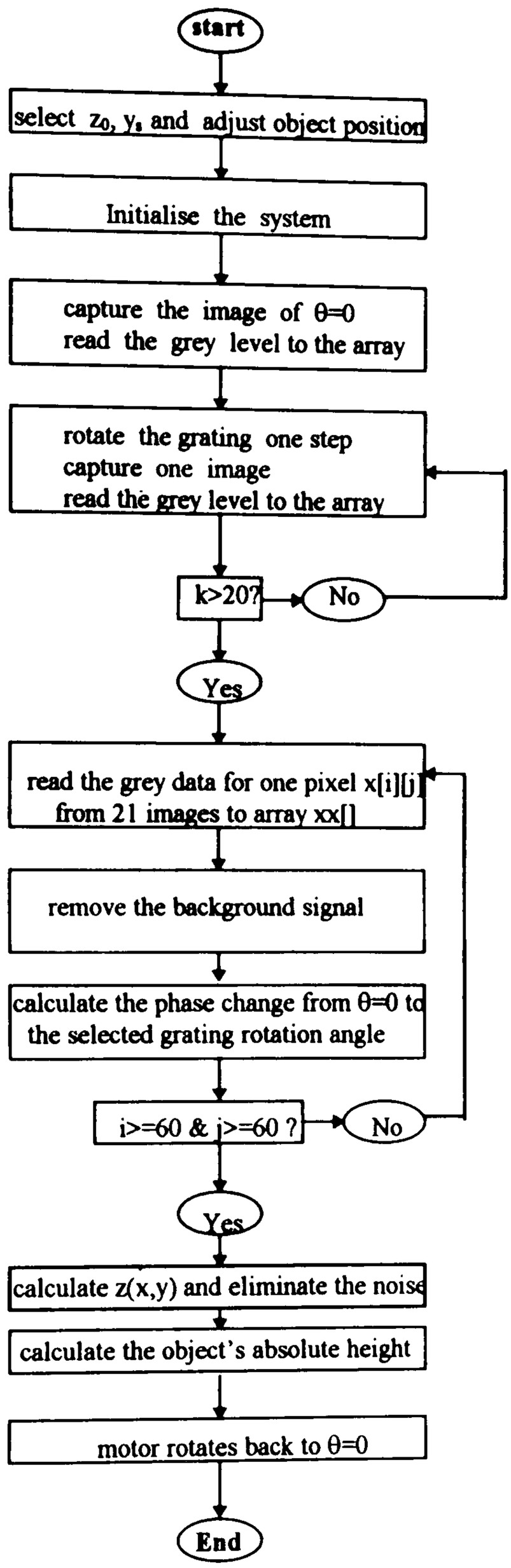

Fig. 3. The block diagram of the experimental procedure.

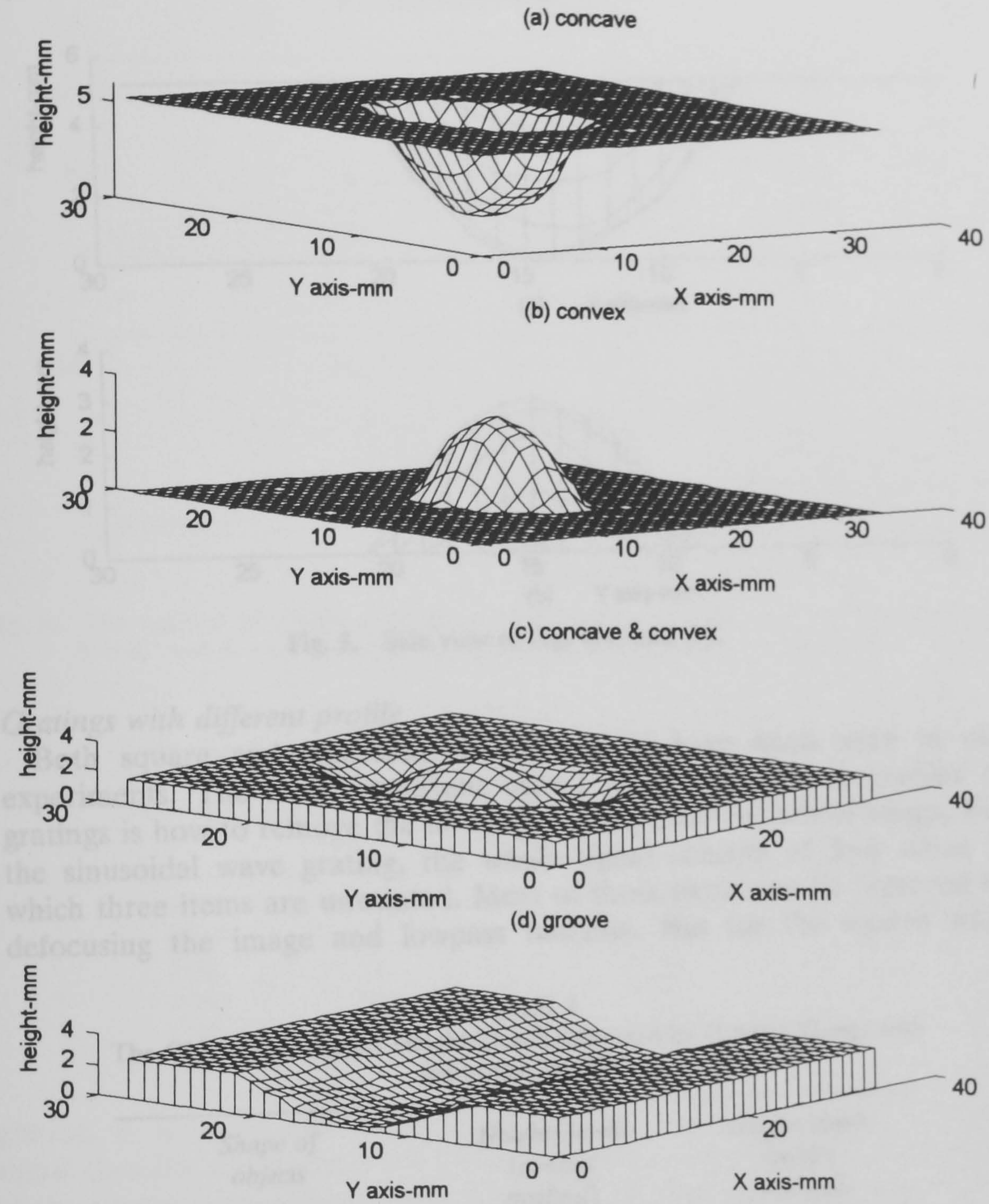

Fig. 4. Three-dimensional plots of concave and convex objects.

the fringe number, n (phase varies, Φ), and the average phase variation, $\Delta\Phi$, for one step are listed in Table 3. So if we consider that the phase change (the phase difference between two adjacent images for one pixel) must not be too big for the motor rotating one step, the large period of grating is better. This is because when the phase difference between adjacent images is too big, it may result in missing the maximum or minimum grey level values which decide the phase values.

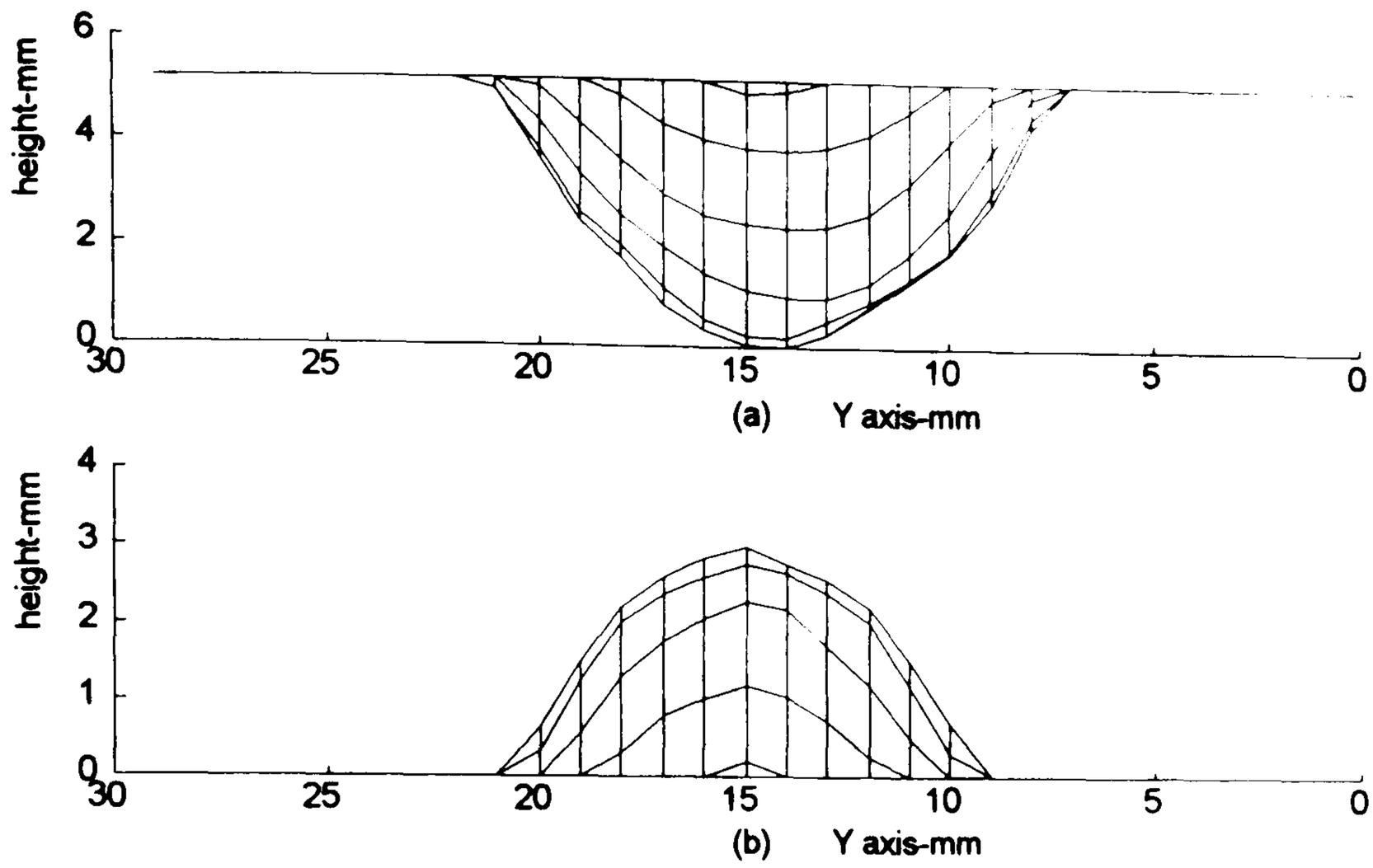

Fig. 5. Side view of Figs 4(a) and (b).

Gratings with different profile

Both square and sinusoidal wave gratings have been used in our experiments. The most important aspect of using different profiles of gratings is how to remove the unwanted items from the whole image. For the sinusoidal wave grating, the whole signal consists of four items in which three items are unwanted. Most of these items can be removed by defocusing the image and lowpass function. But for the square wave

TABLE 1
The Objects' Maximum Height/Depth Obtained by Contact Gauge and the Moiré Method

Shape of objects	*Height/depth (contact method)* (mm)	*Height/depth (moiré method)* (mm)
Convex1	3·017	3·010
Convex2	1·470	1·461
Concave1	1·858	1·865
Concave2	3·102	3·101
Concave3	3·417	3·414
Concave4	5·210	5·206
Concave5	7·600	7·578
Groove	2·661	2·668
Concave and convex	1·421/1·690	1·412/1·698

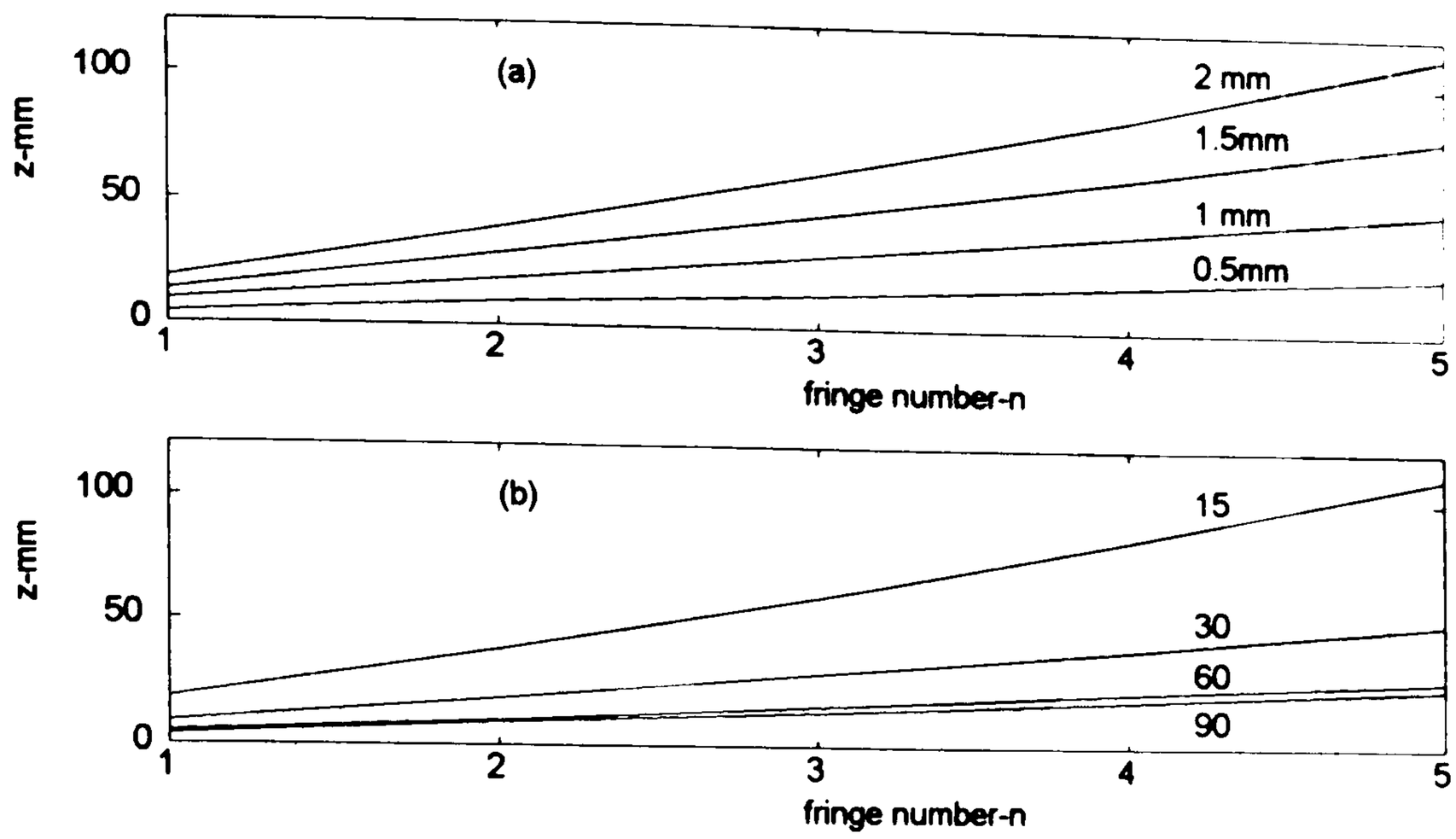

Fig. 6. The relation of z with n for different P_0 and θ_n, $z_0 = 450$ mm, $y_s = 100$ mm: (a) $\theta = 30°$ and $P_0 = 0{\cdot}5$, $1{\cdot}0$, $1{\cdot}5$, 2 mm; (b) $P_0 = 1$ mm and $\theta = 15, 30, 60, 90°$.

TABLE 2
Values for Different Period of Gratings and Rotating angles, when $n = 1$, $z_0 = 420$ mm and $y_s = 100$ mm

P_0/θ	15°	30°	60°	90°
0·508	8·400	4·311	2·478	2·142
0·763	12·758	6·508	3·733	3·229
0·985	16·616	8·440	4·830	4·178
1·360	23·293	11·743	6·699	5·792
1·800	31·393	15·684	8·915	7·699

grating, it is more difficult to eliminate the unwanted items from the signal than the sinusoidal wave grating. From our experience, if the period of the square wave grating is not too large, say less than 1·0 mm, it could be treated in the same way as a sinusoidal wave grating and used in our experiment, and the unwanted items could be removed in the same way as

TABLE 3
Values of n, Φ and $\Delta\Phi$ when $z_h = 5{\cdot}0$ mm, $z_0 = 420$ mm, $y_s = 100$ mm, $\theta_n = 30°$ and $P_0 = 0{\cdot}50$ and $1{\cdot}80$ mm

P_0	Z_h (mm)	$z_{0\cdot5}$ (mm)	z (mm)	n	Φ (deg)	$\Delta\Phi$ (deg)
0·500	5·000	2·110	7·110	1·721	619·8	30·99
1·800	5·000	7·698	12·698	0·815	293·5	14·67

TABLE 4
Values of n, Φ and $\Delta\Phi$ when $z_h = 5{\cdot}0$ mm, $z_0 = 420$ mm, $y_s = 100$ mm, $P_0 = 1{\cdot}0$ mm and rotating angles are 15, 30, 60 and 90°

θ_n	z_h (mm)	$z_{0\cdot5}$ (mm)	z (mm)	n	Φ (deg)	$\Delta\Phi$ (deg)
15°	5·000	8·274	13·274	0·845	304·2	15·2
30°	5·000	4·242	9·242	1·124	404·8	20·2
60°	5·000	2·439	7·439	1·561	562·1	28·1
90°	5·000	2·110	7·110	1·722	619·8	30·9

for sinusoidal wave gratings. We have tried to use the square wave gratings with periods of 1·386 and 1·800 mm; the unwanted items are difficult to remove. Although from theory if a square or circular aperture of certain dimensions is used with the square wave grating, the visibility of the primary fringes would be zero for some θs and unwanted modulation is zero, which is not easy to realise.

Different rotating angles

The grating rotating angle for one measurement affects the experimental results. From eqn (7) and Fig. 6(b) we can see the relation of z and θ_n. The relation between z and θ_n for $n = 1$ is listed in Table 2. The bigger θ_n is, the smaller is z and higher resolution, so for a given z, the bigger θ_n is, the bigger is the phase (fringe number) variation. If the high object needs to be measured, the small angle grating should be rotated. Table 4 lists the values of n, Φ and $\Delta\Phi$ when the angles are 15, 30, 60 and 90° for $z_h = 5$ mm. This relation is similar to the relation for the different period of gratings.

5 CONCLUSION

We have used the absolute moiré contouring experimental system to measure the objects with different shape and dimensions under different conditions—different period and profile of gratings and rotating angle, θ_n. It was found that this system can be used for the measurement of absolute distance between object and grating and the object's height directly without the decision of the 'hills' or 'valleys'.

The accuracy of a few micrometres can be obtained. By changing the rotating angle or period of grating, different accuracy and resolution can be obtained. For different heights of object, a different rotating angle or grating with a suitable period should be chosen to ensure accuracy of the measurement. The square wave grating with period smaller than 1·0 mm can be treated as a sinusoidal wave grating and used in the absolute moiré

contouring system. It takes about 16 s for one measurement. Because all the data depend on the image's grey level values, if the grating is not perfect the results will be affected. More improvements need to be made on eliminating the primary fringes and unwanted items from signals, and making the grating as perfect as possible and reducing the measuring time.

REFERENCES

1. Cline., M., Application of the moiré to the study of mica deformations. *Rev. D'optique,* **4** (1925) 252–59.
2. Idesaula, M., Yatagai, T. & Soma, T., Scanning moiré method and automatic measurement of 3-D shapes. *Appl. Opt.,* **16** (1977) 2152–62.
3. Heiniger, F. & Tschudi, T., Moiré depth contouring. *Appl. Opt.,* **18** (1979) 1577–81.
4. Livnat, A., Kafri, O. & Erez, G., Hills and valleys analysis in optical mapping and its application to moiré contouring. *Appl. Opt.,* **19** (1980) 3396–400.
5. Pirodda, L., Shadow and projection moiré techniques for absolute or relative mapping of surface shapes. *Opt. Engng,* **21** (1982) 640–9.
6. Halioua, M., Krishnamurthy, R. S., Liu, H. & Chiang, F. P., Projection moiré with moving gratings for automated 3-D topography. *Appl. Opt.,* **22** (1983) 850–5.
7. Srinivasan, V., Liu, H. C. & Halioua, M., Automated phase-measuring profilometry of 3-D diffuse objects. *Appl. Opt.,* **23** (1984) 3105–8.
8. Cline, H. E., Lorensen, W. E. & Holik, A. S., Automatic moiré contouring. *Appl. Opt.,* **23** (1984) 1454–9.
9. Lamy, F., Liegeois, C. & Meyrueis, P., Three-dimensional automated pattern recognition using the moiré techniques. *SPIE,* **360** (1982) 345–51.
10. Reid, G. T., Rixon, R. C. & Messer, H. I., Absolute and comparative measurements of three dimensional shape by phase measuring moiré topography. *Opt. Laser Technol.,* **16** (1984) 315–19.
11. Atkinson, J. T. & Lalor, M. J., A novel approach to optical range finding. *SPIE* **701,** *ECOOSA'86*, Florence, 1986, pp. 237–43.
12. Toyooka, S. & Iwaasa, Y., Automatic profilometry of 3-D diffuse objects by spatial phase detection. *Appl. Opt.,* **25** (1986) 1630–3.
13. Engelhardt, K. & Hausler, G., Acquisition of 3-D data by focus sensing. *Appl. Opt.,* **27** (1988) 4684–9.
14. Gasvik, K. J., Hovde, T. & Vadseth, T., Moiré technique in 3-D machine vision. *Opt. Lasers Engng,* **10** (1989) 241–9.
15. Engelhardt, K., Acquisition of 3-D data by focus sensing utilising the moiré effect of CCD camera. *Appl. Opt.,* **30** (1991) 1401–7.
16. Gruber, M. & Hausler, G., Simple, robust and accurate phase-measuring triangulation. *Optik,* **89** (1992) 118–22.
17. Gardenas-Garcia, J. F., Zheng, S. & Shen, F. Z., Implementation and use of an automated projection moiré experimental set-up, *Opt. Lasers Engng,* **21** (1994) 77–98.
18. Xie, X. & Atkinson, J. T., Absolute moiré contouring. *Opt. Lasers Engng* **27** (1996) 149–59.